



JOHANNES GUTENBERG
UNIVERSITÄT MAINZ

Structural and biochemical analysis of *SynDLP*, a bacterial dynamin-like protein with eukaryotic features

Dissertation

zur Erlangung des Grades

„Doktor der Naturwissenschaften“

im Promotionsfach Chemie

am Fachbereich Chemie, Pharmazie, Geographie und Geowissenschaften
der Johannes Gutenberg-Universität Mainz

Lucas Gewehr

Mainz, Juli 2023

D77

1. Berichtstatter: [REDACTED]

2. Berichtstatterin: [REDACTED]

Tag der mündlichen Prüfung:

Die vorliegende Arbeit wurde im Zeitraum von 2019 bis 2023 am Department Chemie der Johannes Gutenberg-Universität in Mainz unter Betreuung von [REDACTED] angefertigt. Ich versichere, dass ich diese Arbeit selbstständig verfasst habe und keine anderen als die angegebenen Quellen und Hilfsmittel verwendet habe.

Table of contents

Table of contents	1
I Summary.....	4
II Zusammenfassung	5
III Publications	6
IV Collaborations	6
1 Introduction.....	7
1.1 Membrane remodeling in eu- and prokaryotes.....	7
1.2 Cyanobacteria and the model organism <i>Synechocystis</i> sp. PCC 6803.....	8
1.2.1 The thylakoid membrane	10
1.3 The dynamin superfamily.....	16
1.3.1 Structure of DLPs	16
1.3.2 Functions of DLPs	19
1.3.3 Membrane remodeling by DLPs	22
1.3.4 <i>SynDLP</i> – a new cyanobacterial DLP.....	23
2 Objectives of this thesis	25
3 Materials and Methods.....	29
3.1 Materials	29
3.1.1 Chemicals.....	29
3.1.2 Buffers and solutions	29
3.1.3 Bacterial strains	32
3.1.4 Media	33
3.1.5 Oligonucleotides.....	34
3.1.6 Plasmids	39
3.1.7 Antibodies	41
3.1.8 Enzymes	41

3.1.9 Kits.....	41
3.1.10 Marker.....	42
3.1.11 Instruments.....	43
3.1.12 Software.....	45
3.2 Methods.....	46
3.2.1 Microbiological methods.....	46
3.2.2 Molecular biological methods.....	46
3.2.3 Preparative methods.....	51
3.2.4 Bioanalytical methods.....	56
3.2.5 Bioanalytical spectroscopy.....	59
3.2.6 Microscopic methods.....	70
4 Results and Discussion.....	77
4.1 <i>SynDLP</i> is a dynamin-like protein of <i>Synechocystis</i> sp. PCC 6803 with eukaryotic features.....	77
4.1.1 Publication.....	77
4.1.2 Abstract.....	79
4.1.3 Introduction.....	80
4.1.4 Results.....	83
4.1.5 Discussion.....	113
4.2 Effect of NaCl and DTT on oligomerization and activity of <i>SynDLP</i>	120
4.2.1 Introduction.....	120
4.2.2 Results.....	121
4.2.3 Discussion.....	128
4.3 Biochemical and biophysical analysis of membrane interaction properties of <i>SynDLP</i> and characterization of potential MIDs.....	131
4.3.1 Introduction.....	131
4.3.2 Results.....	133
4.3.3 Discussion.....	159

4.4 Nucleotide-dependent conformational changes in <i>SynDLP</i>	165
4.4.1 Introduction	165
4.4.2 Results	167
4.4.3 Discussion	175
4.5 Regulation of a disulfide bridge in <i>SynDLP</i> by thioredoxin	179
4.5.1 Introduction	179
4.5.2 Results	180
4.5.3 Discussion	185
4.6 <i>In vivo</i> role of <i>SynDLP</i> in the cyanobacterium <i>Synechocystis</i>	187
4.6.1 Introduction	187
4.6.2 Results	188
4.6.3 Discussion	203
5 Conclusion	207
6 Literature	209
7 Appendix	235
Abbreviations	246
List of Figures	250
List of Tables	254
Danksagung.....	255
Curriculum vitae.....	257

I Summary

Light energy is converted into chemical energy through the process of photosynthesis, which is the basis for complex life on earth. In most oxygenic photosynthetic organisms, a specialized internal membrane system, the thylakoid membrane (TM), harbors protein complexes that enable the conversion of light into chemical energy. There are still many unanswered questions about TM biogenesis and dynamics. Dynamin-like proteins (DLPs) are large mechanochemical GTPases with various membrane-active functions in eukaryotes. Recently, a bacterial DLP (BDLP) was identified in the cyanobacterial model organism *Synechocystis* sp. PCC 6803. The protein was termed *SynDLP* and is possibly involved in TM remodeling in the cyanobacterium. The physiological function of most BDLPs identified to date is unclear. Isolated *SynDLP* was found to be an active GTPase that forms oligomers in solution and interacts with negatively charged TM lipids. Moreover, *SynDLP* does not appear to be essential for *Synechocystis* sp. PCC 6803, at least under standard growth conditions.

My studies clearly confirm that *SynDLP* is a BDLP, as shown by the determined structure of *SynDLP* oligomers. The monomers consist of typical DLP domains. The arrangement of monomers within the oligomer resembles the architecture of some eukaryotic DLPs, here observed for the first time in a BDLP. Thus, *SynDLP* is the closest known ancestor of a group of eukaryotic DLPs. Moreover, *SynDLP* exhibits features unique for DLPs, such as an intramolecular disulfide bridge in the bundle signaling element (BSE) domain and a large intermolecular interface between the BSE and GTPase domains. Both influence the GTPase activity of *SynDLP*. To further study the membrane interaction properties of *SynDLP*, nucleotide-dependent membrane binding of *SynDLP* was visualized via fluorescence microscopy using a fluorescently labeled *SynDLP* variant. Surface plasmon resonance spectroscopy was established to quantify the membrane interaction propensity of *SynDLP*. Finally, a membrane activity of *SynDLP* was detected as it fuses TM-mimicking model membranes *in vitro*. Importantly, expression of native *SynDLP* in *Synechocystis* sp. PCC 6803 was detected using *SynDLP*-specific antibodies.

In summary, the results of this work provide new insights into the structure and function of *SynDLP*, the BDLP of *Synechocystis* sp. PCC 6803. The new information classifies *SynDLP* as a BDLP that is closely related to eukaryotic DLPs.

II Zusammenfassung

Lichtenergie wird durch den Prozess der Photosynthese in chemische Energie umgewandelt, die Grundlage für komplexes Leben auf der Erde. In den meisten oxygen-photosynthetischen Organismen wird die Umwandlung der Lichtenergie durch Proteinkomplexe in einem spezialisierten internen Membransystem, der Thylakoidmembran (TM), ermöglicht. Es gibt allerdings noch viele offene Fragen über die Biogenese und Dynamik der TM. Dynamin-ähnliche Proteine (engl.: *Dynamamin-like proteins*, DLPs) sind große mechanochemische GTPasen mit verschiedenen Funktionen an eukaryotischen Membranen. Kürzlich wurde ein bakterielles DLP (BDLP) in dem cyanobakteriellen Modellorganismus *Synechocystis* sp. PCC 6803 entdeckt. Das Protein wurde *SynDLP* benannt und ist möglicherweise bei der Reorganisation der TM im Cyanobakterium beteiligt. Die physiologische Funktion der meisten bisher entdeckten BDLPs ist unklar. Isoliertes *SynDLP* ist eine aktive GTPase, die in Lösung Oligomere bildet und mit negativ geladenen TM-Lipiden interagiert. Ferner scheint *SynDLP*, zumindest unter standardmäßigen Wachstumsbedingungen, nicht essenziell für *Synechocystis* sp. PCC 6803 zu sein.

Meine strukturellen Untersuchungen von *SynDLP* Oligomeren bestätigen, dass *SynDLP* ein BDLP ist. Die Monomere sind aus typischen DLP-Domänen aufgebaut. Die Anordnung der Monomere innerhalb des Oligomers ähneln der Architektur einiger eukaryotischer DLPs, was hier erstmalig in einem BDLP beobachtet wurde. Somit ist *SynDLP* der nächste bekannte Verwandte einiger eukaryotischer DLPs. Weiterhin besitzt *SynDLP* einige neue und besondere Charakteristika. Neben einer intramolekularen Disulfidbrücke in der *bundle signaling element* (BSE)-Domäne hat *SynDLP* eine große intermolekulare Kontaktfläche zwischen der BSE- und GTPase-Domäne. Beides beeinflusst die GTPase Funktion von *SynDLP*. Des Weiteren wurde die Nukleotid-abhängige Membranbindung von *SynDLP* mittels einer Fluoreszenz-markierten *SynDLP*-Variante durch Fluoreszenzmikroskopie sichtbar gemacht. Oberflächenplasmonenresonanzspektroskopie wurde etabliert, um die Membraninteraktion von *SynDLP* zu quantifizieren. Schließlich wurde gezeigt, dass *SynDLP* Modellmembranen, die die TM imitieren, *in vitro* fusionieren kann. Wichtig ist außerdem, dass die Expression von nativem *SynDLP* in *Synechocystis* sp. PCC 6803 durch den Einsatz spezifischer Antikörper nachgewiesen werden konnte.

Zusammenfassend erlauben die in dieser Arbeit beschriebenen strukturellen und biochemischen Analysen neue Einblicke in die Struktur und Funktion von *SynDLP*, dem BDLP von *Synechocystis* sp. PCC 6803. Die neuen Informationen bestätigen, dass *SynDLP* ein BDLP ist, welches große Ähnlichkeiten zu eukaryotischen DLPs aufweist.

III Publications

Parts of this thesis are published (# = equal contribution):

- Gewehr, L.#, Junglas, B.#, Jilly, R., Franz, J., Zhu, W.E., Weidner, T., Bonn, M., Sachse, C. and Schneider, D. (2023) ‘*SynDLP* is a dynamin-like protein of *Synechocystis* sp. PCC 6803 with eukaryotic features’, *Nature Communications*, 14(1), p. 2156.

The published article is cited in Chapter 4.1.

IV Collaborations

The data presented in this thesis were obtained in collaboration with the following research groups and persons:

- [REDACTED] and [REDACTED], Research Center Jülich
- [REDACTED], [REDACTED] and [REDACTED], Max-Planck-Institute for Polymer Research Mainz
- [REDACTED] and [REDACTED], University of Bayreuth
- [REDACTED] and [REDACTED], Johannes Gutenberg University Mainz

The following projects and theses were supervised during my thesis:

- ‘Identifizierung funktioneller Domänen in einem cyanobakteriellen Dynamin-ähnlichem Protein (*SynDLP*)’, [REDACTED], Bachelor Thesis, 2021
- ‘Influence of Dithiothreitol (DTT) on Oligomerization and GTPase Activity of *SynDLP*’, [REDACTED], Research Internship, 2021
- ‘Biochemische Analyse einer potentiellen Membran-Interaktions-Domäne in *SynDLP*’, [REDACTED], Research Internship, 2022
- ‘Membrane interactions of *SynDLP*’, [REDACTED], Master Thesis, 2022

1 Introduction

1.1 Membrane remodeling in eu- and prokaryotes

A biological cell is the basic unit of life. All living cells are surrounded by a membrane that consists of a lipid bilayer, a physical barrier that separates the inside of a cell from its environment. Eukaryotic cells also contain internal membrane systems to achieve compartmentalization and specialization (Bohuszewicz, Liu and Low, 2016). In addition to functioning as a physical barrier, membranes also act as a scaffold for diverse proteins and protein complexes (Byrne and Iwata, 2002) and, moreover, allow the formation of gradients of various molecules across the membrane. These gradients are utilized in several physiological processes, and *e.g.* a proton gradient across the inner mitochondrial membrane or the thylakoid membranes (TMs) of chloroplasts and cyanobacteria drives adenosine triphosphate (ATP) synthesis (Junge and Nelson, 2015).

A prerequisite for a proper lipid bilayer function is an adequate rigidity to maintain the membrane integrity. Yet, membranes need a certain flexibility to allow continuous remodeling required due to changing environmental conditions (Bohuszewicz, Liu and Low, 2016). Dynamic membrane remodeling is vital for all organisms to maintain the cellular compartmentalization in eukaryotes, as well as maintaining the integrity of prokaryotic membrane systems. In eukaryotes, physiological processes, such as endo-/exocytosis, cell division or intracellular trafficking, require extensive membrane remodeling (Vega-Cabrera and Pardo-López, 2017). Membrane remodeling events often involve the activity of integral or peripheral membrane proteins that modulate the membrane thickness, lipid composition, as well as the curvature of the lipid bilayer either by actively inducing membrane curvature (McMahon and Gallop, 2005) or by passive remodeling via different mechanisms, *e.g.*, protein crowding (Stachowiak *et al.*, 2012) or asymmetric lipid enrichment (McMahon and Gallop, 2005; Bohuszewicz, Liu and Low, 2016). Examples for eukaryotic membrane remodeling proteins are SNARE complexes (Jahn and Scheller, 2006) and BAR-domain-containing proteins (Mim and Unger, 2012).

Bacterial membranes are clearly less complex organized when compared to eukaryotic cells. Yet, dynamic membrane rearrangement has also been observed in bacteria, for example during the formation of outer-membrane vesicles (Zhou *et al.*, 1998) or spore morphogenesis (McKenney, Driks and Eichenberger, 2013). Interestingly, the last decades revealed that many eukaryotic proteins, which are involved in membrane dynamics and/or repair, have homologs

in prokaryotes, which suggests that the underlying mechanisms were invented in a common ancestor of pro- and eukaryotes (Vega-Cabrera and Pardo-López, 2017; Siebenaller and Schneider, 2023). *E.g.*, the proteins FtsA, FtsZ and ZipA mediate membrane constriction during bacterial cytokinesis and were identified to be homologous of the eukaryotic proteins actin, tubulin and MAP-Tau (Bork, Sander and Valencia, 1992; Hale and Boer, 1997; Löwe and Amos, 1998; RayChaudhuri, 1999; Szwedziak *et al.*, 2014).

1.2 Cyanobacteria and the model organism *Synechocystis* sp. PCC 6803

Cyanobacteria are photoautotrophic prokaryotes that perform oxygenic photosynthesis. Together with other primary oxygen producers, like plants and algae, they are responsible for the production of all atmospheric oxygen that is consumed by aerobic species, showing a pivotal role of cyanobacteria in the ecosystem earth (Stanier, 1977; Knoll, 2008). Cyanobacteria are characterized by a high resilience, whereby they can populate various habitats, such as marine or freshwater. Even extreme environments, such as volcanic ash, can be populated by cyanobacteria (Gaysina, Saraf and Singh, 2019). The progenitors of current cyanobacterial species appeared around 3.5 billion years ago, probably as the first oxygenic autotrophs. The emergence of cyanobacteria had a huge impact on the atmosphere, transforming the previously reducing into an oxidizing atmosphere with enriched oxygen (Holland, 2006; Knoll, 2008). This event enabled the evolution of life based on an aerobic metabolism, which is more efficient compared to an anaerobic metabolism (Jiang *et al.*, 2012).

Current cyanobacteria and chloroplasts have a common evolutionary ancestor. The endosymbiotic theory suggests the uptake of an early oxygenic photoautotrophic prokaryotic cell into a eukaryotic cell, finally leading to the incorporated prokaryotic cell evolving into chloroplasts (Martin *et al.*, 2002). Cyanobacteria are also discussed in the context of light-driven biotechnology (Abed, Dobretsov and Sudesh, 2009), as they are relatively easy to cultivate and can be used to produce biofuel (Al-Haj *et al.*, 2016) or anti-inflammatory substances (Choi *et al.*, 2012). Further applications are the use of whole cyanobacterial cells as nutritional supplements (Khan, Bhadouria and Bisen, 2005), biofertilizers (Song *et al.*, 2005; Kiran, Madhu and Satyanarayana, 2015) or photosynthetic biofuel cells (Morishima *et al.*, 2007). However, the use of cyanobacterial cells for large-scale biotechnological applications is still limited due to the insufficient photosynthetic efficiency (Luan, Zhang and Lu, 2020).

As a result of the common evolutionary origin, cyanobacterial cells and chloroplasts show a great functional and structural similarity, and consequently, cyanobacteria are important model organisms for studies on photosynthesis (Stanier, 1977; Martin *et al.*, 2002). In this work, the frequently used cyanobacterial model organism *Synechocystis* sp. PCC 6803 (hereafter: *Synechocystis*) was investigated. Working with *Synechocystis* provides some benefits, such as its natural competence (Barten and Lill, 1995), a relatively short doubling time of approx. 12 h (Vermass, Rutherford and Hansson, 1988) and its glucose tolerance (Anderson and McIntosh, 1991). Moreover, *Synechocystis* was the first phototrophic organism with a completely sequenced genome (Kaneko *et al.*, 1996; Ikeuchi and Tabata, 2001).

The structure of a typical *Synechocystis* cell is illustrated in Fig. 1.1. The unicellular organism is surrounded by an outer and a cytoplasmic membrane (CM), which are separated by a cell wall consisting of a peptidoglycan layer (Meene *et al.*, 2006). The outer membrane can be coated by a proteinaceous surface layer (S-layer) (Šmarda *et al.*, 2002). The cytoplasm contains several elements, such as carboxysomes, which is a cyanobacterial microcompartment used for CO₂-fixation (L.-N. Liu *et al.*, 2021), ribosomes and a genome consisting of multiple copies of an identical, circular DNA (Griese, Lange and Soppa, 2011). The protein complexes of the photosynthetic light reaction are localized in an extra internal membrane system called the TMs, which will be described in more detail in the following chapter.

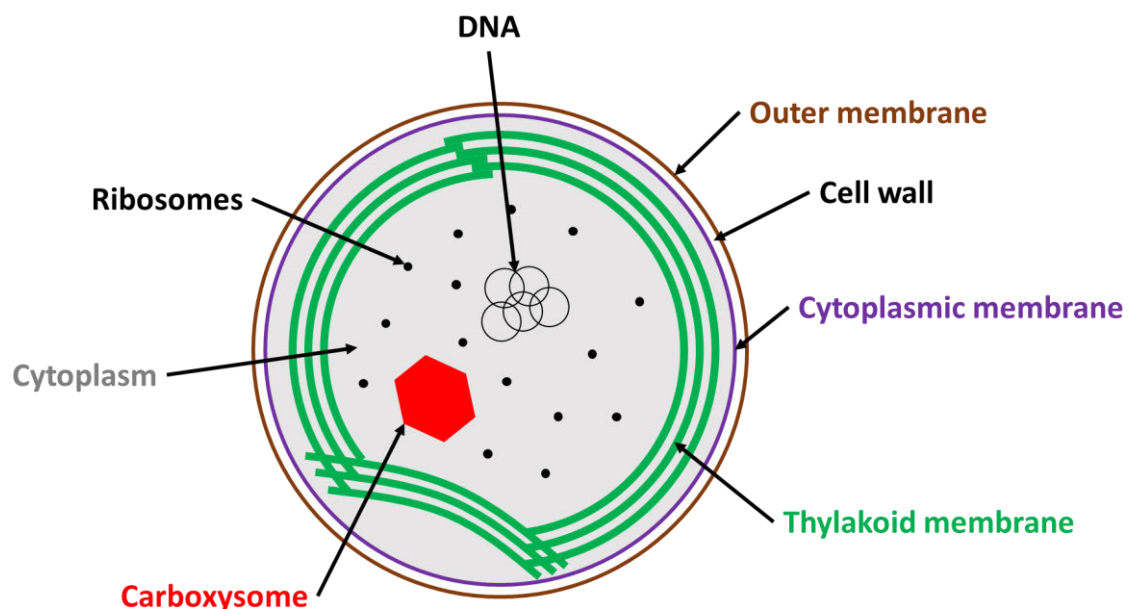


Figure 1.1: Schematic representation of a *Synechocystis* cell.

A typical *Synechocystis* cell is surrounded by the outer membrane (brown) and the CM (purple), which are separated by a cell wall (white). The TM (green) is an additional internal membrane system that encloses the thylakoid lumen. Other structures, such as the genomic DNA (black circles), ribosomes (black dots) or carboxysomes (red) are located within the cytoplasm (light grey).

1.2.1 The thylakoid membrane

1.2.1.1 Photosynthesis

The TMs are a completely separated internal membrane system in cyanobacteria and chloroplasts, which has in fact a pseudo-organelle character. An additional cell compartment is surrounded by the TMs called the thylakoid lumen. The TMs harbor the protein complexes involved in the photosynthetic light reaction (Fig. 1.2) (Lea-Smith *et al.*, 2016; Liu, 2016).

In the photosynthetic light reaction, the energy of sunlight is converted into chemical energy in the form of reduced nicotinamide adenine dinucleotide phosphate (NADPH) and ATP. In more detail, in cyanobacteria, the light energy is absorbed by phycobilisomes (PBS) that are equipped with appropriate pigments and transferred to the reaction center of photosystem II (PS II). Here, the excitation of a certain chlorophyll pair leads to a charge separation whereby electrons are released into the electron transport chain. The electron gap in the PS II reaction center is filled by the oxidation of water molecules at a water splitting complex. This reaction also produces oxygen and protons are released into the thylakoid lumen. The excited electrons in PS II next reduce plastoquinone (PQ), a redox mediator localized within the TM, which passes the electrons on to the cytochrome b_6f complex (cyt b_6f). This complex additionally mediates proton transport from the cytoplasm to the thylakoid lumen. The next electron acceptor in the electron transport chain is the soluble redox mediator plastocyanin (PC) that transfers the electrons to photosystem I (PS I). Again, using light energy, the electrons can be excited and are transferred to ferredoxin (FD). The FD-NADP⁺ reductase (FNR) catalyzes the transfer of the electrons to the final acceptor NADP⁺ (oxidized nicotinamide adenine dinucleotide phosphate) resulting in the formation of the reduction equivalent NADPH. This reaction consumes protons in the cytoplasm. At the end, water splitting at PS II, the H⁺-pump activity of the cyt b_6f and the NADPH formation build up a proton gradient across the TM, which can be used by the ATP synthase to produce ATP via phosphorylation of adenosine diphosphate (ADP). The two products of the light reaction (ATP, NADPH) are subsequently used for the energy intense synthesis of glucose via reduction of CO₂ in the Calvin-Benson cycle (Shevela, Pishchalnikov and Eichacker, 2013; Lea-Smith *et al.*, 2016; Liu, 2016).

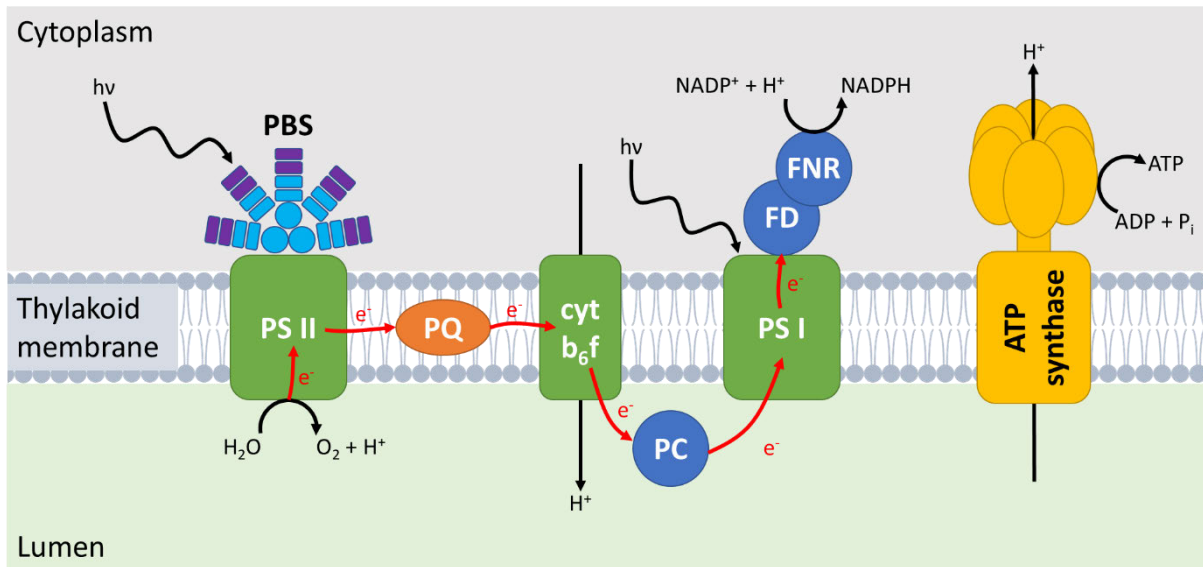


Figure 1.2: Schematic overview of the photosynthetic light reaction in the TMs.

The protein complexes of the photosynthetic light reaction are localized within the TMs. PBS collect and transfer the light energy to PS II, from which the excited electrons are transferred to PQ, the cyt b_6f , PC, PS I, FD and finally, catalyzed by the FNR, to NADP^+ leading to the generation of NADPH. The resulting electron gap in PS II is filled by water oxidation. A proton gradient is built up during electron transport that can be used for ATP synthesis by the ATP synthase.

The light reaction with the described linear electron transport chain is precisely regulated in cyanobacteria and chloroplasts. Depending on varying requirements of ATP *vs.* NADPH, the electron transport chain can partly shift to a cyclic electron transport via transfer of electrons from FD to PQ resulting in an increased proton gradient and finally increased ATP/NADPH ratio (Bernát, Waschewski and Rögner, 2009; Yamori and Shikanai, 2016). Remarkably, the cyanobacterial TMs also contain the protein complexes of the respiratory chain. Thus, the photosynthetic and respiratory electron transfer chains act simultaneously in the same compartment (Vermaas, 2001; Mullineaux, 2014). In fact, both electron chains overlap due to the usage of identical redox components. Besides electrons from PS II, the PQ pool can be reduced by electrons originating from respiratory complexes, *i.e.* the type 1 NAD(P)H dehydrogenase and/or the succinate dehydrogenase (Ogawa, 1991; Cooley, Howitt and Vermaas, 2000; Ohkawa *et al.*, 2000; Vermaas, 2001). Furthermore, electrons of the PQ pool can be utilized by a Q-oxidase resulting in reduction of oxygen and water formation, and FD can be used to transfer electrons to terminal oxidases to reduce molecular oxygen.

1.2.1.2 Lipid composition and the structure of the TM

Compared to other biological membranes, the TM shows a unique lipid composition that is highly conserved among oxygenic phototrophic organisms (Yoshihara and Kobayashi, 2022). The TM lipid composition is dominated by the galactolipids monogalactosyldiacylglycerol (MGDG), digalactosyldiacylglycerol (DGDG) and sulfoquinovosyldiacylglycerol (SQDG). Furthermore, the TM contains the negatively charged phospholipid phosphatidylglycerol (PG). Analysis of lipid compositions in *Synechocystis* total membranes showed that the neutral galactolipids MGDG and DGDG represent 52 – 59% and 12 – 17% of the whole lipids, respectively. The negatively charged lipids SQDG and PG make up 16 – 22% and 8 – 11%, respectively (Wada and Murata, 1989; Boudière *et al.*, 2014), as summarized in Fig. 1.3. Note that the values refer to the lipid composition of the TMs plus the envelope, which contains the lipids of outer membrane and CM. However, it has been shown for another cyanobacterium that the lipid composition of TM and envelope differ only slightly (Murata *et al.*, 1981). Additionally, in *Synechocystis* membranes a small amount of monoglucosyldiacylglycerol (MGlcDG) is present, which is probably a biosynthetic precursor of MGDG (Boudière *et al.*, 2014; Sato, 2015).

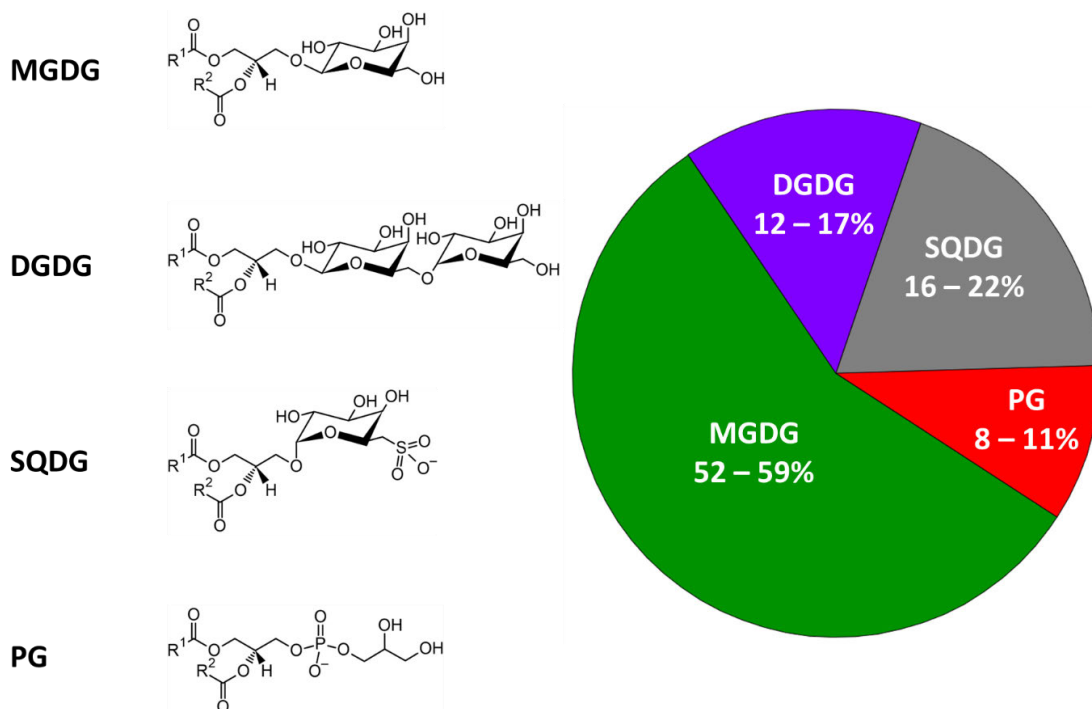


Figure 1.3: Lipid composition of *Synechocystis* total membranes.

The TMs and the envelope of *Synechocystis* mainly consist of the three galactolipids MGDG, DGDG and SQDG, as well as the phospholipid PG. The chemical structures show that SQDG and PG have negatively charged headgroups (R¹ and R² = fatty acid residues). The relative amounts shown on the right summarize lipid compositions described in two different publications (Wada and Murata, 1989; Boudière *et al.*, 2014).

The lipid composition can vary among different cyanobacterial species and may include other lipids in case of eukaryotic chloroplasts (Block *et al.*, 2007; Jouhet, Maréchal and Block, 2007; Boudière *et al.*, 2014). Remarkably, the amount of the major lipid species MGDG in TMs is always above 50%, indicating a pivotal role in TMs structure and photosynthesis. Yet, in contrast to the remaining TM lipids, MGDG forms inverse hexagonal lipid structures (H_{II} phase) in absence of other lipids or proteins (Sanderson and Williams, 1992). Therefore, the formation of a functional TM bilayer is only possible due to the presence of membrane proteins and/or additional lipid species (Lee, 2000; Simidjiev *et al.*, 2000). Moreover, a constant negative charge seems to be a prerequisite for functional TMs, since the loss of negatively charged lipids, either by decreased SQDG or decreased PG content, is usually compensated by increased PG content or, conversely, SQDG (Güler *et al.*, 1996; Essigmann *et al.*, 1998; Aoki *et al.*, 2004). The negative surface charge of the TMs is important for interactions of lipids with integral as well as peripherally attached membrane proteins. However, SQDG and PG cannot functionally replace each other completely, as *e.g.*, PG has essential roles in the stabilization of cyanobacterial PS I and II (Sato *et al.*, 2000; Yoshihara and Kobayashi, 2022).

Between cyanobacteria and chloroplasts, the structure of the TMs network differs. In eukaryotic chloroplasts the TMs are arranged as thylakoid stacks (grana thylakoids) that possess high amounts of PS II and are connected with unstacked areas (stroma thylakoids) containing high amounts of PS I and ATP synthase (Adam *et al.*, 2011). The structure of TMs can be tuned via varying the lipid composition, and *e.g.*, it has been shown that the predominant, conically shaped lipid MGDG appears in higher concentrations in highly curved TM regions (Gounaris *et al.*, 1983). The cyanobacterial TMs are usually less complex organized compared to chloroplast TMs, yet a spatial arrangement of the photosystems can be observed (Olive *et al.*, 1997; Lea-Smith *et al.*, 2016; Liu, 2016; Huokko *et al.*, 2021). The TMs structure can also significantly vary between different cyanobacterial species (Herrero and Flores, 2008). *E.g.*, *Synechocystis* shows curved, parallelly arranged TMs that converge close to the CM, whereas *Synechococcus* strains form no such highly curved TMs regions (Rast, Heinz and Nickelsen, 2015; Huokko *et al.*, 2021). However, the functions of the TMs are conserved in the corresponding species, albeit the TMs structures can differ remarkably. Special cases are cyanobacteria from the genus *Gloeobacter*, *e.g.*, *Gloeobacter violaceus* or *Gloeobacter kilaueensis*, as they completely lack an internal TM system. In these species, the complexes of the photosynthetic light reaction are located within the CM (Rippka, Waterbury and Cohen-Bazire, 1974; Saw *et al.*, 2013).

1.2.1.3 TM biogenesis and dynamics

Although the TM is highly important for life on earth, there are still many open questions concerning its biogenesis (Rast, Heinz and Nickelsen, 2015; Siebenaller and Schneider, 2023). In eukaryotic cells, the chloroplasts develop from undifferentiated proplastids, which lack a developed TM system. Triggered by environmental changes, *e.g.*, exposition to light, proplastids can differentiate into chloroplasts (Waters and Langdale, 2009). It is discussed that several processes occur during this differentiation process. *E.g.*, the inner envelope membrane of the plastids might form a continuum with the developing internal membrane system via invaginations in the early stage of plastid differentiation. Additionally, vesicles release from the inner envelope membrane has been observed and the vesicles subsequently fuse to build the TM system consisting of stroma and grana thylakoids (Rosinski and Rosen, 1972; Pribil, Labs and Leister, 2014; Rast, Heinz and Nickelsen, 2015; Mechela, Schwenkert and Soll, 2019).

The processes involved in biogenesis of cyanobacterial TMs are still largely enigmatic. The complex and unique architecture of the TM (Chapter 1.2.1.2) clearly requires a highly coordinated assembly of the membrane and protein components. Thus far, a *de novo* synthesis of cyanobacterial TMs cannot be excluded, however, they are most likely built from preexisting remnants of the TM (Barthel *et al.*, 2013; Mullineaux and Liu, 2020; Siebenaller and Schneider, 2023). Biosynthesis of proteins, lipids and pigments might take place in the CM, and transport to preexisting TMs is enabled either by direct connections between TM and CM or a vesicle transport system (Nickelsen *et al.*, 2011). A fluorescence-based study suggests a vesicular transport system in *Synechocystis* (Schneider *et al.*, 2007). A study on the three-dimensional structure of *Synechocystis* identified a connection between TM and CM (Meene *et al.*, 2006). However, in most studies, a direct connection between the TM and the CM has not been identified. The TMs rather appear to converge close to the CM, finally resulting in local contact sites named thylapses that might play a specific role in TM biogenesis (Schneider *et al.*, 2007; Rast *et al.*, 2019; Mullineaux and Liu, 2020; Siebenaller and Schneider, 2023). In a recent study, thylapse-like structures could also be identified in the cyanobacterium *Synechococcus elongatus* PCC 7942 (Huokko *et al.*, 2021).

The TM harbors the complex photosynthetic machinery and requires regulated protein activities and continuous membrane remodeling to adapt this machinery to changing environmental conditions, especially under conditions of light stress (Rottet, Besagni and Kessler, 2015). As already mentioned, the TM contains proteins, pigments, and cofactors besides the lipids. In fact, the protein amount makes up around 60% in a weight-to-weight ratio with lipids in pea

chloroplasts (Chapman, De-Felice and Barber, 1983). Although not developed as strongly as in plant TMs, the cyanobacterial TMs also show a lateral heterogeneity. This leads to the formation of functional membrane domains that are spatially separated, likely enabling a better regulation of the photosynthetic light reaction (Agarwal *et al.*, 2010; Liu, 2016; Mullineaux and Liu, 2020; Huokko *et al.*, 2021). Another mechanism regulating cyanobacterial photosynthesis is the mobility of the PBS along the cytoplasmic surface of the TMs, which enables an adapted supply of light energy to the two photosystems PS I and PS II in response to changing light conditions. This process is known as state transitions. (Olive *et al.*, 1997; Joshua and Mullineaux, 2004; Mullineaux and Emlyn-Jones, 2005; Liu, 2016).

In addition to proteins directly involved in photosynthesis, proteins act on the regulation of the TM structure and composition by continuous membrane remodeling and repair. In cyanobacteria, several proteins have been suggested to be involved in TM remodeling (Siebenaller and Schneider, 2023). *E.g.*, proteins of the DedA superfamily might have a scramblase function in cyanobacterial TMs or CMs (Keller and Schneider, 2013). The CurT protein in *Synechocystis* seems to be crucial for correct TM biogenesis and especially for the formation of highly curved TM regions (Heinz *et al.*, 2016). The recently discovered AncM protein has been suggested to act as an antagonist to CurT in shaping the TM ultrastructure (Ostermeier *et al.*, 2022). Proteins of the SPFH superfamily might be involved in the formation of lipid microdomains, which are crucial for PS II biogenesis and/or repair (Knoppová *et al.*, 2022). Other examples of membrane remodeling proteins in cyanobacteria are the IM30 (also referred to as Vipp1) protein and its homolog PspA, which potentially have a crucial role in formation, maintenance, dynamics and/or repair of the TMs (Westphal *et al.*, 2001; Fuhrmann *et al.*, 2009; Gao and Xu, 2009; Hennig *et al.*, 2015; Heidrich, Thurotte and Schneider, 2017; Junglas *et al.*, 2021). Both proteins are homologous to the ESCRT-III core subunit of the eukaryotic ESCRT complex, which is pivotally involved in several membrane fission, fusion, and repair processes (Gupta *et al.*, 2021; J. Liu *et al.*, 2021; Junglas *et al.*, 2021). Interestingly, all the described cyanobacterial proteins with potential roles in TM dynamics have eukaryotic homologs that are typically better characterized (Siebenaller and Schneider, 2023). Furthermore, dynamin-like proteins (DLPs) are membrane remodeling proteins with well-established functions in membrane dynamics and/or repair in eukaryotes (Praefcke and McMahon, 2004). These proteins are also found in (cyano)bacteria (Blick, 1999; Low and Löwe, 2006; Jilly *et al.*, 2018). Thus, it is feasible to also assume a role of DLPs in cyanobacterial TM dynamics.

1.3 The dynamin superfamily

The dynamin superfamily, hereafter referred to as DLPs, is a protein family of mechanochemical enzymes that hydrolyze guanosine triphosphate (GTP) (= GTPases). Unlike other GTPases, such as Ras-like GTPases (Lu *et al.*, 2016), DLPs are characterized by a relatively large molecular mass of >60 kDa. The energy gained via GTP hydrolysis is typically used for membrane remodeling by either fission or fusion of a membrane template (Praefcke and McMahon, 2004; Daumke and Praefcke, 2016). Almost 40 years ago, the interferon-induced myxovirus resistance protein (Mx) was identified as the first member of the DLP family (Staelheli *et al.*, 1986). However, dynamin, the namesake of the protein family, was discovered shortly after Mx and isolated from a calf brain (Shpetner *et al.*, 1989). Isolated dynamin was shown to hydrolyze GTP after activation by tubulin (Shpetner and Vallee, 1992). The prototypical dynamin (Dyn1) is mainly expressed in synaptic cells. Two more isoforms were identified in mammalian cells: Dyn2 is ubiquitously expressed in different cell types, whereas Dyn3 is exclusively found in brain, lung, and testis tissue (Cook, Urrutia and McNiven, 1994; Cook, Mesa and Urrutia, 1996). While DLPs were initially assumed to be eukaryotic inventions, in 1999 a bioinformatic study predicted the existence of bacterial DLPs (BDLPs) (Blick, 1999). Interestingly, the first biochemically and structurally characterized BDLP originates from a cyanobacterium (*Nostoc punctiforme*) (Low and Löwe, 2006).

1.3.1 Structure of DLPs

DLPs are typically identified via sequence alignment of conserved GTP-binding motifs as well as their relatively large molecular mass. The conserved GTP-binding motifs include the G1 motif or P-loop, the G2-motif or switch I, the G3-motif or switch II and the G4-motif (Fig. 1.4) (Praefcke and McMahon, 2004; Daumke and Praefcke, 2016), all located in a domain called the GTPase domain (GD).

	<u>G1/P-loop</u>	<u>G2/switch I</u>	<u>G3/switch II</u>	<u>G4</u>
Dyn1	34 IAVVGGQSAGKSSVLEN ⁵⁰	63 IVTRR ⁶⁷	133 TLVDLPGMTK ¹⁴²	202 GVITKLDLMD ²¹¹
MxA	73 IAVIGDQSSGKSSVLEA ⁸⁹	101 IVTRC ¹⁰⁵	175 TLIDLPGITR ¹⁸⁴	244 GILTKPDLVD ²⁵³
AtFz1	352 MVIVGEFNSGKSTVINA ³⁶⁸	381 PTTNE ³⁸⁵	423 NIVDTPGTNV ⁴³²	481 FILNKSDIYR ⁴⁹⁰
ScMgm1	213 IVVIGSQSSGKSSVLES ²²⁹	242 MVTRR ²⁴⁶	314 SLVDLPGYIQ ³²³	382 GVITKLDLVD ³⁹¹
NpBDLP	72 LLVLGDMKRKGKSTFLNA ⁸⁸	101 PCTAV ¹⁰⁵	177 EIVDSPGLND ¹⁸⁶	235 FLVNAWDQVR ²⁴⁴
MsIniA	41 VVIAGQLKQKGSQLLNS ⁵⁷	70 ESTVL ⁷⁴	140 AFVDTPGVGG ¹⁴⁹	198 IVATKTDLYP ²⁰⁷
EcLeoA	56 IALLGAFSDGKTSVIAA ⁷²	86 DESSD ⁹⁰	105 EIVDTPGLFG ¹¹⁴	174 FVINKMDEV ¹⁸³
Consensus	GxxxxGKS	T	DxxG	T/NxxD

Figure 1.4: Conserved GTP-binding motifs in DLPs.

Amino acid sequences of selected DLPs highlight the four conserved GTP-binding motifs in the GD. The DLP sequences are derived from the sequences of the eukaryotic representatives human Dyn1 as well as MxA, Fz1 from *Arabidopsis thaliana* (AtFz1) and Mgm1 from *Saccharomyces cerevisiae* (ScMgm1). BDLP sequences originate from *Nostoc punctiforme* (NpBDLP), *Mycobacterium smegmatis* (MsIniA) and *E. coli* (EcLeoA).

While DLPs are multidomain proteins only the GD is conserved on the sequence level. In the past years, several high-resolution structures of eukaryotic DLPs as well as BDLPs were determined revealing a conserved domain arrangement (Jimah and Hinshaw, 2018; Ford and Chappie, 2019). Besides the globular GD, DLPs consist of an α -helical bundle signaling element (BSE) domain that connects the GD to an also α -helical stalk domain. Typically, a membrane interaction domain (MID) is located at the tip of the stalk domain (Fig. 1.5) (Prakash, Praefcke, *et al.*, 2000; Low and Löwe, 2006; Kong *et al.*, 2018).

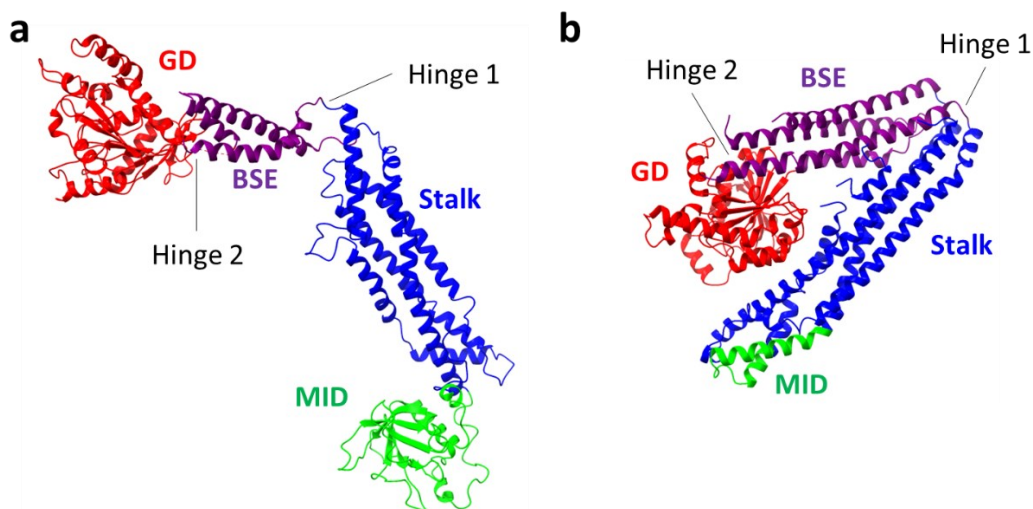


Figure 1.5: Monomer structure of DLPs.

(a) Structure of a human Dyn1 monomer (PDB: 6DLU) in ribbon representation. The GD, BSE, stalk and MID are colored in red, purple, blue and green, respectively. The positions of the two hinges connecting either stalk and BSE (Hinge 1) or BSE and GD (Hinge 2) are highlighted. (b) Monomer structure of the bacterial *NpBDLP* (PDB: 2J69) in ribbon representation. Coloring as in (a). Additionally, the two hinges are labeled.

Eukaryotic and bacterial proteins can be structurally categorized into the DLP class by looking at the conserved domain architecture (Fig. 1.6). Typically, the largest parts of the proteins are attributed to the globular GD and the α -helical stalk. The BSE is split into three parts (BSE1-3) on the primary sequence level (Ford and Chappie, 2019). The stalk is usually interrupted by an MID of varying size, and some DLPs are even anchored in the membrane by transmembrane domains (TMDs) (Gao, Sage and Osteryoung, 2006; Bian *et al.*, 2011; Yan *et al.*, 2015, 2020; Chandhok, Lazarou and Neumann, 2018; Yu *et al.*, 2020). Besides the conserved domains, a few DLP group members contain additional domains, and *e.g.*, classical dynamin has a C-terminal proline-rich domain (PRD), which could not be structurally determined so far due to its high flexibility. Therefore, the PRD is usually omitted from the constructs used for structure determination (Ford and Chappie, 2019).

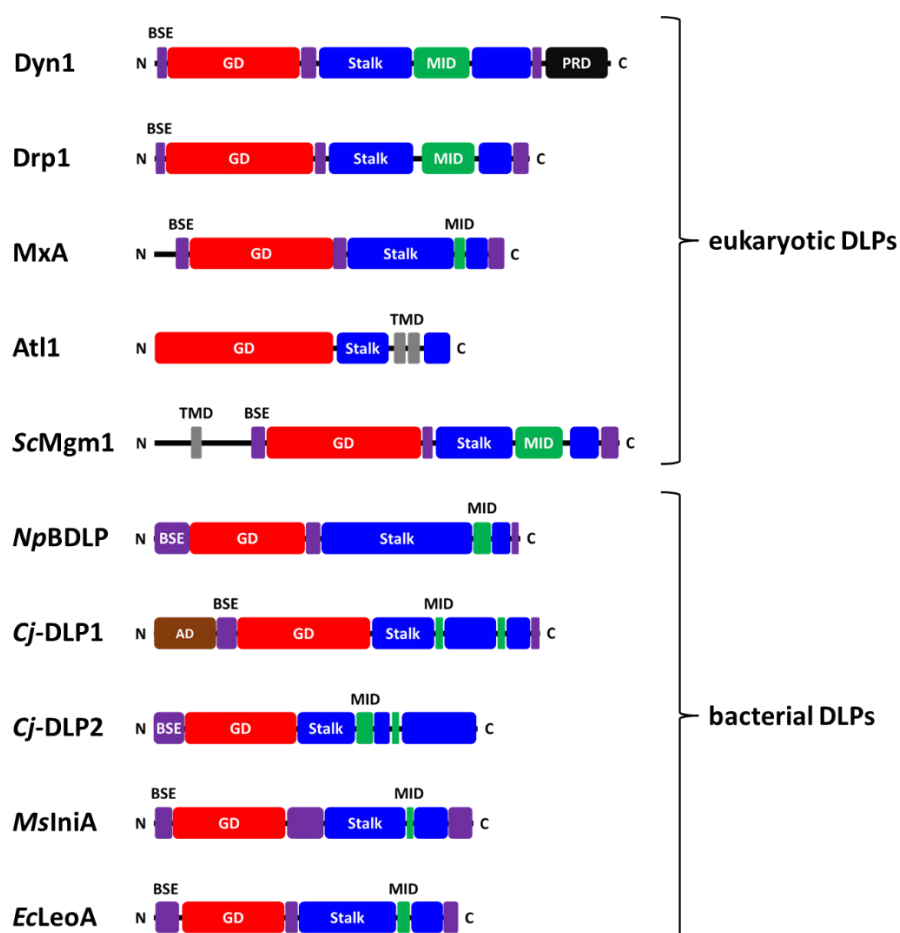


Figure 1.6: Structure-based domain architecture of DLPs.

The domain arrangement of several DLPs derived from solved structures is shown. The eukaryotic representatives are human Dyn1 (PDB: 3SNH), Drp1 (PDB: 4BEJ), MxA (PDB: 3SZR), atlastin1 (At11, PDB: 3QOF) and fungal *ScMgm1* (PDB: 6QL4). The members of the BDLP subclass are *NpBDLP* (PDB: 2J69), *Campylobacter jejuni* DLP pair 1/2 (*Cj-DLP1/2*, PDB: 5OWV), *MsIniA* (PDB: 6J73) and *EcLeoA* (PDB: 4AUR). N = N-terminus, C = C-terminus, GD = GTPase domain (red), BSE = bundle signaling element (purple), stalk (blue), MID = membrane interaction domain (green), PRD = proline-rich domain (black), TMD = transmembrane domain (gray), AD = assembly domain (brown).

Another characteristic of many DLPs, especially eukaryotic representatives, is their propensity to oligomerize. *In vitro*, the assembly of DLP monomers/dimers/tetramers into regular oligomers is typically triggered by the addition of nucleotides or a suitable membrane template (Daumke and Praefcke, 2016; Ford and Chappie, 2019). Interestingly, the hitherto characterized BDLPs typically showed no such oligomerization behavior and form small assemblies regardless of the addition of nucleotides or membranes (Bürmann *et al.*, 2011; Michie *et al.*, 2014; Wang *et al.*, 2019). So far, solely for the cyanobacterial *Np*BDLP a membrane-triggered oligomerization has been shown *in vitro* (Low *et al.*, 2009). A special case in the protein family of DLPs is the bacterial *Cj*-DLP1/2, which forms heterotetramers in solution consisting of two dynamin-like polypeptide chains that assemble via a unique assembly domain (Liu, Noel and Low, 2018).

1.3.2 Functions of DLPs

Functionally, most DLPs can be subdivided into either membrane *fusion* or *fission* DLPs (Ramachandran and Schmid, 2018). Both processes are necessary to ensure the integrity of a biological membrane system. Since the discovery of DLPs, many distinct functions of proteins belonging to this protein family have been elucidated in eukaryotic cells that will be described in more detail in the following.

1.3.2.1 Functions of eukaryotic DLPs

In mammalian, insect, and fungal cells, DLPs are usually involved in the remodeling of the plasma membrane or organelle membranes. The classical dynamin is a *fission* DLP that is involved in clathrin-mediated endocytosis. It catalyzes the scission of clathrin-coated vesicles from the plasma membrane (Hinshaw and Schmid, 1995; Mettlen *et al.*, 2009; Ramachandran, 2011). Other *fission* DLPs remodel the membranes of cell organelles. *E.g.*, dynamin-related protein 1 (Drp1) is recruited by specific receptors to the outer mitochondrial membrane, where it oligomerizes and constricts the membrane for organelle division. This process is crucial for mitochondrial inheritance, genome maintenance as well as metabolic adaptation and conserved in eukaryotic species (Bleazard *et al.*, 1999; Smirnova *et al.*, 2001; Kraus and Ryan, 2017; Kalia *et al.*, 2018). The *fusion* DLP mitofusin is a counterpart of Drp1 as it is a membrane anchored DLP that is involved in the fusion of outer mitochondrial membranes from adjacent mitochondria (Cao *et al.*, 2017; Chandhok, Lazarou and Neumann, 2018). Other examples for

fusion DLPs in eukaryotic cells include OPA1 and Mgm1, which act on inner mitochondrial membranes and are required for the maintenance of the cristae structure in the inner mitochondrial membrane (Frezza *et al.*, 2006; Meeusen *et al.*, 2006; Yan *et al.*, 2020; Yu *et al.*, 2020). Furthermore, the DLPs atlastin and Sey1p catalyze the fusion of the endoplasmic reticulum membrane (Orso *et al.*, 2010; Anwar *et al.*, 2012).

Potential DLPs have also been identified in plant cells, most notably in the plant model organism *Arabidopsis thaliana*. *E.g.*, the *fission DLPs* AtDRP3A, AtDRP3B and AtDRP5B are suggested to be involved in the division of several organelles, such as mitochondria, peroxisomes, and chloroplasts (Arimura and Tsutsumi, 2002; Gao *et al.*, 2003; Aung and Hu, 2009, 2012; Fujimoto *et al.*, 2009; Zhang and Hu, 2009). Interestingly, the *fusion DLP* AtFzl is located inside the chloroplasts at the TM as well as at the inner envelope, probably anchored in the membrane via a TMD. Mutants with a knocked-out AtFzl encoding gene showed defects in the morphology of chloroplasts and TMs, indicating a crucial role of this protein for the organization of the TM network in chloroplasts (Gao, Sage and Osteryoung, 2006). Recently, a homolog of AtFzl was identified in the unicellular alga *Chlamydomonas reinhardtii* (CrFzl) and it was shown that CrFzl promotes the fusion of TMs during mating (Findinier, Delevoye and Cohen, 2019).

Some proteins are categorized as DLPs due to structural and biochemical features, despite lacking a membrane fission or fusion activity. *E.g.*, Mx proteins are dynamin-like GTPases that are induced by interferons. Mx proteins inactivate viral proteins and can inhibit the viral replication, thus, they are involved in viral resistance mechanisms. The *in vivo* function of Mx proteins is probably membrane-independent. However, as they conserve the mechanochemical core, structure, and assembly mode, Mx proteins are classified as DLPs (Staehele *et al.*, 1986; Richter *et al.*, 1995; Gao *et al.*, 2010). Other examples for DLPs acting in viral resistance in eukaryotic cells are the also interferon-induced guanylate-binding proteins (GBPs) (Vestal and Jeyaratnam, 2011; Kutsch and Coers, 2021). *E.g.*, the activity of GBP1 is essential for suppressing the replication of the hepatitis C virus (Itsui *et al.*, 2009).

Furthermore, proteins belonging to the class of Eps15-homology domain-containing proteins (EHDs) are also classified as DLPs, although they hydrolyze ATP instead of GTP. EHDs are involved in several membrane remodeling processes in eukaryotic cells, such as the formation of ciliary vesicles, the vesicle fission and fusion at sorting endosomes or the regulation of caveolae dynamics (Daumke *et al.*, 2007; Moren *et al.*, 2012; Lu *et al.*, 2015; Insinna *et al.*, 2019; Solinger *et al.*, 2020).

1.3.2.2 Functions of BDLPs

Over two decades ago, genes coding for BDLPs have been identified in bacterial genomes (Blick, 1999). In the meantime, few BDLPs have been characterized to some extent, however, yet the exact physiological function of a BDLP in a prokaryotic cell remained elusive for a long time. The first characterized BDLP was identified in the cyanobacterium *Nostoc punctiforme* (*Np*BDLP; in the literature often simply referred to as BDLP) (Low and Löwe, 2006). It has been shown that *Np*BDLP is a GTPase, oligomerizes on membranes and has a typical DLP structure. Additionally, the *in vivo* localization in the filamentous cyanobacterium has been uncovered to be at the periphery of the cells. However, a clear physiological function of the protein has not yet been established (Low and Löwe, 2006; Low *et al.*, 2009). The BDLP *Ec*LeoA is a virulence factor in *E. coli* involved in toxin release, suggested by the reduced secretion of vesicles in an *ecleoA* knock-out strain of enterotoxigenic *E. coli* (Brown and Hardwidge, 2007; Michie *et al.*, 2014). *Ms*IniA from *Mycobacterium smegmatis* is a *fission DLP* and might have a role in plasma membrane remodeling to contribute to mycobacterial drug resistance (Wang *et al.*, 2019). The related proteins *Mt*IniA and *Mt*IniC from *Mycobacterium tuberculosis* mediate the secretion of extracellular vesicles (Gupta *et al.*, 2023). The two BDLPs *Sv*DynA and *Sv*DynB are suggested to be crucial for cell division in *Streptomyces venezuelae* (Schlimpert *et al.*, 2017). Another BDLP pair has been identified in the pathogen *Campylobacter jejuni*. *Cj*-DLP1/2 was structurally and biochemically characterized showing some interesting features (see Chapter 1.3.1), however, a defined *in vivo* function is not known (Liu, Noel and Low, 2018).

Finally, in 2022, the first and so far only distinct physiological function of a BDLP has been elucidated for the BDLP of *Bacillus subtilis* (*Bs*DynA) (Guo *et al.*, 2022). It has already been shown that *Bs*DynA is a *fusion DLP* with involvement in cell membrane surveillance under environmental stress conditions (Bürmann *et al.*, 2011; Sawant *et al.*, 2016; Guo and Bramkamp, 2019). After phage infection, *Bs*DynA provides a novel resistance mechanism against the lytic replication cycle of the phages. During the final step of the lytic cycle, *Bs*DynA stabilizes the CM to prevent phage release from an infected cell, and, thus, delays the lysis of other host cells (Guo *et al.*, 2022).

1.3.3 Membrane remodeling by DLPs

The mechanism of membrane remodeling mediated by *fission DLPs* has been extensively studied over the past decades, especially for the prototypical dynamin. For dynamin-catalyzed membrane constriction, the protein, which forms dimers or tetramers in solution, further assembles on a membrane tube into helical filaments mediated by defined contacts in the stalk domain (Fig. 1.7) (Warnock, Hinshaw and Schmid, 1996; Stowell *et al.*, 1999; Chappie *et al.*, 2011; Reubold *et al.*, 2015; Daumke and Praefcke, 2016). The GDs from adjacent rungs within the helical polymer dimerize, bind and hydrolyze GTP. This leads to a conformational change of the proteins mediated by domain movements via the two hinges (Fig. 1.5). The domain rearrangement comprises a power stroke that pulls the helical turns against each other and, finally, constricts the membrane tube to a hemifission state. The GD dimer is now destabilized and dissociates. After guanosine diphosphate (GDP)-release, the nucleotide binding pocket can bind a new GTP molecule, which initiates a recovery stroke. The GD then dimerizes with the next GD from the adjacent rung in the filament and the cycle repeats (Fig. 1.7). Each cycle reduces the diameter of the membrane tube by approx. 1 nm, finally leading to full membrane fission after several cycle repetitions (Chappie *et al.*, 2010; Reubold *et al.*, 2015; Antony *et al.*, 2016; Daumke and Praefcke, 2016; Kong *et al.*, 2018).

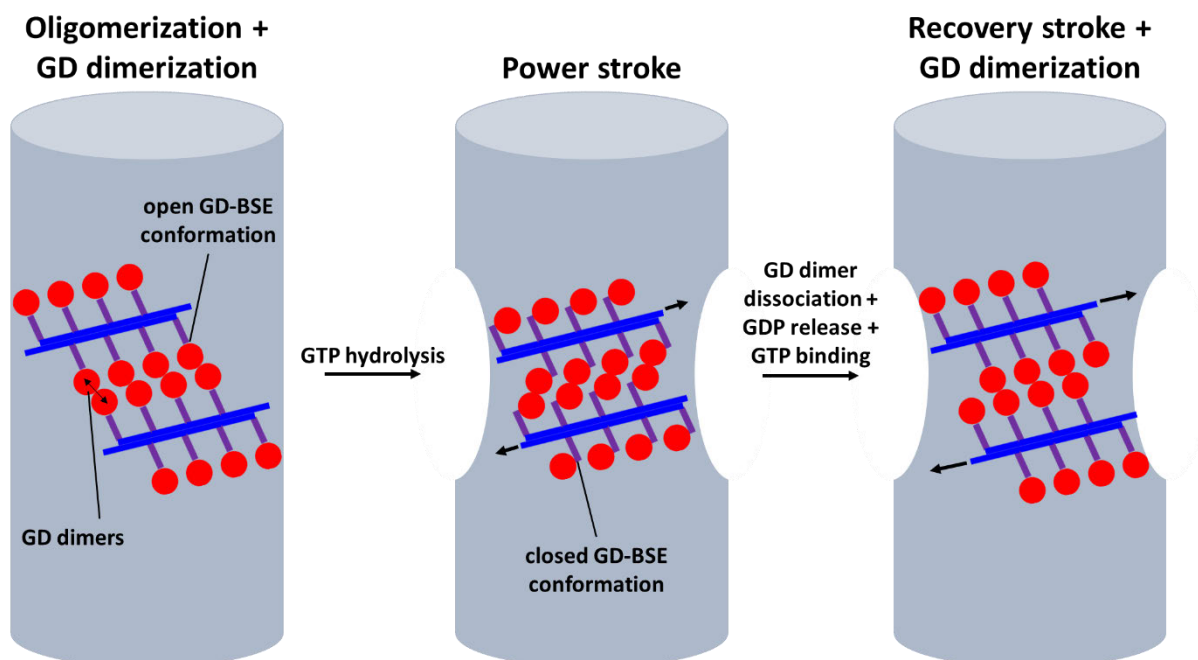


Figure 1.7: Dynamin-mediated membrane constriction.

A helical dynamin filament binds to a membrane tube (gray). Three important intermediate states of the membrane constriction catalyzed by dynamin are shown. Details are explained in the text. The GD, BSE, and stalk are colored in red, purple and blue, respectively. The MID of dynamin was omitted for clarity.

While the described mechanism of dynamin-mediated membrane fission is well understood, the exact operating principle of *fusion DLPs* is still enigmatic, yet mechanisms have been suggested for several fusogenic DLPs. *E.g.*, atlastin, the DLP that fuses the endoplasmic reticulum membrane, initially destabilizes the lipid bilayer by a C-terminal amphipathic helix to enable membrane fusion (Liu *et al.*, 2012). Then homotypic membrane fusion of adjacent membranes happens via nucleotide-dependent dimerization of adjacent GDs. A similar membrane fusion mechanism has been proposed for the transmembrane DLPs Sey1p and mitofusin (Yan *et al.*, 2015; Cao *et al.*, 2017). The membrane fusion activity of Mgm1 might proceed via tubulation of membranes and subsequent fusion of the highly curved and destabilized tubules (Yan *et al.*, 2020). In the case of BDLPs, a fusion mechanism was proposed for the heterotetrameric DLP pair *Cj*-DLP1/2. After homotypic tethering of adjacent membranes, structural rearrangements within the protein lead to membrane convergence and eventually membrane fusion (Bramkamp, 2018; Liu, Noel and Low, 2018). However, there are still many open questions concerning the exact mechanism of DLP-catalyzed membrane fusion.

1.3.4 *SynDLP* – a new cyanobacterial DLP

As already mentioned, a role of a BDLP in remodeling of cyanobacterial TMs is well conceivable. Several putative BDLP candidates have been identified in the genome of the cyanobacterial model organism *Synechocystis* based on sequence alignments searching for the conserved GD motifs (Kaneko *et al.*, 1996; Jilly, 2018; Jilly *et al.*, 2018). One of these candidates has been further investigated *in vivo* and *in vitro* and was shown to fulfill typical DLP features. Therefore, the newly discovered putative DLP originating from *Synechocystis* has been termed *SynDLP* (Jilly, 2018).

SynDLP is encoded in the genome of *Synechocystis* by the open reading frame (orf) *slr0869* (following the nomenclature of the CyanoBase database (Nakamura *et al.*, 1998)). The recombinant production and purification of *SynDLP* has been established (Jilly, 2018). The isolated protein hydrolyses GTP and interacts with negatively charged TM lipids *in vitro*. Furthermore, *SynDLP* binds in a highly ordered way to and intercalates into a planar lipid monolayer. The protein forms large oligomers already in solution in the absence of nucleotides and/or membranes, which is a unique feature for a BDLP. All the described features are hallmarks of DLPs, and, thus, *SynDLP* is probably a member of this protein class. Additionally, *SynDLP* forms a disulfide bridge that has been assumed to be intermolecular (Jilly, 2018). This disulfide bridge possibly regulates the GTPase function of the protein. *In vivo* studies revealed

that *SynDLP* is non-essential for the viability of the cyanobacterial cells. No clear phenotype could be observed in a *syndlp* knock-out strain of *Synechocystis* thus far, at least under normal growth conditions (Jilly, 2018). Further investigation on *SynDLP* is necessary to unequivocally identify the protein as a new BDLP and to elucidate its function within the organism.

2 Objectives of this thesis

The conversion of light energy into chemical energy during photosynthesis is the basis of the complexity and diversity of life evolved on earth. The energy conversion is catalyzed by the complexes of the photosynthetic light reaction, which are embedded in an intricate membrane system called the TM. There are many open questions concerning the dynamics of the TM system. Potentially, peripheral membrane proteins, such as dynamin-like GTPases, are involved in TM remodeling. Understanding the dynamics of the TMs would not only shed light on intriguing biological structures and processes but could also have a significant impact on biotechnological approaches that take advantage of photosynthesis. The putative DLP *SynDLP* has been identified in the unicellular photosynthetic model organism *Synechocystis* and has already been characterized to some extent (Jilly, 2018).

My project mainly focused on the biochemical and biophysical analysis of isolated *SynDLP* combined with a structural analysis of *SynDLP* oligomers. Furthermore, the *in vivo* localization and a putative function in the cell were investigated to provide clues to the role of *SynDLP* in the cyanobacterium. In more detail, the following topics were studied:

1. Structure determination of *SynDLP* oligomers

SynDLP forms large, ordered oligomers already in solution (Jilly, 2018). However, the exact size, shape, and the structure of the monomers within the oligomer were unknown. Therefore, one aim of this work was the high-resolution structure determination of *SynDLP* oligomers using cryo-electron microscopy (cryo-EM). The structure could not only help to analyze the protein in more detail on a molecular level but also unequivocally define *SynDLP* as a BDLP.

2. Influence of salts and DTT on *SynDLP* oligomerization and activity

DLPs are often sensitive to varying salt concentrations and low concentrations of the reducing agent dithiothreitol (DTT) are sometimes added in the storage buffers of isolated DLPs (Warnock, Hinshaw and Schmid, 1996; Meglei and McQuibban, 2009; Bürmann *et al.*, 2011; Bustillo-Zabalbeitia *et al.*, 2014; Liu, Noel and Low, 2018). Therefore, the influence of salts, especially NaCl, and DTT on the oligomerization behavior, thermodynamic stability as well as GTPase activity were investigated using analytical size exclusion chromatography (SEC) and electron microscopy (EM),

circular dichroism (CD) and fluorescence spectroscopy as well as a GTPase assay, respectively.

3. Position and influence of the disulfide bridge in *SynDLP*

A special feature of *SynDLP* is the formation of a disulfide bridge between two conserved cysteine residues. It has already been shown that the disulfide bridge affects the GTPase activity (Jilly, 2018). The localization of the disulfide bridge in the oligomer was identified in the cryo-EM structure. The influence of the disulfide bridge on the thermodynamic stability of *SynDLP* was studied using CD and fluorescence spectroscopy.

4. Interaction of *SynDLP* with thioredoxin

As already mentioned, *SynDLP* forms a disulfide bridge that affects its GTPase function. A regulation of the redox state of the disulfide bridge *in vivo* by a thioredoxin (Trx) is possible. Therefore, the gene coding for the major Trx isoform of *Synechocystis* was cloned, and the protein expressed and purified. Interaction of the isolated Trx with *SynDLP* was tested with a focus on the formation of the disulfide bridge.

5. Influence of nucleotides on *SynDLP* structure and assembly

Typically, nucleotides modulate the assembly and conformation of DLPs (Daumke and Praefcke, 2016). Consequently, the influence of nucleotides on the *SynDLP* structure, assembly and thermodynamic stability was investigated. In addition, a truncated monomeric *SynDLP* construct, derived from the structure, was designed and the encoding gene was cloned. The protein was expressed and purified to facilitate the investigation of nucleotide-dependent GD-interactions.

6. Effect of oligomerization on the *SynDLP* GTPase activity

Many DLPs show increased GTPase activities upon oligomerization (Daumke and Praefcke, 2016; Jimah and Hinshaw, 2018). Based on the cryo-EM structure, an assembly-defective *SynDLP* variant was designed and the encoding gene was cloned. The mutant protein was expressed and purified to study the effect of oligomerization on protein integrity and GTPase activity via a GTPase assay.

7. Visualization and quantification of *SynDLP*'s membrane binding

SynDLP has been shown to interact with negatively charged TM lipids (Jilly, 2018). One aim of this thesis was to establish a more quantitative membrane binding assay for *SynDLP* to potentially compare membrane binding of various protein variants or binding to different lipid compositions. Therefore, surface plasmon resonance (SPR) spectroscopy was tested as a quantitative method. Moreover, *SynDLP* binding to giant unilamellar vesicles (GUVs) was investigated in a nucleotide-dependent manner under the fluorescence microscope. For this purpose, the production of GUVs was established and a gene coding for a *SynDLP* variant tagged with a green fluorescent protein (GFP) was cloned and the resulting protein was expressed and purified.

8. Identification of the *SynDLP* MID

DLPs show a conserved domain architecture. The GD, BSE and stalk domain can usually directly be derived from the structure (Jimah and Hinshaw, 2018; Ford and Chappie, 2019). However, the MID shows a greater structural variability and cannot always easily be extracted from the structure. Thus, another goal of this project was the identification of *SynDLP* regions that could be responsible for membrane interaction based on either protein sequence or structure.

9. Membrane remodeling catalyzed by *SynDLP*

Hitherto, no membrane remodeling activity of *SynDLP* has been identified (Jilly, 2018). In this work, potential membrane remodeling events caused by *SynDLP* were investigated using model membrane systems and visualization of remodeled membranes by negative stain EM as well as cryo-EM. Moreover, a potential membrane fusion activity was quantitatively measured using dynamic light scattering (DLS) and a membrane fusion assay.

10. Native expression of *SynDLP* and *in vivo* localization

SynDLP is not essential in the cyanobacterium *Synechocystis*. Evidence for its expression in a cyanobacterial cell was still missing (Jilly, 2018). Thus, one goal of this thesis was to prove the expression of *SynDLP* in living *Synechocystis* cells. Additionally, the *in vivo* localization of *SynDLP* was studied by expressing a GFP-

tagged *SynDLP* variant in *Synechocystis* and visualization of the cells as well as the GFP-tagged protein under the fluorescence microscope.

11. *In vivo* function of *SynDLP*

In previous studies, no clear phenotype of a *syndlp* knock-out *Synechocystis* strain was identified (Jilly, 2018). EM images of *Synechocystis* wt cells and of the *syndlp* knock-out strain were acquired to look for phenotypical differences. The only functional characterized BDLP so far is involved in the protection against cell lysis after phage infection (Guo *et al.*, 2022). Inspired by this, *Synechocystis* strains which allow inducible expression of lytic phage proteins (Asada, Shiraiwa and Suzuki, 2019) were generated to test for effects caused by the absence or overexpression of *SynDLP* in these strains after induction of lysis.

3 Materials and Methods

3.1 Materials

3.1.1 Chemicals

All chemicals were purchased from Carl Roth GmbH + Co. KG (Karlsruhe, GER), Sigma-Aldrich Chemie GmbH (Taufkirchen, GER), Merck KGaA (Darmstadt, GER), Thermo Fisher Scientific (Waltham, MA, USA), AppliChem GmbH (Darmstadt, GER), New England Biolabs (Ipswich, MA, USA) and VWR International GmbH (Darmstadt, GER). Lipids were purchased from Avanti Polar Lipids, Inc (Birmingham, AL, USA) and ATTO-TEC GmbH (Siegen, GER).

3.1.2 Buffers and solutions

For the preparation of buffers and solutions, deionized water was used, filtered and degassed, if necessary. The composition of the buffers and solutions is listed in Table 3.1.

Table 3.1: Composition of used buffers and solutions.

Notation	Composition
Antibiotic stock solutions	
Ampicillin	100 mg/ml ampicillin 50% (v/v) ethanol
Kanamycin	30 mg/ml kanamycin
Chloramphenicol	30 mg/ml chloramphenicol in ethanol
SDS-PAGE	
Stacking gel buffer	1.5 M Tris-HCl, pH 6.8 0.4% (w/v) SDS
Separation gel buffer	500 mM Tris-HCl, pH 8.8 0.4% (w/v) SDS
5x SDS sample buffer	250 mM Tris-HCl, pH 6.8 10% (w/v) SDS 0.2% (w/v) bromphenol blue 50% (v/v) glycerol 500 mM DTT (non-reducing conditions: without 500 mM DTT)

SDS running buffer	25 mM Tris-HCl, pH 8.3 192 mM glycine 0.1% (w/v) SDS
Coomassie staining solution	0.125% (w/v) Coomassie Brilliant Blue R-250 40% (v/v) ethanol 2% (v/v) phosphoric acid
Coomassie destaining solution	30% (v/v) ethanol 2% (v/v) phosphoric acid

Western Blot

TBST buffer	20 mM Tris-HCl, pH 7.8 150 mM NaCl 0.05% (v/v) Tween20
Transfer buffer	25 mM Tris-HCl, pH 7.6 192 mM glycine 20% (v/v) ethanol
Blocking buffer	5% (w/v) milk powder in TBST buffer

Agarose gel electrophoresis

TAE buffer	40 mM Tris-HCl, pH 8.3 20 mM acetic acid 1 mM EDTA
------------	--

Protein purification

Lysis buffer	50 mM Na ₂ HPO ₄ , pH 8.0 300 mM NaCl 10 mM imidazole 10% (v/v) glycerol
Washing buffer	50 mM Na ₂ HPO ₄ , pH 8.0 300 mM NaCl 10% (v/v) glycerol
Elution buffer	50 mM Na ₂ HPO ₄ , pH 8.0 300 mM NaCl 500 mM imidazole 10% (v/v) glycerol
Storage buffer	20 mM HEPES, pH 7.4 0.2 mM DTT

Immunoprecipitation

Thylakoid buffer	50 mM HEPES, pH 7.0 150 mM NaCl 5 mM MgCl ₂ 25 mM KCl 10% (v/v) glycerol
IP lysis buffer	20 mM imidazole, pH 6.8 100 mM KCl 2 mM MgCl ₂ 300 mM sucrose 0.2% (v/v) Triton X-100
IP detergent-free buffer	20 mM imidazole, pH 6.8 100 mM KCl 2 mM MgCl ₂ 300 mM sucrose
IP washing buffer	20 mM imidazole, pH 6.8 100 mM KCl 2 mM MgCl ₂ 300 mM sucrose 0.04% (v/v) Triton X-100

Assay buffers

Reaction buffer	20 mM HEPES, pH 7.4 150 mM NaCl 5 mM MgCl ₂ 7.5 mM KCl 0.2 mM DTT
Insulin reduction buffer	20 mM HEPES, pH 7.4 0.13 mM insulin 2 mM EDTA 0.33 mM DTT

Gibson assembly

5x isothermal reaction mix	500 mM Tris-HCl, pH 7.5 50 mM MgCl ₂ 1 mM dNTP mix 50 mM DTT 250 mg/ml PEG-8000 5 mM NAD ⁺
----------------------------	---

1.33x Gibson assembly master mix	26.67% (v/v) 5x isothermal reaction mix 25 U/ml Phusion [®] HF DNA polymerase 4 U/ml T5 exonuclease 4 U/ml <i>Taq</i> DNA ligase
----------------------------------	--

Genomic DNA extraction

TES buffer	5 mM Tris-HCl, pH 8.5 5 mM EDTA 50 mM NaCl
TE buffer	10 mM Tris-HCl, pH 7.5 0.1 mM EDTA
CTAB solution	10% (w/v) CTAB 0.7 M NaCl

3.1.3 Bacterial strains

The bacterial strains used for cloning, protein production and *in vivo* experiments are listed in Table 3.2.

Table 3.2: Bacterial strains used in this study.

Strain	Genotype	Origin
<i>Escherichia coli</i>		
XL1-Blue	<i>recA1 endA1 gyrA96 thi-1 hsdR17 supE44 relA1 lac</i> [F proAB lacIqZΔM15 Tn10 (Tetr)]	Agilent Technologies (Santa Clara, CA, USA)
Rosetta-gami [™] 2(DE3)	Δ(<i>ara-leu</i>)7697 Δ <i>lacX74</i> Δ <i>phoA PvuII phoR araD139 ahpC galE galK rpsL</i> (DE3) F'[<i>lac⁺ lacI^q pro</i>] <i>gor522::Tn10 trxB pRARE2</i> (Cam ^R , Str ^R , Tet ^R)	Novagen (Darmstadt, GER)
Clear Coli [®] BL21(DE3)	F <i>ompT hsdSB</i> (r _B ⁻ m _B ⁻) <i>gal dcm lon</i> λ(DE3 [<i>lacI lacUV5-T7 gene 1 ind1 sam7 nin5</i>]) <i>msbA148 ΔgutQΔkdsD ΔlpxLΔlpxMΔpagPΔlpxPΔeptA</i>	Novagen (Darmstadt, GER)

BL21-gold(DE3)	<i>F⁻dcm⁺ Hte ompT hsdS_{(r_B⁻ m_B⁻) gal λ (DE3) endA (Tet^R)}</i>	Novagen (Darmstadt, GER)
Tuner TM (DE3)	<i>F⁻ ompT hsdS_B (r_B⁻ m_B⁻) gal dcm lacY1(DE3)</i>	Novagen (Darmstadt, GER)

***Synechocystis* sp. PCC 6803**

<i>Synechocystis</i>	wt	Conrad Mullineaux (London, UK)
Δ syndlp	Δ slr0869::Km ^R	(Jilly, 2018)
pCK306-syndlp	Δ sll0410:: <i>rhaBAD slr0869</i> Km ^R <i>rhaS</i>	This work
pCK306-megfp-syndlp	Δ sll0410:: <i>rhaBAD megfp-slr0869</i> Km ^R <i>rhaS</i>	This work
Δ phoA	Δ sll0654::Km ^R	This work
<i>lic</i>	Δ sll0654:: <i>S. enterica</i> phage P22 <i>orf13+19+15</i> Km ^R	This work
Δ syndlp- Δ phoA	Δ slr0869::Km ^R Δ sll0654::Cm ^R	This work
Δ syndlp- <i>lic</i>	Δ slr0869::Km ^R Δ sll0654:: <i>S. enterica</i> phage P22 <i>orf13+19+15</i> Cm ^R	This work

3.1.4 Media

LB medium was used for the growth of *E. coli* cultures. *Synechocystis* strains were cultivated in BG11 medium (Rippka *et al.*, 1979). The compositions are listed in Table 3.3. After sterilization of the media, antibiotics were added, if required. BG11 medium was typically supplemented with 5 mM sterile glucose after sterilization for mixotrophic growth conditions. For the preparation of phosphate-free BG11 medium, 0.175 mM K₂HPO₄ was replaced by 0.35 mM KCl to keep an equal amount of K⁺.

Table 3.3: Media used for growth of microorganisms.

Notation	Composition
LB medium	10 g/l tryptone 5 g/l yeast extract 10 g/l NaCl
LB agar	1.5 g/l agar in LB medium
1000x trace minerals	46.3 mM boric acid 9.1 mM MnCl ₂ x 4 H ₂ O 0.77 mM ZnCl ₂ x 7 H ₂ O 1.6 mM Na ₂ MoO ₄ x 2 H ₂ O 0.32 mM Co(NO ₃) ₂ x 6 H ₂ O 0.17 mM CuSO ₄ x 5 H ₂ O
100x BG-FPC	1.76 M NaNO ₃ 3.1 mM citric acid 24.5 mM CaCl ₂ x 2 H ₂ O 30.4 mM MgSO ₄ x 7 H ₂ O 0.28 mM Na ₂ EDTA x 2 H ₂ O
BG11 medium	5 mM HEPES, pH 8.2 1x trace minerals 1x BG-FPC 22.6 μM ferric ammonium citrate 0.19 mM Na ₂ CO ₃ 0.175 mM K ₂ HPO ₄
BG11 agar	15 g/l Difco Bacto™ agar 12.1 mM Na ₂ S ₂ O ₃ x 5 H ₂ O in BG11 medium

3.1.5 Oligonucleotides

Oligonucleotides were purchased from Sigma-Aldrich Chemie GmbH (Taufkirchen, GER) and are listed in Table 3.4.

Table 3.4: Oligonucleotides used in this study. F = forward, R = reverse.

Notation	Sequence (5' – 3')	Application
Gibson assembly		
F_pET303_SynDLP	CTTAAGAAGGAGGTCTAGAATGC	Gibson assembly using <i>SynDLP</i> variants as insert and pET303 as vector
R_SynDLP_pET303	ATATGTCCAAGATTGCGCCCAATG CATTGGGGCGCAATCTTGGACATAT GCATTCTAGACCTCCTTCTTAAAG	
F_HPRN552-555AAAA	GCGGCCGCAGCGTCCACAGCTCCTT TTATTGCAGTTTTG	pET303- <i>SynDLP</i> _{HPRN- AAAA} and pET303-
R_HPRN552-555AAAA	AAGGAGCTGTGGACGCTGCGGCCG CACTTTCGTTGCTCGCTTATAGGC	mEGFP- <i>SynDLP</i> _{HPRN- AAAA} cloning
F_558-565GS	GGCAGCGGCAGCGGCAGCGGCAGC GAGGCTTTATATTATCTTGC	pET303- <i>SynDLP</i> _{558-565GS} and pET303- <i>SynDLP</i> _{558- 565GS} -eGFP cloning
R_558-565GS	GCTGCCGCTGCCGCTGCCGCTGCCT GTGGAATTACGAGGATGAC	
F_648-665GS	GGCTCGGGTTCAGGGTCAGGTTCC GGTTCTGGCTCCGGTTCGGGTCGG GTTCTCAGCAAACCTCCAGGGTTA TGATG	pET303- <i>SynDLP</i> _{648-665GS} and pET303-mEGFP- <i>SynDLP</i> _{648-665GS} cloning
R_648-665GS	AGAACCCGACCCGGAACCGGAGCC AGAACCGGAACCTGACCCTGAACC CGAGCCACTTCCCGCACATAACG ATCAC	
F_667-675GS	CTCGGGTTCGGGATCAGGCTCTGGT GCGATCGTGGAAGCG	pET303- <i>SynDLP</i> _{667-675GS} and pET303-mEGFP- <i>SynDLP</i> _{667-675GS} cloning
R_667-675GS	ACCAGAGCCTGATCCCGAACCCGA GCCCTGGAGAGTTTGCCGGAATTG ATAAATGG	
F_694-705GS	GAAGGTAGCGGCTCAGGATCGGGC AGTGGTTCAGGAAGCCAAACCGTC AATAATACCC	pET303- <i>SynDLP</i> _{694-705GS} and pET303- <i>SynDLP</i> _{694- 705GS} -eGFP cloning
R_694-705GS	GTTTGGCTTCTGAACCACTGCCCG ATCCTGAGCCGCTACCTTCAAATC TAGTTTTAGCAACTCC	

F_BSE1Ala	CAGGAAGCGACACTCCGCGCGCAG CAGGCGACCGCGATTGTGGCGACG GCCTTAGCGAAGGCAGCGTCCCCC CGGTTTGAAATTGTTTTTG	pET303- <i>SynDLP</i> _{BSE1Ala}
R_BSE1Ala	GCCTGCTGCGCGCGGAGTGTGCGCTT CCTGCGCCAGAAGCGCGATTA GCGCAACTTGCTCCGCGAGATTCTG ACATTGGGGCGCAATC	cloning
F_R320A	GAGGGTTTAATTCAGTCGCAATTTG CGGATAATTCTAGGGTCTATAAAA CCAG	pET303- <i>SynDLP</i> _{R320A} and pET303-
R_R320A	CTGGTTTTATAGACCCTAGAATTAT CCGCAAATTGCGACTGAATTAAC CCTC	<i>SynDLP</i> _{R320A-E585A} cloning
F_E585A	GGAAGATGCTTTCATAGAAGCTATT CATGCGCTAGTTAAAAATTTCTTTC AACGATTAGGCG	pET303- <i>SynDLP</i> _{E585A} and pET303-
R_E585A	CGCCTAATCGTTGAAAGAAATTTTT AACTAGCGCATGAATAGCTTCTATG AAAGCATCTTCC	<i>SynDLP</i> _{R320A-E585A} cloning
F_MGD	ATTAAACAGAAAATCGATCTTTACC AAACGAGTATTGTTAGCATTAAATG AATGTTTAAAAGCCATGCAAATTTT TGAGCAGTTACCTCACCACCACCAC CACCAC	pET303- <i>SynDLP</i> -MGD
R_MGD	TGGTAAAGATCGATTTTCTGTTTAA TCTCCGATTGTAACGGGAATTGCG AGCAATTTTCGAACCGCCAGATCCT GAACCCGAGCCGGGCTGACTATCT AACTGC	cloning
F_pET303_GD	CTTTAAGAAGGAGGTCTAGAATGC ATCTGTCCCCCGGTTTGAATTTG	
R_GD_pET303	CAATTTCAAACCGGGGGGACAGAT GCATTCTAGACCTCCTTCTTAAAG	pET303- <i>SynDLP</i> -GD
F_GD_pET303	GGTCTTTATTTAGCAGAGGAAAAA TATCCTCACCACCACCACCACCT G	cloning

F_pCK306_mEGFP	CGGGTAAGTTTATAATATACAAAG GAGGTAGAAATGAGCAAAGGAGA AGAACTTTTCACTGG	pCK306-mEGFP-
R_mEGFP_pCK306	CCAGTGAAAAGTTCTTCTCCTTTGC TCATTTCTACCTCCTTTGTATATTAT AACTTACCCG	SynDLP cloning
F_pET303_SynTrxA	CTTTAAGAAGGAGGTCTAGAATGC ATATGAGTGCTACCCCTCAAGTTTC CG	
R_SynTrxA_pET303	GCGTCGGAAACTTGAGGGGTAGCA CTCATATGCATTCTAGACCTCCTTC TTAAAGTTAAAC	pET303-SynTrxA
F_SynTrxA_pET303	CCCTAGAAAAATATCTTTCCGAAA ACCTGTACTTCCAGGGTCAATTCCT CGAGCACCACCACCACCACCTG	cloning
R_pET303_SynTrxA	CTCGAGGAATTGACCCTGGAAGTA CAGGTTTTTCGGAAAGATATTTTTCT AGGGTGCTGG	
F_PhxA-down_CmR	CAGTGTTACAACCAATTAACCAATT CTGATTACGCCCCGCCCTGCCACTC	
R_PhxA-down_CmR	GAGTGGCAGGGCGGGGCGTAATCA GAATTGGTTAATTGGTTGTAACACT G	pGEM-T-Easy-PhxA-
F_PhxA-up_CmR	GTTGGAACCTCTTACGTGCCGATCA CAATTGCTTTAGAAATTTCTCAATC AGG	Cm ^R and pGEM-T- Easy-PhxA-LIC-Cm ^R cloning
R_PhxA-up_CmR	CCTGATTGAGAAATTTCTAAAGCA ATTGTGATCGGCACGTAAGAGGTT CCAAC	
F_PhxA-LIC_CmR	GTTGGAACCTCTTACGTGCCGATCA TTCTTATTTTAAGCACTGACTCCTG ATG	pGEM-T-Easy-PhxA-
R_PhxA-LIC_CmR	CATCAGGAGTCAGTGCTTAAAATA AGAATGATCGGCACGTAAGAGGTT CCAAC	LIC-Cm ^R cloning

Sequencing primer			
Slr0869_seq1	TATGCGAGGCGGGGA	Sequencing of pET303-based plasmids with inserts encoding <i>SynDLP</i> variants	
Slr0869_seq4	GGAAATATCGTGAGCAAACG		
Slr0869_seq5	ATGTCCAAGATTGCGCCCC		
Slr0869_seq6	CTGCATCTGCAACTATTTCTGC		
Slr0869_seq7	CGTAGAGCAATACATAACGG		
F_slr0869_upstream	TATCAAGCTTGGGAGTGGCACAAG AAACAA		Sequencing after transformation of
R_slr0869_downstream	TAGTGGATCCTGCTTGTATGTCAGA AAGGT		<i>Synechocystis</i> gene locus <i>slr0869</i>
F_pCK306_seq	CCACAATTCAGCAAATTGTG	Sequencing of pCK306-based plasmids	
R_pCK306_seq1	AACACCCCTTGTATTACTGT		
R_pCK306_seq2	GGAGCCGGGGTTCTATCGCC		
F_hom-left-pCK306	GGCAGGTATTCTGGCTA	Sequencing after transformation of	
R_hom-right-pCK306	GCACCAAGGTGGTAATT		<i>Synechocystis</i> gene locus <i>sll0410</i>
pPhoA_seq1	ATGCTCTGCCAGTGTTAC	Sequencing of pGEM-T-Easy-based plasmids	
pPhoA_seq2	GCTTGATGGTCGGAAGAG		
pPhoA_seq3	CTATGCAACAACGTGGCG		
pPhoA_seq4	CACTGACTCCTGATGTACTCC		
pPhoA_seq5	GCTTACCGGATACCTGTC		
pPhoA_seq6	GATGCCCTGTTCTTTG		
pPhoA_seq7	TTGGCCGCAGTGTTATC		
pPhoA_seq8	TGCCCGCTTTCCAGTC		
F_PhoA-down_seq	GTCAGCTAGGACGTATAACTC	Sequencing after transformation of	
R_PhoA-up_seq	GGCGGTTTTACTTCAAC		<i>Synechocystis</i> gene locus <i>sll0654</i>

3.1.6 Plasmids

Table 3.5 lists the plasmids used in this study. In principle, the pET303 vector was used for overexpression of proteins in *E. coli*. Constructs based on the pCK306 vector (Kelly *et al.*, 2018) and the pGEM-T-Easy vector (Asada, Shiraiwa and Suzuki, 2019) were used for transformation of *Synechocystis* cells. Example plasmid maps of the used vectors are shown in the appendix (Figs. A1-A3).

Table 3.5: Plasmids used in this study.

Plasmid	Resistance	Origin
pET303	Amp ^R	Thermo Fisher Scientific (Waltham, MA, USA)
pET303- <i>SynDLP</i>	Amp ^R	(Jilly, 2018)
pET303- <i>SynDLP</i> _{C777A}	Amp ^R	(Jilly, 2018)
pET303- <i>SynDLP</i> -eGFP	Amp ^R	This work
pET303-mEGFP- <i>SynDLP</i>	Amp ^R	This work
pET303- <i>SynDLP</i> _{HPRN-AAAA}	Amp ^R	This work
pET303-mEGFP- <i>SynDLP</i> _{HPRN-AAAA}	Amp ^R	This work
pET303- <i>SynDLP</i> _{BSE1Ala}	Amp ^R	This work
pET303- <i>SynDLP</i> _{558-565GS}	Amp ^R	This work
pET303- <i>SynDLP</i> _{558-565GS} -eGFP	Amp ^R	This work
pET303- <i>SynDLP</i> _{648-665GS}	Amp ^R	This work
pET303-mEGFP- <i>SynDLP</i> _{648-665GS}	Amp ^R	This work
pET303- <i>SynDLP</i> _{667-675GS}	Amp ^R	This work
pET303-mEGFP- <i>SynDLP</i> _{667-675GS}	Amp ^R	This work
pET303- <i>SynDLP</i> _{694-705GS}	Amp ^R	This work
pET303- <i>SynDLP</i> _{694-705GS} -eGFP	Amp ^R	This work
pET303- <i>SynDLP</i> _{R320A}	Amp ^R	This work
pET303- <i>SynDLP</i> _{E585A}	Amp ^R	This work
pET303- <i>SynDLP</i> _{R320A-E585A}	Amp ^R	This work
pET303- <i>SynDLP</i> -MGD	Amp ^R	This work
pET303- <i>SynDLP</i> -GD	Amp ^R	This work
pET303- <i>SynTrxA</i>	Amp ^R	This work
pCK306	Km ^R	(Kelly <i>et al.</i> , 2018)
pCK306- <i>SynDLP</i>	Km ^R	This work
pCK306-mEGFP- <i>SynDLP</i>	Km ^R	This work
pGEM-T-Easy-PhoA	Amp ^R , Km ^R	(Asada, Shiraiwa and Suzuki, 2019)
pGEM-T-Easy-PhoA-LIC	Amp ^R , Km ^R	(Asada, Shiraiwa and Suzuki, 2019)
pGEM-T-Easy-PhoA-Cm ^R	Amp ^R , Cm ^R	This work
pGEM-T-Easy-PhoA-LIC-Cm ^R	Amp ^R , Cm ^R	This work

3.1.7 Antibodies

Table 3.6: Antibodies used in this study.

Notation	Properties	Epitope	Source	Dilution
α -SynDLP	Polyclonal (rabbit)	SynDLP ₃₀₀₋₈₁₂	Davids Biotechnologie (Regensburg, GER); (Jilly, 2018)	1:2000
α -rabbit-HRP	Polyclonal (goat)	Antibodies from rabbit	Sigma-Aldrich Chemie GmbH (Taufkirchen, GER)	1:160000
His•Tag [®] antibody HRP	Monoclonal	His-tag	Novagen (Darmstadt, GER)	1:2000

3.1.8 Enzymes

Table 3.7: Enzymes used in this study and their manufacturers.

Enzyme	Manufacturer
<i>DpnI</i> restriction endonuclease	New England Biolabs (Ipswich, MA, USA)
Phusion [®] HF DNA polymerase	New England Biolabs (Ipswich, MA, USA)
T5 exonuclease	New England Biolabs (Ipswich, MA, USA)
<i>Taq</i> DNA Ligase	New England Biolabs (Ipswich, MA, USA)
Pyruvate kinase/lactic dehydrogenase mix (PK/LDH)	Sigma-Aldrich Chemie GmbH (Taufkirchen, GER)

3.1.9 Kits

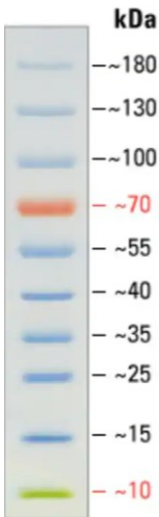
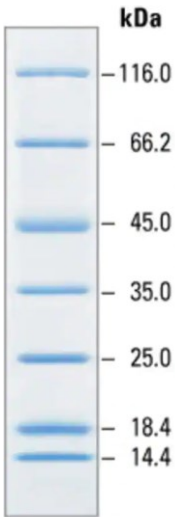
Table 3.8: Kits used in this study and their manufacturers.

Kit	Manufacturer
NucleoSpin [™] Gel and PCR Clean-up	Macherey-Nagel [™] (Düren, GER)
NucleoSpin [™] Plasmid	Macherey-Nagel [™] (Düren, GER)
Pierce [™] BCA protein assay	Thermo Fisher Scientific (Waltham, MA, USA)
Pierce [™] BCA-RAC assay (reducing agent compatible)	Thermo Fisher Scientific (Waltham, MA, USA)
TGX [™] FastCast [™] Acrylamide kit, 10%	Bio-Rad (Munich, GER)
Amersham [™] ECL Prime [™] Western Blotting Detection Reagent	VWR International GmbH (Darmstadt, GER)
Malachite green phosphate assay kit	Abcam (Berlin, GER)

3.1.10 Marker

Table 3.9 lists and illustrates the markers used for sodium dodecyl sulfate polyacrylamide gel electrophoresis (SDS-PAGE) analysis as well as agarose gel electrophoresis.

Table 3.9: Markers used in this study.

Marker	PageRuler™ Prestained Protein Ladder, 10 bis 180 kDa	Pierce™ Unstained Protein MW Marker	Thermo Scientific™ O'GeneRuler 1 kb DNA Ladder, Ready-to-Use- 250-10,000 bp																																													
Source	Thermo Fisher Scientific (Waltham, MA, USA)	Thermo Fisher Scientific (Waltham, MA, USA)	Thermo Fisher Scientific (Waltham, MA, USA)																																													
Illustration (by manufacturer)	 <p>kDa</p> <ul style="list-style-type: none"> ~180 ~130 ~100 ~70 ~55 ~40 ~35 ~25 ~15 ~10 	 <p>kDa</p> <ul style="list-style-type: none"> 116.0 66.2 45.0 35.0 25.0 18.4 14.4 	 <table border="1"> <thead> <tr> <th>bp</th> <th>ng/0.5 µg</th> <th>%</th> </tr> </thead> <tbody> <tr><td>10000</td><td>30.0</td><td>6.0</td></tr> <tr><td>8000</td><td>30.0</td><td>6.0</td></tr> <tr><td>6000</td><td>70.0</td><td>14.0</td></tr> <tr><td>5000</td><td>30.0</td><td>6.0</td></tr> <tr><td>4000</td><td>30.0</td><td>6.0</td></tr> <tr><td>3500</td><td>30.0</td><td>6.0</td></tr> <tr><td>3000</td><td>70.0</td><td>14.0</td></tr> <tr><td>2500</td><td>25.0</td><td>5.0</td></tr> <tr><td>2000</td><td>25.0</td><td>5.0</td></tr> <tr><td>1500</td><td>25.0</td><td>5.0</td></tr> <tr><td>1000</td><td>60.0</td><td>12.0</td></tr> <tr><td>750</td><td>25.0</td><td>5.0</td></tr> <tr><td>500</td><td>25.0</td><td>5.0</td></tr> <tr><td>250</td><td>25.0</td><td>5.0</td></tr> </tbody> </table>	bp	ng/0.5 µg	%	10000	30.0	6.0	8000	30.0	6.0	6000	70.0	14.0	5000	30.0	6.0	4000	30.0	6.0	3500	30.0	6.0	3000	70.0	14.0	2500	25.0	5.0	2000	25.0	5.0	1500	25.0	5.0	1000	60.0	12.0	750	25.0	5.0	500	25.0	5.0	250	25.0	5.0
bp	ng/0.5 µg	%																																														
10000	30.0	6.0																																														
8000	30.0	6.0																																														
6000	70.0	14.0																																														
5000	30.0	6.0																																														
4000	30.0	6.0																																														
3500	30.0	6.0																																														
3000	70.0	14.0																																														
2500	25.0	5.0																																														
2000	25.0	5.0																																														
1500	25.0	5.0																																														
1000	60.0	12.0																																														
750	25.0	5.0																																														
500	25.0	5.0																																														
250	25.0	5.0																																														

3.1.11 Instruments

Table 3.10: Instruments used in this study and their manufacturers.

Instrument	Notation	Manufacturer
CD spectrometer	J-815	JASCO cooperation (Tokyo, JPN)
	J-1500	JASCO cooperation (Tokyo, JPN)
CD spectrometer	MTPC-490S	JASCO cooperation (Tokyo, JPN)
temperature controller		
Cell homogenizer	SpeedMill PLUS	Analytik Jena (Jena, GER)
Centrifuge	Allegra X-15R	Beckmann Coulter (Krefeld, GER)
	Avanti J-26XP	Beckmann Coulter (Krefeld, GER)
	Centrifuge 5424	Eppendorf (Hamburg, GER)
	Centrifuge 5415 R	Eppendorf (Hamburg, GER)
	Centrifuge 5810 R	Eppendorf (Hamburg, GER)
	Optima™ MAX-XP ultracentrifuge	Beckmann Coulter (Krefeld, GER)
Chemiluminescence detection system	Stella	Raytest (Straubenhardt, GER)
	Fusion FX	Vilber (Eberhardzell, GER)
Dynamic light scattering system	Zetasizer Nano S-Size	Malvern Panalytical (Malvern, UK)
Electron microscope	FEI Tecnai G2 12 BioTwin	FEI Company (Hillsboro, OR, USA)
	120 kV Talos L120C	Thermo Fisher Scientific (Waltham, MA, USA); FEI Company (Hillsboro, OR, USA)
	200 kV Talos Arctica G2	Thermo Fisher Scientific (Waltham, MA, USA)
Electron microscope detection system	TemCam-F416R	Tietz Video and Image Processing Systems GmbH (Gauting, GER)
	BioQuantum K3	Gatan, Inc. (Pleasanton, CA, USA)
Electrophoresis chamber	Mini-Protean 3 Cell	Bio-Rad (Munich, GER)
	PerfectBlue Gelsystem	PeqLab (Erlangen, GER)
Electrophoresis power supply	PowerPac Basic	Bio-Rad (Munich, GER)
	PeqPower 300	PeqLab (Erlangen, GER)
Extruder	Mini-Extruder	Avanti Polar Lipids, Inc (Birmingham, AL, USA)
Fluorescence microscope	Axio Observer.Z1	Carl Zeiss Microscopy (Jena, GER)

Fluorescence spectrometer	FluoroMax-4 FP-8500	Horiba Scientific (Kyoto, JPN) JASCO cooperation (Tokyo, JPN)
Gel documentation	Quantum-ST4 1100/26MX	PeqLab (Erlangen, GER)
Gel filtration	ÄKTA purifier 10 ÄKTA prime	GE Healthcare (Munich, GER) GE Healthcare (Munich, GER)
Gel scanner	ViewPix 700	Biostep (Burkhardtsdorf, GER)
Glow discharge system	Emitech K100x PELCO easiGlow	Emitech SAS (Versailles, FRA) Ted Pella Inc. (Redding, CA, USA)
Heating block/shaker	Thermomixer comfort	Eppendorf (Hamburg, GER)
Heating plate/magnetic stirrer	MR Hei-Standard	Heidolph (Schwabach, GER)
High pressure homogenizer	LM20 Microfluidizer [®]	Microfluidics [™] (Westwood, MA, USA)
Horizontal shaker	Duomax 1030	Heidolph (Schwabach, GER)
Incubator (<i>E. coli</i>)	Binder Inkubator Serie BF	Binder (Tuttlingen, GER)
Incubator (<i>Synechocystis</i>)	Economic Deluxe, ECD01E	Snijders Scientific (Tilburg, NL)
Incubator shaker	Multitron HT	Infors (Bottmingen, CH)
Overhead shaker	CMV-ROM	Fröbel (Lindau, GER)
pH-Meter	pH211 Microprocessor 632 pH-Meter	HANNA Instruments (Vöhringen, GER) Metrohm (Herisau, CH)
Photometer	Novaspec Plus Ultrospec 10 Cell density meter Nanodrop 2000C Lambda 35	Amersham Biosciences (Little Chalfont, UK) Amersham Biosciences (Little Chalfont, UK) Thermo Scientific (Darmstadt, GER) Perkin Elmer (Rodgau, GER)
Plasma Cleaner	Yocto	Diener electronics (Ebhausen, GER)
Plate Reader	FLUOstar Omega PowerWave XS	BMG Labtech GmbH (Ortenberg, GER) BioTek Instruments, Inc. (Winooski, VT, USA)
Plunge-freeze system	Vitrobot Mark IV	Thermo Fisher Scientific (Waltham, MA, USA)
QCM system	qCell T Series	3T Analytik (Tuttlingen, GER)

Rotors	JA-25.50	Beckmann Coulter (Krefeld, GER)
	JLA-8.1	Beckmann Coulter (Krefeld, GER)
	MLA-130	Beckmann Coulter (Krefeld, GER)
	TLA-100	Beckmann Coulter (Krefeld, GER)
Sonifier	HTU SONI-130 MiniFIER	G. HEINEMANN Ultraschall- u. Labortechnik (Schwäbisch Gmünd, GER)
SPR system	Biacore T200	Cytiva (Munich, GER)
Thermocycler	Thermocycler Primus 25	PeqLab (Erlangen, GER)
	Biometra T-Personal 48	Gemini B.V. (Apeldoorn, NL)
	Thermocycler	
Western Blot system	Trans-Blot Turbo Transfer System	Bio-Rad (Munich, GER)

3.1.12 Software

Table 3.11: Software applied in this study.

Application	Software	Version
Data analysis	Excel	Microsoft Professional Plus 2019
	Origin 2019	9.60
Figure editing	Microsoft PowerPoint	Microsoft Professional Plus 2019
	Adobe Photoshop	2023 V5
Image analysis and editing	Fiji-ImageJ	2.9.0
Literature management	Mendeley	1.19.8
Protein structures	Chimera	1.16
	ChimeraX	1.4
	PyMol	2.5.3
Sequence analysis	SnapGene® Viewer	4.2.11
	BioEdit	7.2.5
Text editing	Word	Microsoft Professional Plus 2019

3.2 Methods

This section describes the general routine of the performed methods. Deviations are stated in the respective chapters.

3.2.1 Microbiological methods

3.2.1.1 Cultivation of *E. coli* cells

E. coli cells were either cultivated as liquid cultures in LB medium (Table 3.3) in a shaking incubator (Multitron HT, Infors, Bottmingen, CH) at 37°C and 180 or 115 rpm, or plated on LB agar plates in an incubator (Binder Inkubator Serie BF, Binder, Tuttlingen, GER) at 37°C. If necessary, the LB medium and the LB agar plates contained antibiotics (100 µg/ml ampicillin, 30 µg/ml kanamycin or 30 µg/ml chloramphenicol). The optical density (OD) of a liquid culture was measured at 600 nm using an Ultrospec 10 Cell density meter (Amersham Biosciences, Little Chalfont, UK).

3.2.1.2 Cultivation of *Synechocystis* cells

Synechocystis cells were either cultivated as liquid cultures in BG11 medium (Table 3.3) in a shaking incubator (Multitron HT, Infors, Bottmingen, CH) at 30°C and 130 rpm or plated on BG11 agar plates in an incubator (Economic Delux, ECD01E, Snijders Scientific, Tilburg, NL) at 30°C. Typically, the cells were grown photomixotrophically. Therefore, the BG11 medium was supplemented with 5 mM glucose and liquid cultures as well as the BG11 agar plates were illuminated with 30 µE of cold-white light. 50 µg/ml kanamycin or chloramphenicol were added to the BG11 medium, if necessary. OD values of the liquid cultures were determined at 750 nm via a Novaspec Plus (Amersham Biosciences, Little Chalfont, UK). Note that for the recording of growth curves no antibiotics were included in the BG11 medium to exclude any side effects.

3.2.2 Molecular biological methods

3.2.2.1 Polymerase chain reaction

The polymerase chain reaction (PCR) method was used to selectively amplify DNA fragments. The amplified PCR products were then used for molecular cloning by Gibson assembly

(Chapter 3.2.2.2). The DNA was amplified by the Phusion[®]HF DNA polymerase (New England Biolabs, Ipswich, MA, USA). The typical composition of a PCR reaction is shown in Table 3.12. The used primers as well as the DNA templates are listed in Table 3.4 and 3.5, respectively.

Table 3.12: Typical pipetting scheme of a PCR reaction with a total volume of 50 μ l used for molecular cloning.

Ingredient	Stock concentration	Volume [μ l]
Sterile MP-H ₂ O		23
Phusion GC-Buffer	5x	10
dNTPs	2 mM	5
DMSO	100%	1.5
DNA template	0.4 ng/ μ l	5
Forward primer	10 μ M	2.5
Reverse primer	10 μ M	2.5
Phusion [®] HF DNA polymerase	2 U/ μ l	0.5

Table 3.13 summarizes the PCR program ran either in a Thermocycler Primus 25 (PeqLab, Erlangen, GER) or a Biometra T-Personal 48 Thermocycler (Gemini B.V., Apeldoorn, NL). The exact annealing temperature depended on the properties of the respective primers. The time of the elongation step was adjusted to the maximum PCR product size, considering an amplification speed of the Phusion[®]HF DNA polymerase of 2 – 4 kbp per minute.

Table 3.13: PCR program used for DNA amplification.

Step	Temperature [°C]	Time [min]	Cycles
Initial denaturation	98	2	
Denaturation	98	0.5	30x
Annealing	50 - 72	0.5	
Elongation	72	2 - 5	
Final elongation	72	10	

Normally, 50 μ l PCR product was incubated with 20 U of the restriction endonuclease *DpnI* (New England Biolabs, Ipswich, MA, USA) for 1 h at 37°C to digest the parental DNA template. Correct size and purity of the amplified DNA fragments were verified via agarose gel

electrophoresis. Typically, a 1% agarose gel in TAE buffer was run for 40 min at 150 V in a PerfectBlue Gelsystem (PeqLab, Erlangen, GER). After staining DNA-containing bands via incubation of the gel in an ethidium bromide solution for 15 – 20 min, the UV fluorescence of the ethidium bromide was detected in a Quantum-ST4 1100/26MX (PeqLab, Erlangen, GER).

3.2.2.2 Gibson assembly

Multiple DNA fragments can be joined via the molecular cloning method Gibson assembly in a single, isothermal reaction (Gibson *et al.*, 2009). During this reaction, linear vector and insert DNA fragments with overlapping ends are partially digested at their 5' ends by the activity of an exonuclease. The resulting single-stranded ends of vector and insert DNA fragments can now anneal. A DNA polymerase incorporates nucleotides into the gaps and, finally, a DNA ligase links the DNA strands. This allows for the combination of any desired vector and insert in a seamless and correctly ordered way in contrast to, *e.g.*, cloning methods based on endonucleases.

The overlapping ends of vector and insert DNA fragments were introduced by the respective primers (Table 3.4). Both DNA fragments were amplified by PCR (Chapter 3.2.2.1). After digestion of the PCR products with *DpnI*, the DNA was purified using the NucleoSpin™ Gel and PCR Clean-up (Macherey-Nagel™, Düren, GER) kit. The DNA concentration (c_{DNA}) in the purified PCR products was determined via a Nanodrop 2000C (Thermo Scientific, Darmstadt, GER) using Equation (1):

$$c_{DNA} = \frac{A_{260}}{d * \varepsilon} \quad (1)$$

Here, A_{260} refers to the measured absorption at 260 nm, d to the pathlength in cm and ε is the extinction coefficient of the DNA (for double stranded DNA: $\varepsilon = 0.02 \text{ (ng/}\mu\text{l)}^{-1} \text{ cm}^{-1}$). 100 ng vector DNA fragment was mixed in a 1:3 molar ratio with the insert DNA fragment in a total volume of 5 μl . 15 μl 1.33x Gibson assembly master mix were added to the DNA mix. The whole reaction mixture was incubated for 30 min at 50°C, as the used exonuclease, DNA polymerase and DNA ligase (Table 3.1) are all active at this temperature.

3.2.2.3 Transformation of *E. coli* cells

E. coli cells were transformed with the DNA constructs generated in the Gibson assembly reaction (Chapter 3.2.2.2). Therefore, 100 µl chemically competent XL1-Blue cells (Agilent Technologies, Santa Clara, CA, USA) were mixed with the whole Gibson assembly reaction mix (20 µl) and incubated on ice for 30 min. Bacterial plasmid uptake was induced by a heat-shock at 42°C for 1 min. The bacterial cells prefer the uptake of correctly assembled DNA constructs, due to their circular organization compared to the linear vector and insert DNA fragments. The cells were then cooled on ice for 2 min followed by the addition of 800 µl LB medium and incubation at 37°C for 1 h shaking at 500 rpm (Thermomixer comfort, Eppendorf, Hamburg, GER). The cells were centrifuged at 5000g for 2 min (Centrifuge 5424, Eppendorf, Hamburg, GER) and 700 µl of the supernatant was decanted. The bacterial cell pellet was resuspended in the remaining LB medium and plated on an LB agar plate containing either 100 µg/ml ampicillin, 30 µg/ml kanamycin or 30 µg/ml chloramphenicol. The LB agar plate was incubated at 37°C overnight. Individual clones were picked from the plate to inoculate 5 ml LB medium supplemented with 100 µg/ml ampicillin and grown at 37°C shaking at 180 rpm (Multitron HT, Infors, Bottmingen, CH).

3.2.2.4 Plasmid preparation

After growing a transformed *E. coli* liquid culture overnight (Chapter 3.2.2.3), the amplified plasmids were prepared using the NucleoSpin™ Plasmid (Macherey-Nagel™, Düren, GER) kit according to the manufacturer's instructions. DNA concentration of the purified plasmids was determined via measuring the absorption at 260 nm using a Nanodrop 2000C (Thermo Scientific, Darmstadt, GER) and Equation (1).

3.2.2.5 Transformation of *Synechocystis* cells

The cyanobacterium *Synechocystis* is naturally competent (Barten and Lill, 1995) and, thus, DNA uptake proceeds without pretreatment of the cells. For transformation with a plasmid, a liquid culture of *Synechocystis* was photomixotrophically grown to an OD₇₅₀ of 0.6 – 1. The cells were harvested at 2500g, 10 min, RT (Allegra X-15R, Beckmann Coulter, Krefeld, GER) and resuspended in fresh BG11 medium to an OD₇₅₀ of 2.5. 400 µl cell suspension was transferred into a sterile glass tube and mixed with 5 µl plasmid. After incubation overnight at 30°C and 30 µE (Economic Delux, ECD01E, Snijders Scientific, Tilburg, NL), the cell

suspension was plated on a BG11 agar plate supplemented with 5 mM glucose and 10 µg/ml of the respective antibiotic. After 2 – 3 weeks, appearing colonies were picked with an inoculation loop and plated onto a new BG11 agar plate containing 20 µg/ml antibiotic. In this way, the antibiotic concentration in the BG11 agar plates was gradually increased up to 100 µg/ml (typically in the following steps: 10 µg/ml, 20 µg/ml, 30 µg/ml, 50 µg/ml, 75 µg/ml, 100 µg/ml) to allow homologous recombination and complete segregation of the cyanobacterial genome. After reaching the final antibiotic concentration on the BG11 agar plates, a liquid culture with BG11 medium containing 5 mM glucose and 75 µg/ml antibiotic was inoculated with the cells from the plate and after growth to an OD₇₅₀ of >3, the liquid culture was diluted into fresh BG11 medium supplemented with 5 mM glucose and 100 µg/ml antibiotic (starting OD₇₅₀ = 0.2).

3.2.2.6 DNA isolation from *Synechocystis* cells

After transformation of *Synechocystis* cells (Chapter 3.2.2.5), complete segregation of the genome was verified via PCR (Chapter 3.2.2.1) using primers (Table 3.5) binding to the regions flanking the transformed genomic areas. The length of the amplified PCR products was then analyzed by agarose gel electrophoresis (Chapter 3.2.2.1). The DNA templates for the PCR were obtained by phenolic DNA extraction. Therefore, a *Synechocystis* liquid culture was grown to an OD₇₅₀ of 1 – 2 and cells were harvested by centrifugation of 30 ml culture at 5000g, 10 min, RT (Allegra X-15R, Beckmann Coulter, Krefeld, GER). The supernatant was discarded, and the cell pellet was washed 3 – 4 times with 30 ml TES buffer. After the final washing step, the cell pellet was resuspended in 1.6 ml TES buffer, transferred to a 2 ml reaction tube, and again centrifuged at 16000g, 1 min, 4°C (Centrifuge 5415 R, Eppendorf, Hamburg, GER). The pellet was resuspended in 495 µl TES buffer and 5 µl lysozyme (200 mg/ml) was added, followed by incubation at 37°C for 30 min. The following steps were performed in a fume hood. 600 µl ROTI[®]Phenol (lower phase) and 50 µl sodium lauryl sarcosinate (10%, w/v) were added to the reaction tube and incubated for 15 min at RT with gentle shaking (Duomax 1030, Heidolph, Schwabach, GER). The sample was centrifuged at 16000g, 4°C, 10 min and the upper phase was transferred into a new 1.5 ml reaction tube using a cut pipette tip. After the addition of 5 µl ribonuclease (RNase) (10 mg/ml), the mixture was incubated for 15 min at 37°C. Subsequently, 100 µl NaCl (5 M), 80 µl CTAB solution (cut pipette tip) and 600 µl chloroform/isoamyl alcohol (24:1) were added, followed by incubation for 15 min at RT with gentle shaking. The sample was spun down at 16000g, 4°C, 5 min and the upper phase was transferred using a cut pipette tip into a fresh 1.5 ml reaction tube. The sample was mixed with

one volume (approx. 600 μ l) of isopropanol (no vortexing) and immediately centrifuged at 16000g, 4°C, 10 min for DNA precipitation. After decanting the supernatant, the DNA pellet was washed with 1 ml ethanol (70%, v/v) and again centrifuged at 16000g, 4°C, 5 min. The supernatant was discarded, and the DNA pellet air dried overnight. On the next day, the DNA pellet was dissolved in 100 μ l TE buffer and the DNA concentration was determined using a Nanodrop 2000C (Thermo Scientific, Darmstadt, GER) and Equation (1).

3.2.3 Preparative methods

3.2.3.1 Heterologous protein expression in *E. coli*

For the overexpression of recombinant proteins in *E. coli*, 50 μ l chemically competent Rosetta-gamiTM 2(DE3), Clear Coli[®] BL21(DE3), BL21-gold(DE3) or TunerTM(DE3) cells (Novagen, Darmstadt, GER) were transformed with 3 μ l of an isolated DNA plasmid, as described above for XL1-Blue cells (Chapter 3.2.2.3). The plasmids used for transformation were based on the pET303 vector (Thermo Fisher Scientific, Waltham, MA, USA) and, thus, allowed for selection of successfully transformed cells by ampicillin and for induction of protein overexpression by isopropyl- β -D-thiogalactopyranoside (IPTG).

After transformation, individual clones were picked and used to inoculate 50 ml LB medium containing 100 μ g/ml ampicillin. Liquid cultures were grown overnight at 37°C and 180 rpm (Multitron HT, Infors, Bottmingen, CH). On the next day, the whole 50 ml preculture was diluted into 2 l LB medium containing 100 μ g/ml ampicillin. The main culture was grown at 37°C and 115 rpm until an OD₆₀₀ of approx. 0.6 was reached. Then protein expression was induced via addition of 1 mM IPTG, and the culture was grown at 20°C and 115 rpm overnight. In the following day, cells were harvested by centrifugation at 5000 rpm, 10 min, 4°C (Avanti J-26XP, JLA-8.1, Beckmann Coulter, Krefeld, GER) and the resulting cell pellets were snap frozen in liquid nitrogen and stored at -20°C until further usage.

3.2.3.2 Protein purification

To isolate overexpressed proteins, frozen cell pellets (Chapter 3.2.3.1) were resuspended in lysis buffer (Table 3.1) supplemented with protease inhibitor cocktail (1:1000 diluted, Sigma-Aldrich Chemie GmbH, Taufkirchen, GER) and homogenized using a Potter-Elvehjem device. Cell lysis was performed by four runs in an LM20 Microfluidizer[®] (MicrofluidicsTM,

Westwood, MA, USA) at a pressure of 18000 psi, and the crude cell extract was centrifuged at 15000g, 10 min, 4°C (Avanti J-26XP, JA-25.50, Beckmann Coulter, Krefeld, GER) to remove cell debris.

Protein purification was typically performed by a combination of affinity chromatography using a Ni-NTA matrix followed by SEC. Therefore, a Ni-NTA matrix (Protino[®], Macherey-Nagel, Düren, GER), which was stored in 20% (v/v) ethanol at 4°C, was washed two times with MP-H₂O and two times with lysis buffer. During each washing step, the Ni-NTA matrix was centrifuged at 500g, 5 min, 4°C (Allegra X-15R, Beckmann Coulter, Krefeld, GER). The supernatant of the crude cell extract was mixed with the equilibrated Ni-NTA matrix and incubated for 2 h at 4°C in an overhead shaker (CMV-ROM, Fröbel, Lindau, GER) to allow binding of the recombinant, His-tagged protein to the Ni-NTA matrix. After that, the Ni-NTA matrix was washed twice in each case with 10 column volumes (CV) washing buffer supplemented with either 20 mM, 40 mM, or 50 mM imidazole, respectively, to wash off unspecifically bound proteins. Finally, the target protein was eluted from the Ni-NTA matrix using elution buffer in four elution steps (first three steps with 1 CV elution buffer, fourth step with 0.5 CV elution buffer).

Next, the combined eluate was incubated with 20 mM DTT for 30 min on ice and concentrated to a final volume of approx. 5.5 ml using an Amicon[®]Ultra-15 centrifugal filter (Merck KGaA, Darmstadt, GER) with a molecular weight cut-off (MWCO) of 50, 30 or 3 kDa, depending on the molecular mass of the target protein. The proteins were further purified via SEC using an ÄKTA purifier 10 system (GE Healthcare, Munich, GER) and an appropriate column. The column material and the resulting pore size depended on the molecular mass of the investigated proteins. Generally, proteins with a high molecular mass and the propensity to form oligomers (*e.g.*, *SynDLP* wt) were purified via a self-packed Sephacryl[®] S-400 HR column (Cytiva, Freiburg, GER; CV = approx. 120 ml). Truncated monomeric *SynDLP* variants (*e.g.*, the minimal GD (MGD) construct of *SynDLP* (*SynDLP*-MGD)) were loaded on a Superdex[®] 200 Hi-Load 16/600 column (Cytiva, Freiburg, GER) and *SynTrxA* with a low molecular mass on a Superdex[®] 75 Hi-Load 16/600 pg column (Cytiva, Freiburg, GER). Typically, the columns were washed with 2 CV MP-H₂O and equilibrated with 2 CV storage buffer. The flow rate was set to 0.25 – 1 ml/min, depending on the used column. Main peak fractions were collected and concentrated using an Amicon[®]Ultra-15 centrifugal filter with an appropriate MWCO. The final protein sample was aliquoted, snap frozen in liquid nitrogen and stored at -20°C. Single steps of the purification procedure as well as the purity of the final protein sample were analyzed

via SDS-PAGE (Chapter 3.2.4.2). Typically, the protein concentration was determined using a Pierce™ BCA protein assay kit or, if the stored protein solution contained reducing agents like DTT, a Pierce™ BCA-RAC assay (reducing agent compatible) kit (Thermo Fisher Scientific, Waltham, MA, USA).

3.2.3.3 Immunoprecipitation

For the analysis of natively expressed *SynDLP* in the cyanobacterium *Synechocystis*, it was necessary to concentrate the protein via immunoprecipitation (IP) due to a low expression level and/or a too low affinity of the antiserum. Therefore, 100 ml of a *Synechocystis* liquid culture was photomixotrophically grown (Chapter 3.2.1.2) to an OD₇₅₀ of 1 – 2. Cell harvesting was performed by centrifugating the culture at 5000g, 10 min, 20°C (Allegra X-15R, Beckmann Coulter, Krefeld, GER) and the cell pellet was washed twice with 50 ml thylakoid buffer (Table 3.1). After removal of the supernatant, the cell pellet was resuspended in 1 ml IP lysis buffer. If a cell fractionation into membrane and soluble fraction was necessary after cell lysis, the cell pellet was resuspended in 1 ml IP detergent-free buffer. The cell suspension was transferred into a 1.5 ml reaction tube, snap frozen in liquid nitrogen, and directly thawed at 37°C (Thermomixer comfort, Eppendorf, Hamburg, GER). Next, the cell suspension was pipetted into a 2 ml screw cap tube and 30 µl undiluted protease inhibitor cocktail (Sigma-Aldrich Chemie GmbH, Taufkirchen, GER) was added. Approx. 1/3 of the height of the 2 ml screw cap tube was filled with glass beads (Sigma-Aldrich Chemie GmbH, Taufkirchen, GER; Ø 0.5 mm) and the cell lysis was performed using a cell homogenizer (SpeedMill PLUS, Analytik Jena, Jena, GER) in interval mode with 1 min shaking and 1 min cooling on ice for four rounds. The crude cell extract was centrifuged at 5000g, 5 min, 4°C (Centrifuge 5415 R, Eppendorf, Hamburg, GER) to remove the glass beads and cell debris. This centrifugation step was repeated two times with the supernatant (first time at 1000g, 5 min, 4°C and second time at 16000g, 10 min, 4°C) to get rid of any remaining glass beads. If necessary, the membrane and soluble fraction of the cell lysate were separated via an additional ultracentrifugation step at 100,000g, 40 min, 4°C (Optima™ MAX-XP ultracentrifuge, MLA-130, Beckmann Coulter, Krefeld, GER). The supernatant containing the soluble fraction was transferred into a 1.5 ml reaction tube and Triton X-100 (final concentration: 0.2%, v/v) was added. The pellet containing the membrane fraction was solubilized in an equal volume of IP lysis buffer supplemented with 30 µl undiluted protease inhibitor cocktail using a Potter-Elvehjem device.

The native *SynDLP* was immunoprecipitated from the cell lysate using Protein A-Sepharose beads (Sigma-Aldrich Chemie GmbH, Taufkirchen, GER) coupled with the α -*SynDLP* antibody (Table 3.6). Therefore, 10 mg Protein A-Sepharose beads were washed two times with 200 μ l MP-H₂O, each time centrifuged at 1500g, 5 min, 4°C (Centrifuge 5415 R, Eppendorf, Hamburg, GER). Then, the Protein A-Sepharose beads were washed with 200 μ l IP lysis buffer and, finally, resuspended in 100 μ l IP lysis buffer to result in a 10% (w/v) suspension. The bead suspension was incubated at least 2 h at 4°C. After removal of the glass beads from the cell lysate or the cell lysate fractionation, respectively, 20 μ l of the prepared Protein A-Sepharose bead suspension (10%, w/v, cut pipette tip) were added per 500 μ l lysate, membrane and soluble fraction, respectively. The mixture was incubated for 1 h at 4°C rotating in an overhead shaker (CMV-ROM, Fröbel, Lindau, GER) to bind any unspecific proteins of the cell lysate to the Protein A-Sepharose beads. The sample was centrifuged at 1500g, 5 min, 4°C to remove the beads with undesired binding partners. The supernatant was transferred into a new 1.5 ml reaction tube and 30 μ l fresh Protein A-Sepharose bead suspension (10%, w/v, cut pipette tip) plus 0.5 μ l undiluted α -*SynDLP* antibody were added per 500 μ l sample volume. The mixture was incubated for 1.5 h at 4°C rotating in an overhead shaker to allow for α -*SynDLP* binding to the Protein A-Sepharose beads as well as binding of the *SynDLP* epitope to the paratope of α -*SynDLP*. After centrifugation at 1500g, 5 min, 4°C, the supernatant was decanted, and the beads were washed with 1 ml IP washing buffer for 10 min at 4°C rotating in an overhead shaker. The beads were again centrifuged at 1500g, 5 min, 4°C and this washing step was repeated. Then, the beads were washed with 1 ml MP-H₂O for 5 min at 4°C rotating in an overhead shaker and centrifuged at 1500g, 5 min, 4°C. After removing as much supernatant as possible, 5 μ l 5x SDS sample buffer (including DTT) was added to the beads and the sample was boiled at 95°C for 5 min. As much supernatant as possible was loaded on an SDS-PAGE gel and after SDS-PAGE (Chapter 3.2.4.2), *SynDLP*-containing bands were visualized by Western Blot analysis (Chapter 3.2.4.3) using the α -*SynDLP* as primary and an α -rabbit-HRP conjugate as secondary antibody.

3.2.3.4 LUV preparation

Large unilamellar vesicles (LUVs), also referred to as liposomes, were prepared to enable the investigation of proteins with spherical lipid bilayers as model membranes with a defined lipid composition. The phospholipids DOPG (1,2-dioleoyl-*sn*-glycero-3-phosphoglycerol), DMPG (1,2-dimyristoyl-*sn*-glycero-3-phosphoglycerol), DOPC (1,2-dioleoyl-*sn*-glycero-3-

phosphocholine), the galactolipids MGDG, DGDG and SQDG, the fluorescently labeled lipids LissRhod-PE (Lissamine Rhodamine PE; 1,2-dioleoyl-*sn*-glycero-3-phosphoethanolamine-N-(Lissamine Rhodamine B sulfonyl) (ammonium salt)) and NBD-PE (1,2-distearoyl-*sn*-glycero-3-phosphoethanolamine-N-(7-nitro-2-1,3-benzoxadiazol-4-yl)) as well as the biotinylated lipid biotinyl-Cap-DOPE (1,2-dioleoyl-*sn*-glycero-3-phosphoethanolamine-N-(cap biotinyl)) were all purchased from Avanti Polar Lipids, Inc. (Birmingham, AL, USA). The lipids were dissolved in an organic solvent (either CHCl₃/MeOH 2:1, v/v, or 100% CHCl₃) and stored at -20°C. For the preparation of LUVs, the organic solvent was evaporated under a gentle nitrogen gas stream followed by vacuum desiccation overnight to remove any traces of solvent. The dried lipid film was hydrated in a buffer depending on the respective experiment and LUVs were generated by five cycles of freezing in liquid nitrogen and thawing at 37°C. The LUVs were extruded 15 times through an appropriate filter (Nucleopore Track-Etch Membrane, Whatman, Sigma-Aldrich GmbH, Taufkirchen, GER) using a Mini-Extruder (Avanti Polar Lipids, Inc., Birmingham, AL, USA), if necessary.

3.2.3.5 GUV preparation

Membrane binding of proteins was also analyzed using GUVs as model membrane system. GUVs were produced by gel-assisted swelling of lipids on a dried polyvinyl alcohol (PVA) film (Weinberger *et al.*, 2013). 25 µl of a 1% (w/v) PVA (molecular mass 145,000 Da, Sigma-Aldrich Chemie GmbH, Taufkirchen, GER) solution were placed on a glass coverslip (Ø 10 mm) and heated to 50°C for 30 min. After cooling to RT, 8 µl of a 1 mg/ml lipid mixture (70% DOPC/30% DOPG, w/w), containing 0.04% (w/w) of the fluorescent lipid ATTO633-PE (ATTO633-1,2-dioleoyl-*sn*-glycero-3-phosphoethanolamine; ATTO-TEC GmbH, Siegen, GER), was spread on the PVA film. The organic solvent was removed in a vacuum desiccator for 30 min. The glass coverslip was transferred into a 24-well-plate and GUVs formed upon addition of 400 µl reaction buffer (Table 3.1). After at least 1 h of swelling, the GUV-containing solution was removed from the glass coverslip and transferred into a 2 ml reaction tube using a cut pipette tip until further use.

3.2.4 Bioanalytical methods

3.2.4.1 Analytical size exclusion chromatography

The molecular mass of proteins and protein assemblies was estimated using analytical SEC also referred to as analytical gel filtration. For analytical purposes, the columns Superdex 200 Increase 3.2/300 and Superose™ 6 Increase 3.2/300 (Cytiva, Freiburg, GER) were used due to their small CV of approx. 2.4 ml combined with a high resolution. For larger proteins and protein complexes, the Superose™ 6 Increase 3.2/300 column with a fractionation range of approx. 5 – 5000 kDa was used. The separation of smaller proteins was typically performed on the Superdex 200 Increase 3.2/300 column (Cytiva, Freiburg, GER) with a narrower fractionation range of approx. 10 – 600 kDa. Unless otherwise specified, the columns were operated at a flow rate of 0.03 ml/min at 7°C on an ÄKTA purifier 10 system (GE Healthcare, Munich, GER), and the elution of protein was monitored via the absorption at 280 nm. The columns were stored in 20% (v/v) ethanol and washed with 2 CV MP-H₂O, followed by equilibration with 2 CV of a salt-containing buffer, e.g., reaction buffer (Table 3.1). Before sample application, the protein solution was centrifuged at 16000g, 10 min, 4°C (Centrifuge 5415 R, Eppendorf, Hamburg, GER) to avoid the loading of any larger aggregates onto the column. Then, 30 µl of a sample with a protein concentration in the range of 10 µM was applied to the column using a Hamilton™ syringe.

For the investigation of nucleotide-dependent assembly of *SynDLP*-MGD, 10 µM *SynDLP*-MGD was incubated in reaction buffer with 2 mM nucleotides for 30 min at 4°C. The interaction with the nucleotides GTP (Sigma-Aldrich Chemie GmbH, Taufkirchen, GER), GDP (Thermo Fisher (Kandel) GmbH, Kandel, GER), GDP-ALF₄ or with the non-hydrolysable GTP analog guanosine-5'-[(β,γ)-imido]triphosphate (GMPPnP; Sigma-Aldrich Chemie GmbH, Taufkirchen, GER) was tested. The transition state analog GDP-AIF₄ was generated from a mixture of 2 mM GDP, 2 mM AlCl₃ and 20 mM NaF. After incubation, a Superdex 200 Increase 3.2/300 column, equilibrated with reaction buffer, was loaded with 30 µl of the reactions. Proteins were eluted using an ÄKTA purifier 10 system at 7°C and a flow rate of 0.04 ml/min.

The columns were calibrated using common globular standard proteins with a known molecular mass to estimate the molecular mass of the sample proteins. The following standard proteins with the corresponding molecular mass were used and 30 µl were loaded at the indicated concentrations: cytochrome c (12.4 kDa, 1 mg/ml), RNase A (13.7 kDa, 3 mg/ml), carboanhydrase (29 kDa, 1.5 mg/ml), ovalbumin (44 kDa, 4 mg/ml), albumin (66 kDa, 3 mg/ml), conalbumin (75 kDa, 3 mg/ml), alcohol dehydrogenase (150 kDa, 5 mg/ml), aldolase

(158 kDa, 2 mg/ml), β -amylase (200 kDa, 4 mg/ml), ferritin (440 kDa, 0.3 mg/ml), thyroglobulin G (669 kDa, 0.5 mg/ml).

3.2.4.2 SDS-PAGE

Proteins were separated in an electric field solely depending on their molecular mass using a discontinuous SDS-PAGE (Laemmli, 1970). The gels were prepared either by using the TGX™ FastCast™ Acrylamide kit, 10% (Bio-Rad, Munich, GER) following the manufacturer's instructions or by pipetting the ingredients shown in Table 3.14 for the respective acrylamide percentages. The compositions of the separation gel buffer and stacking gel buffer are shown in Table 3.1. Ammonium peroxodisulfate (APS) and tetramethylethylenediamine (TEMED) were added at the end to initiate the radical polymerization.

Table 3.14: Composition of SDS-PAGE separation and stacking gels.

Percentage	Separation gel			Stacking gel
	10%	12%	16%	6%
H ₂ O [ml]	5	4.5	3.5	6
Acrylamide [ml]	2.5	3	4	1.5
Separation gel buffer [ml]	2.5	2.5	2.5	-
Stacking gel buffer [ml]	-	-	-	2.5
10% (w/v) APS [μ l]	50	50	50	50
TEMED [μ l]	20	20	20	20

Prior to sample application, 1/5 volume 5x SDS sample buffer was added to the sample and the mixture was boiled at 95°C for 5 min to destroy any quaternary, tertiary, and secondary structures of the proteins. Additionally, the SDS covers the charge of the proteins leading to an SDS/protein complex with a negative net charge and a constant mass/charge ratio. Thus, the migration velocity of the complex in an electric field solely depends on the molecular mass of the protein monomer. For non-reducing conditions, the DTT was omitted from the 5x SDS sample buffer to prevent the breakage of disulfide bridges. After sample application, the SDS-PAGE was performed in a Mini-Protean 3 Cell (Bio-Rad, Munich, GER) filled with SDS running buffer at a voltage of 120 – 200 V for approx. 1 h. Protein-containing bands were stained via incubation of the gels in Coomassie staining solution on a horizontal shaker (Duomax 1030, Heidolph, Schwabach, GER) for 1 h, followed by destaining of the background in Coomassie destaining solution for 2 h. Finally, the gel was transferred into H₂O and image

acquisition was performed on the next day using a ViewPix 700 (Biostep, Burkhardtsdorf, GER).

3.2.4.3 Western Blot

After separation of proteins by their molecular mass via SDS-PAGE (Chapter 3.2.4.2), protein bands could be immunologically visualized, alternatively to unspecific Coomassie Brilliant Blue staining, after Western blotting. After SDS-PAGE, the protein bands in the gel were transferred to a polyvinylidene difluoride (PVDF) membrane in an electric field at 25 V for 30 min perpendicular to the gel using the Trans-Blot Turbo Transfer System (Bio-Rad, Munich, GER). The membrane was blocked with blocking buffer (Table 3.1) for 1 h on a horizontal shaker (Duomax 1030, Heidolph, Schwabach, GER) and washed with TBST buffer (4x 5 min). Then, either the α -SynDLP or the His•Tag[®] antibody HRP conjugate (Table 3.6) was applied to the PVDF membrane as primary antibody and incubated for 1 h on a horizontal shaker. After washing the membrane four times with TBST buffer for 5 min, an α -rabbit-HRP conjugate was applied to the membrane as secondary antibody, in case α -SynDLP was the primary antibody, to allow detection of SynDLP. After incubation for 1 h on a horizontal shaker, the membrane was again washed with TBST buffer (4x 5 min) and, finally, the membrane was stained using the Amersham[™] ECL Prime[™] Western Blotting Detection Reagent (VWR International GmbH, Darmstadt, GER). Immunologically stained bands were detected and visualized using the chemiluminescence detection systems Stella (Raytest, Straubenhardt, GER) or Fusion FX (Vilber, Eberhardzell, GER).

3.2.4.4 Sedimentation assay

Oligomerization of SynDLP under different buffer conditions or in the presence of different nucleotides was tested using a sedimentation assay. Typically, 0.5 μ M SynDLP was incubated in reaction buffer for 30 min on ice, optionally supplemented with 2 mM of the nucleotides GTP (Sigma-Aldrich Chemie GmbH, Taufkirchen, GER), GDP (Thermo Fisher (Kandel) GmbH, Kandel, GER) or the non-hydrolysable GTP analog GMPPnP (Sigma-Aldrich Chemie GmbH, Taufkirchen, GER), respectively. The mixture was spun down in an ultracentrifuge at 60000g, 30 min, 4°C (Optima[™] MAX-XP ultracentrifuge, TLA-100, Beckmann Coulter, Krefeld, GER). The supernatant was collected, and the pellet was resuspended in an equal volume 1x SDS sample buffer (Table 3.1). The supernatant as well as a sample taken before

ultracentrifugation were prepared with 5x SDS sample buffer as described in detail in Chapter 3.2.4.2. Equal volumes of all samples were applied to an SDS-PAGE gel (Chapter 3.2.4.2). After electrophoresis and Coomassie Brilliant Blue staining of the protein bands, the band intensities were determined using the software Fiji-ImageJ (Schindelin *et al.*, 2012).

3.2.4.5 DTT titration

The effect of the reducing agent DTT on the stability of the disulfide bridge in *SynDLP* was investigated via DTT titration. Therefore, isolated *SynDLP* was incubated with different DTT concentrations (final concentrations: 0 – 500 mM) in 20 mM HEPES buffer pH 7.4 for 15 min at RT. The samples were prepared with 5x SDS sample buffer (without DTT) (Table 3.1) and analyzed via SDS-PAGE as described in detail in Chapter 3.2.4.2.

For the study of a potential interaction between *SynDLP* and a recombinant Trx of *Synechocystis* (*SynTrxA*), 2 μ M *SynDLP* was incubated in a buffer containing 2 mM EDTA, 20 mM HEPES buffer pH 7.4 with different DTT concentrations (final concentrations: 0 – 500 mM), either in the presence or the absence of 6 μ M *SynTrxA* for 30 min at RT. Sample preparation with 5x SDS sample buffer (without DTT) and SDS-PAGE analysis were performed as described above (Chapter 3.2.4.2).

3.2.5 Bioanalytical spectroscopy

3.2.5.1 GTPase assay

The GTPase activity was measured with a modified version of a continuous, regenerative, coupled GTPase assay (Ingerman and Nunnari, 2005; Jilly, 2018). Here, GTP turnover is coupled to the oxidation of NADH (nicotinamide adenine dinucleotide) to NAD⁺ by the activity of a pyruvate kinase and a lactate dehydrogenase, allowing for the spectroscopic measurement of NADH oxidation via a decrease in the absorption at 340 nm, since the oxidized NAD⁺ shows no absorption at this wavelength.

Initially, a master mix was prepared containing phosphoenolpyruvate (final concentration: 1 mM), PK/LDH (final concentration: 2.33%, v/v, Table 3.7) and NADH (final concentration: 0.6 mM; Carl Roth GmbH + Co. KG, Karlsruhe, GER) in reaction buffer (Table 3.1). Different GTP (Sigma-Aldrich Chemie GmbH, Taufkirchen, GER) concentrations (final concentrations: 0 – 5 mM) were dissolved in 20 mM HEPES buffer pH 7.4 and the master mix was added to

the samples containing the various GTP concentrations. The mixtures were incubated for 15 min at 4°C to convert any remaining GDP present in the GTP stock, putatively due to autohydrolysis of GTP. Protein with a final concentration of 0.5 μM as well as pure storage buffer (blank) were pipetted into a 96-well-plate and the GTP-containing master mix was added, leading to a final volume of 150 μl per well. The absorption at 340 nm was measured in a microplate reader (FLUOstar Omega, BMG Labtech GmbH, Ortenberg, GER) over 2 – 3 h at 30°C to ensure the complete NADH oxidation even at the lowest GTP concentrations. The GTPase activities at different GTP concentrations were calculated by subtraction of the absolute value of the slope of the respective blank measurement from the absolute value of the maximal linear decrease of the absorption ($\frac{\Delta A_{340}}{\Delta t}$) in the protein-containing samples. With this blank-corrected decrease of the absorption at 340 nm ($\frac{\Delta A_{340,corr}}{\Delta t}$), the GTP hydrolysis activity per minute and enzyme molecule was calculated as follows (Equation (2)):

$$Activity = \frac{\Delta A_{340,corr}}{\Delta t} * \frac{1}{d * \epsilon * c_{Protein}} \quad (2)$$

Here, d refers to the thickness of a sample volume of 150 μl in a 96-well-plate (0.38 cm), and ϵ is the molar extinction coefficient of NADH at 340 nm (6220 M⁻¹ cm⁻¹). After plotting the calculated activities against the GTP concentrations, the data points were fitted by application of the Michaelis-Menten equation (Equation (3)) to, finally, determine the Michaelis-Menten constant (K_m) and the turnover rate (k_{cat}).

$$Activity ([GTP]) = \frac{[GTP] * k_{cat}}{[GTP] + K_m} \quad (3)$$

In some cases, the data points were fitted using the Hill equation (Equation (4)):

$$Activity ([GTP]) = \frac{[GTP]^n * k_{cat}}{[GTP]^n + K_D^n} \quad (4)$$

Here, the additional parameter n refers to the Hill coefficient and K_D to the half-saturation constant.

3.2.5.2 Malachite green phosphate assay

As the continuous, regenerative, coupled GTPase assay described in Chapter 3.2.5.1 regenerates any GDP to GTP during the measurement, it is not suitable for the determination of a GDP hydrolysis activity. Therefore, a malachite green phosphate assay was used to measure a

putative GDP hydrolysis activity of *SynDLP*. This is a colorimetric assay that measures the free inorganic phosphate (P_i) formed during the hydrolysis of a nucleotide.

The malachite green phosphate assay was performed using the Malachite green phosphate assay kit (Abcam, Berlin, GER). Initially, a potential phosphate contamination of the used reaction buffer (Table 3.1) as well as solely 1 μ M *SynDLP* was tested to exclude a P_i signal from any other sources than nucleotide hydrolysis. The samples were prepared following the manufacturer's instructions and the absorption at 635 nm was measured using a microplate reader (PowerWave XS, BioTek Instruments, Inc., Winooski, VT, USA). Then, a concentration series of *SynDLP* (0.1 – 1 μ M) was incubated with 0.5 mM GDP (Thermo Fisher (Kandel) GmbH, Kandel, GER) in reaction buffer for 6 h at 30°C. A blank with 0.5 mM GDP and without protein was incubated at the same conditions. The samples were prepared and measured as described above. The absorption value of the blank measurement was subtracted from the protein samples and the P_i -release at the respective protein concentrations was calculated using a standard row with known P_i -concentrations according to the manufacturer's instructions.

3.2.5.3 Mant-GTP binding assay

Nucleotide binding affinities of proteins were determined using the fluorescently labeled nucleotide Mant-GTP (Jena Bioscience, Jena, GER), which shows an increasing fluorescence intensity as well as anisotropy after binding to the active site of a GTPase. Therefore, increasing protein concentrations (0 – 4 μ M) were incubated with 1 μ M Mant-GTP in reaction buffer (Table 3.1) for 30 min at 20°C. The fluorescence anisotropy of the samples was measured ten times with $\lambda_{ex} = 355$ nm, $\lambda_{em} = 448$ nm, slits of 7 nm, at 20°C using a FluoroMax-4 fluorescence spectrometer (Horiba Scientific, Kyoto, JPN). The results were averaged, the fluorescence anisotropy values were plotted against the protein concentration and the data points were fitted via a quadratic binding equation assuming a one-site specific binding model (Equation (5)):

$$r(x) = r_0 + r_{max} * \frac{(F+x + K_D) - \sqrt{(F+x + K_D)^2 - 4*x*F}}{2*F} \quad (5)$$

The parameters are defined as follows: r refers to the fluorescence anisotropy, r_0 to the fluorescence anisotropy of Mant-GTP without added protein, r_{max} to the maximum fluorescence anisotropy, F to the Mant-GTP concentration and x to the protein concentration. K_D corresponds to the dissociation constant.

3.2.5.4 CD spectroscopy

Secondary structures as well as the thermal stability of proteins was analyzed using CD spectroscopy in the UV range. For the recording of a CD spectrum, typically 1 μ M protein was buffered in either 10 mM HEPES buffer pH 7.4 or 1 mM sodium phosphate (NaPi) buffer pH 7.4 using an Amicon®Ultra-4 centrifugal filter (Merck KGaA, Darmstadt, GER) with an appropriate MWCO. The spectra were recorded using a J-815 or a J-1500 CD spectrometer (JASCO cooperation, Tokyo, JPN) equipped with a temperature-controlled cell holder (MTPC-490S, JASCO cooperation, Tokyo, JPN). Normally, the spectral range was set to 200 – 250 nm with a scan rate of 50 nm/min, 1 nm steps, 5 nm bandwidth, 1 s data integration time, 8-time accumulation, 1 mm cell length and a temperature of 20°C.

CD spectra were measured at increasing temperatures to test the thermal stability of proteins. Therefore, the spectra were recorded in the range of 200 – 250 nm with a scan rate of 100 nm/min, 1 nm steps, 5 nm bandwidth, 1 s data integration time, 1-time accumulation, 1 mm cell length at increasing temperatures. The starting temperature was 20°C, and the samples were heated in 2°C steps with a heating rate of 1°C/min up to 96°C. The single spectra were smoothed using the Savitzky-Golay filter in the JASCO software package and the CD value at 222 nm was extracted from each spectrum. Each condition was individually measured three times and the data sets were interpolated since the single measurements were obtained at slightly varying actual temperatures. After interpolation, the data sets were normalized, averaged and the θ at 222 nm was plotted against the temperature, resulting in a melting curve. A transition temperature (T_m) was extracted from the melting curve by fitting of the data points via an adapted Boltzmann fit (Equation (6)). The fit assumes a two-state unfolding mechanism allowing for linear slopes in the plateau regions of the melting curve:

$$\theta_{meas}(T) = \frac{(T * m_N + \theta_N) - (T * m_D + \theta_D)}{1 + e^{\frac{T - T_m}{dT}}} + (T * m_D + \theta_D) \quad (6)$$

Here, θ_{meas} corresponds to the measured ellipticity at 222 nm and T to the temperature. θ_N and θ_D are the ellipticities at the plateau areas of the native or rather the denatured protein and m_N and m_D are the linear slopes of the corresponding plateaus.

3.2.5.5 ANS fluorescence thermal shift assay

Complementary to the CD spectroscopy (Chapter 3.2.5.4), the thermal stability of proteins was investigated via a fluorescence thermal shift assay (FTSA) using the fluorescent dye 8-

anilinonaphthalene-1-sulfonic acid (ANS). Compared to CD spectroscopy, this allows using more diverse buffer systems as well as the addition of substances that would interfere with the CD signal, like, *e.g.*, nucleotides. After mixing with proteins, ANS shows an increased fluorescence emission when it is bound to hydrophobic regions located at protein surfaces of correctly folded proteins or to hydrophobic areas becoming accessible due to protein unfolding. Thus, it is possible to use ANS to monitor protein unfolding.

Typically, 5 μM protein was mixed with 50 μM ANS (Sigma-Aldrich Chemie GmbH, Taufkirchen, GER) and, if necessary, 2 mM nucleotide in reaction buffer (Table 3.1). The fluorescence emission was recorded using a FP-8500 fluorescence spectrometer (JASCO cooperation, Tokyo, JPN) in the range of 400 – 600 nm upon ANS excitation at 370 nm. The excitation and emission slits were set to 2.5 nm. The integration time was set to 0.1 s and the scan rate to 200 nm/min with 1 nm steps. Fluorescence emission spectra were recorded at increasing temperatures in the range of 20 – 90°C heated in 1°C steps with a heating rate of 1°C/min. The fluorescence emission intensity at 470 nm was used to describe the folding state of the protein. For each condition, three independent measurements were combined, and the data sets were interpolated, as the actual temperatures varied in the single measurements. The data sets were averaged and the F_{470} was plotted against the temperature to obtain a melting curve. A T_m was determined as described for the CD spectroscopy (Equation (6)) using an adapted Boltzmann fit (Equation (7)):

$$F_{meas}(T) = \frac{(T * m_N + F_N) - (T * m_D + F_D)}{1 + e^{\frac{T - T_m}{dT}}} + (T * m_D + F_D) \quad (7)$$

Here, F_{meas} refers to the measured fluorescence emission intensity at 470 nm, T is the temperature, F_N and F_D are the fluorescence emission intensities at the plateau areas of native and denatured protein, m_N and m_D are the linear slopes of the corresponding plateau regions. Noteworthy, fitting with Equation (7) was not applied to the entire measured temperature range, since the ANS fluorescence strongly depends on the temperature and not only on binding to a folded or unfolded protein. Thus, the data were fitted in a temperature range of 20 – 25°C capturing the transition phase.

3.2.5.6 Laurdan fluorescence assay

Membrane interaction of proteins was investigated using the fluorescent dye Laurdan (6-dodecanoyl-N,N-dimethyl-2-naphthylamine; Sigma-Aldrich Chemie GmbH, Taufkirchen,

GER). Laurdan incorporates into lipid bilayers and shows fluorescence emission properties that depend on the polarity of its direct environment. Changes in the membrane polarity can be caused, *e.g.*, by protein binding to the membrane surface, and, thus, the Laurdan fluorescence emission can be used to monitor membrane binding events.

For the Laurdan fluorescence assay, liposomes with defined lipid compositions were prepared as model membranes (Chapter 3.2.3.4, no extrusion). Typically, the liposomes contained DOPC and one of the TM lipids MGDG, DGDG, SQDG or DOPG in a certain ratio and Laurdan was added to the lipid mixture at a molar ratio of 1:500 (Laurdan:lipid) prior to liposome formation. Liposomes were prepared in 20 mM HEPES buffer pH 7.4 and 0.1 mM liposomes were incubated either with 0.5 μ M protein or, for membrane binding curves, with increasing protein concentrations up to 10 μ M protein. The protein-liposome mixtures were incubated for 30 – 60 min at 25°C and the Laurdan fluorescence emission spectra were measured using a FluoroMax-4 fluorescence spectrometer (Horiba Scientific, Kyoto, JPN) at 25°C in the range of 400 – 550 nm upon excitation at 350 nm. Excitation and emission slits were set to 3 nm. For the quantification of changes in the Laurdan fluorescence emission spectrum, the Generalized Polarization (*GP*) value (Parasassi and Gratton, 1995) was calculated for each spectrum (Equation (8)):

$$GP = \frac{I_{440} - I_{490}}{I_{440} + I_{490}} \quad (8)$$

Here, I_{440} and I_{490} are the fluorescence emission intensities of Laurdan at 440 and 490 nm, respectively. ΔGP values were calculated via subtraction of the *GP* value of sole liposomes without protein. For membrane binding curves, the measured *GP* values were plotted against the protein concentration and the data points were fitted by a biphasic model combining a hyperbolic and a linear phase (Equation (9)):

$$GP(x) = (y_0 + m * x) + GP_{max} \frac{x}{K_D + x} \quad (9)$$

Here, x corresponds to the protein concentration, y_0 to the intercept of the y-axis and m to the slope of the linear phase. GP_{max} refers to the maximum *GP* value and K_D to the dissociation constant.

3.2.5.7 Dynamic light scattering

DLS was used to determine size distributions of liposomes and proteins. Liposomes were prepared as previously described (Chapter 3.2.3.4) in storage buffer (Table 3.1) and, typically, extruded to 100 nm. For the investigation of protein-triggered membrane fusion events, 0.1 mM liposomes with a lipid composition of 60% MGDG/40% DOPG (*w/w*), 1 μ M *SynDLP* or a mixture of both were incubated in reaction buffer for 15 min at RT. The size distribution in the samples was measured in a Zetasizer Nano S-Size (Malvern Panalytical, Malvern, UK) at 25°C using backscatter. Three individual samples were measured three times after an equilibration time of 60 s and evaluated using the manufacturer's software to obtain an intensity-weighted size distribution.

3.2.5.8 Membrane fusion assay

The membrane fusion activity of proteins was tested using a FRET (Förster resonance energy transfer)-based liposome fusion assay. In principle, liposomes were labeled with two fluorescent dyes in a sufficient concentration to form a FRET-pair. When the labeled liposomes were mixed with unlabeled liposomes without fluorescent dyes, membrane fusion events were measurable due to the redistribution of the FRET dyes as a decrease in FRET efficiency or rather an increase in donor fluorescence.

For the membrane fusion assay, unlabeled 60% MGDG/40% DOPG (*w/w*) liposomes were prepared as described in Chapter 3.2.3.4 in storage buffer (Table 3.1) with extrusion to 100 nm. Labeled liposomes contained 0.8 mol% of the FRET-dyed lipids NBD-PE and LissRhod-PE each and were prepared the same way. Mock fused liposomes with only 0.08 mol% of each fluorescently labeled lipid were prepared and measured to correct for bleaching. Next, labeled and unlabeled liposomes were mixed at a ratio of 1:9 (*v/v*). Protein solutions were incubated in reaction buffer for 10 min at 25°C prior to mixing with the liposomes. Then, the protein solution containing different final protein concentrations (0 – 5 μ M) was rapidly mixed with the mixture of labeled and unlabeled liposomes (final concentration: 0.1 mM), and the measurement was started immediately. The fluorescence emission kinetic of the FRET donor NBD-PE was monitored at 535 nm upon excitation at 460 nm for 15 min at 25°C using a FluoroMax-4 fluorescence spectrometer (Horiba Scientific, Kyoto, JPN). The slits for excitation and emission were set to 2 nm and 10 nm, respectively. Relative fusion activities were obtained by the conversion of the raw fluorescence data using Equation (10):

$$Fusion\ activity(t) = \frac{I - I_0}{I_M - I_0} \quad (10)$$

Here, I_0 refers to the NBD-PE fluorescence emission intensity of the negative control measured without protein, I_M to the intensity of the mock fused liposomes and I to the measured sample at every point in time t . Initial fusion rates were defined as the slope of a linear regression of the first 20 s of every fusion curve.

3.2.5.9 Sum frequency generation spectroscopy

Sum frequency generation (SFG) spectroscopy was performed by [REDACTED] (Jilly, 2018) in cooperation with [REDACTED] (Max-Planck-Institute for Polymer Research, Mainz, GER), [REDACTED] (Aarhus University, DNK) and [REDACTED]. SFG spectroscopy was used to get selective information about *SynDLP*'s orientation and conformation at membrane-buffer interfaces.

Two laser beams are required for the generation of an SFG signal. SFG experiments were carried out with a constant laser in the visible range and a tunable laser in the infrared (IR) range. The two laser beams overlap at the sample, resulting at light generation at their sum-frequency ($\omega_{SFG} = \omega_{VIS} + \omega_{IR}$). The pulses were provided by a Ti:sapphire laser (Mai Tai, Spectra-Physic, Santa Clara, CA, USA), amplified by a femtosecond regenerative amplifier (Spitfire Ace, Santa Clara, CA, USA) and pumped by an Nd:YLF laser (Empower, Spectra-Physics, Santa Clara, CA, USA). The pulse repetition rate of the resulting beam was 1 kHz with a duration of about 40 fs and a power of about 5 mJ at 800 nm. The laser beam then passed through a beam splitter. The IR beam was generated in an optical parametric amplifier (TOPAS, Light Conversion, Vilnius, Lithuania) using one part of the beam. Detection of the SFG signal was performed by an EMCCD camera (Newton, Andor, Belfast, Northern Ireland). The spectra were recorded in the polarization setting ssp (s-SFG, s-VIS, and p-IR) and averaged for 600 s, respectively. The background was subtracted, and the spectra were normalized using a non-resonant reference spectrum (gold-coated silicon wafer) to further analyze the spectra. The spectra were fitted assuming a Lorentzian line shape by the software OriginTM (OriginLab Corporation, Northampton, MA, USA). Typically, SFG spectroscopy was performed on a DMPG monolayer in buffer containing 20 mM HEPES buffer pH 7.4, 150 mM NaCl, 7.5 mM KCl, 5 mM MgCl₂. 0.5 μ M *SynDLP* was injected in the subphase by a syringe. Optionally, 2 mM GTP were added.

3.2.5.10 Surface plasmon resonance spectroscopy

SPR spectroscopy was performed in cooperation with [REDACTED] and [REDACTED]. SPR spectroscopy is an optical method allowing the sensitive determination of affinity, specificity, and kinetic parameters of various interaction processes, *e.g.*, protein-membrane interactions. SPR spectroscopy was used as a potential method to quantify binding of *SynDLP* (and variants) to different liposome membranes. In the applied setup, the liposomes were used as the ligand and therefore had to be immobilized on an SPR-compatible sensor chip. The streptavidin-coated SA sensor chip (Cytiva, Munich, GER) was used for liposome immobilization. Thus, liposomes were produced with a small proportion of biotinylated lipids (biotinyl-Cap-DOPE) to allow for the formation of a streptavidin-biotin complex between liposomes and the SA sensor chip.

Liposomes containing 99.5% DOPG/0.5% biotinyl-Cap-DOPE (*w/w*) were prepared in reaction buffer (Table 3.1) as described in detail in Chapter 3.2.3.4 with extrusion to 100 nm. SPR analyses were performed using a Biacore T200 (Cytiva, Munich, GER). Initially, the SA sensor chip was equilibrated by three injections with 90 μ l of a solution containing 1 M NaCl, 50 mM NaOH at a flow rate of 10 μ l/min. Then, 1 mM of the prepared 99.5% DOPG/ 0.5% biotinyl-Cap-DOPE (*w/w*) liposome solution was injected onto the SA sensor chip at a flow rate of 10 μ l/min for 540 s. Typically, approx. 2000 RU (response unit) of liposomes was captured on one flow cell of the SA sensor chip (one chip contains four flow cells). Since neither bound *SynDLP* could be removed from immobilized liposomes by washing nor the regeneration of a flow cell by washing off liposomes from the SA sensor chip worked, the experimental setup was designed as single cycle measurements. This means that after immobilizing liposomes on a flow cell, increasing protein concentrations were injected over the same flow cell without complete dissociation of the protein between injection of the individual protein concentrations. *SynDLP* was buffered into reaction buffer and injected over the immobilized liposomes with increasing concentrations (10 nM, 50 nM, 100 nM, 500 nM, 2000 nM) at a flow rate of 30 μ l/min at 25°C. Each *SynDLP* concentration was injected with a contact time of 180 s followed by a dissociation step with reaction buffer injected for 60 s at a flow rate of 30 μ l/min. The final dissociation step after injection of the highest protein concentration lasted 1200 s. 2 mM GTP were added to the protein solution before injection over the SA sensor chip to test for the influence of the nucleotide. Sensorgrams were recorded using the Biacore T200 control software (version 3.2.1; Cytiva, Munich, GER) and analyzed using the Biacore evaluation software (version 3.2.1; Cytiva, Munich, GER). A blank sensorgram was obtained by the injection of protein solution

over one ligand-free flow cell of the SA sensor chip that was only equilibrated with reaction buffer prior to protein injection. The blank sensorgram allows for the subtraction of the refractive index background and, thus, the subtraction of non-specific interactions of the protein with the chip surface. The sensorgrams were referenced and then normalized to obtain a baseline. Binding affinities were calculated assuming a 1:1 binding algorithm (Equation (11)) (*Biacore Insight Evaluation Software, User Manual*):

$$R_{eq} = \frac{c * R_{max}}{c + K_D} + R_{off} \quad (11)$$

Here, R_{eq} refers to the steady state binding response level, c to the analyte (protein) concentration and K_D is the equilibrium dissociation constant. R_{off} corresponds to the response in the absence of analyte and R_{max} to the maximal analyte binding capacity of the surface.

3.2.5.11 Protein aggregation assay

Protein aggregation kinetics were monitored via measuring elastic light scattering, particularly in the context of the influence of DTT on protein aggregation. Therefore, *SynDLP* was stored in 20 mM HEPES buffer pH 7.4 after protein purification (Chapter 3.2.3.2) instead of storage buffer. For the measurement, 3.2 μ M protein was buffered into 20 mM HEPES buffer pH 7.4, 150 mM NaCl, 7.5 mM KCl, 5 mM MgCl₂ in the presence or absence of 10 mM DTT. Elastic light scattering was measured over time in a FluoroMax-4 fluorescence spectrometer (Horiba Scientific, Kyoto, JPN) at λ_{ex} and $\lambda_{em} = 600$ nm at 25°C. The excitation and emission slits were set to 1 nm.

3.2.5.12 Fluorescence spectroscopy of intact *Synechocystis* cells

The expression of proteins tagged with a GFP in *Synechocystis* cells was quantified by fluorescence spectroscopy. Therefore, *Synechocystis* liquid cultures, either wt or a strain transformed with the plasmid pCK306-mEGFP-*SynDLP* (Table 3.2, 3.5, Chapter 3.2.2.5), were grown to an OD₇₅₀ of approx. 1 (Chapter 3.2.1.2). Then, 1 mg/ml rhamnose was added to the cultures to induce expression of proteins regulated by the *rhaBAD* promoter system (Kelly *et al.*, 2018). 24 h after rhamnose-addition, the liquid cultures were diluted to an OD₇₅₀ of 0.5 and a fluorescence emission spectrum was measured in a FluoroMax-4 fluorescence spectrometer (Horiba Scientific, Kyoto, JPN) in the range of 490 – 560 nm upon excitation at 470 nm at 25°C. The excitation and emission slits were set to 8 nm.

3.2.5.13 Determination of chlorophyll concentration

For determining the chlorophyll concentration in *Synechocystis* liquid cultures (Chapter 3.2.1.2), chlorophyll was extracted from the cells using methanol. Therefore, 1 ml cell culture was centrifuged at 1000g, 5 min, RT (Centrifuge 5424, Eppendorf, Hamburg, GER) and the cell pellet was resuspended in 1 ml methanol. The chlorophyll was extracted via incubation for 5 min at RT on a horizontal shaker (Duomax 1030, Heidolph, Schwabach, GER), followed by sample centrifugation at 16000g, 5 min, RT. An absorption spectrum of the supernatant in the UV/Vis area was recorded using a Lambda 35 photometer (Perkin Elmer, Rodgau, GER) to obtain the A_{652} and $A_{665.2}$ values. The chlorophyll *a* (Chl *a*) concentration ($c_{Chl a}$) was determined using the following Equation (12) (Porra, Thompson and Kriedemann, 1989):

$$c_{Chl a} = 16.29 * A_{665.2} - 8.54 * A_{652} \quad (12)$$

The resulting $c_{Chl a}$ has the unit $\mu\text{g Chl } a$ per ml cell culture and was extrapolated to an $\text{OD}_{750} = 1$ to compare the Chl *a* content in different strains. The concentration of Chl *a* of each strain was measured three times and the mean was calculated.

3.2.5.14 Insulin reduction assay

The *in vitro* activity of recombinant *SynTrxA* was analyzed using an established insulin reduction assay (Holmgren, 1979) with modifications. Briefly explained, insulin forms a heterodimer consisting of an A and a B chain, which are connected via two disulfide bridges. The disulfide bridges can be reduced by the activity of a Trx, leading to the formation of free insulin subunits. The assay takes advantage of the fact that the free B chain is insoluble in aqueous buffers. Thus, the formation of free B subunit and with this the reduction of the disulfide bridges can be measured as increasing turbidity using a photometer. The reaction is coupled to the reduction of oxidized Trx by DTT to regenerate the enzymatic activity of Trx.

For the measurement, 130 μM insulin (from bovine pancreas) was dissolved in a buffer containing 20 mM HEPES buffer pH 7.4, 2 mM EDTA, 330 μM DTT, and 3 μM *SynTrxA* was added. No *SynTrxA* was present in a control measurement. The kinetics of the scattering of the reaction mixtures were measured in a Lambda 35 photometer (Perkin Elmer, Rodgau, GER) via monitoring the absorption at 650 nm at 25°C. A blank measurement was performed without DTT and *SynTrxA* and subtracted from the protein-containing sample and the control measurement, respectively.

3.2.6 Microscopic methods

3.2.6.1 Fluorescence microscopy of GUVs

GUVs were prepared in reaction buffer as described in detail in Chapter 3.2.3.5 and placed into a 24-well-plate or a microscopic observation chamber. The GUVs were allowed to settle for at least 1 h before carefully adding 0.8 μM protein with a C- or N-terminally fused GFP-tag. 1 mM of the nucleotides GTP, GDP or GMPPnP, respectively, was added 5 min after protein addition to the GUVs. In general, GUV observation and image recording were performed after 1 – 2 h using an Axio Observer.Z1 fluorescence microscope with the Colibri 7 illumination module (Carl Zeiss Microscopy, Jena, GER). The GUVs containing the fluorophore ATTO633 and the fluorescent GFP were detected using appropriate filters (ATTO633: channel AF647, filter $\lambda_{\text{ex}} = 625 - 655$ nm, filter $\lambda_{\text{em}} = 665 - 715$ nm, 100 ms exposure time; GFP: channel EGFP, filter $\lambda_{\text{ex}} = 450 - 490$ nm, filter $\lambda_{\text{em}} = 500 - 550$ nm, 15 ms exposure time). Background subtraction and further image processing was carried out using the Fiji-ImageJ software (Schindelin *et al.*, 2012).

3.2.6.2 Fluorescence microscopy of *Synechocystis* cells

Cyanobacterial cells can be visualized using fluorescence microscopy due to their intrinsic chlorophyll fluorescence caused by the pigments localized in the TM. Additionally, the co-localization of GFP-tagged proteins in *Synechocystis* cells can be investigated, as the GFP is excited in the green gap of chlorophyll (*e.g.*, reviewed here (Yokoo, Hood and Savage, 2015)). Another application of this method was the visualization of lysed *Synechocystis* cells by the usage of the DNA-intercalating fluorophore propidium iodide.

Therefore, thin agarose patches consisting of 400 μl 2% agarose in MP-H₂O were prepared on a microscope slide. 10 – 20 μl of a *Synechocystis* liquid culture was transferred onto the agarose patch and covered with a cover glass. Images were recorded using an Axio Observer.Z1 fluorescence microscope with the Colibri 7 illumination module (Carl Zeiss Microscopy, Jena, GER) via the 63x oil immersion objective. The chlorophyll fluorescence was detected using appropriate filters (channel mRF12, filter $\lambda_{\text{ex}} = 559 - 585$ nm, filter $\lambda_{\text{em}} = 600 - 690$ nm, 20 ms exposure time). Bright field images (20 ms exposure time) were recorded to detect the cyanobacterial cell walls.

For the visualization of GFP-tagged proteins, a strain transformed with the plasmid pCK306-mEGFP-SynDLP (Table 3.2, 3.5, Chapter 3.2.2.5) was grown to an OD₇₅₀ of approx. 1 (Chapter

3.2.1.2) and expression of mEGFP-*SynDLP* was induced by the addition of 1 mg/ml rhamnose (Kelly *et al.*, 2018). On the next day, 10 μ l of the liquid culture was observed under the fluorescence microscope as described above. The GFP fluorescence was detected using appropriate filters (channel EGFP, filter λ_{ex} = 450 – 490 nm, filter λ_{em} = 500 – 550 nm, 50 ms exposure time). Images of the same section in the different recorded channels were overlaid using the software Adobe Photoshop.

Visualization of lysed *Synechocystis* cells was performed particularly in the context of lysis-inducible cells (LIC). The plasmids for generating lysis-inducible *Synechocystis* cells were kindly provided by [REDACTED] (University of Tsukuba, JPN). Via these genetically engineered *Synechocystis* cells, a potential *in vivo* function of *SynDLP* was investigated by comparison of the vulnerability to induced cell lysis of *Synechocystis* wt vs. the knock-out strain Δ *syndlp*. Therefore, *Synechocystis* wt and the Δ *syndlp* strain were transformed (Chapter 3.2.2.5) with the plasmids pGEM-T-Easy-PhoA-LIC or pGEM-T-Easy-PhoA-LIC-Cm^R (Table 3.5), respectively, to generate the lysis-inducible strains *lic* and Δ *syndlp-lic* (Table 3.2). An empty vector control (EVC) was produced by transformation of *Synechocystis* wt and Δ *syndlp* with pGEM-T-Easy-PhoA and pGEM-T-Easy-PhoA-Cm^R, respectively, to obtain the strains Δ *phoA* and Δ *syndlp- Δ phoA*. As the expression of the three *lic* genes (originating from the *S. enterica* bacteriophage P22) is induced under phosphate-deficient conditions (Asada, Shiraiwa and Suzuki, 2019), liquid cultures of the *Synechocystis* strains wt, Δ *phoA*, *lic*, Δ *syndlp*, Δ *syndlp- Δ phoA* and Δ *syndlp-lic* were grown in phosphate-free BG11 medium (Chapter 3.1.4). Therefore, the cells, which were previously cultivated in BG11 medium supplemented with phosphate, were washed three times with phosphate-free BG11 medium (centrifugation steps at 2500g, 10 min, 20°C; Allegra X-15R, Beckmann Coulter, Krefeld, GER). Finally, the cells were cultivated in phosphate-free BG11 medium supplemented with 5 mM glucose at a starting OD₇₅₀ of 0.1. On the next day, 500 μ l liquid culture was centrifuged at 2500g, 10 min, RT (Centrifuge 5424, Eppendorf, Hamburg, GER) and 400 μ l of the supernatant was decanted. The cell pellet was resuspended in the remaining 100 μ l. A propidium iodide solution was prepared by dissolving 1.05 mg propidium iodide powder in 1 ml buffer containing 137 mM NaCl, 2.7 mM KCl, 10 mM Na₂HPO₄, 1.8 mM KH₂PO₄, pH 7.4 and stored at 4°C with protection from light. 5 μ l propidium iodide solution was added to 100 μ l resuspended cells to achieve a final propidium iodide concentration of 50 μ g/ml. The mixture was incubated at 4°C for 15 min in the dark. Propidium iodide can intercalate into DNA and then shows an increased fluorescence signal that can be visualized under the fluorescence microscope. However, propidium iodide is not membrane-permeable and, thus, can only penetrate lysed cells and reach the DNA here.

After incubation with propidium iodide, 20 μl of the cell suspension was placed on an agarose patch prepared on a microscopic slide, and the *Synechocystis* cells were visualized under the fluorescence microscope as described above. The propidium iodide fluorescence was detected using appropriate filters (channel EGFP, filter $\lambda_{\text{ex}} = 450 - 490 \text{ nm}$, filter $\lambda_{\text{em}} = 500 - 550 \text{ nm}$, 50 ms exposure time).

3.2.6.3 Negative stain electron microscopy

Size and shape of protein oligomers were analyzed by EM. For sample preparation, the proteins were typically incubated in reaction buffer (Table 3.1). 5 μl protein solution was blotted onto a glow-discharged (Emitech K100x glow discharger, Emitech SAS, Versailles, FRA) CF400-Cu grid (Electron Microscopy Sciences, Hatfield, PA, USA), incubated for 30 s, negatively stained with 3 x 3 μl 2% uranyl acetate and air-dried. Side-blotting using filter paper was performed between the solution applications. The sample on the grid was measured in a Tecnai G2 12 BioTwin (FEI Company, Hillsboro, OR, USA) with an acceleration voltage of 120 kV and images were visualized using a TemCam-F416 (Tietz Video and Image Processing Systems GmbH, Gauting, GER).

Negative stain EM was also performed in cooperation with [REDACTED] and [REDACTED] at the Research Center Jülich, GER. Here, 3.5 μl sample was applied to glow-discharged (PELCO easiGlow glow discharger, Ted Pella Inc., Redding, CA, USA) continuous carbon grids (Cu 300 hex grids; Electron Microscopy Sciences, Hatfield, PA, USA; in-house coated with carbon film). After sample incubation on the grid for 1 min, the grid was side-blotting using filter paper and washed with 3.5 μl water. Negative staining was performed with 3.5 μl 2% uranyl acetate for 30 s, followed by air-drying. The sample on the grid was imaged using a 120 kV Talos L120C electron microscope (Thermo Fisher Scientific, Waltham, MA, USA; FEI Company, Hillsboro, OR, USA) equipped with a CETA camera at a pixel size of 4.05 $\text{\AA}/\text{pixel}$ (36 kx magnification) and a nominal defocus of 1.0 – 2.5 μm .

3.2.6.4 Cryo-electron microscopy

Cryo-EM was performed in cooperation with [REDACTED] and [REDACTED] (Research Center Jülich, GER) to solve the structure of *SynDLP* oligomers in the apo state. *SynDLP* forms filamentous, ordered oligomers in solution, making it a perfect candidate for structure determination via cryo-EM. The following steps including sample preparation,

microscopic imaging, image processing as well as map interpretation and model building were performed by ██████████ at the Research Center Jülich.

Therefore, samples were prepared by applying 3.5 μ l *SynDLP* in 20 mM HEPES buffer pH 7.4, 5 mM MgCl₂, 7.5 mM KCl (for sample details see Table 3.15) to glow-discharged (PELCO easiGlow glow discharger, Ted Pella Inc., Redding, CA, USA) Quantifoil grids (R1.2/1.3 Cu 200 mesh; Electron Microscopy Sciences, Hatfield, PA, USA). The grids were plunge-frozen in liquid ethane by a Thermo Fisher Scientific Vitrobot Mark IV (Thermo Fisher Scientific, Waltham, MA, USA) set to 90% humidity at 20°C, blotting force of -10, blotting time 3 s. Micrographs were recorded using a 200 kV Talos Arctica G2 electron microscope (Thermo Fisher Scientific, Waltham, MA, USA) equipped with a Bioquantum K3 (Gatan, Inc., Pleasanton, CA, USA) detector operated by EPU (Thermo Fisher Scientific, Waltham, MA, USA). Details of the data collection are shown in Table 3.15.

Table 3.15: Details of cryo-EM sample preparation and data collection. *Processed in super resolution with 0.8685 Å/pixel.

Sample	<i>SynDLP</i>
Protein concentration [mg/ml]	3.0
Liposome concentration [mg/ml]	-
Nucleotide concentration [mM]	-
Magnification	49 kx
Physical pixel size [Å]	1.737*
Frames	30
Total dose [$e^-/\text{Å}^2$]	26.5
Defocus range [μ m]	2.0 – 4.0
Movies	8322

3.2.6.5 Cryo-EM image processing

For image processing of the data set of *SynDLP* (Chapter 3.2.6.4), movie frames were gain-corrected, dose weighted, and aligned in super-resolution by cryoSPARC Live (Punjani, 2020). The auto picker implemented in cryoSPARC Live was used to produce the initial 2D classes. The following image processing steps were all performed using cryoSPARC (Punjani *et al.*, 2017). The seven classes with the best look were used as templates for the template picker. The resulting 10,000,000 particles were extracted with a box size of 450 pixel (Fourier cropped to 256 pixel) and subjected to several rounds of 2D classification. After that, the cleaned set of particles contained 2,685,000 particles. Further division of the particles was performed by *ab*

initio reconstruction into two classes. The first class comprised 1,806,000 particles and was used for further processing. With the *ab initio* model of the first class the refinement was performed using multiple rounds of non-uniform refinement and heterogenous refinement with an imposed C2 symmetry. In the end, the particles were re-extracted to the full resolution (super-resolution) and subjected to non-uniform refinement (including group and per-particle CTF refinement), followed by local refinement. The final reconstruction was based on 977,200 particles and the global resolution was determined by Fourier shell correlation (FSC) (with auto-masking, FSC = 0.143). Determination of the local resolution as well as local filtering were performed using cryoSPARC.

3.2.6.6 Cryo-EM map interpretation and model building

The 3D reconstruction generated as described in Chapter 3.2.6.5 was further interpreted to finally obtain a model of the protein structure. Therefore, the 3D reconstruction was B-factor sharpened in cryoSPARC (Terwilliger *et al.*, 2018). The handedness of the final map was determined by rigid-body fitting the BSE-domain of *NpBDLP* (Low and Löwe, 2006) into the final map using ChimeraX (Goddard *et al.*, 2018; Pettersen *et al.*, 2021). A *de novo* model of the BSE domain was built in Coot (Emsley *et al.*, 2010) using the locally filtered map. As the resolution in the periphery of the map was too low, it did not allow for model building of the GD. Thus, a GD model including the amino acids 48 – 423 of *SynDLP* was generated using AlphaFold2 (Jumper *et al.*, 2021; Mirdita *et al.*, 2021). An overlap of 40 amino acids at the N- and C-terminus of the GD was included in the model to combine the AlphaFold2 model with the *de novo* model. The AlphaFold2 model was fitted to the 3D reconstruction via molecular dynamics flexible fitting (MDFF) using ISOLDE (Croll, 2018) and fused to the *de novo* model. The resulting monomer model includes the amino acids 1 – 793 of *SynDLP*, as the C-terminal amino acids 794 – 812 were too flexible to be identified in the final map. Manual refinement of the monomer model was performed using Coot and ISOLDE before completion of the 3D reconstruction was realized by filling a total of eight monomers via rigid-body extending. The non-crystallographic symmetry (NCS) parameters for the octamer were acquired by phenix.find_ncs. Next, the model of the octamer was subjected to two cycles of auto-refinement with *phenix.real_space_refine* (Afonine *et al.*, 2018) with NCS constraints and NCS refinement. Local map sharpening was performed using LocSCALE (Jakobi, Wilmanns and Sachse, 2017). The model was subjected to a final inspection followed by validation using *phenix.validate_opn_cryoem* (Afonine *et al.*, 2018)/*Molprobity* (Williams *et al.*, 2018). The cryo-

EM map and the *SynDLP* atomic model were deposited in the corresponding databank under the IDs EMD-14993 and PDB-7ZW6, respectively.

3.2.6.7 EM of *Synechocystis* cells

EM micrographs of *Synechocystis* thin sections were recorded in cooperation with [REDACTED] and [REDACTED] (University of Bayreuth, GER). The EM images were intended to show phenotypical differences between *Synechocystis* wt and the Δ *syndlp* strain (Table 3.2). Therefore, liquid cultures of these strains were grown under photomixotrophic conditions (Chapter 3.2.1.2). 20 ml liquid culture was harvested at 1811g, 10 min, RT (Allegra X-15R, Beckmann Coulter, Krefeld, GER). The supernatant was decanted, and the cell pellet was resuspended in 20 mM HEPES buffer pH 7.0 to obtain an OD₇₅₀ of 5. The cell suspension with an OD₇₅₀ of 2.5 was mixed 1:1 with 10% glutaraldehyde (25% solution in water from SERVA Electrophoresis GmbH, Heidelberg, GER) to fix the cells finally in 5% glutaraldehyde. The following sample preparation as well as microscopic imaging were performed by [REDACTED] and [REDACTED] at the University of Bayreuth. The samples were centrifuged at 3300g for 10 min, washed with double distilled H₂O for 10 min at RT and centrifuged again. For staining, a 2% OsO₄ solution (w/v, in double distilled water) was applied to the sample followed by incubation for 120 min at 4°C. The samples were spun down at 6600g for 10 min and washed with double distilled H₂O. This washing step was repeated twice. Next, the samples were picked up in 2% agar, cut into small blocks, and washed in double distilled H₂O for 5 min. The samples were dehydrated via incubation in increasing concentrations of ethanol (30%, 50%, 70%, 95%) for 15 min each at 4°C (30% and 50% ethanol) or -20°C (70% and 95% ethanol), respectively. Subsequently, samples were further dehydrated three times in 100% ethanol for 20 min at -20°C, one time in ethanol/propylene oxid (1:1) for 15 min at -20°C and twice in propylene oxide for 15 min at -20°C. After the dehydration steps, the solvent was replaced by gradually increasing the concentration of EPON resin: starting with EPON/propylene oxide (1:3) for 3 – 4 h at -20°C, followed by EPON/propylene oxide (1:1) overnight at -20°C, EPON/propylene oxide (3:1) for 3 – 4 h at RT, EPON (100%) for 3 – 4 h at RT and finally EPON (100%) overnight at RT. Next, the samples were polymerized for 2 – 3 d at 60°C in an embedding capsule. Ultrathin sections of the sample were cut using an Ultracut UCT ultramicrotome (Leica Microsystems, Wetzlar, GER) equipped with a diamond knife (Type Ultra 45°, Diatome, Biel, CH). The sections were collected on pioloform-coated copper slotted grids (Plano, Wetzlar, GER) and staining was performed using uranyl acetate and lead citrate. The samples were

analyzed using a JEM-1400Plus transmission electron microscope (JEOL, Tokyo, JAP) operated at 80 kV and images were recorded with a JEOL Ruby CCD camera (3296 x 2472 pixel).

4 Results and Discussion

4.1 *SynDLP* is a dynamin-like protein of *Synechocystis* sp. PCC 6803 with eukaryotic features

4.1.1 Publication

Gewehr, L.^{1,8}, Junglas, B.^{2,3,8}, Jilly, R.¹, Franz, J.⁴, Zhu, W.E.¹, Weidner, T.⁵, Bonn, M.⁴, Sachse, C.^{2,3,6} and Schneider, D.^{1,7} (2023) ‘*SynDLP* is a dynamin-like protein of *Synechocystis* sp. PCC 6803 with eukaryotic features’, *Nature Communications*, 14(1), p. 2156.

¹ Department of Chemistry, Biochemistry, Johannes Gutenberg University Mainz, Mainz, Germany.

² Ernst Ruska-Centre for Microscopy and Spectroscopy with Electrons (ER-C-3): Structural Biology, Jülich, Germany.

³ Institute for Biological Information Processing (IBI-6): Cellular Structural Biology, Jülich, Germany.

⁴ Max Planck Institute for Polymer Research, Ackermannweg 10, 55128 Mainz, Germany.

⁵ Department of Chemistry, Aarhus University, Langelandsgade 140, 8000 Aarhus C, Denmark

⁶ Department of Biology, Heinrich Heine University, Universitätsstr. 1, Düsseldorf, Germany.

⁷ Institute of Molecular Physiology, Johannes Gutenberg University Mainz, Mainz, Germany.

⁸ These authors contributed equally: Lucas Gewehr, Benedikt Junglas

The contributions of each author are listed in Table 4.1 according to the *CRedit taxonomy* (Allen *et al.*, 2014).

Table 4.1: Author contributions of “*SynDLP is a dynamin-like protein of *Synechocystis* sp. PCC 6803 with eukaryotic features*”.

Conceptualization	Complete study	██████████
Writing	Complete study	████████████████████
Supervision, Project administration, Funding acquisition, Resources	Protein characterization	██
	Electron microscopy	██
	SFG spectroscopy	██
Figures (numbers refer to the original publication)	Methodology, Investigation, Formal analysis	Data visualization
Fig. 1a	LG	LG
Fig. 1b-h	██████████	██
Fig. 2a-c	LG	LG
Fig. 3a-g	LG, ██████████	LG
Fig. 4a-f	LG, ██████████	LG
Fig. 5a, b	██	LG
Fig. 5c, d	██████████	LG
Fig. 6	LG	LG
Fig. 7a-c	LG	LG
Supplementary Fig. 1a, b	LG, █	LG
Supplementary Fig. 2	LG	LG
Supplementary Fig. 3a, b	LG	LG
Supplementary Fig. 4	██	LG
Supplementary Fig. 5a, b	██	██
Supplementary Fig. 6	LG	LG
Supplementary Fig. 7a	LG	LG
Supplementary Fig. 7c-d	██	██
Supplementary Fig. 8a, b	LG	LG
Supplementary Fig. 9	LG	LG
Supplementary Fig. 10a	██	██
Supplementary Fig. 10b, c	LG	LG
Supplementary Fig. 11a	██	LG
Supplementary Fig. 11b-d	LG	LG
Supplementary Fig. 12	LG	LG
Supplementary Fig. 13a-c	██	██
Supplementary Fig. 14a-d	LG	LG
Supplementary Fig. 15	██████████	LG
Supplementary Fig. 16a, b	██████████	LG

Supplementary Fig. 17	■	LG
Supplementary Fig. 18	LG	LG
Supplementary Fig. 19a, b	LG	LG
Supplementary Fig. 20a, b	LG	LG
Supplementary Fig. 21	LG, ■	LG
Supplementary Fig. 22	LG	LG

The following chapter cites in principle the published article with some exceptions: the Supplementary Figs. are integrated in the main text or in the appendix of this thesis at the indicated positions; the rearranged figures as well as the tables have been renumbered in accordance with this thesis; the citation of references has been rearranged in accordance with this thesis; the methods section has been removed because the performed experimental designs are described in the methods section of this thesis (Chapter 3.2).

4.1.2 Abstract

Dynamin-like proteins are membrane remodeling GTPases with well-understood functions in eukaryotic cells. However, bacterial dynamin-like proteins are still poorly investigated. *SynDLP*, the dynamin-like protein of the cyanobacterium *Synechocystis* sp. PCC 6803, forms ordered oligomers in solution. The 3.7 Å resolution cryo-EM structure of *SynDLP* oligomers reveals the presence of oligomeric stalk interfaces typical for eukaryotic dynamin-like proteins. The bundle signaling element domain shows distinct features, such as an intramolecular disulfide bridge that affects the GTPase activity, or an expanded intermolecular interface with the GTPase domain. In addition to typical GD-GD contacts, such atypical GTPase domain interfaces might be a GTPase activity regulating tool in oligomerized *SynDLP*. Furthermore, we show that *SynDLP* interacts with and intercalates into membranes containing negatively charged thylakoid membrane lipids independent of nucleotides. The structural characteristics of *SynDLP* oligomers suggest it to be the closest known bacterial ancestor of eukaryotic dynamin.

4.1.3 Introduction

Cells employ membrane remodeling proteins for diverse physiological processes, including endocytosis, exocytosis, membrane fusion and fission, and membrane repair (Andrews, Almeida and Corrotte, 2014; Bohuszewicz, Liu and Low, 2016; Haucke and Kozlov, 2018). Efficient membrane repair mechanisms are also indispensable for cells to cope with membrane damage, finally ensuring cell survival. Membrane remodeling is vital to maintain cellular compartmentalization by membrane-enclosed organelles in eukaryotes, as well as the maintenance of prokaryotic membrane systems. In fact, within the last decade, proteins have been identified in prokaryotes, which are involved in membrane repair and/or dynamics. Many of these proteins are homologs of proteins previously assumed to be eukaryotic inventions. Examples are the proteins FtsA, FtsZ and ZipA, which mediate membrane constriction during bacterial cytokinesis, and are homologous to the eukaryotic proteins tubulin, actin, and MAP-Tau (Bork, Sander and Valencia, 1992; Hale and Boer, 1997; Löwe and Amos, 1998; RayChaudhuri, 1999; Szwedziak *et al.*, 2014).

Similarly, dynamins and dynamin-like proteins (DLPs) were originally assumed to be eukaryotic inventions until, in 1999, a bioinformatic study predicted the existence of bacterial DLPs (BDLPs) (Blick, 1999). In eukaryotes, DLPs are involved in various membrane remodeling processes, such as endocytosis or fission and fusion of organelle membranes (Hinshaw and Schmid, 1995; Smirnova *et al.*, 2001; Gao, Sage and Osteryoung, 2006; Mettlen *et al.*, 2009; Zhang and Hu, 2009; Orso *et al.*, 2010; Ban *et al.*, 2017; Findinier, Delevoye and Cohen, 2019). Unlike small (Ras-like) GTPases, DLPs are large mechanochemical GTPases with a molecular mass >60 kDa that use the energy gained via GTP hydrolysis for membrane binding and/or remodeling (Daumke and Praefcke, 2016). When bound, GTP is hydrolyzed, and cleavage of the γ -phosphate induces conformational changes leading to movements of conserved DLP domains relative to each other. The inorganic phosphate is then released, resulting in a GDP-bound DLP. Upon GDP dissociation, a new GTP can bind to the nucleotide-free enzyme to start a new cycle (Wittinghofer and Vetter, 2011).

While DLP family members are typically not highly conserved on the sequence level, with the exception of the GTPase domain (GD), the resolved structures reveal a conserved modular arrangement of all DLPs: The globular GD at the protein's N-terminus is typically followed by an α -helical bundle signaling element (BSE) or neck domain that connects the GD to an α -helical stalk or trunk domain. Most DLPs additionally have membrane interaction domains (MIDs) of varying designs (Jimah and Hinshaw, 2018; Ford and Chappie, 2019).

The GD, the only structural element of DLPs that is conserved at the sequence level, is characterized by a low μM nucleotide binding-affinity plus a relatively high basal GTPase activity, at least when compared to other GTPases. *E.g.*, Ras-like GTP-binding proteins require GTPase-activating proteins (GAPs) for nucleotide hydrolysis, whereas DLPs operate independently of GAPs (Praefcke and McMahon, 2004; Gasper *et al.*, 2009; Chappie *et al.*, 2010; Karim and Aronsson, 2014; Karim *et al.*, 2014). Yet, the GTPase activity of DLPs typically increases when DLP monomers oligomerize, as the GTPase activity is regulated by intermolecular GD contacts leading to a head-to-head dimerization of adjacent GDs. *E.g.*, dynamin dimers/tetramers show a basal GTPase activity of $\sim 1 \text{ min}^{-1}$ when free in solution. Yet, upon binding to membranes, dynamins oligomerize on the membrane surface, resulting in GTPase-activating GD contacts and release of auto-inhibitory GD-MID contacts (Gasper *et al.*, 2009; Chappie *et al.*, 2010; Reubold *et al.*, 2015). This can finally increase the GTPase activity >100 -fold (Tuma, Stachniak and Collins, 1993; Warnock, Hinshaw and Schmid, 1996; Stowell *et al.*, 1999).

Functionally, the majority of eukaryotic DLPs can be subdivided into either (i) membrane fission or (ii) membrane fusion DLPs (Ramachandran and Schmid, 2018). Dynamin, the founder and namesake of the dynamin superfamily, is a *fission DLP*, involved in clathrin-mediated endocytosis (Hinshaw and Schmid, 1995; Mettlen *et al.*, 2009; Ramachandran, 2011). Other *fission DLPs*, such as Drp1 and DRP3A, act on cell organelles, involving mitochondria and peroxisomes (Smirnova *et al.*, 2001; Zhang and Hu, 2009). Conversely, *fusion DLPs*, such as mitofusin, OPA1 or atlastin, fuse the mitochondrial outer membrane, the mitochondrial inner membrane or the endoplasmic reticulum membrane, respectively (Orso *et al.*, 2010; Ban *et al.*, 2017; Cao *et al.*, 2017). The fusogenic DLP Fzl is involved in the remodeling of thylakoid membranes (TMs) in chloroplasts (Gao *et al.*, 2003; Gao, Sage and Osteryoung, 2006; Findinier, Delevoye and Cohen, 2019).

About two decades ago, a BDLP was characterized for the first time in the cyanobacterium *Nostoc punctiforme* (*NpBDLP*) (Low and Löwe, 2006). While the physiological functions of BDLPs are mostly enigmatic, a BDLP of *Bacillus subtilis* (*BsDynA*) has recently been shown to be involved in membrane stabilization and defense against phage infection (Guo *et al.*, 2022). For other BDLPs, several physiological functions were proposed, such as vesicle release or biogenesis (*EcLeoA*, *MsIniA*) and crucial involvement in cytokinesis (*SvDynA/B*) (Brown and Hardwidge, 2007; Michie *et al.*, 2014; Schlimpert *et al.*, 2017; Gupta *et al.*, 2020). As their eukaryotic counterparts, also BDLPs appear to be either involved in membrane fission or

fusion, and, *e.g.*, *MsIniA* has a membrane fission activity whereas *BsDynA* and *Cj-DLP1/2* are able to fuse membranes, at least *in vitro* (Bürmann *et al.*, 2011; Liu, Noel and Low, 2018; Wang *et al.*, 2019).

Recently, a BDLP has also been identified in the genome of the cyanobacterium *Synechocystis* sp. PCC 6803 (*SynDLP*) (Jilly *et al.*, 2018). In contrast to other prokaryotes, cyanobacteria typically contain an uncommon second, completely separated internal membrane system besides the cytoplasmic membrane, the TMs where the photosynthetic light reaction takes place. TMs have a rather unique lipid composition, with the two neutral galactolipids monogalactosyldiacylglycerol (MGDG) and digalactosyldiacylglycerol (DGDG) being the major membrane lipids, plus the negatively charged lipids sulfoquinovosyldiacylglycerol (SQDG) and the only phospholipid phosphatidylglycerol (PG) (Wada and Murata, 1989; Dorne, Joyard and Douce, 1990). There are still many open questions concerning the biosynthesis of TMs, *e.g.*, whether the TMs are completely assembled *de novo* or not (Rast, Heinz and Nickelsen, 2015; Huokko *et al.*, 2021). Due to the photosynthetic light reaction, TMs are highly vulnerable to light stress and are continuously remodeled (Rottet, Besagni and Kessler, 2015), and thus, proteins mediating membrane remodeling and/or repair via membrane fusion and fission are required. As the involvement of DLPs in membrane dynamics and/or repair is well-established in eukaryotes, it is feasible to also assume involvement of *SynDLP* in similar processes in *Synechocystis* sp. PCC 6803. Yet, currently *SynDLP* solely is a predicted DLP and no information as to its structure and function are available.

Here, we show that purified *SynDLP* is a *bona fide* DLP that specifically interacts with negatively charged TM lipids. Furthermore, *SynDLP* assembles into ordered high molecular mass oligomers. The structure of *SynDLP* oligomers reveals oligomeric interfaces in the stalk domain typical for eukaryotic *fission DLPs*. Based on an analysis of an intramolecular disulfide bridge stabilizing the BSE and an assembly-impaired *SynDLP* variant, we propose a GTPase activity-regulating function for the BSE domain. The interaction of *SynDLP* with negatively charged lipid headgroups is nucleotide-independent.

4.1.4 Results

Cryo-EM structure of SynDLP oligomers

Recently, in a bioinformatic analysis, the orf *slr0869* of the *Synechocystis* sp. PCC 6803 genome has been identified to encode a DLP (*SynDLP*) (Jilly *et al.*, 2018). A sequence alignment and homology search revealed the presence of a GD with the typical GTP-binding motifs, including the G1-motif/P-loop, the G2-motif/switch I, the G3-motif/switch II and the G4-motif, all hallmarks of dynamin-like GTPases (Daumke and Praefcke, 2016; Jimah and Hinshaw, 2018; Ford and Chappie, 2019). *SynDLP* appears not to be essential in the cyanobacterium under standard growth conditions (Fig. 4.1a) albeit it is expressed *in vivo* (Fig. 4.1b). A typical sodium dodecyl sulfate polyacrylamide gel electrophoresis (SDS-PAGE) analysis of isolated, heterologously produced *SynDLP* is shown in Fig. 4.2.

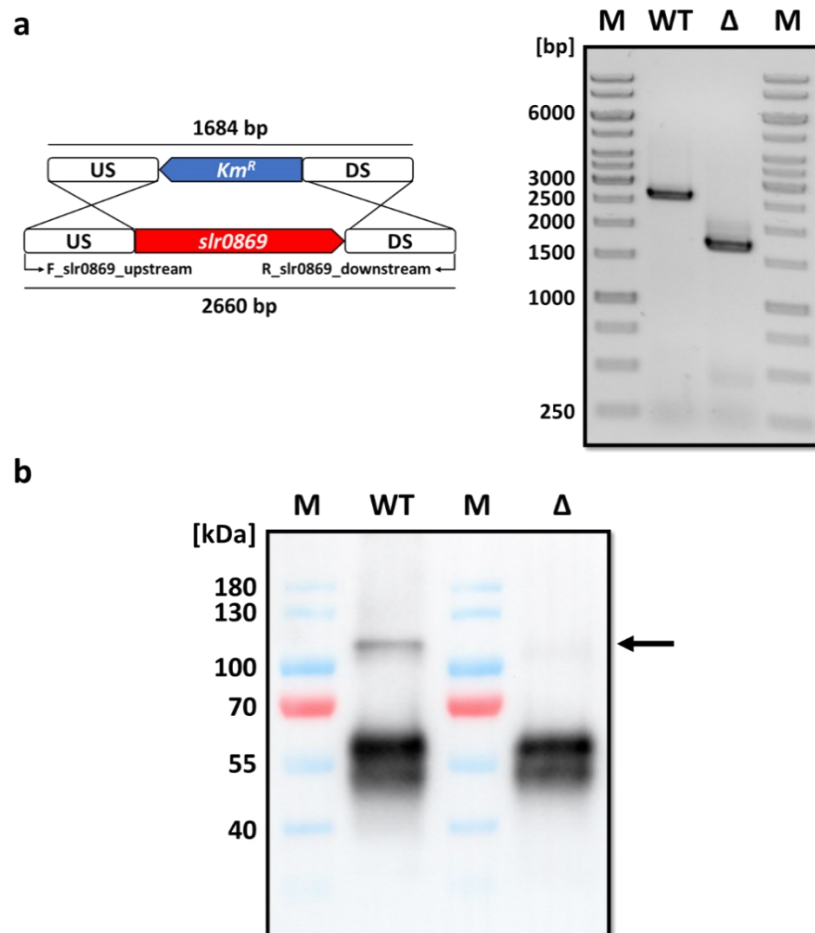


Figure 4.1: *SynDLP* expression *in vivo*.

(a) A *SynDLP* knock-out strain (Δ) was generated via homologous recombination using a plasmid containing flanking regions up- and downstream (US and DS in the scheme) of the gene coding for *SynDLP* (*slr0869*) and a kanamycin resistance cassette (Km^R) between the flanking regions. For selection, the strain was grown in BG11 medium (Rippka *et al.*, 1979) containing up to 100 $\mu\text{g/ml}$ kanamycin. After phenolic DNA extraction of the strains, complete gene deletion was verified by PCR

using the primer pair F_slr0869_upstream and R_slr0869_downstream (Table 3.4), followed by restriction digestion of the template DNA using the restriction enzyme *DpnI* and subsequent separation of the PCR products via agarose gel electrophoresis. DNA containing bands were stained using ethidium bromide. The expected PCR product size for the wt is 2660 bp and for the *slr0869* knocked-out strain 1684 bp, respectively. M = marker. Representative agarose gel of three independent experiments showing the same results. As the *slr0869* gene could be completely deleted, the native *SynDLP* protein appears to be non-essential for the cyanobacterium, at least under the chosen growth conditions. The deletion strain grows like the wt and did not show severe defects in photosynthetic performance. Thus, our initial *in vivo* experiments indicated no altered phenotype of the *SynDLP* knock-out strain, at least under standard growth conditions. (b) 100 ml of *Synechocystis* sp. PCC 6803 WT culture and the *SynDLP* knock-out strain were grown in a shaking incubator at 130 rpm, 30°C and illuminated with 30 μE to an OD₇₅₀ = 1.4. After cell disruption, *SynDLP* was immunoprecipitated using Sepharose-Protein A beads and an antibody raised in a rabbit against part of *SynDLP* (α -*SynDLP*; dilution: 1:2000; Davids Biotechnologie, Regensburg, Germany). The truncated *SynDLP* variant used for antibody production consisted of aa 300 – 812 to omit the conserved GD residues in the nucleotide-binding site (Fig. 4.3h) and, thus, increase the specificity of the antibody. The immunoprecipitated proteins were separated via SDS-PAGE and *SynDLP* was visualized by Western Blot analysis using α -*SynDLP* as primary and α -Rabbit-HRP conjugate (Dilution: 1:160000; Sigma-Aldrich Chemie GmbH, Taufkirchen, Germany) as secondary antibody. The height of a *SynDLP* control band is marked by an arrow. The lower bands at ca. 55 kDa resulted from cross-reactions of the antibodies used for immunoprecipitation and Western Blot. M = marker. Representative Western Blot of two independent experiments showing the same results.

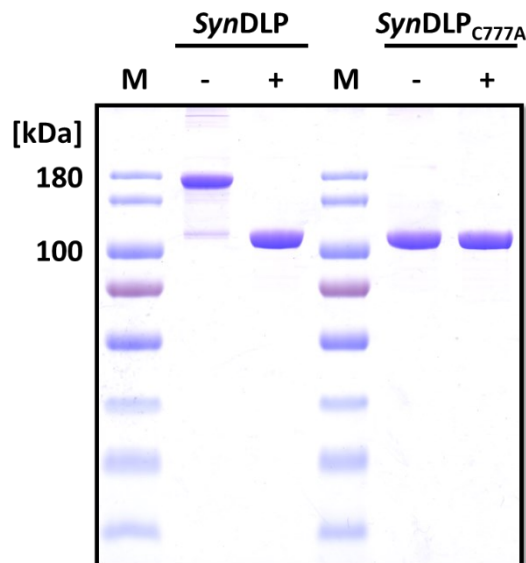


Figure 4.2: The C777A mutation abolishes the formation of the intramolecular disulfide bridge.

Purified *SynDLP* and *SynDLP_{C777A}* were analyzed via SDS-PAGE under reducing (100 mM DTT, lane +) and non-reducing (0.1 mM DTT, lane -) conditions. M = marker. Representative gel of three independent experiments showing the same results.

Analytical size exclusion chromatography revealed that *SynDLP* forms oligomers in solution, a feature typically observed when DLPs bind nucleotides or membranes (Fig. 4.3a). Yet, in contrast to other BDLPs, *SynDLP* forms high-molecular mass oligomers already in complete absence of an externally added membrane template and/or nucleotides. In a sedimentation

assay, the addition of GTP or GDP led to only marginal changes in the sedimentation behavior of *SynDLP*, indicating only a minor shift to larger structures in the presence of GTP and to smaller structures after GDP addition (Fig. 4.4). When we visualized *SynDLP* by cryo-EM using prepared plunge-frozen vitrified specimen, we observed short oligomeric filaments of bent half-moon shape (Fig. 4.3b) with typical lengths of about 100 nm and a curvature radius of ~50 nm. Noteworthy, in contrast to biochemical assays, EM micrographs were acquired in the absence of NaCl, as the oligomeric filaments appeared longer and more defined under these conditions (Fig. 4.5) and therefore more suitable for structural analysis. Class averages of these elongated oligomers revealed a width of 150 Å and a repeating unit every 60 Å along the oligomer (Fig. 4.3c). Using a segmented single-particle analysis workflow (for details see Fig. A4), we determined the structure of *SynDLP* oligomers at an overall resolution of 3.7 Å (Fig. 4.3d, Table 4.2). The local resolution varied from 3.0 to 3.5 Å at the stalk domain to 5.0 to 7.0 Å at the GD, presumably due to tighter contacts between the well-packed stalk domains and looser contacts between adjacent GDs. The last 19 residues at the C-terminus could not be resolved in the cryo-EM density, and thus, the final refined atomic model includes amino acids (aa) 1 – 793 of *SynDLP*. Based on the determined cryo-EM map, we built a model of 8 *SynDLP* monomers, which represents a smaller part of the segmented *SynDLP* oligomer structure. When the determined octamer is extended, matching the observed dimensions of the 2D class averages, it will consist of ~40-50 monomers. The curvature radius of 50 nm of the *SynDLP* oligomers is rather high compared to similar assemblies of other DLPs that typically assemble in the presence of membranes and/or nucleotides. Here, the curvature radius is usually in the range of 13 to 26 nm (reviewed here (Ford and Chappie, 2019)). However, other DLP assemblies also show a low curvature comparable to *SynDLP*, e.g., Drp1 (Kalia *et al.*, 2018).

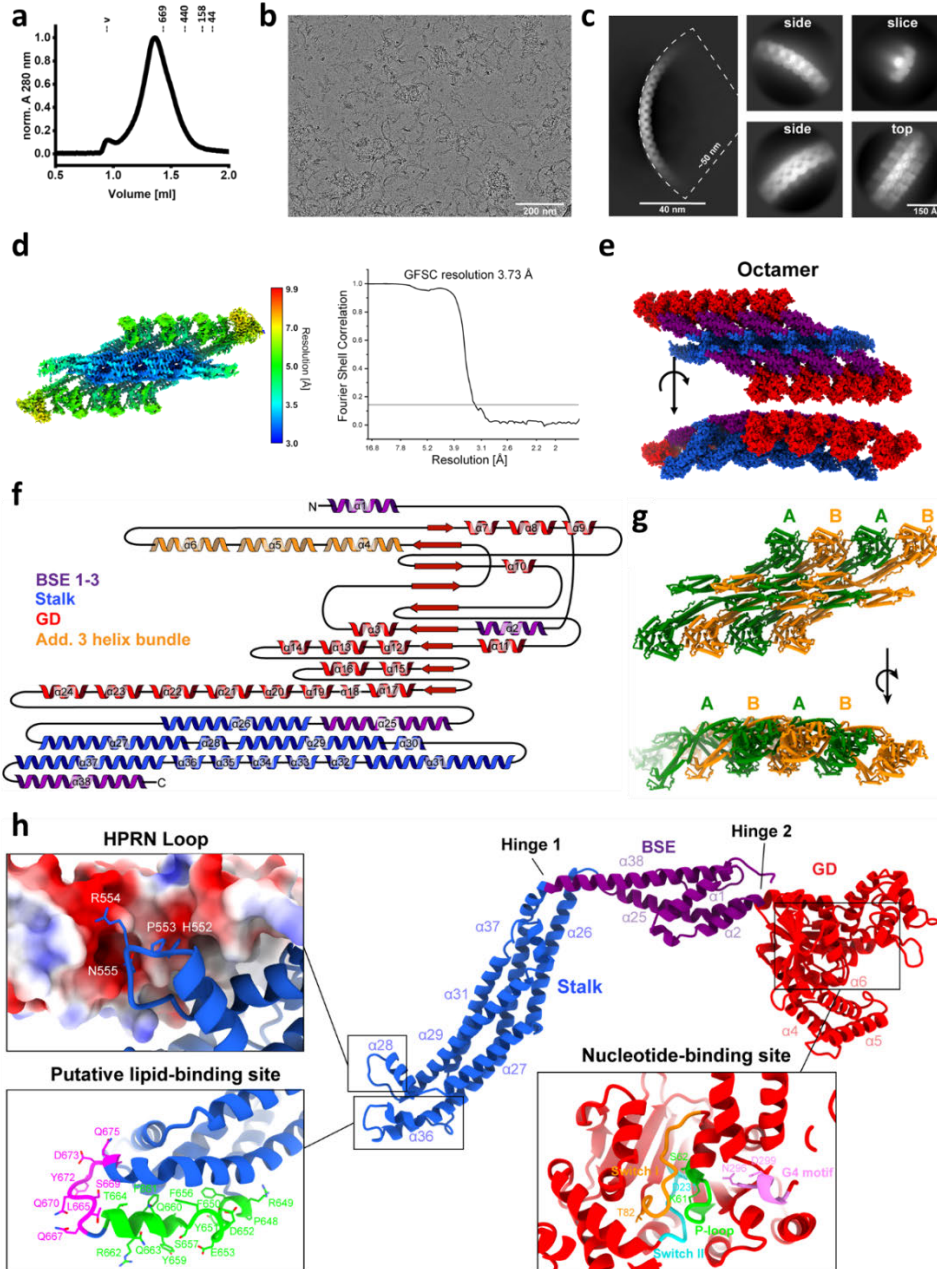


Figure 4.3: Cryo-EM structure of oligomeric *SynDLP*.

(a) Analytical size exclusion chromatography of *SynDLP* (black) revealed the formation of oligomeric structures that are larger than common standard proteins (standard proteins' peak positions and molecular masses in kDa are indicated, v = void volume). Absorption values at 280 nm were normalized (0 – 1). (b) Cryo-EM micrograph of *SynDLP* oligomers. The data set of 8322 micrographs was measured one time (no independent replicates). (c) Class averages of *SynDLP* oligomers with an enlarged oligomer side view including the curvature radius (left) and focused views of side, top, and slice view. (d) Local resolution map and FSC curve (with auto-masking) of the *SynDLP* reconstruction. (e) Model of a *SynDLP* octamer with GD (red), BSE1-3 (purple) and stalk (blue). (f) Secondary structure topology plot of *SynDLP* with additional α -helices of the enlarged *SynDLP* GD colored in orange. (g) Model of a *SynDLP* octamer highlighting the sequential arrangement of monomers within the oligomer. Alternating monomers are colored in green and orange, respectively. (h) Model of the *SynDLP* monomer, including structural features. GD, BSE and stalk are colored as in (e). Zoomed insets show the HPRN loop with the electrostatic surface of neighboring monomers, two putative lipid-binding sites at the tip of the stalk colored in magenta and green, respectively, and conserved motifs in the nucleotide-binding site of the GD: P-loop, switch I, switch II and G4 motif colored in green, orange, cyan and pink, respectively.

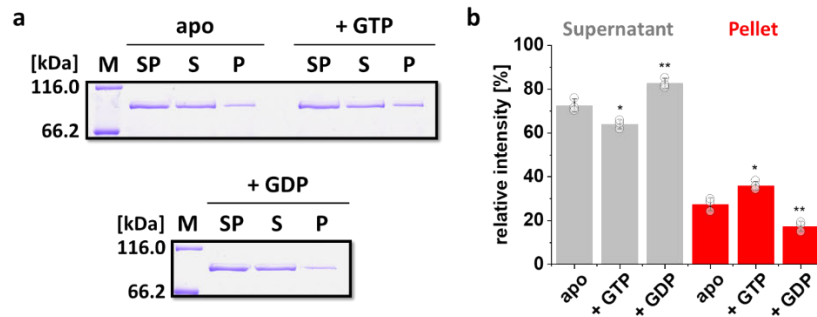


Figure 4.4: Oligomerization of *SynDLP* in the presence of nucleotides.

A sedimentation assay was performed to estimate the oligomerization behavior of *SynDLP* in the presence vs. absence of nucleotides. 0.5 μM *SynDLP* were incubated with or without 2 mM GTP/GDP in reaction buffer at 4°C for 30 min. One part of the reaction was removed before ultracentrifugation to receive the combined sample of supernatant and pellet (SP). After ultracentrifugation (60000g, 30 min, 4°C), the supernatant (S) was subtracted, and the pellet (P) was resuspended in an equal volume of SDS sample buffer. All samples were transferred into SDS sample buffer, boiled at 95°C for 5 min, and separated via SDS-PAGE. M = marker. (a) A representative gel showing the distribution of *SynDLP* into S and P fractions dependent on the added nucleotide. (b) SDS-PAGE gel band intensities were determined using the software Fiji-ImageJ (Schindelin *et al.*, 2012). Grey bars show the relative band intensities of the supernatant and red bars those of the pellet. Mean of independent experiments ($n = 3$) and error bars (S.D.) are shown. Single measurements are shown as circles. ns = not significant ($P > 0.05$), * $P < 0.05$, ** $P < 0.01$, *** $P < 0.001$ based on a two-sided unpaired Student's t-test. Either the GTP ($P = 0.014$) or the GDP ($P = 0.0096$) bound state are compared to the respective apo state.

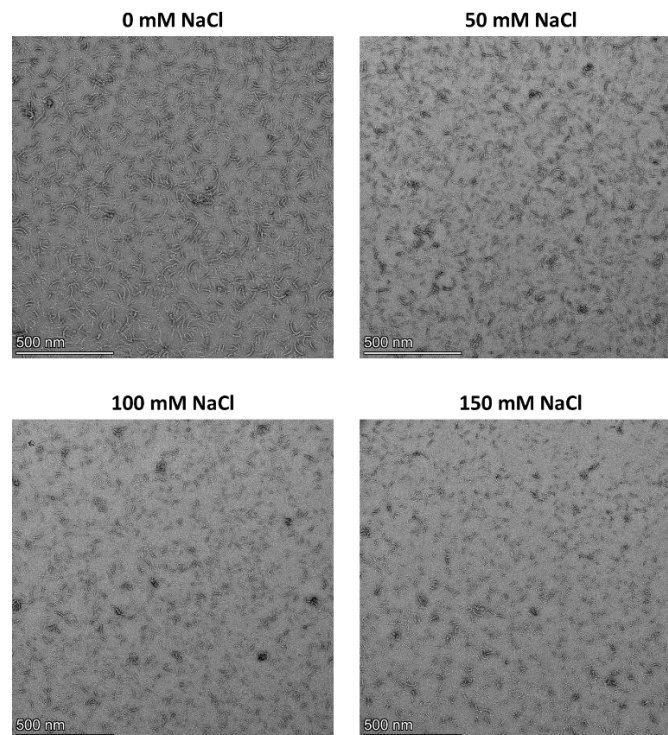


Figure 4.5: Effect of increasing NaCl concentration on shape and size of *SynDLP* oligomers.

Negative stain EM micrographs of 10 μM *SynDLP* in 20 mM HEPES pH 7.4, 7.5 mM KCl, 5 mM MgCl_2 , 0.2 mM DTT and increasing NaCl concentrations (0, 50, 100, 150 mM). Data sets were measured one time (no independent replicates).

Table 4.2: Cryo-EM data collection and refinement statistics

Data collection and processing	SynDLP
Number of movies collected	8,322
Magnification	x49,000
Voltage [kV]	200
Electron exposure [$e^-/\text{\AA}^2$]	26.5
Underfocus range [μm]	2.0 – 4.0
Physical pixel size [\AA]	1.737
Detector	Gatan K3
Symmetry imposed	C2
Final no. of particles	977,199
Global map resolution [\AA , FSC = 0.143]	3.7
Local map resolution range [\AA]	3.0 – 9.9
Initial model used (PDB code)	-
Model refinement	SynDLP
Model resolution	3.7
CC mask	0.60
CC box	0.79
CC peaks	0.53
CC volume	0.5.9
Map sharpening B-factor [\AA^2]	-184
Model composition	
Nonhydrogen atoms	101,416
Protein residues	6344
RMSDs	
Bond lengths [\AA]	0.004
Bond angles [$^\circ$]	0.926
Validation	
MolProbity score	1.59
Clashscore	8.56
Rotamer outliers [%]	0.31
Ramachandran plot	
Favored [%]	97.35
Allowed [%]	2.65
Disallowed [%]	0.00
Deposition IDs	
EMDB	14993
PDB	7ZW6

The *SynDLP* structural model revealed a domain architecture typical for eukaryotic *fission DLPs* (Reubold *et al.*, 2015; Kalia *et al.*, 2018) (Fig. 4.3e-g). The GD is flanked by parts of the BSE domain (N-terminally by BSE1, C-terminally by BSE2) followed by a stalk domain. The BSE3 domain part is located C-terminally to the stalk (Figs. 4.3f, 4.6). The monomer model revealed a globular GD, linked via a flexible hinge region (hinge 2) to the mainly α -helical BSE domain, which is connected to an α -helical stalk via hinge 1 (Fig. 4.3h). The oligomer structure showed a stalk backbone connected via a complex interaction network (Fig. 4.7) from which the BSE domains and the GDs protrude laterally outwards (Fig. 4.3e). The projected center of the stalk domains lies on a curve conferring the curvature of the *SynDLP* oligomers. A loop consisting of an HPRN motif, which mediates critical contacts to neighboring monomers via electrostatic interactions (see below), as well as putative lipid-binding sites are located at the tip of the stalk (Fig. 4.3h). Note that molecular details of the GD are more difficult to annotate due to the intermediate resolution of this part.

	10	20	30	40	50	60			
	MSKIAPO	<u>CC</u> ON	LREQVNQLIE	LLRQEP	TLRS	QQDTSIVETA	LGKALSP	FE	IVFAGAFSAG
	70	80	90	100	110	120			
	K	SMLINALLE	RELLYSAEGH	ATGTECHIEY	ANANEERVVL	TFLSEAEIRQ	QALILAKYLN		
	130	140	150	160	170	180			
	VNVGDLNINQ	PEAVKVVSQY	CQKIIEAEGG	ENKSERAKQA	NALHLLLI	GIF EQNRERINTY			
	190	200	210	220	230	240			
	QNSTYSMDQL	NFSSLAEAAAG	YARRGANSAV	LKRLDYFCNH	SLLKDG	NVLV DLPGIDAPVY			
	250	260	270	280	290	300			
	EDAERAYRKI	ESPDTS	AVIC	VLKPA	AAGDM	SAEETQLLER	ISKNHGIRDR	VFYVFNRIDY	
	310	320	330	340	350	360			
	TWYNTQLRQR	LEGLIQSQFR	DNSRVYKTSG	LLGPHYGSQVK	QTNSTRFGL	DSIFATTIKG			
	370	380	390	400	410	420			
	FDGEEETPQF	VSEFNNYCAN	SGKLLSTAFR	VSVNGYETSN	ENYVRILSEW	GIPLV	DQLIH		
	430	440	450	460	470	480			
	DSGIESFRSG	IGLYL	AEEKY	PELFATLAND	LQPLCIALRQ	FYLENYRQLD	SQPREIAAMK		
	490	500	510	520	530	540			
	AQELTLLNQE	MQNLGIEFKK	YMSAQINDVV	IGNDREFDQD	FTKLKARMVA	RLEDELLKTFY			
	550	560	570	580	590	600			
	VMNAYKRATE	<u>SHPRN</u>	STAPF	I AVLVEALYY	LANELED	AFI EAIHEL	VKNF FQRLGDRLRK		
	610	620	630	640	650	660			
	VDCYHQVYRL	VGNDGGIEQL	LRRAEEDITK	ALVNEARTEC	DRYVRES	PRF YDEGTF	FSIYC		
	670	680	690	700	710	720			
	<u>FRQTL</u>	<u>QQTSQ</u>	<u>GYDQA</u>	IVEA	EPAIKELLKL	DPEPKVFNTV	RKNFRQTVNN	TLKTHLLPMA	
	730	740	750	760	770	780			
	EEQAQIILEQ	YDVARKYREQ	TLEQDAEEKI	ARNSRLQSEI	KQKIDLYQTS	IVSINE	<u>CLKA</u>		
	790	800	810						
	<u>MQIFEQLPVI</u>	<u>TES</u>	DITKQAE	IVADADFVEI	VE				

Figure 4.6: Annotated amino acid sequence of *SynDLP*.

SynDLP domains are highlighted derived from the structure (Fig. 4.3): BSE1-3 in violet, GD in red, stalk in blue. The four substituted residues in the *SynDLP*_{HPRN-AAAA} mutant are typed orange and underlined. The two cysteines forming an intramolecular disulfide bridge are marked in yellow. The crucial active site residue K61 is highlighted in cyan. The two putative MIDs investigated in this study are marked in green or magenta, respectively.

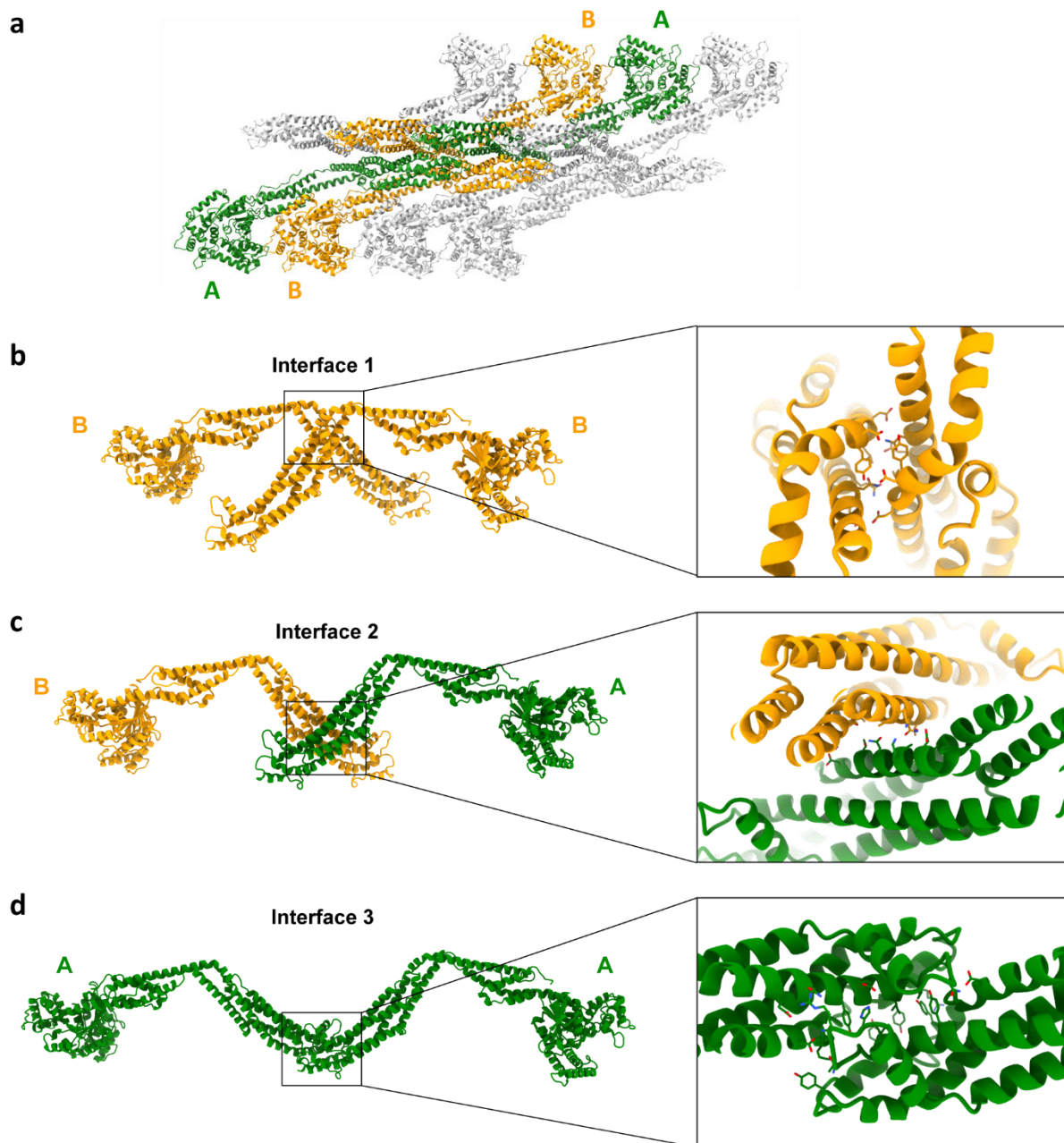


Figure 4.7: Oligomerization interfaces in *SynDLP*.

(a) *SynDLP* structure in ribbon representation illustrating the position of the monomers shown in (b) – (d) within the oligomer in the same colorization. Isolated dimers of the *SynDLP* oligomer are shown in ribbon representation and highlight oligomerization (b) interface 1, (c) interface 2 and (d) interface 3 including molecular details with intermolecular contact residues shown as sticks and colored by element in the zoomed sections. Monomers are colored in green and orange, respectively.

SynDLP is a potential bacterial ancestor of eukaryotic DLPs

The *SynDLP* monomer structure revealed typical DLP features (Fig. 4.3h). The structure of *SynDLP* oligomers resembles the assembly of eukaryotic *fission DLPs* via a complex network of interactions in the stalk domain, mainly mediated by three distinct interfaces (Fig. 4.7b-d). Interestingly, these interfaces are conserved in some eukaryotic DLPs (Gao *et al.*, 2010; Reubold *et al.*, 2015; Kalia *et al.*, 2018), yet, have not been reported in any prokaryotic DLP structure thus far (Fig. 4.8a). A surface conservation plot of *SynDLP* revealed highly conserved residues in the nucleotide-binding pocket of the GD and laterally at the stalk (Fig. 4.9a, red-violet, Fig. A5), which correspond to the conserved GD motifs and the oligomerization interfaces 2 and 3 (Figs. 4.3h, 4.7c, d). Structural analysis of isolated *SynDLP* domains showed an increased size of the GD compared to other DLP GDs (Fig. 4.9b). In fact, the *SynDLP* GD is >100 aa larger than typical dynamin-like GDs as it contains additional loops and α -helices (Fig. 4.10a). In a structural alignment with eukaryotic and bacterial DLP representatives, the estimated root-mean-square deviation (RMSD) of C α positions at 8.5 – 10.2 Å indicate a closer relation of *SynDLPs* α -helices in the stalk domain to the eukaryotic DLP members Dyn3 and MxA as opposed to other bacterial members at >14 Å (Fig. 4.9c), which is in line with the stalk-mediated assembly thus far observed solely in eukaryotic representatives (Fig. 4.8a). The close relation of *SynDLP* to eukaryotic DLPs is further supported by structural alignments of isolated BSE domains (Fig. 4.10b). Taken together, *SynDLP* is a prokaryotic DLP with an enlarged GD and shows structural features not observed in BDLPs before. Thus, *SynDLP* is the closest known bacterial ancestor of a class of eukaryotic DLPs, such as dynamin or MxA.

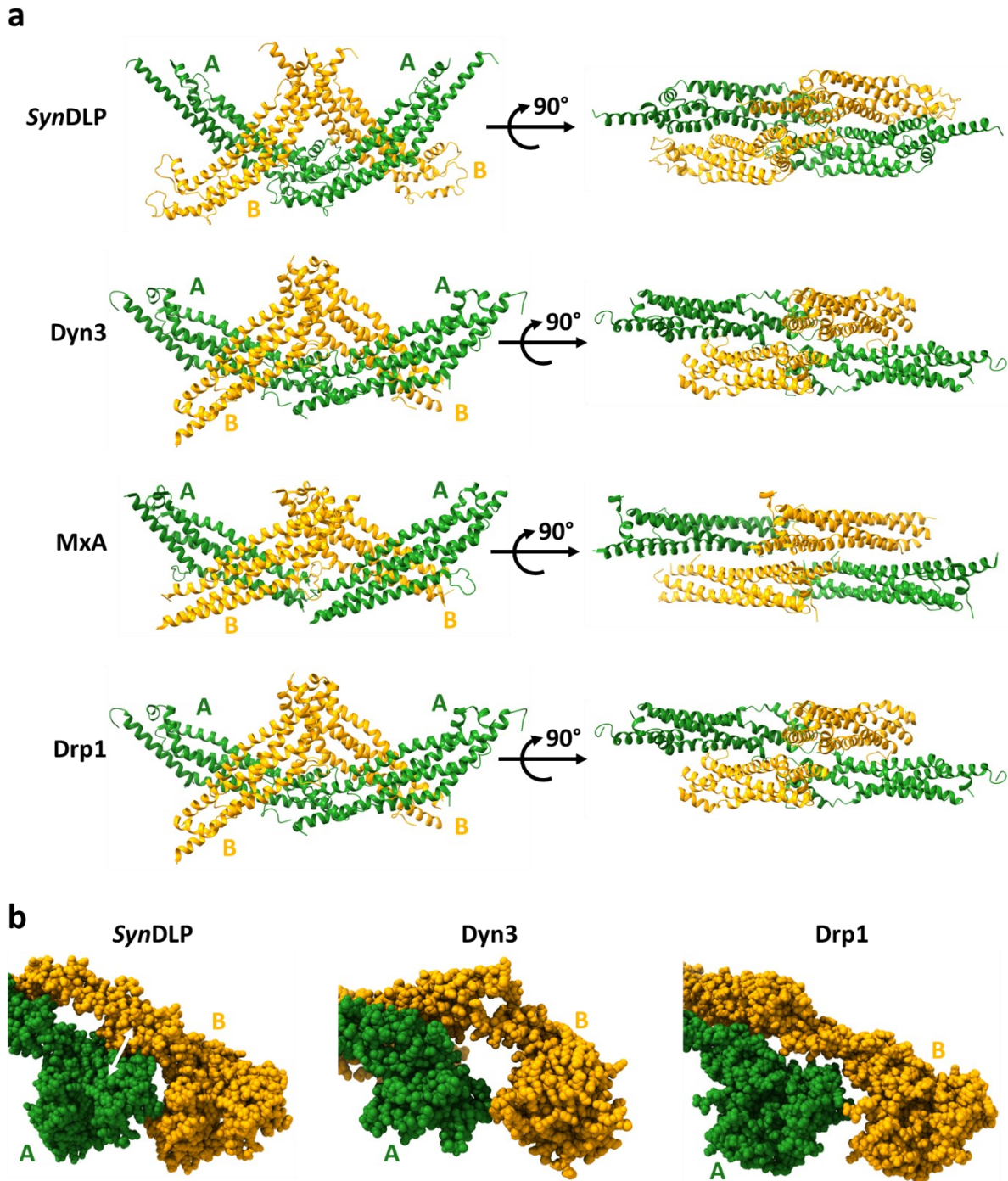


Figure 4.8: Comparison of oligomeric interfaces in different DLPs.

(a) Tetramers of *SynDLP* (this study), *Dyn3* (PDB: 5A3), *MxA* (PDB: 3LJB) and *Drp1* (PDB: 5WP9) in ribbon representation showing common oligomerization interfaces in the stalk domain. Monomers are marked in green and orange, respectively. The GD and the BSE are omitted for clarity. (b) Longitudinal GD-GD contacts and the intermolecular GD-BSE interface of *SynDLP* is compared to *Dyn3* and *Drp1*. GD and BSE of two adjacent monomers within the oligomers are shown. The two monomers are colored green and orange, respectively. The enlarged GD-BSE interface in *SynDLP* is highlighted by a white arrow.

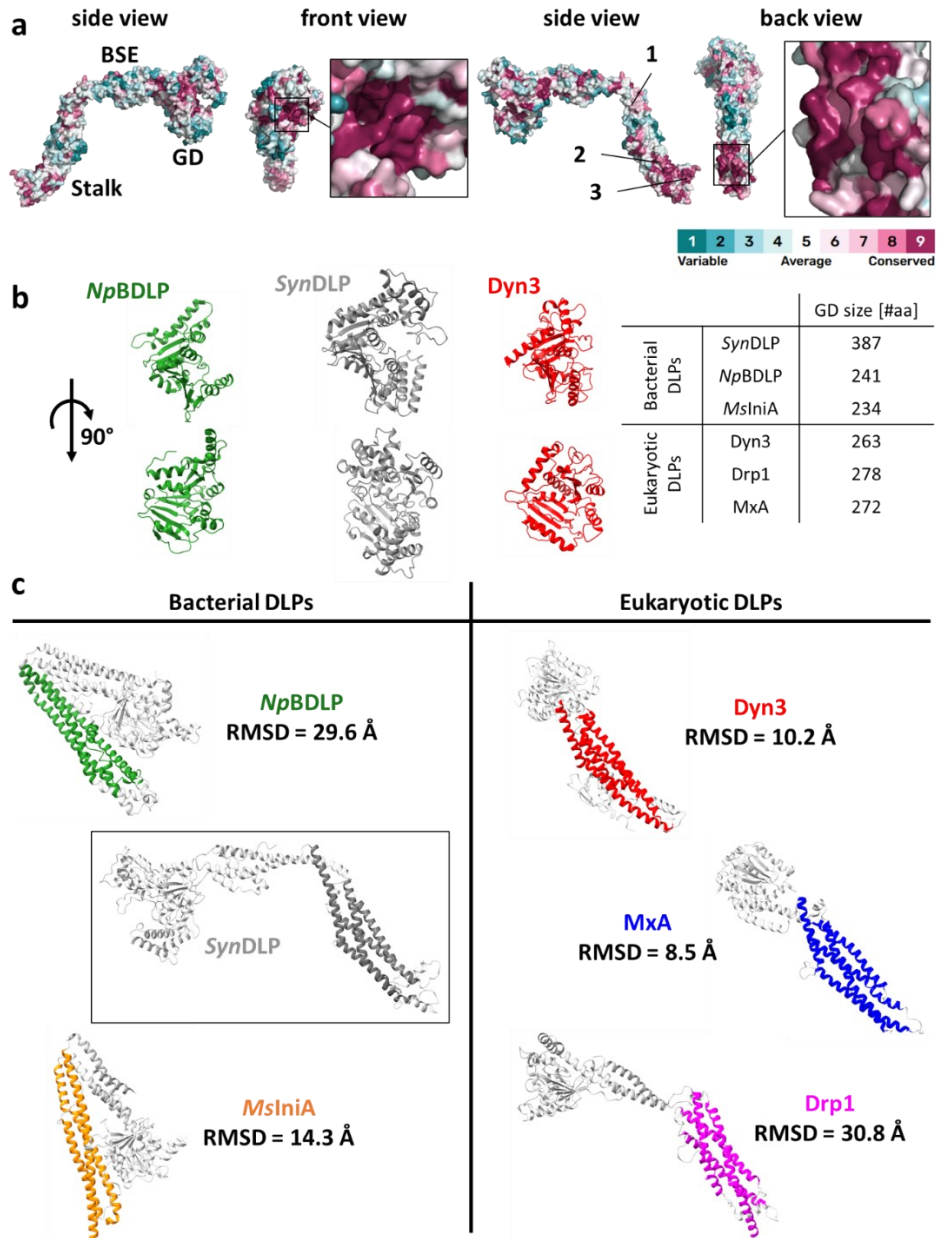


Figure 4.9: Structural comparison of *SynDLP* with other bacterial and eukaryotic DLP structures.

(a) A surface conservation plot showed amino acids in the *SynDLP* structure that are conserved in other DLP sequences. The surface conservation plot was produced using ConSurf (Glaser *et al.*, 2003; Landau *et al.*, 2005; Ashkenazy *et al.*, 2010, 2016; Celniker *et al.*, 2013). The color key ranges from 1 (cyan, variable regions) to 9 (red-violet, conserved regions). The evaluation of single residues conservation in the primary sequence is shown in Fig. A5. The position of GD, BSE, and stalk are highlighted in the first side view. The oligomerization interfaces 1 – 3 are labeled in the second side view. (b) Structural side-by-side comparison of dynamin-like GDs from *SynDLP* (gray) with a bacterial (*NpBDLP*, PDB: 2J69, green) and a eukaryotic representative (*Dyn3*, PDB: 5A3F, red). The table summarizes the size of different GDs (*SynDLP*, *NpBDLP* (PDB: 2J69), *MsIniA* (PDB: 6J73), *Dyn3* (PDB: 5A3F), *Drp1* (PDB: 5WP9) and *MxA* (PDB: 3SZR)). (c) Structural arrangement of α -helices in the stalk domains of *SynDLP* (gray) and four other DLPs was compared by structural alignment of the domains leading to C α -RMSD values larger than 10. The areas used for the structural alignments are highlighted in green (*NpBDLP*), orange (*MsIniA*), red (*Dyn3*), blue (*MxA*) or magenta (*Drp1*) and the remaining structural elements not used for the alignment are colored in light gray. For details about the number of aligned residues, see Fig. 4.10c.

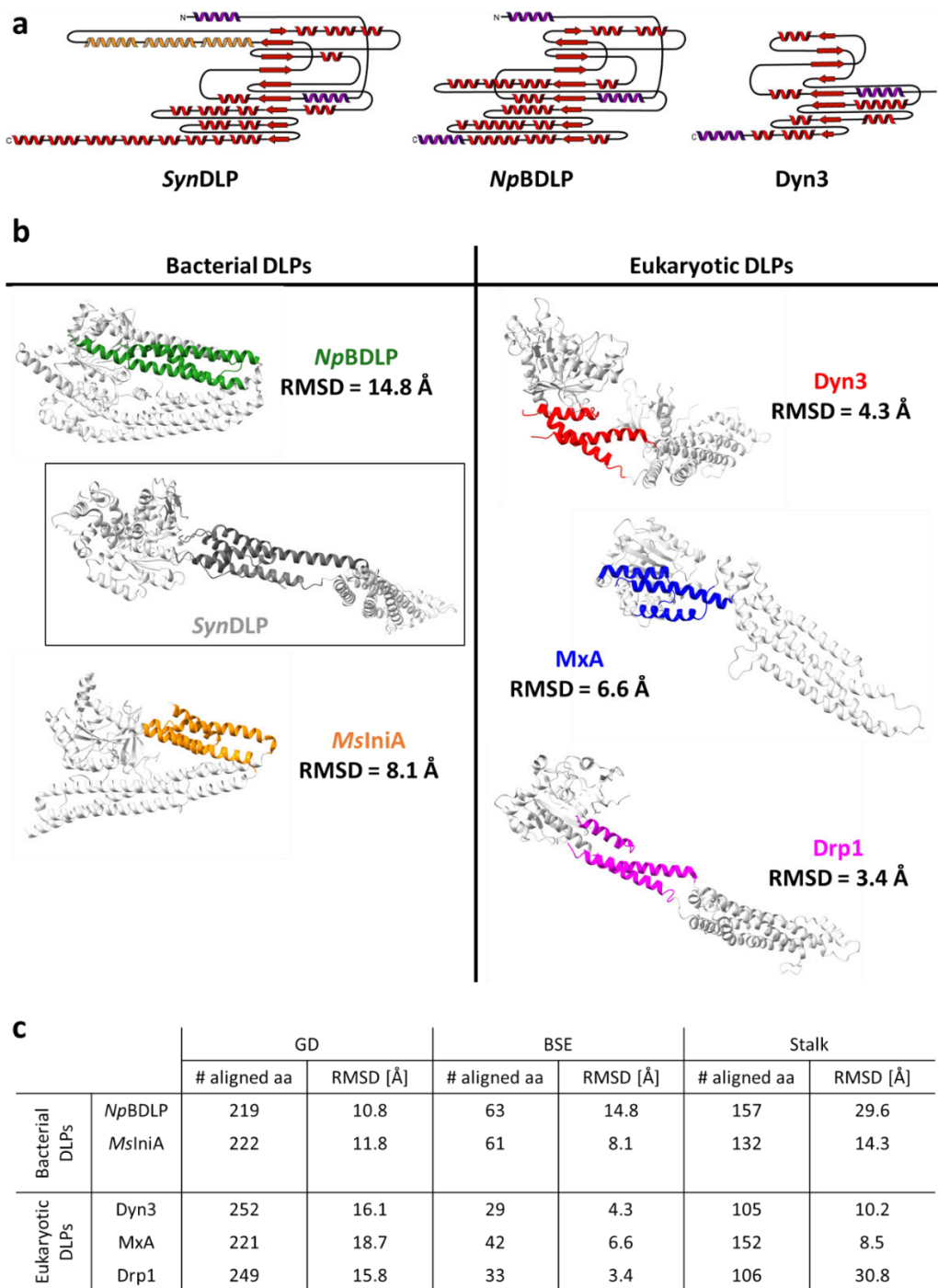


Figure 4.10: Structural comparison of DLP domains.

(a) Topology plots of the GDs derived from the *SynDLP* structure, *NpBDLP* (PDB: 2J69) and *Dyn3* (PDB: 5A3F). α -helices and β -sheets of the GD are colored in red and α -helices of the BSE domain in purple. The additional α -helices of the *SynDLP* GD are colored in orange. (b) In the monomer model of *SynDLP*, the structure of the BSE (gray) was aligned with the BSE of the BDLPs *NpBDLP* (PDB: 2J69, green) and *MslniA* (PDB: 6J73, orange) and with the eukaryotic representatives *Dyn3* (PDB: 5A3F, red), *MxA* (PDB: 3SZR, blue) and *Drp1* (PDB: 5WP9, magenta). RMSD values are given. The regions used for the alignments are highlighted by color and the remaining protein regions are colored in light gray. (c) A table that summarizes the structural alignments performed in this study. An indicated number of amino acids from the domains of the *SynDLP* monomer structure was aligned to the respective domains of the corresponding bacterial and eukaryotic DLPs leading to the $C\alpha$ -RMSD values.

An intramolecular disulfide bridge in the BSE domain influences the SynDLP GTPase activity

The *SynDLP* structure indicated the formation of an intramolecular disulfide bridge between C8 and C777 that covalently connects the BSE1 and BSE3 domains (Fig. 4.11a). In fact, the migration behavior of *SynDLP* in SDS-PAGE analysis changed depending on the DTT concentration (Fig. 4.11b): at low DTT concentrations, *i.e.*, when the disulfide bridge is established, *SynDLP* ran at an increased apparent molecular mass whereas it ran at the predicted molecular mass in the presence of DTT. To study the structural impact of the intramolecular disulfide bridge, a *SynDLP* variant was generated by mutating one of the involved cysteines (C777) to alanine. In the resulting protein (*SynDLP*_{C777A}) the formation of the disulfide bridge was prevented (Fig. 4.2). When analyzed via size exclusion chromatography, *SynDLP*_{C777A} behaved like *SynDLP* wt (Fig. 4.11c), and thus, the C777A mutation apparently does not affect *SynDLP* oligomer formation. In addition, the mutant protein seemed to be correctly folded at the secondary structure level as indicated by circular dichroism (CD) spectra of *SynDLP* wt and *SynDLP*_{C777A}, which were identical at 20°C (Fig. 4.11d). Yet, the mutation affected the thermodynamic stability of *SynDLP*. The thermal stability of *SynDLP* wt and *SynDLP*_{C777A} was investigated by thermal denaturation of the proteins. Unfolding of the secondary structure was monitored via recording CD spectra in the far UV at increasing temperatures (Fig. 4.11e). The spectra were dominated by minima at 208 and 222 nm, due to the high content of α -helices. While from the melting curve of *SynDLP* wt (Fig. 4.11e, black) a $T_{m,CD}$ of $49.5 \pm 0.3^\circ\text{C}$ was calculated, the $T_{m,CD}$ of the *SynDLP*_{C777A} variant (Fig. 4.11e, red) was determined to be $43.7 \pm 0.3^\circ\text{C}$ (Table 4.3), showing that *SynDLP*_{C777A} is less stable than the wt. This observation was further elucidated via an ANS fluorescence thermal shift assay (ANS-FTSA), which monitors changes in the tertiary and quaternary structure of proteins and thus complements the CD measurements. The $T_{m,ANS-FTSA}$ was shifted by $\sim 8^\circ\text{C}$ from $46.7 \pm 0.1^\circ\text{C}$ to $39.0 \pm 0.1^\circ\text{C}$ for the mutant (Fig. 4.11f, Table 4.3), which further confirmed the lowered thermodynamic stability of *SynDLP*_{C777A} compared to *SynDLP* wt.

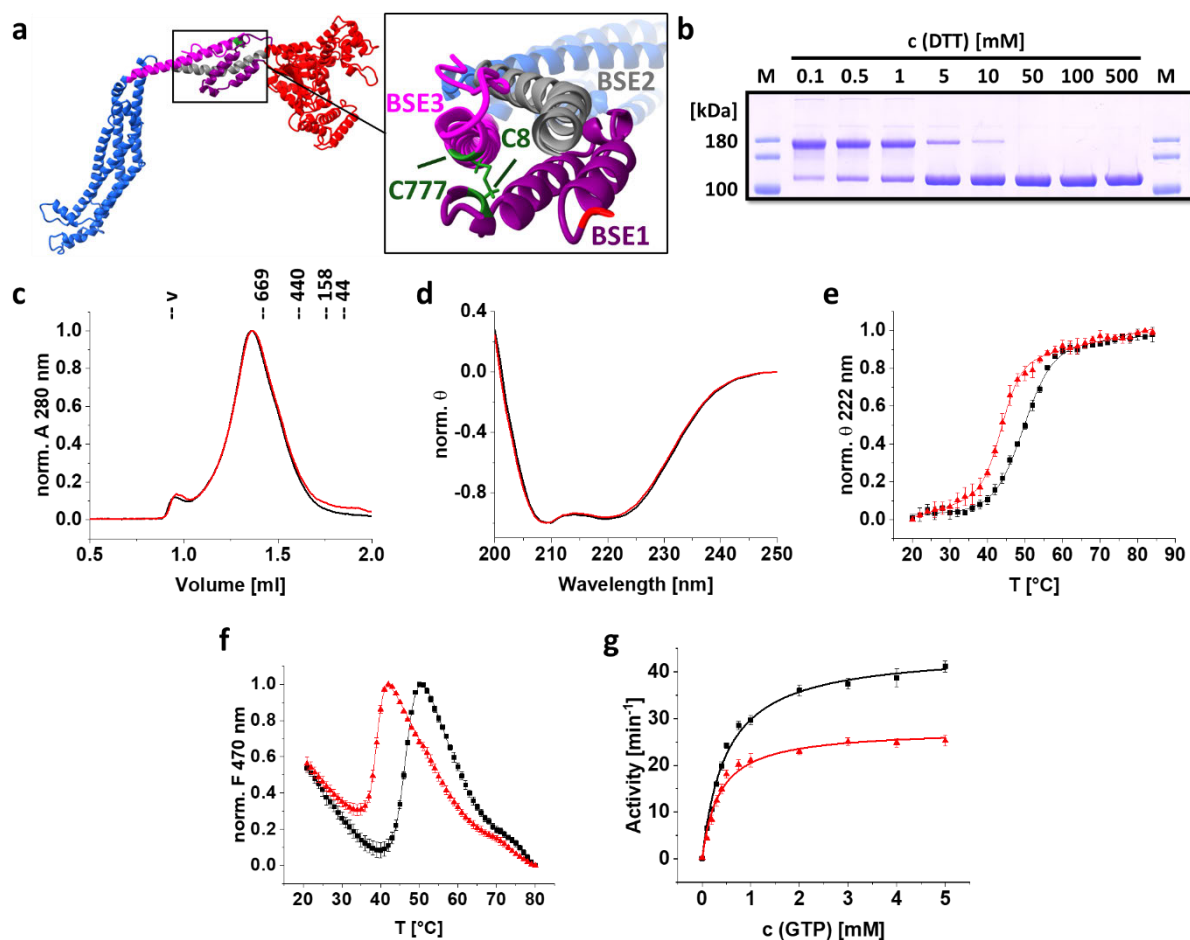


Figure 4.11: Structural stabilization and enhanced GTPase activity by an intramolecular disulfide bridge in the BSE domain.

(a) Ribbon representation of a *SynDLP* monomer. C8 and C777, forming an intramolecular disulfide bridge that connects BSE1 and BSE3, are highlighted in green. BSE1, which consists of two α -helices, BSE2 and BSE3 are colored purple, gray and magenta, respectively. GD colored in red, stalk in blue. (b) *SynDLP* was incubated with different DTT concentrations (the final concentrations after adding SDS sample buffer are given). The amount of *SynDLP* with an intact disulfide bridge depended on the DTT concentration (band with intact bridge at ~ 180 kDa, band with reduced cysteines at ~ 100 kDa). M = marker. Representative gel from two independent experiments with the same result. (c) Analytical size exclusion chromatography of *SynDLP*_{C777A} (red) compared to *SynDLP* wt (black) revealed the formation of oligomeric structures for both proteins. A_{280} values were normalized (0 – 1) for better comparison. (d) CD spectra of 1 μ M *SynDLP* wt (black) and *SynDLP*_{C777A} (red). Mean of three measurements is shown. For comparison, the spectra were normalized (θ value at 250 nm set to 0, minimum θ set to -1). (e) The thermal stability of *SynDLP* (black) and *SynDLP*_{C777A} (red) was monitored using CD spectroscopy. The ellipticities at 222 nm were plotted against the temperature, normalized (0 – 1) and fitted with an adapted Boltzmann fit (Equation (6)). The fit curves are shown as lines. Mean of independent measurements ($n = 3$) and error bars (S.D.) are shown. (f) Measured ANS-FTSA of *SynDLP* wt (black) and *SynDLP*_{C777A} (red). ANS fluorescence intensities at 470 nm were plotted against the temperature and normalized (0 – 1) for better comparison. A temperature range capturing the transition phase was fitted with an adapted Boltzmann fit (Equation (7)). Fit curves are shown as lines. The mean of three independent experiments and error bars (S.D.) are displayed. (g) The GTPase activity of *SynDLP* wt (black) and *SynDLP*_{C777A} (red) were measured in a continuous, regenerative, coupled assay. The mean and error bars (S.D.) of three independent experiments are shown. The data points were fitted using Equation (3).

Table 4.3: Transition temperatures of *SynDLP* variants determined via CD spectroscopy and ANS-FTSA

	$T_{m, CD} [^{\circ}C]$	$T_{m, ANS-FTSA} [^{\circ}C]$
<i>SynDLP</i>	49.5 ± 0.3	46.7 ± 0.1
<i>SynDLP</i> _{C777A}	43.7 ± 0.3	39.0 ± 0.1
<i>SynDLP</i> _{HPRN-AAAA}	46.4 ± 0.1	44.9 ± 0.1

As DLPs catalyze the hydrolysis of GTP to GDP and P_i , the GTPase activity of *SynDLP* and *SynDLP*_{C777A} was determined next via a continuous, regenerative, coupled GTPase assay. Typically, the GTPase assay was performed with 0.5 μ M protein, as *SynDLP* showed a concentration-dependent GTPase activity at low protein concentrations yet reaching a plateau at protein concentrations $>0.3 \mu$ M (Fig. 4.12a), and in the presence of the monovalent cations Na^+ and K^+ , which were shown to activate the GTP hydrolysis catalyzed by DLPs (Chappie *et al.*, 2010). *E.g.*, the omission of NaCl led to a clear decrease of the *SynDLP*s GTPase activity (Fig. 4.12b). A mutation of a conserved residue in the P-loop (K61A) considerably reduced the GTPase activity, as previously observed for dynamin and other DLPs, which demonstrated a related GTPase mechanism (Fig. 4.12c). The GTPase activities of *SynDLP* wt and C777A followed a typical Michaelis-Menten kinetic (Fig. 4.11g), and consequently the data were fitted with a hyperbolic curve (Equation (3)). The turnover rate (k_{cat}) and the Michaelis-Menten constant (K_m) were determined, as summarized in Table 4.4. Apparently, with a k_{cat} of $44.6 \pm 1.0 \text{ min}^{-1}$ *SynDLP* had a relatively high basal GTPase activity (Fig. 4.11g, black). Yet, the turnover rate of the *SynDLP*_{C777A} mutant was significantly reduced by almost 40% compared to the wt (Fig. 4.11g, red, Table 4.4).

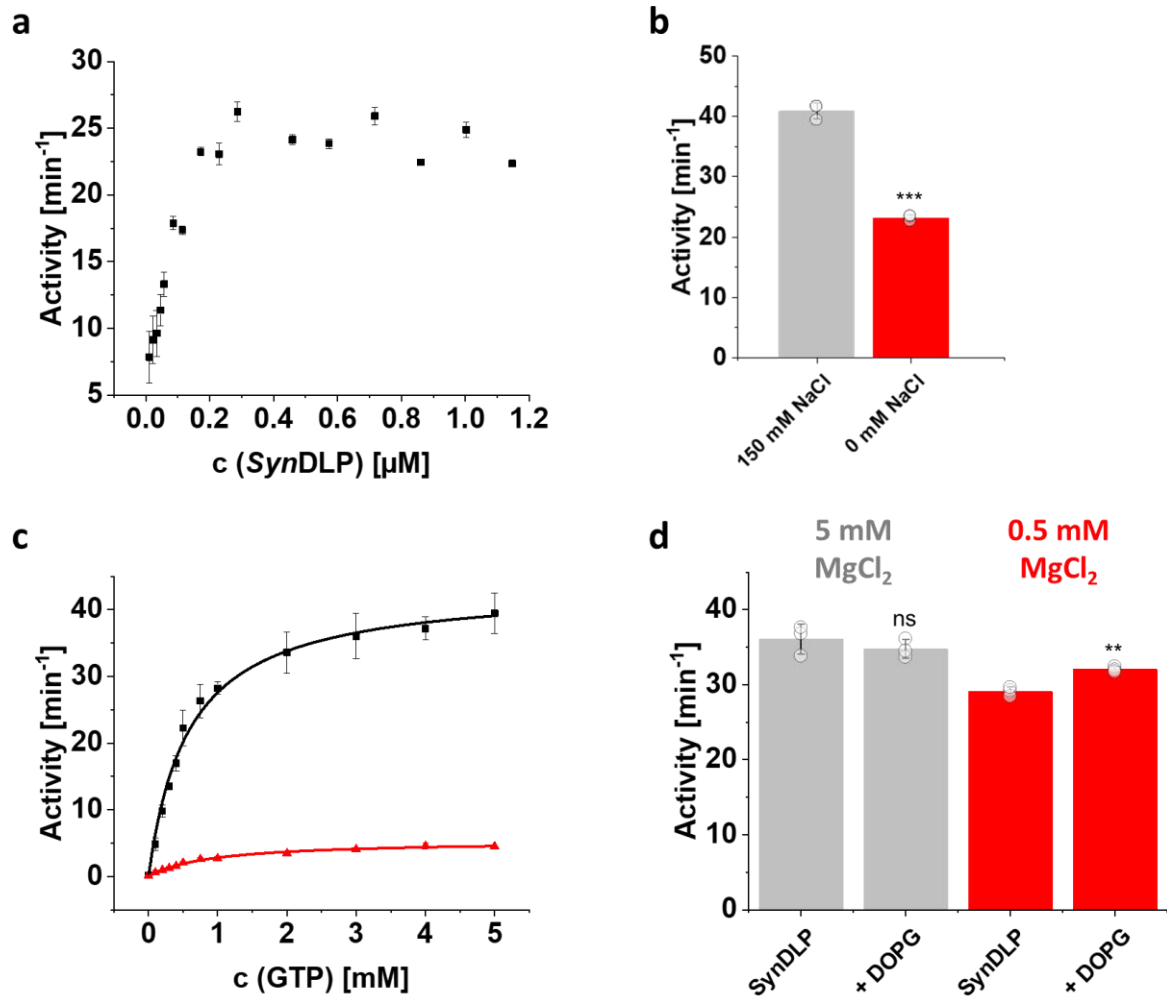


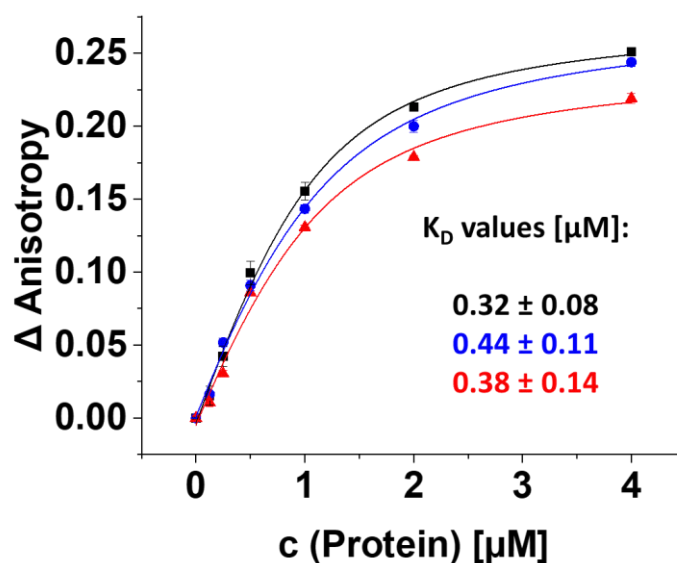
Figure 4.12: The *SynDLPs* GTPase activity.

(a) The GTPase activity of increasing *SynDLP* concentrations (black) was measured in a continuous, regenerative, coupled assay at a GTP concentration of 1 mM. Mean of independent measurements ($n = 3$) and S.D. are shown. (b) GTPase activity of *SynDLP* wt was measured at a GTP concentration of 5 mM under standard conditions (presence of 150 mM NaCl, gray) and in the absence of NaCl (red). Mean of three measurements and error bars (S.D.) are shown. Single measurements are shown as circles. ns = not significant ($P > 0.05$), * $P < 0.05$, ** $P < 0.01$, *** $P < 0.001$ based on a two-sided unpaired Student's t-test. $P = 0.000025$. (c) The GTPase activities of 0.5 μ M *SynDLP* wt (black) and *SynDLP*_{K61A} (red) were measured. Mean of three measurements and error bars (S.D.) are shown. The kinetic parameters of the *SynDLP*_{K61A} mutant were determined as $k_{cat} = 5.4 \pm 0.2 \text{ min}^{-1}$ and $K_m = 0.91 \pm 0.07 \text{ min}^{-1}$ (for *SynDLP* wt see Table 4.4). (d) GTPase activity of *SynDLP* wt was determined at 5 mM GTP in the absence or presence of 20 μ M DOPG LUVs (extruded to 100 nm) either with 5 mM (gray) or 0.5 mM MgCl₂ (red). LUVs were added with the assay components. Mean of three measurements and error bars (S.D.) are shown. Single measurements are displayed as circles. ns = not significant ($P > 0.05$), * $P < 0.05$, ** $P < 0.01$, *** $P < 0.001$ based on a two-sided unpaired Student's t-test. The activity in the absence of LUVs is compared to the activity of *SynDLP* plus DOPG for the respective MgCl₂ concentrations (5 mM MgCl₂: $P = 0.38$; 0.5 mM MgCl₂: $P = 0.0018$).

Table 4.4: Kinetic parameters describing the GTPase activity of *SynDLP* variants

	k_{cat} [min^{-1}]	K_m [mM]
<i>SynDLP</i>	44.6 ± 1.0	0.50 ± 0.04
<i>SynDLP</i> _{C777A}	27.7 ± 0.8	0.35 ± 0.04
<i>SynDLP</i> _{HPRN-AAAA}	17.0 ± 0.2	0.33 ± 0.02

Next, GTP binding affinities of *SynDLP* wt and C777A were determined via fluorescence anisotropy measurements using the GTP analog Mant-GTP (Fig. 4.13). Based on this assay, both proteins have similar nucleotide-binding affinities in the three-digit nanomolar range. As both proteins showed no residual (measurable) GTPase activity at 0 mM GTP (negative control without nucleotide; first data point in each curve) although a GTP regenerating system was added, we conclude that no significant amount of GTP/GDP has been co-purified with the proteins. This is supported by the low A_{260}/A_{280} ratio of 0.7 determined via absorption spectroscopy using purified *SynDLP*, a value indicating that no nucleotides were bound.

**Figure 4.13: GTP binding affinities of *SynDLP* variants.**

GTP binding of *SynDLP* variants was measured using Mant-GTP (Jena Bioscience, Jena, Germany). Therefore, increasing concentrations of *SynDLP* wt (black), *SynDLP*_{C777A} (blue) and *SynDLP*_{HPRN-AAAA} (red) were incubated with 1 μM Mant-GTP in reaction buffer at 20°C for 30 min. The change in the fluorescence anisotropy was measured ten times ($\lambda_{\text{ex}} = 355$ nm, $\lambda_{\text{em}} = 448$ nm, slit widths corresponding to 7 nm and 7 nm, $T = 20^\circ\text{C}$) using a Fluoromax-4 spectrometer (Horiba Scientific, Kyoto, Japan) and the results averaged. The data points show mean of independent experiments ($n = 3$) and standard deviation and were fitted using a quadratic binding equation assuming a one-site specific binding model (Equation (5)).

Uncommon GD contacts enhance the SynDLP GTPase activity

In the *SynDLP* oligomer structure we observed an expanded intermolecular GD-BSE1 interface (Figs. 4.3h, 4.8b). The role of the intermolecular GD-BSE1 interface in *SynDLP* oligomers was addressed via analysis of an assembly-defective *SynDLP* variant. *SynDLP* oligomerizes via an intricate interaction network in the stalk domain by contacts of defined interfaces as already mentioned (Fig. 4.7). As a general feature, structurally related DLPs form a stable dimer via interface 2. The basic dimeric unit can tetramerize or further oligomerize via interfaces 1 and 3. The latter is non-symmetric and mediates lateral contacts between parallelly oriented stalks. Following previous studies on diverse DLPs where oligomerization was disturbed by mutations, we replaced the residues ⁵⁵²HPRN⁵⁵⁵ in a highly conserved loop at the tip of the stalk domain that is part of oligomerization interface 3 (Figs. 4.3h, 4.14a) (Gao *et al.*, 2010; Faelber *et al.*, 2011; Fröhlich *et al.*, 2013; Fribourgh *et al.*, 2014; Bohuszewicz and Low, 2018) by four alanines.

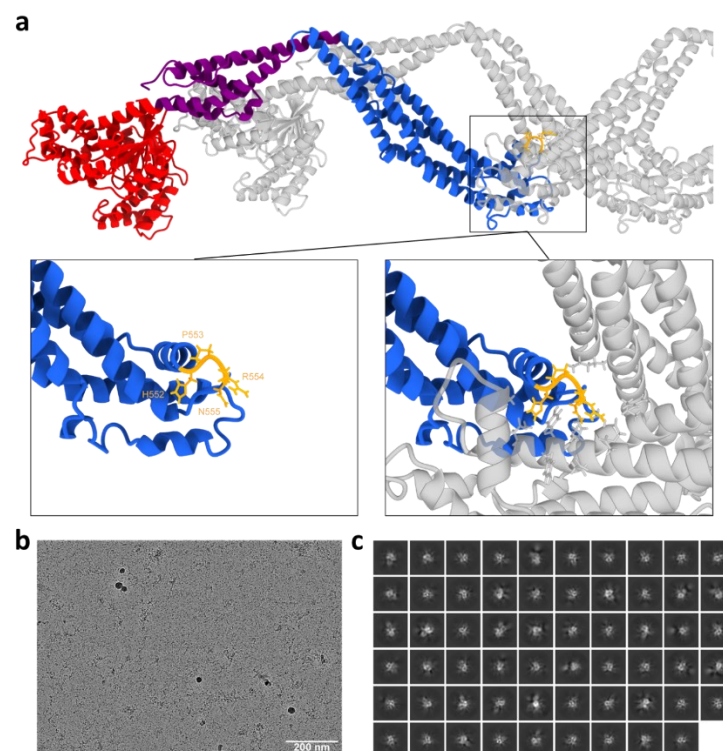


Figure 4.14: Mutation of oligomerization interface 3 residues.

(a) An isolated tetramer of the *SynDLP* oligomer is shown as ribbon representation in grey. The domains are colored in one monomer (GD in red, BSE in purple, stalk in blue). The zoomed sections show four residues (⁵⁵²HPRN⁵⁵⁵) colored in orange and as sticks that lie on a loop in the oligomerization interface 3 either in one monomer (left) or together with contacting monomers (right). ⁵⁵²HPRN⁵⁵⁵ were substituted to AAAA to impair the assembly of *SynDLP* oligomers. (b) Cryo-EM micrograph of *SynDLP*_{HPRN-AAAA}. The entire protein sample before analytical gel filtration (see Fig. 4.15c) was analyzed (no single fractions). Data set was measured one time (no independent replicates). (c) 2D class averages of *SynDLP*_{HPRN-AAAA} particles (250,000 particles with 272 Å box dimension).

The migration behavior of *SynDLP*_{HPRN-AAAA} on an SDS PAGE gel (Fig. 4.15a) and the wt-like shape of the CD spectrum (Fig. 4.15b) indicated proper secondary structure formation as well as the formation of the stabilizing disulfide bridge within the BSE of the mutated protein. Yet, analytical size exclusion chromatography of *SynDLP*_{HPRN-AAAA} revealed an apparent MW of ~174 kDa, indicating formation of dimers (Fig. 4.15c, red), which was previously also observed for other DLPs carrying the equivalent mutations (Faelber *et al.*, 2011; Fröhlich *et al.*, 2013; Fribourgh *et al.*, 2014). The hampered oligomerization was also confirmed by cryo-EM micrographs (Fig. 4.14b, c). Thermal denaturation of *SynDLP* and *SynDLP*_{HPRN-AAAA} was monitored via CD spectroscopy and ANS-FTSA to investigate the impact of oligomerization on the thermodynamic stability. With both methods, a slight decrease of the T_m of *SynDLP*_{HPRN-AAAA} was observed, which indicated that oligomerization promotes the thermodynamic stability (Fig. 4.15d, e, Table 4.3). Compared to *SynDLP* wt (Fig. 4.15e, black), the ANS-FTSA curve of *SynDLP*_{HPRN-AAAA} (Fig. 4.15e, red) indicated increased hydrophobic, ANS-accessible surface regions, visible as an increased starting $F_{470\text{ nm}}$ value at 20°C. Most likely, surface regions, which are not covered in the assembly-defective mutant protein, are now ANS accessible, leading to an increased initial ANS fluorescence emission.

Next, the GTPase activity of *SynDLP*_{HPRN-AAAA} was measured to evaluate the impact *SynDLP* oligomerization has on its GTP hydrolyzing activity. If *SynDLP*_{HPRN-AAAA} dimerization via oligomeric interface 2 is assumed (Fig. 4.7), the assembly-defective protein is not expected to form the intermolecular GD contacts anymore that were observed in the *SynDLP* wt oligomers. The activity of *SynDLP* wt (black) and *SynDLP*_{HPRN-AAAA} (red) at different substrate concentrations is shown in Fig. 4.15f. As the wt, the activity of *SynDLP*_{HPRN-AAAA} followed a typical Michaelis-Menten kinetic. The fit with a hyperbolic curve revealed a k_{cat} of $17.0 \pm 0.2 \text{ min}^{-1}$ for *SynDLP*_{HPRN-AAAA} (Table 4.4), and thus, the turnover rate was reduced by ~60% in case of the assembly-defective protein. The GTP binding affinity of the mutant appeared not to be significantly affected as indicated by a Mant-GTP binding assay (Fig. 4.13).

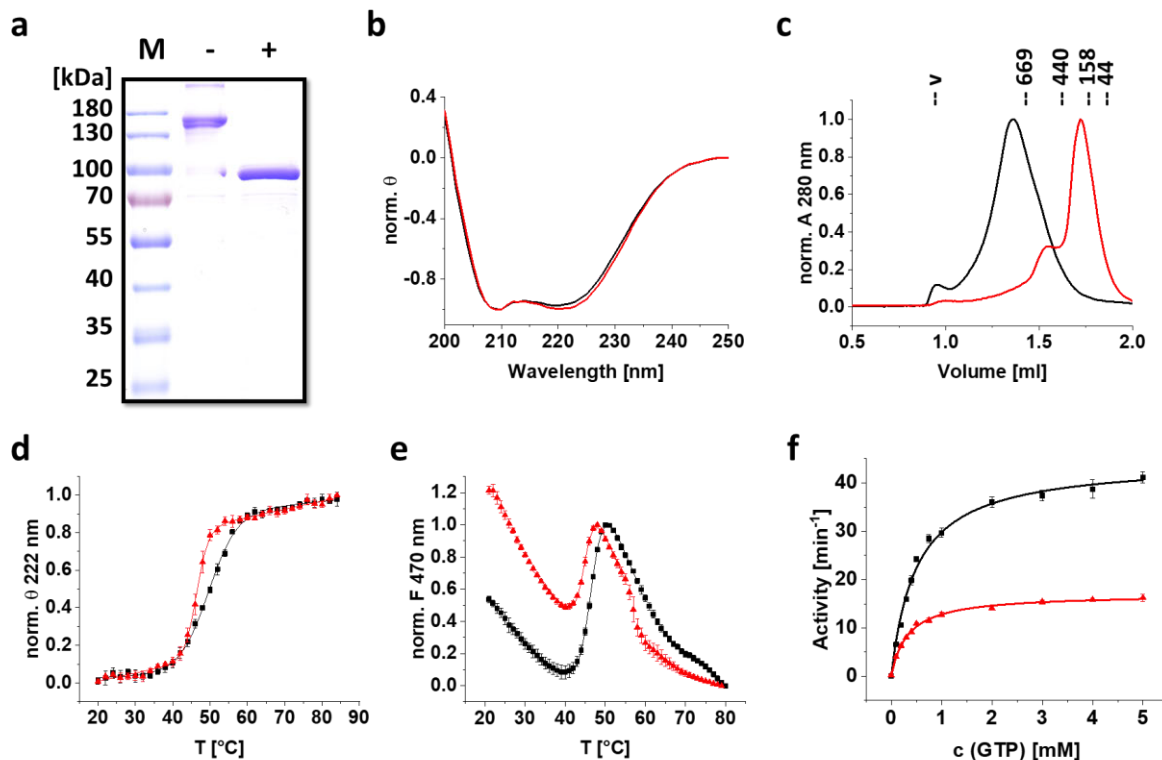


Figure 4.15: Biochemical analysis of *SynDLP*_{HPRN-AAAA}.

(a) Purified *SynDLP*_{HPRN-AAAA} was analyzed via SDS-PAGE in the presence of 0.1 mM DTT (lane -) or 100 mM DTT (lane +). The calculated molecular mass of the protein is 93 kDa. The SDS-PAGE analysis revealed a single band at ~100 kDa (lane +) without showing further protein bands, thus the protein was $\geq 95\%$ pure. M = marker. Representative gel of two independent experiments showing the same results. (b) CD spectra of *SynDLP* wt (black) and *SynDLP*_{HPRN-AAAA} (red). The mean of three measurements is shown. The spectra were normalized (θ value at 250 nm set to 0, minimum θ set to -1) for better comparison. (c) Analytical size exclusion chromatography of *SynDLP* wt (black) and *SynDLP*_{HPRN-AAAA} (red). The elution peak positions of the standard proteins and the corresponding molecular masses are indicated (v = void volume). A_{280} values were normalized (0 – 1) to better compare the chromatograms. (d) CD spectra of *SynDLP* wt (black) and *SynDLP*_{HPRN-AAAA} (red) were recorded at increasing temperatures. The ellipticities at 222 nm were plotted against the temperature, normalized (0 – 1) and fitted with an adapted Boltzmann fit (Equation (6)). The fit curves are displayed as lines. Mean of three independent experiments and error bars (S.D.) are shown. (e) ANS-FTSA measurements of *SynDLP* wt (black) and *SynDLP*_{HPRN-AAAA} (red). ANS fluorescence intensities at 470 nm were plotted against the temperature and normalized (minimum set to 0, main peak set to 1). The temperature range that captured the transition phase was fitted with an adapted Boltzmann fit (Equation (7)). Fit curves are shown as lines. Error bars represent S.D., $n = 3$ (mean of independent measurements). (f) GTPase activity of 0.5 μ M *SynDLP* (black) or *SynDLP*_{HPRN-AAAA} (red). Mean of independent experiments ($n = 3$) and error bars (S.D.) are shown. Data points were fitted using the Michaelis-Menten equation (Equation (3)). The fit curves are displayed as lines.

SynDLP interacts with negatively charged TM lipids

While *SynDLP* is *per se* a soluble protein, membrane interaction of *SynDLP* is a prerequisite for catalyzing membrane dynamics. Thus, the membrane interaction propensity of *SynDLP* was next investigated. First, the membrane interaction of *SynDLP* with the main TM lipid species MGDG, SQDG, DGDG and PG was tested via fluorescence spectroscopy using the fluorescent dye Laurdan as a probe. Importantly, *SynDLP* only very weakly interacted with pure (net uncharged) DOPC membranes, which were used as a control (Fig. 4.16a).

When *SynDLP* was incubated with large unilamellar vesicles (LUVs) containing 50% of DOPC plus 50% of a respective TM lipid, only little membrane interaction was observed in MGDG- or DGDG-containing membranes, whereas a significant increase of the ΔGP was observed when membranes contained SQDG or DOPG (Fig. 4.16a). As these two lipids carry negatively charged headgroups, *SynDLP*-membrane interaction appears to contain a strong electrostatic contribution. Consequently, when *SynDLP* binding to DOPG-containing membranes was analyzed using DOPC membranes with increasing DOPG mole fractions, an increasing interaction of *SynDLP* with membranes was observed (Fig. 4.16b). Based on these observations, all following experiments investigating the interaction of *SynDLP* with membranes were always conducted with PG-containing membranes.

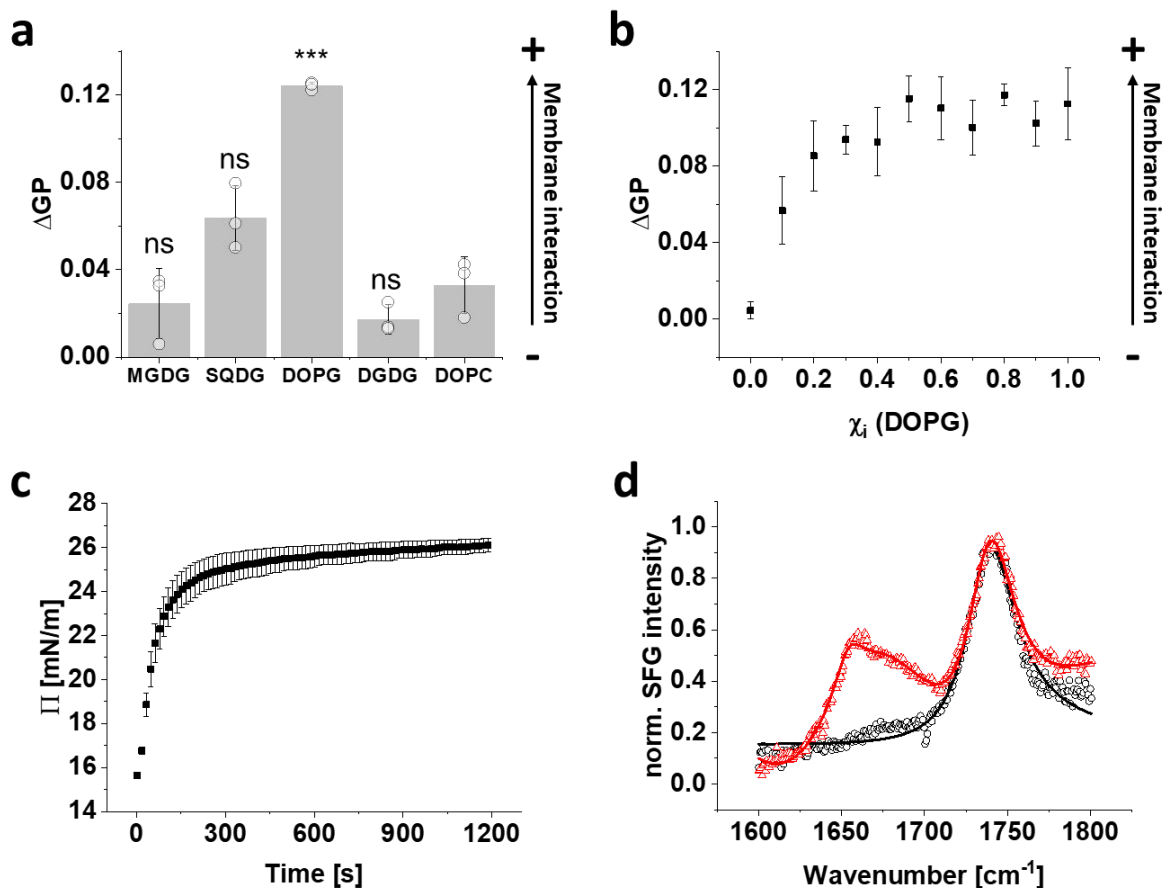


Figure 4.16: Membrane interaction of *SynDLP*.

(a) Fluorescence spectroscopy using Laurdan as a fluorescent probe. LUVs were prepared with 50% DOPC and 50% of the indicated TM lipid (*w/w*) mixed with Laurdan at a 1:500 molar ratio. Laurdan fluorescence emission was measured after 30 min incubation of *SynDLP* and LUVs and the ΔGP value was calculated from the spectra. Mean of three independent experiments (single measurements shown as circles) and error bars (S.D.) are shown. ns = not significant ($P > 0.05$), * $P < 0.05$, ** $P < 0.01$, *** $P < 0.001$ based on a two-sided unpaired Student's *t*-test. The ΔGP values of MGDG ($P = 0.52$), SQDG ($P = 0.055$), DOPG ($P = 0.00028$) or DGDG ($P = 0.14$) are compared to DOPC. Arrow indicates increasing membrane interaction. (b) LUVs were prepared with different DOPG/DOPC molar ratios (Laurdan added at a 1:500 molar ratio). Laurdan fluorescence spectra were recorded after 30 min and ΔGP values (black) were determined from the spectra. Mean of independent measurements ($n = 4$) and error bars (S.D.) are shown. Arrow indicates increasing membrane interaction. (c) Progression of the surface pressure (black) measured over time in parallel to the SFG intensity shown in (d). SFG spectroscopy of $0.5 \mu\text{M}$ *SynDLP* was carried out on a DMPG monolayer under reaction buffer conditions (without DTT). $t = 0$ s corresponds to the moment of *SynDLP* addition. Mean of three independent measurements and error bars (S.D.) are shown. (d) The SFG spectrum in the amide I region of the DMPG monolayer (black) and after *SynDLP* addition and equilibration (red) is shown. A fit of the amide I band is displayed as a line. The mean of three independent measurements is shown. SFG intensity was normalized (0 – 1) for better comparison.

In the here solved *SynDLP*s structure, we recognized two putative MIDs at the tip of the stalk based either on the quaternary (Figs. 4.3h, 4.17a) or the tertiary structure (Fig. 4.17b). However, when these regions were mutated, the isolated recombinant proteins still interacted with DOPG

containing LUVs similar to *SynDLP* wt (Fig. 4.17c, d), and thus these regions (alone) are not responsible for membrane binding of *SynDLP*. Potentially, either other regions of the protein or a larger area involving multiple *SynDLP* parts are responsible for membrane interaction.

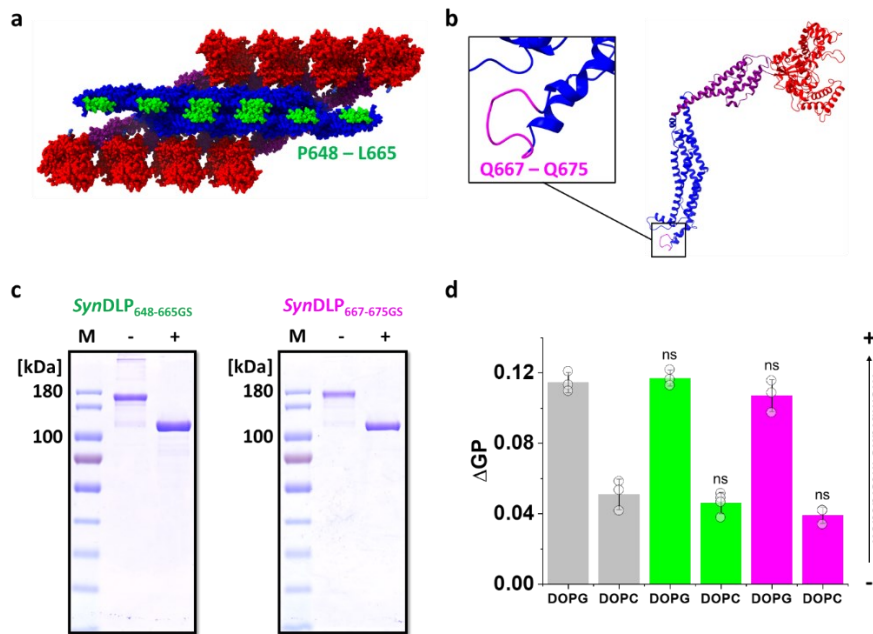


Figure 4.17: Putative membrane interaction domains in *SynDLP*.

Putative membrane interaction sites in the *SynDLP* structure were predicted according to the position of amino acid residues at the tip of the stalk domain. (a) Based on the quaternary structure of *SynDLP* oligomers, a domain consisting of 18 residues (P648 – L665) was identified being a putative MID. A *SynDLP* oligomer is shown with the GD, BSE, stalk and the putative MID colored in red, blue, purple and green, respectively. (b) Another putative MID was determined as a 9 amino acid loop (Q667 – Q675) based on the tertiary structure of a *SynDLP* monomer. A *SynDLP* monomer is shown in ribbon representation, coloring as in (a), except that the putative MID is highlighted in magenta. (c) To investigate the influence of both assumed MIDs on the membrane binding properties of *SynDLP*, the respective amino acids were substituted by multiple repetitions of glycine and serine (GS-linker), leading to the mutant proteins *SynDLP*_{648-665GS} and *SynDLP*_{667-675GS}. The two SDS-PAGE gels showed that the purity of the recombinantly expressed proteins (calculated molecular masses in each case 93 Da), which were purified as described for *SynDLP* wt, is $\geq 95\%$ (lane +: presence of 100 mM DTT). Under non-reducing conditions (0.1 mM DTT, lane -) both mutant proteins migrated at higher molecular masses, indicating correct formation of the intramolecular disulfide bridge established in the BSE domain of *SynDLP*. M = marker. Representative gels of two independent experiments showing the same results. (d) Membrane binding of the assumed membrane interaction-defective mutants was analyzed and compared to *SynDLP* wt via fluorescence spectroscopy using Laurdan as a fluorescent probe. LUVs contained either 50% DOPC and 50% DOPG (*w/w*), which was shown to promote strong interaction with *SynDLP* wt (Fig. 4.16a), or 100% DOPC, each time mixed with Laurdan at a 1:500 molar ratio. Fluorescence emission spectra of Laurdan were measured after 30 min incubation of the proteins and LUVs. ΔGP values were calculated from the spectra. The mean of three measurements and error bars (S.D.) are shown. Single measurements are shown as circles. ns = not significant ($P > 0.05$), * $P < 0.05$, ** $P < 0.01$, *** $P < 0.001$ based on a two-sided unpaired Student's *t*-test. The ΔGP value of either *SynDLP*_{648-665GS} or *SynDLP*_{667-675GS} is compared to *SynDLP* wt plus DOPG or DOPC, respectively. The arrow indicates increasing membrane interaction. Determined ΔGP values of *SynDLP* wt, *SynDLP*_{648-665GS} and *SynDLP*_{667-675GS} are shown as bars colored in grey, green or magenta, respectively.

To obtain structural information about *SynDLP*'s behavior at the lipid-buffer interfaces, we next used sum frequency generation (SFG) spectroscopy to probe *SynDLP* while binding a DMPG lipid monolayer. An SFG spectrum provides information about the interfacial folding and orientation of proteins. The selection rules of SFG dictate that any signal is exclusively generated by proteins bound to the interface while molecules in solution will not contribute (Hosseinpour *et al.*, 2020). Measurements were done in a Langmuir trough at a DMPG monolayer, in which the surface pressure was simultaneously monitored (Franz, Zadel and Weidner, 2017). After spreading a DMPG monolayer onto the reaction buffer, an SFG spectrum was recorded at a constant surface pressure of 15 mN/m (Fig. 4.16c, d). Yet, the surface pressure significantly increased from 15 to ~26 mN/m upon *SynDLP* addition (Fig. 4.16c), indicating *SynDLP* binding to and intercalating into the membrane, resulting in lipid reassembly. When the pure DMPG layer was analyzed via SFG, a resonance signal in the amide I region at around 1738 cm^{-1} arose due to characteristic carbonyl stretch vibrations of the lipid headgroups (Fig. 4.16d, black). After injection of *SynDLP* into the subphase of the trough, a broad amide I band (~1625 to ~1700 cm^{-1}) was observed, originating from protein backbone vibrations (Fig. 4.16d, red), which indicated highly ordered binding of *SynDLP* at the lipid monolayer (Hosseinpour *et al.*, 2020). The data were fitted using methods outlined previously (Pickering *et al.*, 2022). The spectra were dominated by a feature at 1654 cm^{-1} , which is assigned to α -helical structures. Significantly weaker side bands centered at 1633 and 1680 cm^{-1} are assigned to β -strands structure. The dominance of α -helical SFG signal demonstrated that the structure observed via CD and cryo-EM for the solution state is maintained when *SynDLP* binds to DMPG lipid interfaces.

Interestingly, the resonance near 1738 cm^{-1} related to the PG carbonyl group remained largely unchanged after *SynDLP* binding, indicating the lipid head groups remained ordered when interacting with the protein. This supported the assumption of charge interactions involved in the binding mechanism, since such interactions will align the lipid headgroups in the process. To investigate the interactions of *SynDLP* with the lipid acyl chains, we recorded SFG spectra in the C–D stretching range using lipids with perdeuterated acyl chains. The deuteration allows monitoring the state of the lipid layer without interference by protein C–H modes. The spectra (Fig. 4.18) showed a signal increase for the acyl CD₃ modes, which strongly suggested the acyl chains became more ordered with *SynDLP* binding, which could be the result of the ordering effect of charge-charge interactions between protein and lipid interface or intercalation of protein side chains into the lipid layer.

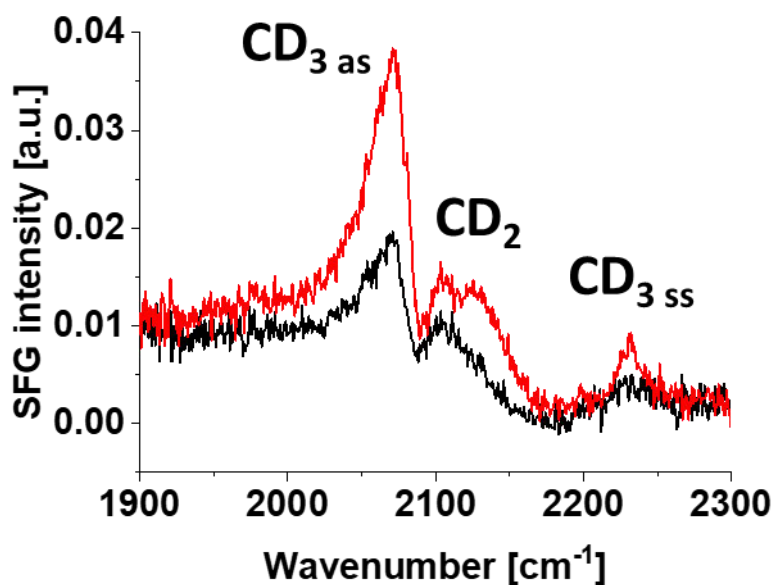


Figure 4.18: SFG spectra of a deuterated DMPG monolayer.

SFG spectra of a deuterated DMPG monolayer were recorded in the C–D stretching region before (black) and after (red) *SynDLP* binding. The surface pressure was set to 15 mN/m for the pure monolayer. Modes related to the asymmetric (as) and symmetric (ss) stretching mode of the terminal methyl group as well as the chain methylenes are visible. The increase of the signal after *SynDLP* binding shows that the protein partly intercalates with the lipid acyl chains, which increases the molecular alignment.

To glean information about the assembly process of *SynDLP* on lipid surfaces, we have recorded amide spectra as a function of time (Fig. 4.19). While the spectral shape of the protein amide I band centered around 1653 cm⁻¹ was very similar for the interaction time, the intensity grew and then remained constant after 1500 s. The surface tension data showed that binding began to saturate after ca. 250 s. The SFG amplitude, which is sensitive to both the number of proteins and also the orientational order, increased on a similar timescale. While protein assembly often takes place in two steps – fast binding followed by a slower assembly process, the observation that the SFG signal was not lacking behind the surface tension kinetics indicated that *SynDLP* swiftly formed an ordered layer after lipid binding. The secondary and tertiary structures remained stable throughout the assembly process since the spectral shape of the amide I band did not change significantly. This indicated that *SynDLP* binds as a stable, folded unit which then quickly assembled into its final binding pose.

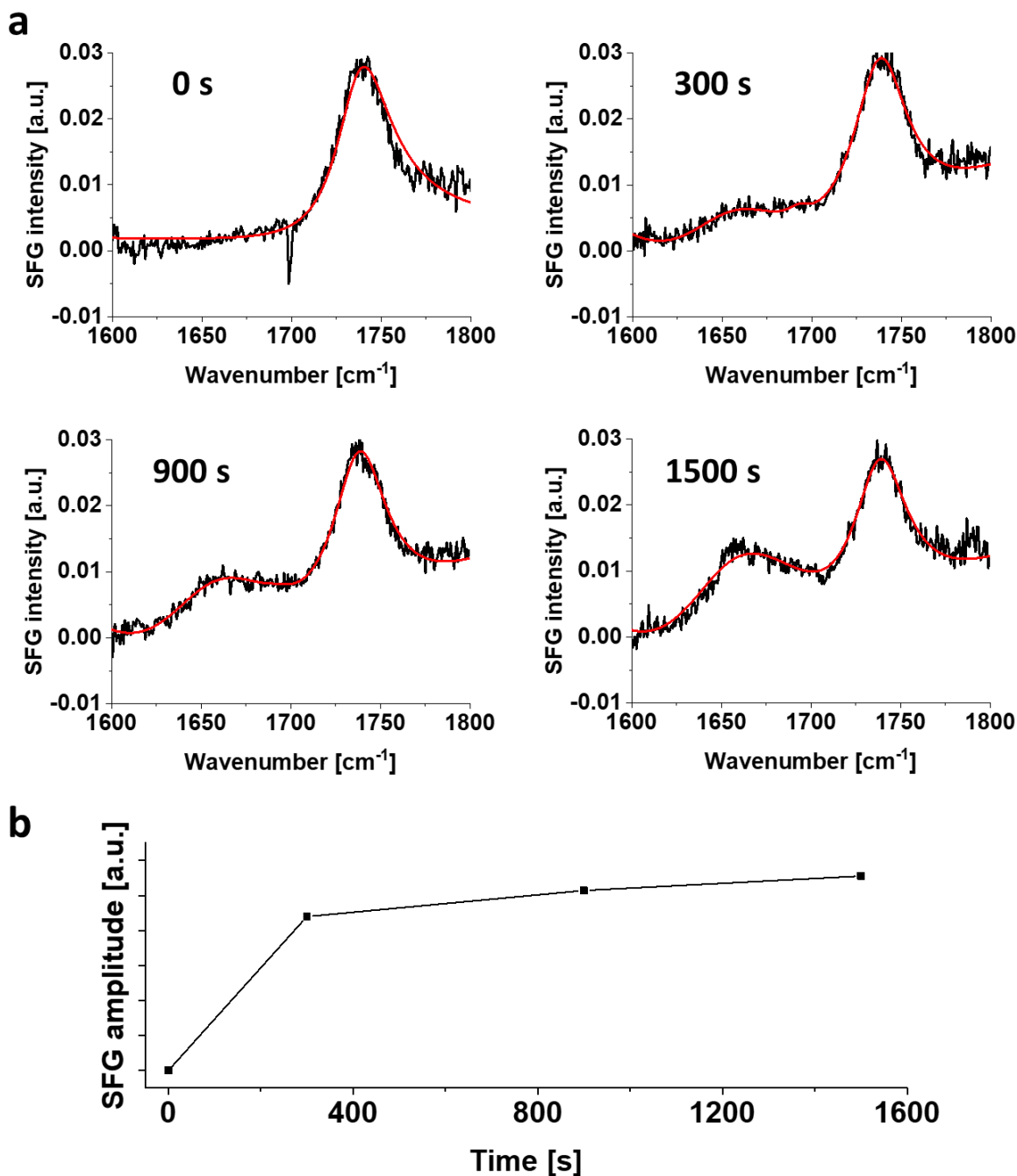


Figure 4.19: Time-dependent SFG spectra of *SynDLP* membrane binding.

(a) SFG amide I spectra (black) of *SynDLP* binding to a DMPG monolayer recorded at different times after the protein injection. Fits are shown as red lines. While the lipid C=O resonance remains almost constant, the protein amide I mode is growing over time. (b) SFG amplitude (black) of the helical component of the SFG peak fit plotted as a function of the time after injection.

As lipid-stimulation of the GTPase activity is a characteristic feature of many (eukaryotic) DLPs (Daumke and Praefcke, 2016), we investigated the interplay between *SynDLP*, PG lipids and GTP. SFG spectra of *SynDLP* bound to a DMPG monolayer with GTP present in solution

(Fig. 4.20) showed that, while the overall amide I signal was somewhat lower than what has been observed without GTP, the spectral shape remained unchanged. Ostensibly, the conformation of *SynDLP* did not respond strongly to the presence of GTP.

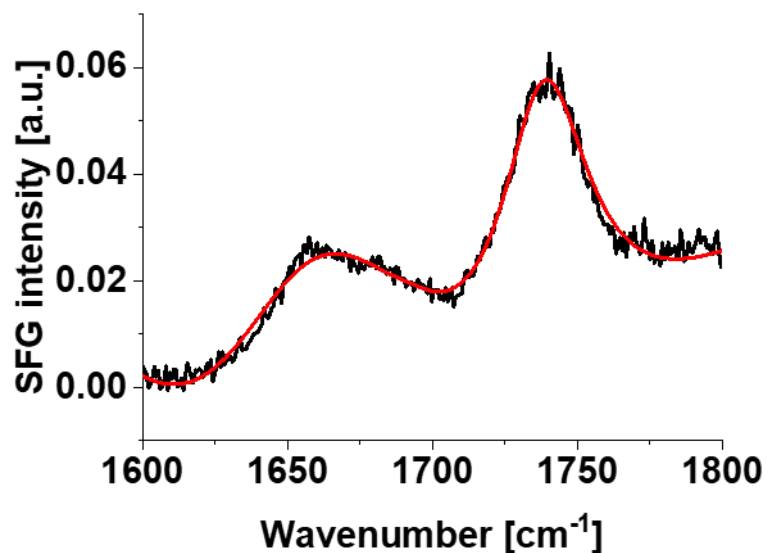


Figure 4.20: SFG spectrum of membrane-bound *SynDLP* with GTP.

SFG amide I spectrum of *SynDLP* bound to a DMPG monolayer in the presence of GTP in solution (black). A fit is displayed as a red line.

We then determined the *SynDLP* GTPase activity in the presence of DOPG LUVs (Fig. 4.21). Yet, unlike many other DLPs, the GTPase activity of *SynDLP* was not stimulated by membrane binding. As the inclusion of 5 mM MgCl_2 in the GTPase assay might lead to clustering of the lipid head groups and, thus, prevent lipid-stimulated GTPase activity, a measurement was additionally performed in the presence of only 0.5 mM $\text{MgCl}_2 \pm$ DOPG LUVs (Fig. 4.12d). Under these conditions, the GTPase activity in the presence of liposomes was slightly increased. Yet, the extent is not comparable to lipid-stimulated GTPase activity observed, *e.g.*, for dynamin (Stowell *et al.*, 1999).

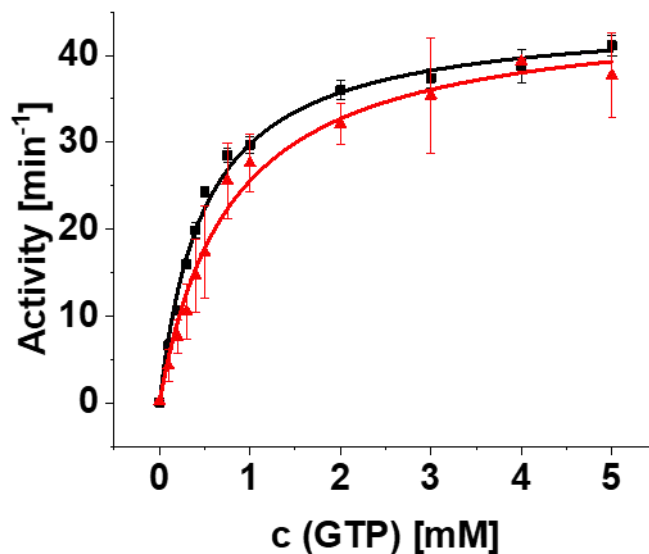


Figure 4.21: Lipid-stimulation of the *SynDLP* GTPase activity.

SynDLP GTPase activities in the presence and absence of LUVs were determined in a continuous, regenerative, coupled assay. Comparison of *SynDLP* under standard measurement conditions (black) and with 50 μM DOPG LUVs (dissolved in reaction buffer, extrusion to 100 nm) added with the assay components (red). Mean of independent experiments ($n = 3$) and error bars (S.D.) are shown. Data points were fitted using the Michaelis-Menten equation (Equation (3)). Fit curves are shown as lines.

SynDLP remodels membranes in vitro

Finally, we tested a putative membrane remodeling activity of *SynDLP*. While, in several cases, the formation of membrane tubes has been observed upon the addition of a DLP to lipids, we did not yet succeed in observing the formation of such structures. However, TM-mimicking LUVs were incubated with *SynDLP* and their size distribution was analyzed via dynamic light scattering (DLS) and compared to protein and LUVs alone (Fig. 4.22a). The LUVs were extruded to 100 nm and showed a signal at the expected size (Fig. 4.22a, black). *SynDLP* alone showed two broad peaks suggesting fractions of smaller and larger assemblies (Fig. 4.22a, red). Yet, the mixture of protein and LUVs showed a prominent peak at higher sizes, indicating the formation of protein-LUV-complexes with fused and/or clustered liposomes. Based on this information, *SynDLP*-triggered membrane fusion was next analyzed with a FRET-based assay using fluorescently labeled MGDG/DOPG LUVs. Fusion of labeled and unlabeled LUVs resulted in an increasing donor fluorescence, since the FRET donor and acceptor are diluted. As simple liposome tethering is not expected to significantly alter the mean distance between the FRET donor and acceptor, this measurement allowed monitoring the kinetics of membrane fusion events. IM30 of *Synechocystis* sp. PCC 6803, a protein with a pronounced fusogenic activity (Hennig *et al.*, 2015), was used as a positive control (Fig. A6). When isolated *SynDLP*

wt was mixed with labeled LUVs, the donor fluorescence increased over time, and the increase in donor fluorescence strongly depended on the *SynDLP* concentration (Fig. 4.22b, c). Conclusively, we observed a potential fusion activity of *SynDLP*, as has been observed previously also for other BDLPs (Bürmann *et al.*, 2011; Sawant *et al.*, 2016; Liu, Noel and Low, 2018).

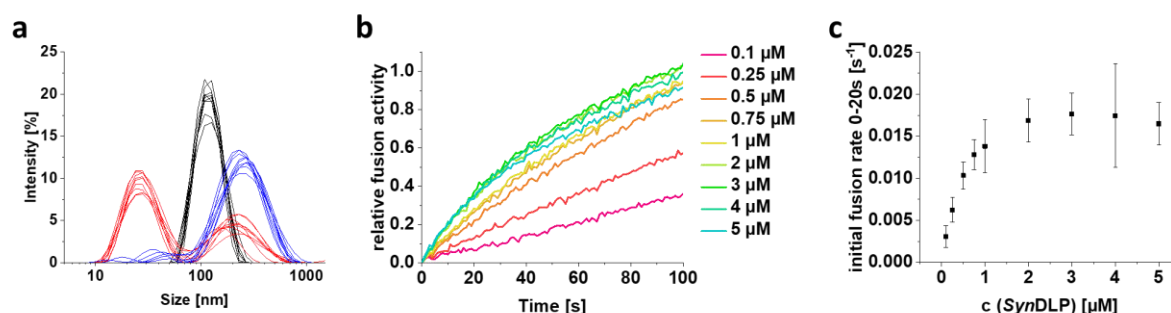


Figure 4.22: Membrane fusion activity of *SynDLP*.

(a) Size distribution of protein and LUVs was analyzed using DLS and relative intensities of the respective sizes are shown. MGDG/DOPG (60%/40%, w/w) LUVs (black), *SynDLP* (red) or a mixture of LUVs and *SynDLP* (blue) were incubated in reaction buffer and measured. From each condition the size distribution of three independent measurements (+ three technical replicates of each measurement) are shown. (b) Fusion of MGDG/DOPG (60%/40%, w/w) LUVs was measured in the presence of increasing *SynDLP* concentrations using a FRET-based fusion assay. Curves showing the donor fluorescence over the first 100 s after mixing LUVs with protein. The relative fusion activities were calculated as described in the methods section. The curves represent the mean of three independent measurements. The whole measurement as well as the positive control containing 2 μM of the fusogenic protein IM30 are shown in Fig. A6. (c) Initial fusion rates (black) were calculated from the curves in (b) defined as the slope of a linear regression of the first 20 s. Mean of independent measurements ($n = 3$) and error bars (S.D.) are shown.

The two investigated mutants *SynDLP*_{C777A} and *SynDLP*_{HPRN-AAAA} also showed an increased donor fluorescence, yet in case of the assembly-defect *SynDLP*_{HPRN-AAAA} mutant with a lower efficiency (Fig. 4.23). Interestingly, the addition of GTP had no impact on the fusogenic activity of *SynDLP* wt (Fig. 4.24). Noteworthy, the here observed membrane fusion activity of *SynDLP* might, in the end, indicate a membrane destabilizing activity, which results in liposome fusion *in vitro*. The exact membrane activity of *SynDLP* will be analyzed with complementing methods in future experiments.

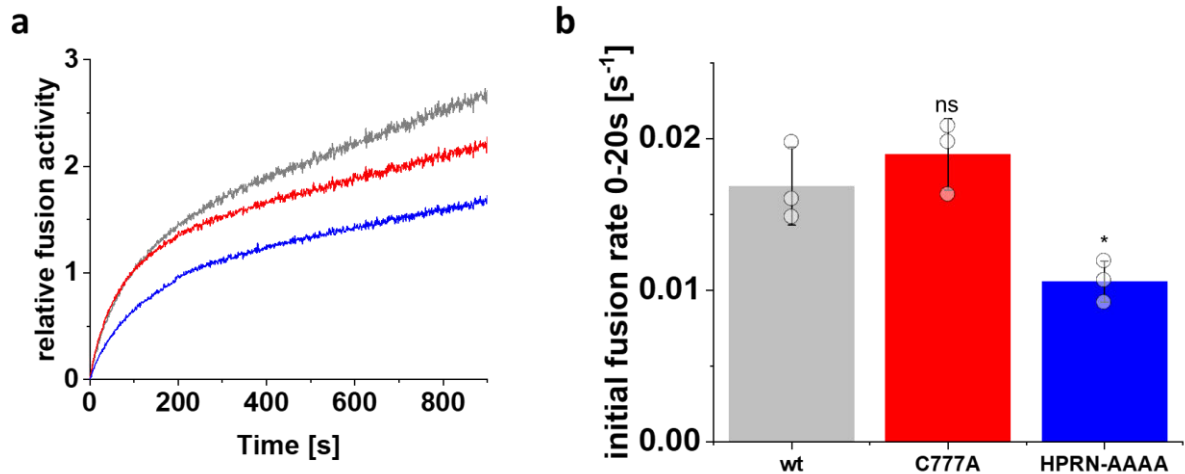


Figure 4.23: Membrane fusion activity of *SynDLP* variants.

Fusion of MGDG/DOPG (60%/40%, *w/w*) LUVs was measured in a FRET-based fusion assay. (a) Comparison of the fusion curves using 2 μ M *SynDLP* wt (gray), *SynDLP*_{C777A} (red) or *SynDLP*_{HPRN-AAAA}, respectively (blue). Calculation of the relative fusion activities is described in the methods section. The curves represent mean of independent measurements ($n = 3$). (b) From the fusion curves in (a) initial fusion rates were defined as the slope of a linear regression of the first 20 s. Mean of three measurements and error bars (S.D.) are shown and compared to the wt. Single measurements are displayed as circles. ns = not significant ($P > 0.05$), * $P < 0.05$, ** $P < 0.01$, *** $P < 0.001$ based on a two-sided unpaired Student's t-test. The initial fusion rate of the wt is compared to *SynDLP*_{C777A} ($P = 0.36$) or *SynDLP*_{HPRN-AAAA} ($P = 0.02$), respectively. Colors as in (a).

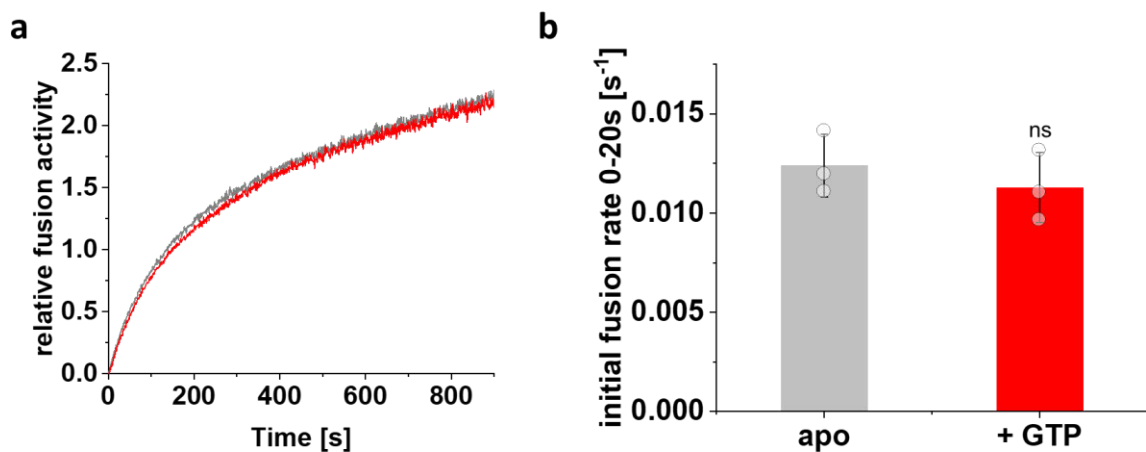


Figure 4.24: Influence of GTP on the membrane fusion activity.

In a FRET-based assay, fusion of MGDG/DOPG (60%/40%, *w/w*) LUVs was measured. (a) Fusion curves determined with 2 μ M *SynDLP* in the absence (gray) or presence of 1 mM GTP (red). The measurements with GTP were performed with 7 mM MgCl₂ (instead of 5 mM MgCl₂) to compensate for nucleotide addition. Moreover, for the calculation of the relative fusion activities (described in method section) an additional negative control including 1 mM GTP and 7 mM MgCl₂ was measured for the sample with GTP. Mean of three independent measurements is shown. (b) Initial fusion rates were calculated via taking the slope from a linear regression of the first 20 s of the fusion curves shown in (a). Mean of independent experiments ($n = 3$) and S.D. are displayed. Single measurements are shown as circles. ns = not significant ($P > 0.05$), * $P < 0.05$, ** $P < 0.01$, *** $P < 0.001$ based on a two-sided unpaired Student's t-test. Coloring is the same as in (a).

4.1.5 Discussion

Biogenesis, maintenance and dynamic rearrangement of cyanobacterial TMs are still not understood on the molecular level. In recent years, some proteins have been identified as being involved in the formation of highly curved membrane regions, in membrane fusion and/or membrane repair. One of the currently best-characterized proteins is IM30 (also known as VIPP1), a bacterial homolog of the ESCRT-III core subunit of the eukaryotic ESCRT complex (Gupta *et al.*, 2021; J. Liu *et al.*, 2021; Junglas *et al.*, 2021). In recent years, several homologs of previously assumed typical eukaryotic proteins involved in membrane dynamics have been identified in bacteria, indicating that processes, which were believed to be of eukaryotic origin, have, in fact, evolved in prokaryotes. Yet, these proteins might fulfill different functions in pro- vs. eukaryotes (Siebenaller and Schneider, 2023).

Cyanobacteria contain several putative genes encoding DLPs, which can be grouped into different clades depending on their genetic context. *E.g.*, in the KGK clade of cyanobacterial DLPs typically a protein containing a KGK domain is encoded downstream of the DLP (Jilly *et al.*, 2018). *SynDLP*, a member of this clade, has recently been identified as a cyanobacterial DLP, and the involvement of *SynDLP* in TM dynamics has been suggested (Jilly *et al.*, 2018). Isolated *SynDLP* forms oligomers of ~40-50 molecules in solution in the absence of nucleotides and/or membranes (Fig. 4.3a, b). Nucleotide- and membrane-independent oligomerization has been reported for eukaryotic DLPs, such as dynamin (Hinshaw and Schmid, 1995). However, this is a unique feature not described in the field of bacterial DLPs thus far (Low and Löwe, 2006; Bürmann *et al.*, 2011; Michie *et al.*, 2014; Liu, Noel and Low, 2018; Wang *et al.*, 2019). Typically, DLPs oligomerize upon nucleotide-binding or upon binding to membrane surfaces (Daumke and Praefcke, 2016), and EM micrographs of the here observed *SynDLP* oligomers (Fig. 4.3b) looked, in fact, very similar to lipid-free oligomers formed by human Drp1 in the presence of GTP (Kalia *et al.*, 2018). However, in contrast to Drp1, *SynDLP* oligomers assemble already in the absence of nucleotides. Within the *SynDLP* oligomer, individual monomers interact via ionic, polar and hydrophobic interactions, similar to what has been observed in other DLP assemblies (Gao *et al.*, 2010; Reubold *et al.*, 2015; Kalia *et al.*, 2018). Based on the *SynDLP* oligomer structure, defined oligomerization interfaces can be assigned in the stalk region (Fig. 4.7). These include interface 2, which mediates the formation of a stable dimeric unit, and interfaces 1 and 3, both critical for assembly of higher-order oligomers (Gao *et al.*, 2010; Reubold *et al.*, 2015). Noteworthy, in contrast to other BDLP structures, such as the structure of *NpBDLP* that is most closely related to *fusion DLPs* (Low and Löwe, 2006;

Low *et al.*, 2009), the here presented *SynDLP* oligomer structure resembles a *fission DLP* structure, similar to classical eukaryotic dynamin or Drp1 (Reubold *et al.*, 2015; Kalia *et al.*, 2018), that has not been observed in bacteria before. Detailed structural comparisons between *SynDLP* and bacterial and eukaryotic DLPs demonstrate a close relationship between *SynDLP* and eukaryotic representatives, indicating *SynDLP* being the closest known bacterial ancestor of eukaryotic dynamin, Drps and Mx proteins (Figs. 4.8, 4.9c, 4.10).

An intramolecular disulfide bridge, which stabilizes the BSE domain, is observed in the *SynDLP* structure (Fig. 4.11a). When the formation of the disulfide bridge was eliminated by replacing C777 with alanine, the resulting protein *SynDLP*_{C777A} was correctly folded and still formed oligomers, yet, its thermodynamic stability, as well as GTPase activity, were significantly reduced (Fig. 4.11c-g, Tables 4.3, 4.4), albeit the mutation does not directly affect the active site. This indicated an impact of the BSE domain on the *SynDLP* GTPase activity. Stabilization of the BSE helix bundle via the formation of an intramolecular disulfide bridge is a concept that has not been described before, and thus far an intramolecular disulfide bridge has solely been observed in the membrane-interacting domain (paddle domain) of the eukaryotic DLP *CtMgm1* (Faelber *et al.*, 2019). Interestingly, the two cysteine residues involved in disulfide bridge formation in *SynDLP* are conserved across the cyanobacterial KGK clade DLPs (Fig. 4.25). Thus, it can be assumed that a disulfide bridge-stabilized BSE domain is a general feature observable in this clade of cyanobacterial DLPs. In fact, several proteins in the cyanobacterial cytoplasm contain disulfide bridges, and the (in part reversible) formation of disulfide bridges is mediated by the thioredoxin system (Florencio *et al.*, 2006; Lindahl and Kieselbach, 2009; Mallén-Ponce, Huertas and Florencio, 2022). Thus, it might even be possible that a reversible formation of the disulfide bridge in the BSE domain is involved in the regulation of the *SynDLP* activity. An extended function of the BSE domain in bacterial DLPs, in general, might be indicated by the observation that all thus far resolved BDLP structures, including the *SynDLP* structure described here (Fig. 4.3h), show a BSE domain consisting of a four-helix bundle (Low and Löwe, 2006; Michie *et al.*, 2014; Liu, Noel and Low, 2018; Wang *et al.*, 2019), whereas eukaryotic DLPs typically have a three-helix bundle BSE. However, albeit *SynDLP* has a four-helical BSE domain, structural alignments indicated a closer relationship to eukaryotic BSE domains (Fig. 4.10), again underlining *SynDLP*'s role as the closest known bacterial ancestor of eukaryotic DLPs.

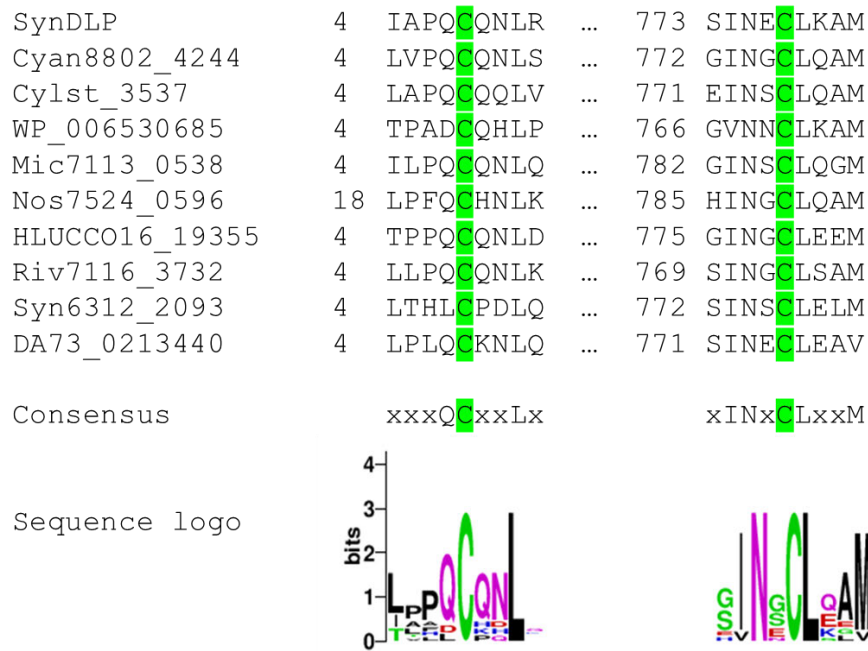


Figure 4.25: Disulfide forming cysteine residues are conserved within cyanobacterial KGK clade DLPs.

Sequence alignment of predicted cyanobacterial dynamin-like GTPases belonging to the KGK clade. The section shows the sequence context of *SynDLP* C8 and C777 residues both colored in green together with corresponding sequence regions of other cyanobacterial KGK clade DLPs. Cyan8802_4244 from *Cyanothece* sp. PCC 8802, Cylst_3537 from *Cylindrospermum stagnale* PCC 7417, WP_006530685 from *Gloeocapsa* sp. PCC 73106, Mic7113_0538 from *Microcoleus* sp. PCC 7113, Nos7524_0596 from *Nostoc* sp. PCC 7524, HLUCCO16_19355 from *Phormidium* sp. OSCR, Riv7116_3732 from *Rivularia* sp. PCC 7116, Syn6312_2093 from *Synechococcus* sp. PCC 6312, DA73_0213440 from *Tolypothrix bonteillei* VB521301.

For most eukaryotic DLPs, such as Dyn1, Drp1, OPA1, Vps1p, Sey1p or Mgm1p, and for BDLPs, like *NpBDLP* or *MsIniA*, basal GTPase activities were characterized by k_{cat} values in the range of $0.04 - 5 \text{ min}^{-1}$ (reviewed here (Jimah and Hinshaw, 2018)), which is lower than the here observed *SynDLP* turnover rate of $\sim 45 \text{ min}^{-1}$ (Table 4.4). However, the GTPase activity of DLPs is often linked to their oligomeric state, and the turnover rate of many DLPs substantially increases upon oligomerization, for example, on an appropriate lipid template (Daumke and Praefcke, 2016; Jimah and Hinshaw, 2018). Mechanistically, a helical DLP polymer forms on the membrane via defined oligomerization contacts in the stalk, followed by the dimerization of GDs from adjacent rungs. This transverse GD-GD interface leads to the stabilization of critical GD residues and finally assembly-stimulated GTPase activity (Ghosh *et al.*, 2006; Chappie *et al.*, 2010; Kong *et al.*, 2018). As mentioned earlier, *SynDLP* forms stable oligomers already in the absence of nucleotides and/or membranes (Fig. 4.3a, b), and putatively oligomerization stimulates its GTPase activity resulting in the measured high basal GTPase activity. Thus, it was reasonable to assume that GD interactions within the *SynDLP* oligomer

stabilize the enzymatic GTPase core, as observed for other DLPs (Chappie *et al.*, 2010; Rennie *et al.*, 2014; Cao *et al.*, 2017). Yet, the determined cryo-EM structure of *SynDLP* did not indicate transverse contacts between GDs of adjacent monomers. Thus, longitudinal GD contacts within the oligomer might stimulate the *SynDLP*'s GTPase activity. The structure of the *SynDLP* oligomers revealed only a small interface between adjacent GDs, whereas a large area of the GD of monomer 1 contacts the BSE1 domain of monomer 2 (Figs. 4.8b, 4.26). The GD-BSE1 contact area is significantly expanded when compared to similar DLP assemblies (Reubold *et al.*, 2015; Kalia *et al.*, 2018) (Fig. 4.8b). Thus, we next analyzed the impact of these contacts on the *SynDLP*'s GTPase activity. A straight-forward mutational approach by substituting the respective contact residues in the GD was not possible, as the residues could not be unequivocally identified in the oligomer structure due to the intermediate resolution of the GD. While we created a mutant where eleven residues in the BSE1 (R12, N16, E20, R23, P26, S30, D33, S35, E38, G42, L45) that contact the GD were replaced, the resulting protein was prone to aggregation and not suitable for subsequent analyses. Therefore, we aimed to analyze an assembly-impaired *SynDLP* variant (*SynDLP*_{HPRN-AAAA}) to reduce the formation of longitudinal GD-GD and BSE1-GD interactions. Isolated *SynDLP*_{HPRN-AAAA} showed lowered thermodynamic stability (Fig. 4.15d, e, Table 4.3) and was predominantly dimeric (Fig. 4.15c). Thus, the mutant protein likely did not establish any lateral contacts to adjacent monomers anymore that involve the GD, which potentially increases the *SynDLP* GTPase activity. The turnover rate of the mutant protein was reduced by ~60% compared to *SynDLP* wt (Fig. 4.15f, Table 4.4). Thus, we propose that uncommon longitudinal interactions between GDs and interactions between the GD and the BSE1 established in the *SynDLP* oligomers result in the observed high basal GTPase activity. This assumption is further supported by the observation that the disulfide bridge stabilizes the BSE domain, which affects the GTPase activity as described above. Taken together, while intramolecular GD-BSE1 interactions are described for other DLPs (Faelber *et al.*, 2011; Reubold *et al.*, 2015), the *SynDLP* structure and the analysis of an assembly-defective mutant indicate an additional role of the BSE domain for GTPase activation. It remains to be shown how *SynDLP* oligomerization and futile GTP hydrolysis might be prevented *in vivo*, likely by accessory proteins.

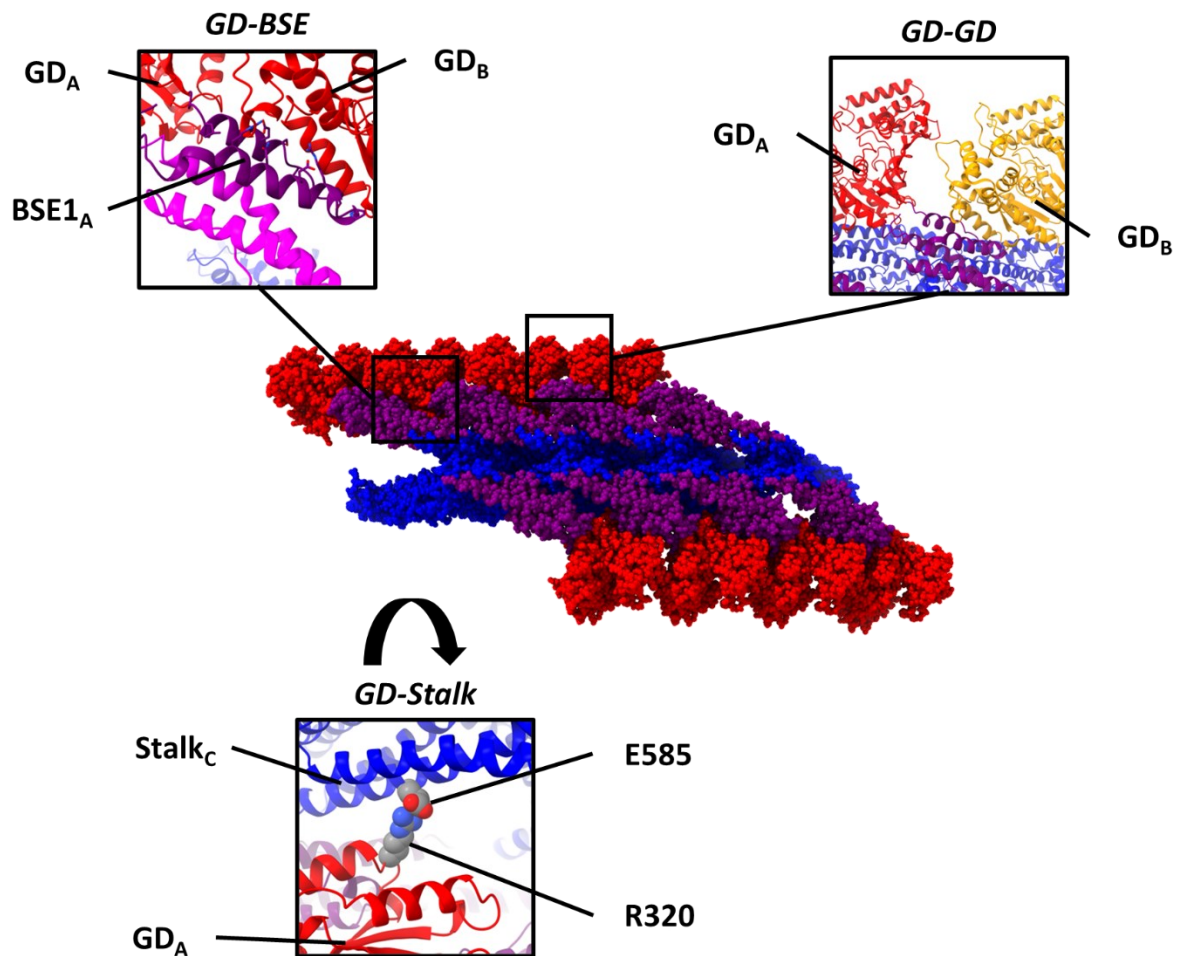


Figure 4.26: Intermolecular domain contacts in the *SynDLP* oligomer.

Structure of a *SynDLP* oligomer is shown in the center. GD, BSE and stalk are colored red, violet and blue, respectively. The three sections zoom areas of contacts of one GD with another polypeptide chain, either between the GD and the BSE domain (GD-BSE; BSE1 colored in purple, BSE2 and BSE3 in magenta; contact residues from the BSE1 domain shown as sticks), between two GDs (GD-GD; GD_A and GD_B colored in red and orange, respectively) or between the GD and the stalk domain (GD-stalk; residues mediating GD-stalk contacts (R320 and E585) are shown as spheres and colored by element).

As DLPs are generally membrane-active, *SynDLP* was proposed to be a peripherally membrane-attached protein. *SynDLP* specifically interacts with negatively charged TM lipids (Fig. 4.16). Interaction with lipids containing a negatively charged headgroup is well-described for other DLPs, such as eukaryotic Drp1 and dynamin, as well as bacterial *BsDyna* and *MsIniA* (Tuma, Stachniak and Collins, 1993; Bustillo-Zabalbeitia *et al.*, 2014; Guo and Bramkamp, 2019; Wang *et al.*, 2019). A common feature of many DLPs is their ability to tubulate liposomes *in vitro*, which illustrates their membrane remodeling capabilities (Accola *et al.*, 2002; Low and Löwe, 2006; Muriel *et al.*, 2009; Liu, Noel and Low, 2018). Yet, we did not succeed to observe *SynDLP*-induced liposome tubulation under the tested experimental conditions. However, *SynDLP* appeared to be capable of fusing liposomes *in vitro* in a nucleotide-independent

process (Fig. 4.22, Fig. A6), albeit the *SynDLP* oligomer structure resembles structural elements typically observed in *fission DLP* structures, as discussed above. The molecular mechanism of DLP-mediated membrane activity still is largely enigmatic. Yet, *SynDLP* interaction with liposomes may result in membrane destabilization, a process needed for both membrane fusion as well as fission. A membrane destabilizing activity is well conceivable due to the observation that *SynDLP* not only binds to but intercalates into PG containing membranes (Fig. 4.16c), which induces perturbations in the lipid structure. Such a disruption of the lipid bilayer structural integrity is also proposed to play a role in atlastin-mediated membrane fusion caused by a C-terminal amphipathic helix (Liu *et al.*, 2012). Like *SynDLP*, *BsDynA* was shown to fuse membranes in absence of nucleotides, at least *in vitro*, and also in case of *BsDynA*, liposome tubulation has not been observed thus far (Bürmann *et al.*, 2011). Recently, an involvement of *BsDynA* in membrane repair after phage infection has been suggested (Guo *et al.*, 2022), and it appears reasonable to assume an involvement of *SynDLP* in membrane repair processes caused by phage infection or other environmental stresses acting on membranes. However, phages infecting *Synechocystis* sp. PCC 6803 cells are not identified yet, and thus, the exact physiological activity of *SynDLP* has to be analyzed in future *in vivo* studies. Potentially, *SynDLP* is involved in the repair of membranes damaged due to the photosynthetic light reaction, *e.g.*, via vesicle patching or budding.

Also, the exact impact of GTP hydrolysis on the physiological *SynDLP* function currently remains open. Looking at the structure of a *SynDLP* monomer (Fig. 4.3h), the connection between stalk and BSE (hinge 1) seems to be rather rigid, whereas hinge 2 consists of flexible loops with conserved proline residues (P47 and P441) known to facilitate a rotation of the BSE towards the GD (Faelber *et al.*, 2011; Anand, Eschenburg and Reubold, 2016). The presented *SynDLP* structure in the apo state shows an ‘open’ BSE conformation. A ‘closed’ BSE conformation in *SynDLP*, which potentially is an intermediate in a GTP hydrolysis cycle, might be observable in structures with bound ligands. The conversion of the ‘open’ to the ‘closed’ conformation is thought to act as a power stroke in membrane remodeling processes (Daumke and Praefcke, 2016). Interestingly, the *in vitro* membrane activity of *SynDLP* appeared to be nucleotide-independent (Figs. 4.22, 4.24).

Taken together, the recently predicted cyanobacterial DLP of *Synechocystis* sp. PCC 6803 (*SynDLP*) is a *bona fide* member of the dynamin superfamily as classified by activity and structure. *SynDLP* is an active GTPase that forms oligomers in solution. The *SynDLP* cryo-EM structure revealed folding and oligomerization interfaces known from several eukaryotic *fission*

DLPs in a BDLP and, thus, *SynDLP* potentially represents a bacterial ancestor of eukaryotic *DLPs*. Furthermore, unique *DLP* features, such as an intramolecular disulfide bridge in the BSE domain that affected the thermodynamic stability plus the GTPase activity of *SynDLP*, and an expanded intermolecular GD-BSE interface were identified in the cryo-EM structure. The presence of such GD interfaces in *SynDLP* oligomers illustrates a distinctive concept for regulating the basal GTPase activity and would, thus, indicate a so far unique role of the BSE domain in a *DLP*. *SynDLP* interacted with negatively charged TM lipids and intercalated into a DMPG monolayer. The classification of *SynDLP* into *fusion* vs. *fission DLPs* is of higher complexity as it showed a membrane destabilizing activity, resulting in liposome fusion *in vitro*, albeit the structure of the *SynDLP* oligomer resembles elements typically observed in *fission DLPs*. Future studies will address the exact mechanism of membrane binding and remodeling including the identification of the membrane binding site, the role of nucleotide binding and hydrolysis, and the *in vivo* function of *SynDLP* in the cyanobacterium.

4.2 Effect of NaCl and DTT on oligomerization and activity of *SynDLP*

4.2.1 Introduction

DLPs are large mechanochemical enzymes that hydrolyze GTP (Praefcke & McMahon, 2004). The monomers typically have a molecular mass of >60 kDa and can further oligomerize triggered by an appropriate environment (Jimah and Hinshaw, 2018; Ford and Chappie, 2019). *E.g.*, the buffer conditions, nucleotide binding or binding to membrane templates regulate the oligomeric state of many DLPs. DLP oligomerization, in turn, regulates the proteins' GTPase activity (Tuma, Stachniak and Collins, 1993; Warnock, Hinshaw and Schmid, 1996; Kochs *et al.*, 2002; Low *et al.*, 2009; Bohuszewicz and Low, 2018; Kalia *et al.*, 2018). The mechanism of the assembly-stimulated GTPase activity has been elucidated on a structural level. After oligomerization of a DLP, typically on an appropriate membrane template, intermolecular GD-GD contacts are established and auto-inhibitory GD-MID contacts are released, which allows easier access of the substrate to the active site plus stabilizes the conformation of flexible GD switch regions that are critical for GTP hydrolysis (Gasper *et al.*, 2009; Chappie *et al.*, 2010; Reubold *et al.*, 2015; Ford and Chappie, 2019).

As already discussed, the oligomeric state and, thus, the GTPase activity of DLPs is not only regulated by membranes, but also by the buffer composition. *E.g.*, dynamin forms larger oligomers at lower NaCl concentrations (in the absence of membranes). The formation of such larger oligomers correlates with an increased GTPase activity (Warnock, Hinshaw and Schmid, 1996). In addition, reducing agents like DTT or β -mercaptoethanol are often ingredients of buffers used for the purification and/or assaying the GTPase activity of DLPs (Warnock, Hinshaw and Schmid, 1996; Bürmann *et al.*, 2011; Ford, Jenni and Nunnari, 2011; Kravets *et al.*, 2012; Fröhlich *et al.*, 2013; Bohuszewicz and Low, 2018; Liu, Noel and Low, 2018). It has been reported for some DLPs that the presence of DTT ensures a stable and active GTPase function of the enzymes (Leonard *et al.*, 2005; Meglei and McQuibban, 2009).

It was already shown that *SynDLP*, the BDLP of *Synechocystis*, forms large oligomers in solution without externally added membranes and/or nucleotides (Chapter 4.1, Fig. 4.3) (Gewehr *et al.*, 2023). The oligomerization behavior as well as the GTPase activity of *SynDLP* depend on the salt concentrations (Chapter 4.1, Figs. 4.5, 4.12b). Furthermore, *SynDLP* forms an intramolecular disulfide bridge that can be reduced by the addition of DTT (Chapter 4.1, Fig. 4.11a, b) (Jilly, 2018; Gewehr *et al.*, 2023). The effect of salts, especially NaCl, and of the reducing agent DTT on *SynDLP*'s oligomerization, thermodynamic stability and GTPase

activity were investigated in more detail to optimize the storage and assay conditions of *SynDLP*. The cryo-EM structure of *SynDLP* oligomers reveals the presence of an intermolecular salt bridge between the GD and the stalk domain (Chapter 4.1, Fig. 4.26) (Gewehr *et al.*, 2023). A mutant lacking this salt bridge was created and characterized to some extent to identify a putative regulating role of such a GD-stalk connection.

4.2.2 Results

DTT influences the assembly and GTPase activity of SynDLP

SynDLP forms an intramolecular disulfide bridge that can be reduced by the reducing agent DTT at concentrations >10 mM (Chapter 4.1, Fig. 4.11b) (Gewehr *et al.*, 2023). The monomer with an intact disulfide bridge migrates at approx. 180 kDa in an SDS-PAGE analysis and at approx. 100 kDa in the reduced state. However, purification of *SynDLP* in complete absence of DTT revealed a diffuse band pattern in a non-reducing SDS-PAGE analysis (Fig. 4.27a, left gel). Addition of 0.1 mM DTT restored the band pattern of one distinct band at approx. 180 kDa (Fig. 4.27a, right gel). Therefore, the effect of DTT on the biochemical properties of *SynDLP* was analyzed in more detail. Analytical SEC showed a shift of *SynDLP* assemblies to larger structures in the complete absence of DTT (Fig. 4.27b). The thermal stability of *SynDLP* oligomers was monitored using CD spectroscopy. Thermal denaturation of *SynDLP* in the absence or presence of 10 mM DTT, respectively, revealed no significant impact of the reducing agent on the protein's thermal stability (Fig. 4.27c, Table 4.5). *SynDLP* shows a decreased solubility at high protein concentrations in salt-containing buffers, *e.g.*, reaction buffer, probably due to aggregation. The protein aggregation kinetic was measured via elastic light scattering in a fluorimeter. *SynDLP* aggregation was observed as an increased elastic light scattering intensity over time (Fig. 4.27d, black). Interestingly, the addition of 10 mM DTT clearly reduced the formation of *SynDLP* aggregates in the salt-containing buffer (Fig. 4.27d, red). Next, the GTPase activity of *SynDLP* was measured either under standard conditions in the presence of 0.2 mM DTT (Fig. 4.27e, red) or without DTT (Fig. 4.27e, black). The absence of DTT had a significant impact on the shape of the Michaelis-Menten curve plus the maximum activity reached only about 60% compared to the measurement in presence of DTT. Additionally, the K_m value was considerably lowered in absence of DTT (Fig. 4.27e, Table 4.5).

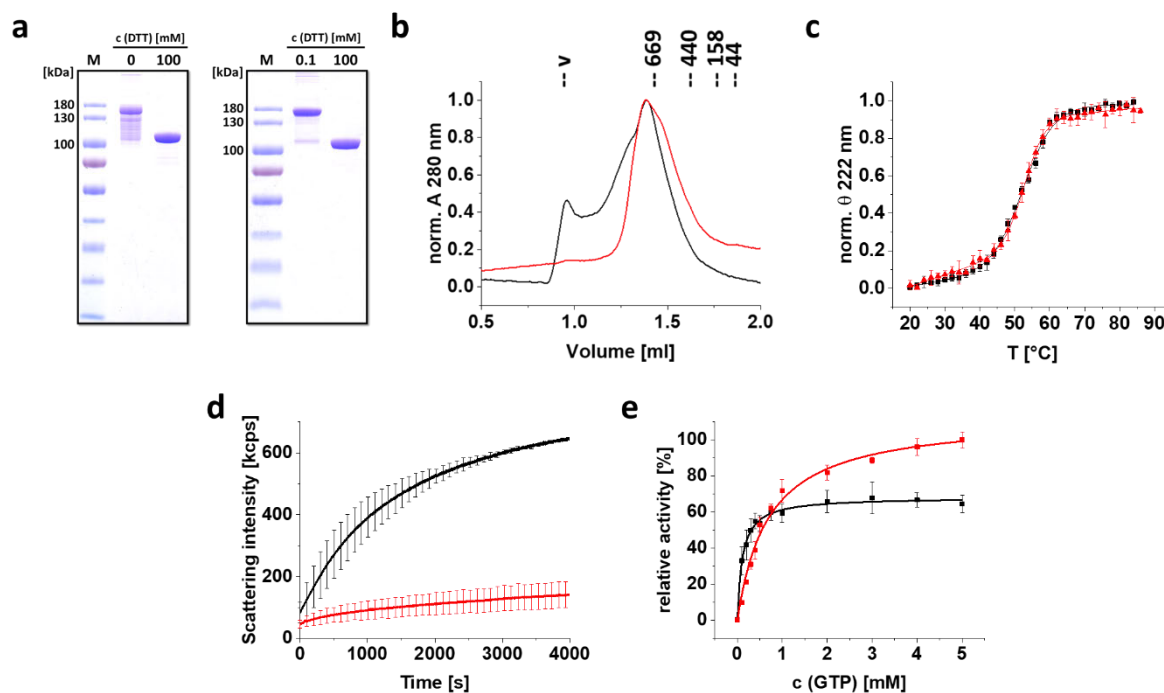


Figure 4.27: Effect of DTT on assembly and GTPase activity of *SynDLP*.

(a) SDS-PAGE analysis of *SynDLP* purified and stored without DTT. The SDS-PAGE samples were boiled in the presence of different DTT concentrations. M = marker. (b) Analytical SEC of *SynDLP* from the same purification (DTT-free buffers). A SuperoseTM 6 Increase 3.2/300 column was equilibrated with 20 mM HEPES buffer pH 7.4, 150 mM NaCl, 7.5 mM KCl, 5 mM MgCl₂ containing either no DTT (black) or 10 mM DTT (red). Elution volumes of typical standard proteins plus the void volume (v) are indicated. (c) CD spectra of *SynDLP* wt in absence (black) or presence of 10 mM DTT (red) were monitored at increasing temperatures in 10 mM HEPES buffer pH 7.4. The measured ellipticities at 222 nm were plotted against the temperature, normalized, and fitted with an adapted Boltzmann fit (Equation (6)). Fit curves are shown as lines. The mean ($n = 3$) and error bars (standard deviation, S.D.) are shown. (d) Protein aggregation kinetics were monitored via elastic light scattering in a fluorimeter. 3.2 μ M *SynDLP* (purified and stored in DTT-free buffers) were measured in 20 mM HEPES buffer pH 7.4, 150 mM NaCl, 7.5 mM KCl, 5 mM MgCl₂ in the absence (black) or presence (red) of 10 mM DTT. Mean ($n = 3$) and error bars (S.D.) are shown. (e) Comparison of the GTPase activity of *SynDLP* stored as well as measured without DTT (black) and stored as well as measured with 0.2 mM DTT (red). The activity was determined with a continuous, regenerative, coupled assay. The mean ($n = 3$) and error bars (S.D.) are shown, and the data points were fitted using Equation (3). The maximum activity of *SynDLP* in the presence of 0.2 mM DTT was set to 100% to obtain relative GTPase activities.

Table 4.5: Parameters describing DTT-dependent properties of *SynDLP*. The values were obtained from experiments in Fig. 4.27.

	$T_{m, CD}$ [°C]	GTPase activity [%]	K_m [mM]
- DTT	52.5 ± 0.4	60.4 ± 0.8	0.11 ± 0.01
+ DTT	52.9 ± 0.2	100.0 ± 3.0	0.69 ± 0.06

Effect of NaCl on SynDLP

The oligomeric state and GTPase activity of DLPs is often very sensitive to the salt conditions (Praefcke and McMahon, 2004). Most experiments concerning the oligomerization and GTPase activity of *SynDLP* were performed in a salt-containing reaction buffer (150 mM NaCl, 7.5 mM KCl, 5 mM MgCl₂, 0.2 mM DTT, 20 mM HEPES buffer pH 7.4) (Chapter 4.1) (Gewehr *et al.*, 2023). The thermal stability of *SynDLP* oligomers in the presence and absence of salts was monitored using the fluorophore ANS as previously described (Chapter 4.1) (Gewehr *et al.*, 2023). The ANS-FTSA allows measuring under more complex buffer conditions (*e.g.*, higher concentrations of salts) compared to thermal denaturation reported via CD spectroscopy. In general, the ANS signal was increased in the presence of salts under reaction buffer conditions (Fig. 4.28a). Comparison of the melting temperatures revealed a slightly increased thermodynamic stability in the absence of salts (Fig. 4.28b, Table 4.6). Since the reaction buffer mainly contains 150 mM NaCl besides smaller amounts of the salts KCl and MgCl₂, the effect of NaCl was investigated in more detail. The influence of NaCl on the oligomerization of *SynDLP* was tested via analytical SEC. The molecular mass of the assemblies shifted slightly towards larger structures with decreasing NaCl concentrations (Fig. 4.28c). Under the same buffer conditions, the GTPase activity of *SynDLP* at varying NaCl concentrations was determined with a continuous, regenerative, coupled GTPase assay. Here, the maximum GTPase activity decreased by approx. 30% from 150 mM NaCl to no NaCl (Fig. 4.28d, Table 4.6). The K_m values did not significantly change.

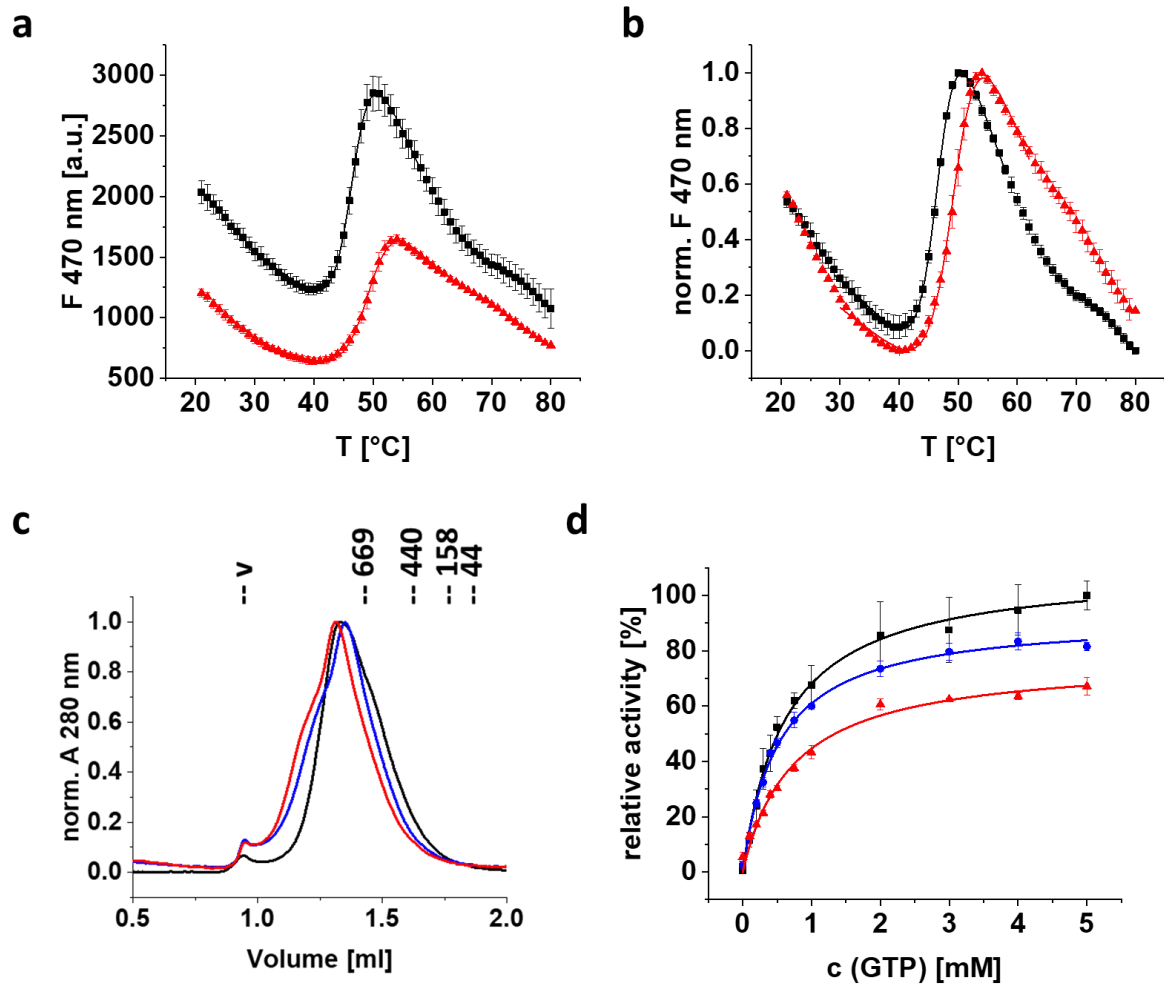


Figure 4.28: Influence of different salt concentrations on the thermal stability, oligomerization and GTPase activity of *SynDLP*.

(a) The thermal stability at different salt conditions was assessed via an ANS-FTSA measurement of *SynDLP* wt either in 20 mM HEPES buffer pH 7.4, 150 mM NaCl, 7.5 mM KCl, 5 mM MgCl₂, 0.2 mM DTT (black) or in 20 mM HEPES buffer pH 7.4, 0.2 mM DTT (red). Fluorescence intensities at 470 nm were plotted against the temperature and the temperature range that captures the transition phase was fitted with an adapted Boltzmann fit (Equation (7)). Fit curves are displayed as lines. Mean ($n = 3$) and error bars representing S.D. are shown. (b) The data points from the ANS-FTSA in (a) were normalized and fitted accordingly. For coloration and description of the statistics see (a). (c) Oligomerization of *SynDLP* was investigated using analytical SEC. A SuperoseTM 6 Increase 3.2/300 column was equilibrated with 20 mM HEPES buffer pH 7.4, 7.5 mM KCl, 5 mM MgCl₂ supplemented with 150 mM (black), 25 mM (blue) or 0 mM NaCl (red). The retention volumes of common standard proteins and the void volume (v) are indicated. (d) The GTPase activity was measured using a continuous, regenerative, coupled assay. The reaction mix was prepared containing 150 mM (black), 25 mM (blue) or no NaCl (red). Mean ($n = 3$) and S.D. are shown. Data points were fitted via Equation (3). For relative GTPase activities, the maximum activity in the presence of 150 mM NaCl was set to 100%.

Table 4.6: Parameters describing salt-dependent properties of *SynDLP*. The values were obtained from experiments in Fig. 4.28.

c (NaCl)	T _{m, ANS-FTSA} [°C]	GTPase activity [%]	K _m [mM]
150 mM	46.7 ± 0.1	100 ± 1.9	0.62 ± 0.04
25 mM	-	84.0 ± 1.4	0.52 ± 0.03
0 mM	49.4 ± 0.1	70.1 ± 2.3	0.73 ± 0.07

Influence of an intermolecular salt bridge between the GD and stalk domain

As already mentioned, intermolecular domain contacts crucially affect the GTPase activity of *SynDLP* (Gewehr *et al.*, 2023). In addition to the already described GD-GD and GD-BSE contacts, the *SynDLP* oligomer structure also revealed an intermolecular contact between the GD and the stalk domain provided by a salt bridge between R320 and E585 (Fig. 4.29, Fig. A7). A role of this salt bridge in the NaCl-dependent oligomerization and GTPase activity of *SynDLP* as previously shown (Chapter 4.1) is well conceivable. Therefore, the mutant *SynDLP*_{R320A-E585A} was created, in which both residues are substituted by an alanine to abolish the formation of the putative intermolecular GD-stalk salt bridge.

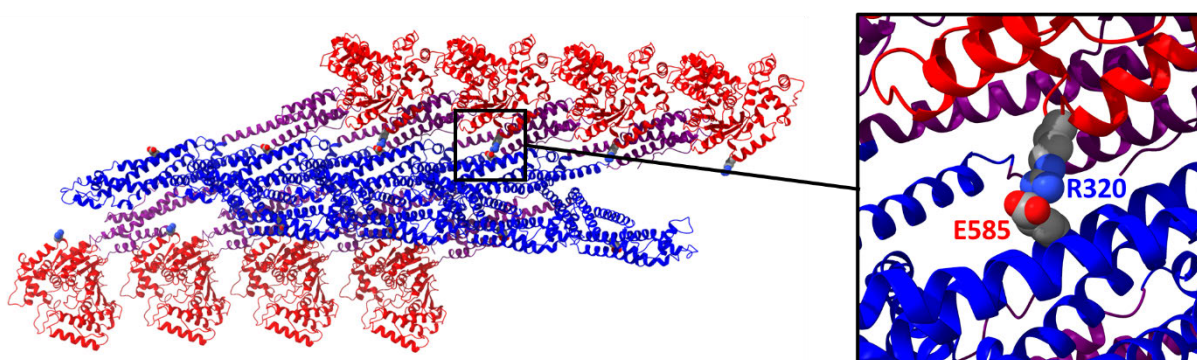


Figure 4.29: Localization of an intermolecular salt bridge between GD and the stalk in the *SynDLP* structure.

Ribbon representation of the *SynDLP* oligomer structure (PDB: 7ZW6). GD, BSE and stalk colored in red, purple and blue, respectively. The zoomed area highlights the position of R320 and E585 (illustrated as spheres and colored by element) that form an intermolecular salt bridge between the GD and the stalk.

The *SynDLP*_{R320A-E585A} mutant was expressed and purified as described for *SynDLP* wt (Chapter 4.1) (Gewehr *et al.*, 2023), yielding a pure protein with an intact intermolecular disulfide bridge (Fig. 4.30a). CD spectra were recorded to evaluate the correct folding of the mutant. The wt-like shape of the CD spectrum indicated proper folding of *SynDLP*_{R320A-E585A} at least on the secondary structure level (Fig. 4.30b). The thermodynamic stability of the mutant protein was monitored using CD spectroscopy and an ANS-FTSA. Both methods showed only slight

differences in the thermal stability of *SynDLP*_{R320A-E585A} compared to *SynDLP* wt (Fig. 4.30c, d). Comparison of the T_m 's, however, revealed converse trends of the two methods. *SynDLP*_{R320A-E585A} had a decreased melting temperature determined by CD spectroscopy, but a slightly increased T_m in the ANS-FTSA (Table 4.7). The molecular mass of *SynDLP*_{R320A-E585A} was investigated using analytical SEC and revealed the presence of two dominant populations (Fig. 4.30e, red). One population formed very large oligomers/aggregates that even eluted in the void volume of the used column. The other population seemed to form structures having masses comparable to *SynDLP* wt (Fig. 4.30e, black). Finally, the GTPase activity of *SynDLP*_{R320A-E585A} was measured. The course of the curve differed from *SynDLP* wt, with the activity of the mutant being considerably increased at lower GTP concentrations (Fig. 4.30f). The data points of the mutant did not follow a typical Michaelis-Menten kinetic. Applying a fit via the Hill equation to the data points adequately displayed the measured data. However, the value for the resulting maximum GTPase activity and especially the extracted K_D value are not reliable due to the large errors (Table 4.7). A visual inspection of the unfitted data suggests similar maximum activity of *SynDLP*_{R320A-E585A} and *SynDLP* wt (Fig. 4.30f).

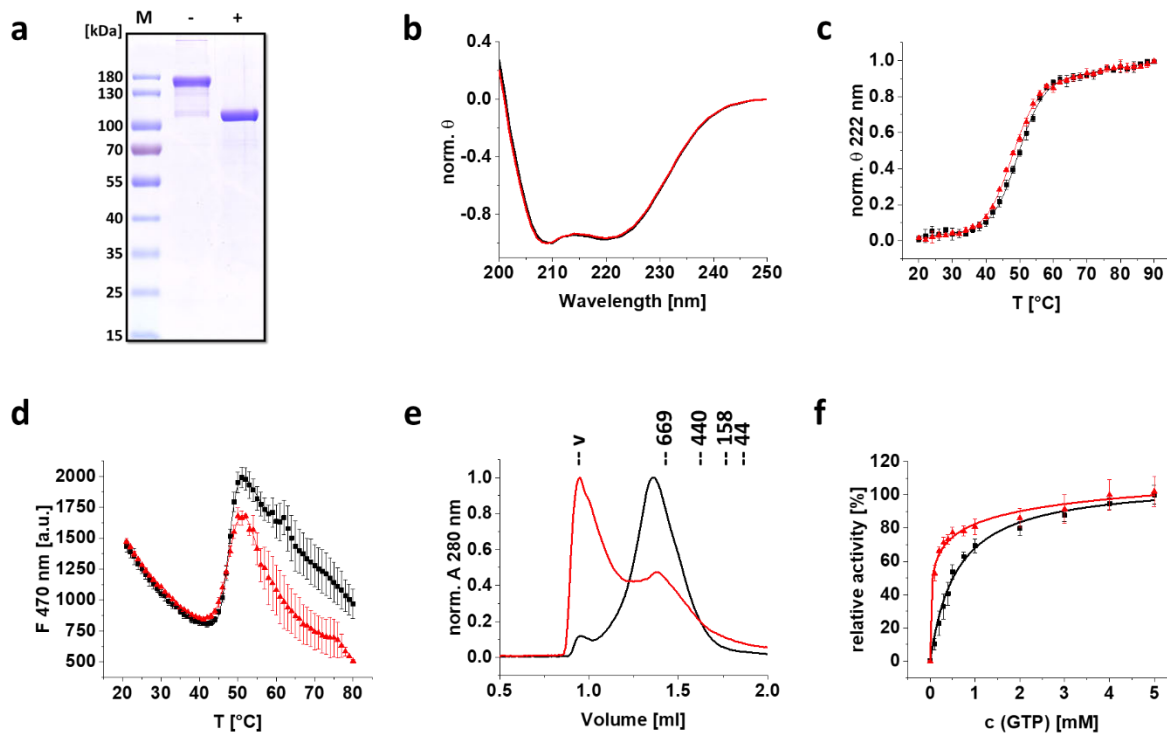


Figure 4.30: Biochemical characterization of *SynDLP*_{R320A-E585A}.

(a) SDS-PAGE analysis of purified *SynDLP*_{R320A-E585A} in the presence of 0.1 mM DTT (lane -) or 100 mM DTT (lane +). The calculated molecular mass of the protein is 93 kDa. As the SDS-PAGE analysis revealed a single band at ~100 kDa (lane +) without further protein bands, the protein was $\geq 95\%$ pure. M = marker. (b) CD spectrum of *SynDLP* wt (black) compared to *SynDLP*_{R320A-E585A} (red) measured in 10 mM HEPES buffer pH 7.4. The mean ($n = 3$) is shown. (c) CD spectra of *SynDLP* wt (black) and *SynDLP*_{R320A-E585A} (red) were monitored at increasing temperatures. The ellipticities at 222 nm were plotted against the temperature, normalized and fitted with an adapted Boltzmann fit (Equation (6)). The fit curves are shown as lines. Mean ($n = 3$) and error bars (S.D.) are shown. (d) ANS-FTSA measurements of 2.5 μ M *SynDLP* wt (black) and *SynDLP*_{R320A-E585A} (red) in reaction buffer. ANS fluorescence intensities at 470 nm were plotted against the temperature. The temperature range that captures the transition phase was fitted with an adapted Boltzmann fit (Equation (7)). Fit curves are shown as lines. Mean ($n = 3$) and error bars representing S.D. are displayed. (e) Analytical SEC of *SynDLP* wt (black) and *SynDLP*_{R320A-E585A} (red) was performed on a SuperoseTM 6 Increase 3.2/300 column equilibrated with reaction buffer. The elution volumes and molecular masses of typical standard proteins and the void volume (v) are indicated. (f) The GTPase activities of *SynDLP* wt (black) and *SynDLP*_{R320A-E585A} (red) were measured using a continuous, regenerative, coupled assay. Mean of independent experiments ($n = 3$) and error bars (S.D.) are shown. Data points were either fitted using the Michaelis-Menten equation (Equation (3), *SynDLP* wt) or the Hill equation (Equation (4), *SynDLP*_{R320A-E585A}). The fit curves are displayed as lines. Relative activities were obtained by setting the maximum activity of *SynDLP* wt to 100%.

Table 4.7: Biochemical properties of *SynDLP*_{R320A-E585A}. The values are derived from measurements shown in Fig. 4.30.

Mutant	$T_{m, CD}$ [°C]	$T_{m, ANS-FTSA}$ [°C]	GTPase activity [% wt]	K_m or K_D [mM]	n
wt	49.4 ± 0.3	47.8 ± 0.1	100 ± 3.0	0.59 ± 0.06	-
R320A-E585A	47.5 ± 0.2	48.3 ± 0.2	137.7 ± 46.3	0.49 ± 1.12	0.31 ± 0.13

4.2.3 Discussion

Oligomerization and the GTPase activity of DLPs in solution are sensitive to salts and reducing agents. Therefore, the influence of NaCl and DTT on the properties of *SynDLP* in the absence of membranes was evaluated. The effect of DTT on the intramolecular disulfide bridge in the BSE domain of *SynDLP* was already discussed in Chapter 4.1 (Gewehr *et al.*, 2023). Here, it was shown that *SynDLP* is prone to aggregation in the complete absence of DTT (Fig. 4.27b, d). The primary sequence of *SynDLP* reveals that the protein contains ten cysteine residues (Fig. A7). Potentially, the complete absence of a reducing agent leads to the formation of incorrect intermolecular disulfide bridges between *SynDLP* monomers from different oligomers, triggering aggregation. The thermodynamic stability of *SynDLP* was not influenced by DTT (Fig. 4.27c, Table 4.5). The maximum GTPase activity was significantly reduced in complete absence of a reducing agent. However, at low substrate concentrations, the GTPase activity was increased leading to a decreased K_m value (Fig. 4.27e, Table 4.5). Together with the diffuse band pattern of *SynDLP* in SDS-PAGE analysis in the absence of DTT (Fig. 4.27a), these results indicated a positive effect of DTT on the integrity of *SynDLP*'s oligomerization and GTPase function. The oligomerization of the eukaryotic DLP Mgm1 has also been shown to be influenced by DTT (Meglei and McQuibban, 2009). Interestingly, Mgm1 also contains an intramolecular disulfide bridge (Faelber *et al.*, 2019). However, the exact effect of DTT on Mgm1 assembly and activity has not been investigated in greater detail. Further experiments would be necessary to fully understand the impact of DTT on DLPs. As a consequence of the here described experiments with *SynDLP* +/- DTT, the purification as well as activity measurements of *SynDLP* were typically performed in the presence of small concentrations (0.1 – 0.2 mM) of DTT (Fig. 4.27a) to maintain the activity of *SynDLP* without reduction of the disulfide bridge in the BSE domain.

The influence of NaCl on the oligomerization of *SynDLP* has already been analyzed via EM as described and discussed in Chapter 4.1 (Fig. 4.5) (Gewehr *et al.*, 2023). The EM images were complemented by analytical SEC, which also showed the formation of larger oligomers with decreasing NaCl concentrations (Fig. 4.28c). This is in line with the observed increased thermodynamic stability of elongated *SynDLP* oligomers in the absence of NaCl (Fig. 4.28a, b, Table 4.6). The GTPase activity measurements indicate that NaCl increases the GTP hydrolysis rate (Fig. 4.28d, Table 4.6), albeit the formation of smaller oligomers with NaCl suggests an opposite effect on the GTPase activity of *SynDLP*, considering that the GTPase activity of *SynDLP* is stimulated by assembly (Gewehr *et al.*, 2023). However, it was shown in Chapter

4.1 that the GTPase activity of *SynDLP* is increased in the presence of Na^+ (Fig. 4.12) (Gewehr *et al.*, 2023), which is in line with the GTPase-activating effect of Na^+ in the active site of dynamin (Chappie *et al.*, 2010). Thus, activation of the GTPase activity by Na^+ in the active site contributes more to GTP hydrolysis than the decreasing effect of reduced oligomerization of *SynDLP*. Increased oligomerization propensity as well as GTPase activity are observed for dynamin at lowered NaCl concentrations (in the absence of a membrane template) (Warnock, Hinshaw and Schmid, 1996). However, experiments with dynamin were not performed in the complete absence of Na^+ as the presence of a monovalent cation is essential for the catalytic machinery of dynamin (Warnock, Hinshaw and Schmid, 1996; Chappie *et al.*, 2010).

The *SynDLP* oligomer structure suggests the presence of an intermolecular salt bridge between the GD residue R320 and the stalk residue E585 (Chapter 4.1, Fig. 4.26) (Gewehr *et al.*, 2023). The *SynDLP*_{R320A-E585A} mutant was created to abolish the formation of this putative salt bridge. The correctly folded mutant protein (Fig. 4.30b) had a thermodynamic stability comparable to *SynDLP* wt (Fig. 4.30c, d). However, the methods applied for investigating the thermodynamic stability showed different trends. The thermal denaturation monitored via CD spectroscopy revealed a T_m of *SynDLP*_{R320A-E585A} lowered by $\sim 2^\circ\text{C}$ compared to *SynDLP* wt (Fig. 4.30c, Table 4.7), whereas the ANS-FTSA indicated a slightly increased T_m of the mutant protein (Fig. 4.30d, Table 4.7). As the intermolecular salt bridge has a potential stabilizing effect on *SynDLP* oligomers, a lowered T_m was expected for the *SynDLP*_{R320A-E585A} mutant due to the missing salt bridge. The slightly increased T_m measured via ANS-FTSA could be explained by the observation that *SynDLP*_{R320A-E585A} forms larger structures than *SynDLP* wt in the used reaction buffer, as shown by analytical SEC (Fig. 4.30e). Interestingly, the R320A-E585A mutation had an impact on *SynDLP*'s GTPase activity, as *SynDLP*_{R320A-E585A} showed an increased GTPase activity at low substrate concentrations and the activity did not follow a typical Michaelis-Menten kinetic (Fig. 4.30f, Table 4.7).

An intermolecular salt bridge between the GD and stalk established by an arginine and a glutamate can also be observed in the structure of Dyn3 tetramers (Fig. 4.31b) (Reubold *et al.*, 2015). However, the impact of this GD-stalk connection in Dyn3 has not yet been analyzed in more detail. Interestingly, the salt bridge between the GD and stalk in *SynDLP* is established between the monomer n and the monomer $n+2$ (Fig. 4.31a), whereas in Dyn3 the directly adjacent monomers are connected (Fig. 4.31b). The effect of such different arrangements within an oligomer as well as the precise role of the putative R320-E585 intermolecular salt bridge in *SynDLP* have to be addressed in future studies.

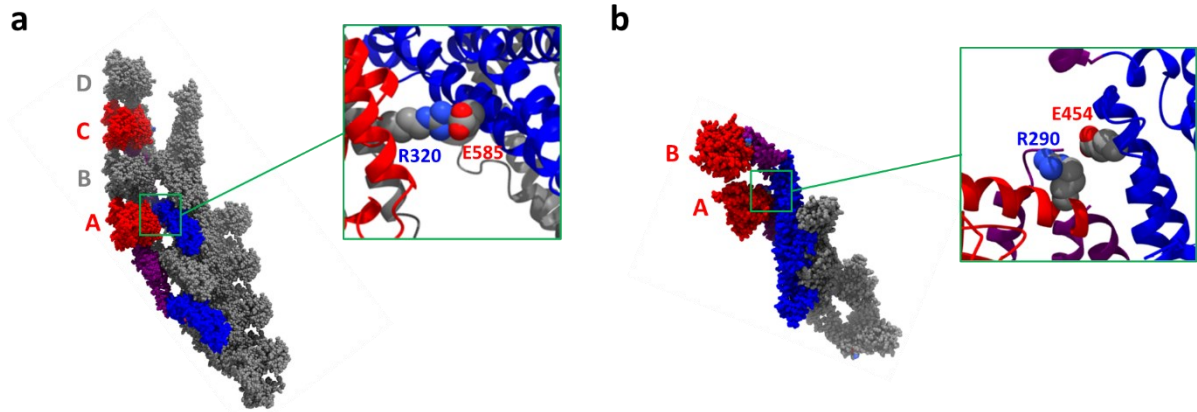


Figure 4.31: An intermolecular GD-stalk connection in *SynDLP* and *Dyn3*.

(a) Structure of a *SynDLP* octamer (PDB: 7ZW6) with the two monomers n and $n+2$ that are connected via a putative salt bridge between the GD and the stalk (GD, BSE and stalk in red, purple and blue, respectively). The remaining monomers are colored in gray. The inset shows the two involved residues R320 and E585 as spheres and colored by element. (b) Structure of a *Dyn3* tetramer (PDB: 5A3F). The two interacting monomers n and $n+1$ with a putative salt bridge between the GD and stalk are colored by domain (same color key as in (a)) and the remaining monomers in gray. The inset highlights the two involved residues R290 and E454 as spheres and colored by element. The MID of *Dyn3* was omitted for clarity.

4.3 Biochemical and biophysical analysis of membrane interaction properties of *SynDLP* and characterization of potential MIDs

4.3.1 Introduction

DLPs are mechanochemical GTPases that use the energy gained via GTP hydrolysis to remodel membranes (Williams and Kim, 2014). Obviously, DLPs require MIDs that enable their interaction with a membrane. Different modes of membrane interaction have been reported for different DLPs. A few members of the DLP family, such as atlastin, Sey1, OPA1 or mitofusin, are anchored in the membrane by TMDs. The TMDs of such proteins were predicted based on the primary sequence supported by investigations on their *in vivo* localization. Yet, the structures of these proteins have previously been resolved only for truncated constructs without the TMD (Bian *et al.*, 2011; Yan *et al.*, 2015; Chandhok, Lazarou and Neumann, 2018; Yu *et al.*, 2020). Members of the DLP subgroup of GBPs contain an MID solely after post-translational modification. *E.g.*, human GBP1 can be farnesylated at the C-terminus, which enables membrane interaction. Thus, the membrane activity of GBP1 is controlled by the addition/removal of a farnesyl moiety (Fres, Müller and Praefcke, 2010; Shydlovskiy *et al.*, 2017).

Most thus far characterized DLPs are peripherally membrane-attached proteins. In recent years, several structures of DLPs have been published that reveal varying designs of the MIDs of peripheral membrane DLPs (Fig. 4.32) (Low and Löwe, 2006; Low *et al.*, 2009; Faelber *et al.*, 2011, 2019; Kong *et al.*, 2018; Liu, Noel and Low, 2018; Wang *et al.*, 2019). In general, eukaryotic DLPs appear to have more complex and enlarged MIDs compared to prokaryotic DLPs. *E.g.*, dynamin, the founder of the DLP family, has a pleckstrin homology (PH) domain as MID and the fungal representative *CtMgm1* (Mgm1 of *Chaetomium thermophilum*) has a bundle of several α -helices and loops that attach the protein to membrane surfaces (Fig. 4.32, upper row) (Faelber *et al.*, 2011, 2019; Kong *et al.*, 2018). The MIDs of BDLPs are less complex but have variable designs. The cyanobacterial *NpBDLP* intercalates via a mainly α -helical region in the membrane, the MID of *Cj-DLP2* consists of loops and short β -sheets and *MsIniA* interacts with negatively charged lipids via a short loop (Fig. 4.32, bottom row) (Low and Löwe, 2006; Low *et al.*, 2009; Liu, Noel and Low, 2018; Wang *et al.*, 2019). Common to all described MIDs of peripherally membrane-attached DLPs is that the MID is located at the tip of the stalk opposite the GD.

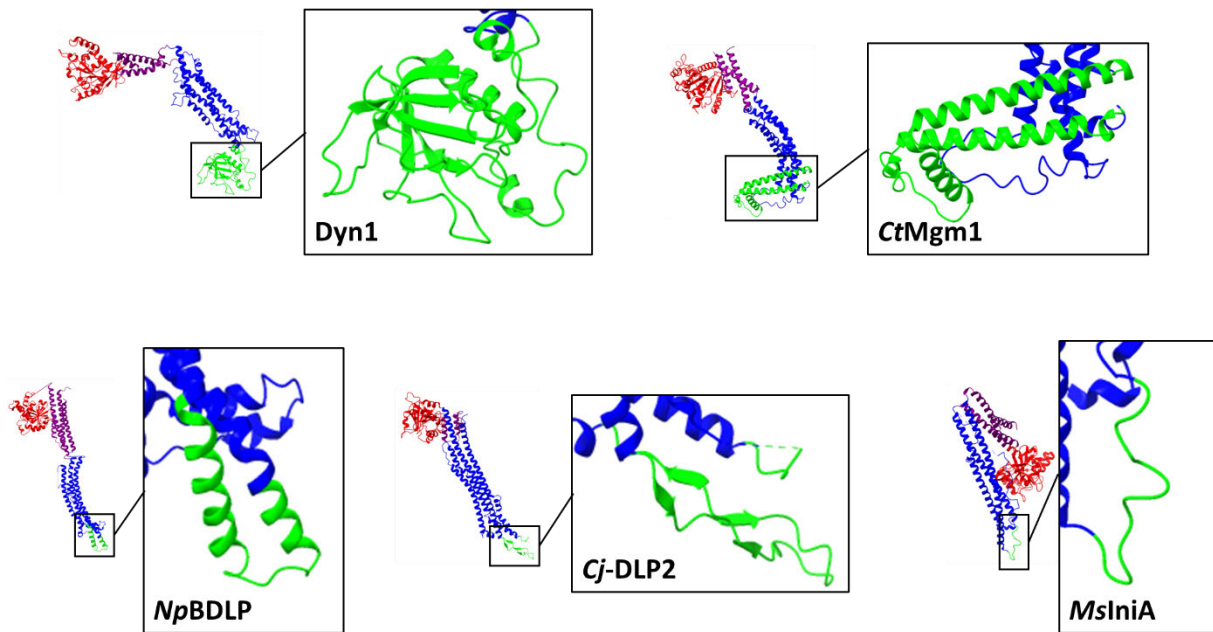


Figure 4.32: Structural comparison of MIDs from peripherally membrane-attached DLPs.

Structures of different DLPs with a resolved MID. Eukaryotic Dyn1 (PDB: 6DLU) and *CtMgm1* (PDB: 6QL4) are compared to the BDLPs *NpBDLP* (PDB: 2W6D), *Cj-DLP2* (PDB: 5OWV) and *MslniA* (PDB: 6J72). GD, BSE, stalk domain and MID are colored in red, purple, blue and green, respectively. The zoomed insets highlight the respective MIDs.

As described above, the now solved structure enabled me to identify putative MIDs in *SynDLP*. Two potential MIDs of *SynDLP* have been mutated and the mutant proteins (*SynDLP*_{648-665GS} and *SynDLP*_{667-675GS}) have been tested for membrane interaction using the Laurdan fluorescence assay, which indicated intact membrane binding in both mutants (Chapter 4.1, Fig. 4.17) (Gewehr *et al.*, 2023). In the following, the results of the complete biochemical characterization of *SynDLP*_{648-665GS} and *SynDLP*_{667-675GS} will be presented. In addition, other potential MIDs of *SynDLP* have been investigated via mutagenesis. The identification of the analyzed putative MIDs was based either on the primary sequence or the solved *SynDLP* structure. The mutant proteins were recombinantly expressed, purified, biochemically characterized and tested for membrane binding using the Laurdan fluorescence assay.

Another goal of this study was to apply membrane binding assays that were not yet used and complement the Laurdan fluorescence assay. Therefore, a membrane binding assay using GUVs was established and all *SynDLP* variants with a mutated potential MID were additionally screened for their binding to GUV membranes. Finally, SPR spectroscopy was tested as a quantitative method to describe the binding of *SynDLP* wt to liposomes and to determine a dissociation constant. Besides the Laurdan fluorescence assay, membrane binding of *SynDLP* has already been analyzed using SFG spectroscopy. Here, it was shown that *SynDLP*

intercalates into a DMPG monolayer, probably by immersion of an MID into the membrane (Chapter 4.1, Fig. 4.16) (Jilly, 2018; Gewehr *et al.*, 2023). The thermodynamic stability of *SynDLP* was monitored via CD spectroscopy in the presence of different liposome species to possibly determine a stabilizing effect of lipids on protein regions after intercalation into the membrane.

4.3.2 Results

The thermodynamic stability of SynDLP is influenced by DOPG liposomes

For *SynDLP* it was demonstrated that it intercalates into PG-containing membranes potentially via an MID with a distinct secondary structure (Chapter 4.1) (Jilly, 2018; Gewehr *et al.*, 2023). Thus, the thermodynamic stability of *SynDLP* was now studied in the presence of liposomes using CD spectroscopy. Therefore, *SynDLP* was incubated with either DOPG or DOPC liposomes. *SynDLP* was expected to interact only weakly with the latter. The CD spectrum of *SynDLP* at 20°C was unaffected by the addition of DOPG or DOPC liposomes (Fig. 4.33a). The *SynDLP* thermal denaturation curve determined in the presence of DOPC liposomes ($T_m = 49.9 \pm 0.2^\circ\text{C}$) (Fig. 4.33b, blue) also showed no significant difference to *SynDLP* in solution ($T_m = 49.4 \pm 0.3^\circ\text{C}$) (Fig. 4.33b, black). However, the course of the thermal denaturation curve considerably changed upon addition of DOPG liposomes (Fig. 4.33b, red). With a T_m of $44.5 \pm 0.2^\circ\text{C}$, the thermodynamic stability was significantly reduced. However, part of the protein seemed to stay folded until heating to approx. 70°C, where a second unfolding process started. This assumption is supported by the single CD spectra determined at increasing temperatures (Fig. 4.34). While the CD spectrum of *SynDLP* alone and in the presence of DOPC liposomes was typical for a mostly unfolded protein at high temperatures, *SynDLP* in the presence of DOPG liposomes was still partially folded at the highest temperatures, as indicated by the clear minimum at about 208 nm. The individual CD spectra measured for the determination of statistically significant thermal denaturation curves are shown in Fig. A8.

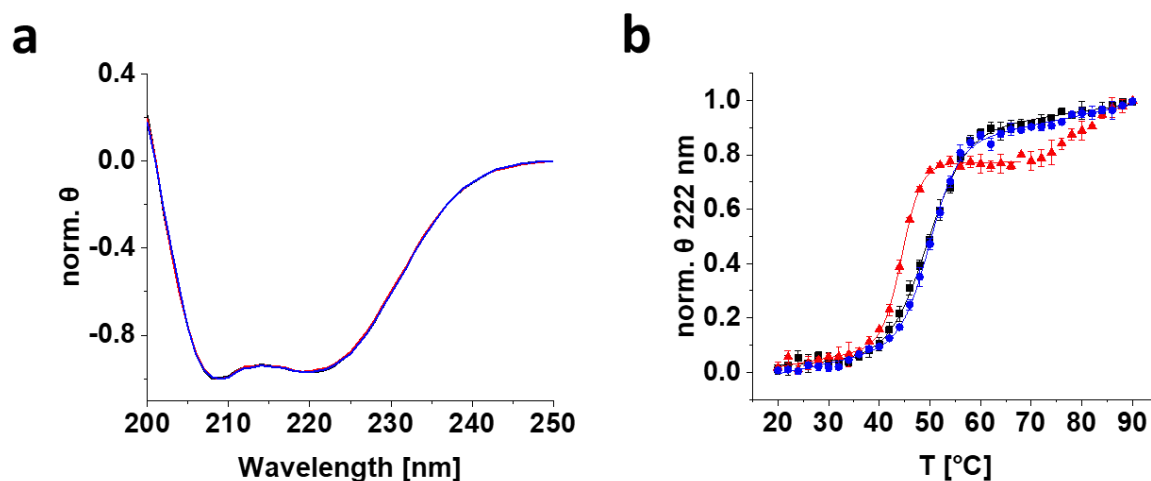


Figure 4.33: CD spectra of *SynDLP* in the presence of liposomes.

(a) CD spectra of 1 μM *SynDLP* wt in the absence (black), or presence of 0.3 mM DOPG (red) or 0.3 mM DOPC liposomes (blue), respectively, measured at 20°C with 8-time accumulation in 10 mM HEPES buffer pH 7.4. The mean ($n = 3$) is shown and the spectra were normalized. Liposomes were extruded to 100 nm. (b) The thermodynamic stability of *SynDLP* +/- liposomes (identical samples as in (a)) was investigated by monitoring the CD spectra (1-time accumulation) at increasing temperatures. The measured ellipticities at 222 nm were plotted against the temperature, normalized, and fitted with an adapted Boltzmann fit (Equation (6)). The fit curves are shown as lines. Mean ($n = 3$) and S.D. are shown. Coloring of the different conditions as in (a).

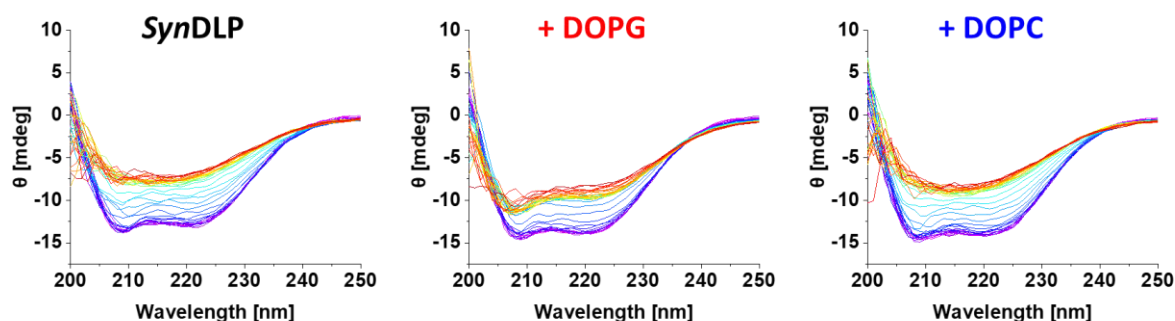


Figure 4.34: Temperature-dependent CD spectra of *SynDLP* in the presence of liposomes.

Typical CD spectra obtained during thermal denaturation of the samples shown in Fig. 4.33b. For each condition, the spectra at increasing temperatures of one measured sample is shown. CD spectra are colored by rainbow colors, starting from 20°C (violet) to 92°C (red).

Establishing a GUV-based membrane binding assay

To investigate the membrane interaction properties of *SynDLP*, a Laurdan fluorescence assay was mainly used so far (Jilly, 2018; Gewehr *et al.*, 2023). However, assays using Laurdan as a fluorescent reporter are difficult to perform in the presence of nucleotides, as the spectroscopic properties of the nucleotides might interfere with the measured signal plus the nucleotides themselves can interact with membranes. Therefore, a GUV-based membrane binding assay

was established as an additional method to study *SynDLP* membrane interaction by visualizing membrane binding in the absence or presence of nucleotides under the fluorescence microscope. A gene coding for a *SynDLP* variant with an N-terminal mEGFP (monomeric enhanced GFP)-tag was cloned to obtain the target protein with a fluorescent reporter. The amino acid sequence of full-length recombinant mEGFP-*SynDLP* is shown in the appendix (Fig. A9).

The mEGFP-*SynDLP* variant was expressed and purified like untagged *SynDLP* wt. SDS-PAGE analysis revealed a pure mEGFP fusion protein (Fig. 4.35a, lane +) with an intact intramolecular disulfide bridge (Fig. 4.35a, lane -). The relatively large mEGFP tag with a molecular mass of approx. 28 kDa potentially disturbs the functionality of the *SynDLP* moiety of the fusion protein. Hence, the GTPase activity of mEGFP-*SynDLP* was determined and compared to the untagged protein. This showed that the fusion protein is active, and the N-terminal mEGFP-tag had only weak impact on the GTPase activity of *SynDLP* (Fig. 4.35b). GFP-derived protein tags often change the oligomerization behavior of the target protein. The integrity of mEGFP-*SynDLP* oligomers was checked by negative stain EM, which revealed the formation of large, filamentous oligomers comparable to *SynDLP* wt (Gewehr *et al.*, 2023) (Fig. 4.35c). Conclusively, the N-terminal mEGFP-tag neither hampers assembly nor the GTPase activity of *SynDLP*, making the fusion protein suitable for further experiments.

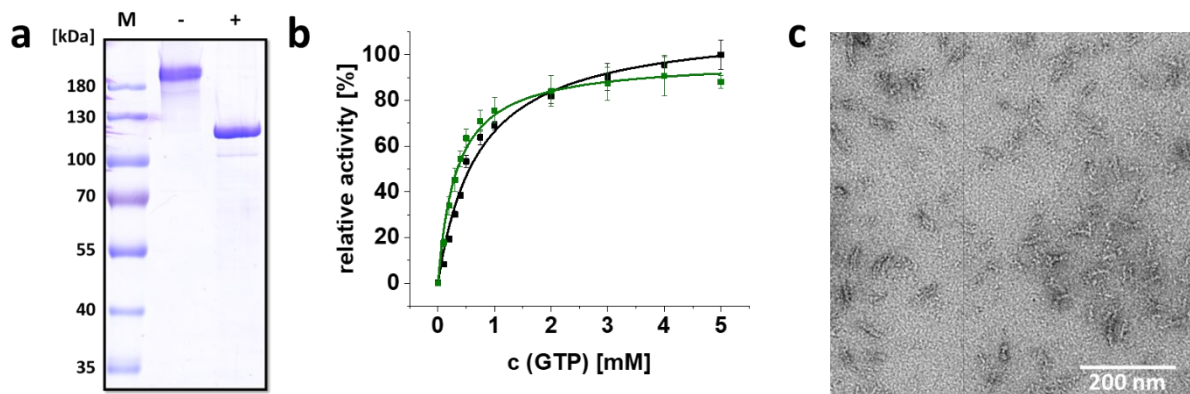


Figure 4.35: Purification, GTPase activity and oligomerization of an mEGFP-tagged *SynDLP* variant.

(a) SDS-PAGE analysis of 2 μg purified mEGFP-*SynDLP* via SDS-PAGE in the presence of 0.1 mM DTT (lane -) or 100 mM DTT (lane +). The protein has a calculated molecular mass of 122 kDa. The SDS-PAGE analysis showed a dominant band between 100 and 130 kDa (lane +) and no further protein bands, thus, the protein was $\geq 95\%$ pure. M = marker. (b) The GTPase activities of mEGFP-*SynDLP* (green) and *SynDLP* wt (black) were measured in a continuous, regenerative, coupled assay. Mean ($n = 3$) and error bars (S.D.) are shown, and the data points were fitted using Equation (3). The maximum activity of *SynDLP* wt was set to 100% to compare relative GTPase activities. (c) Negative stain EM micrograph of 1 μM mEGFP-*SynDLP* in reaction buffer.

GUVs were prepared with a fluorescent reporter lipid (ATTO633-PE) by PVA swelling (Weinberger *et al.*, 2013). This led to vesicles with a size of approx. 5 – 20 μm , which is in a range suitable for visualization under a fluorescence microscope (Fig. 4.36a). When 0.8 μM mEGFP-*SynDLP* plus 1 mM GDP were added to the GUVs, a clear fluorescence signal of mEGFP was observable at the GUV membrane surface after a few minutes. The signal increased during the next 1 – 2 h of incubation (Fig. 4.36b), showing that the GUV membrane binding assay basically works.

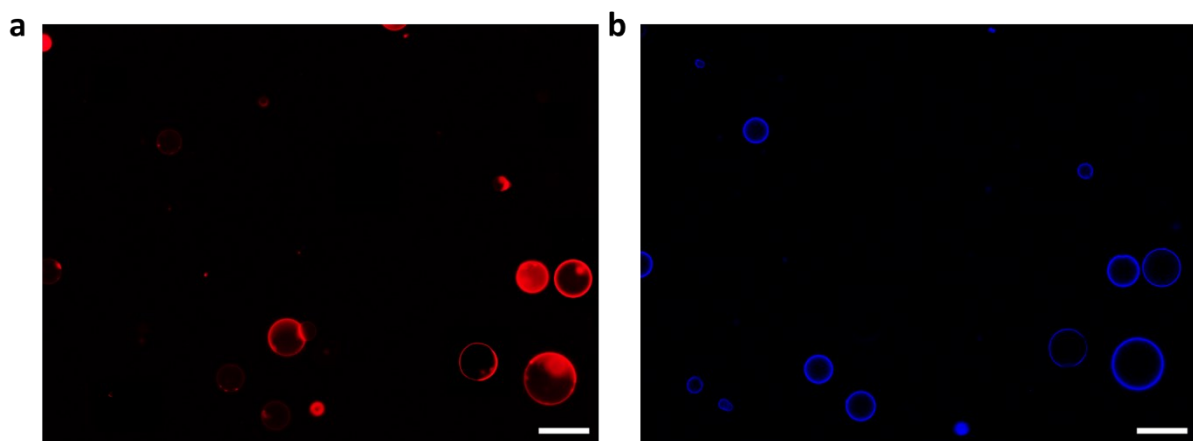


Figure 4.36: Binding of mEGFP-*SynDLP* to GUV membranes.

GUVs (70% DOPC/30% DOPG, *w/w*, ATTO633-PE as fluorescent dye) were produced via PVA swelling and incubated with 0.8 μM mEGFP-*SynDLP*. 5 min after protein addition, 1 mM GDP was added to the mixture. (a) Typical fluorescence micrograph visualizing the GUV membrane fluorescence (red) via the fluorescence of the ATTO633 dye located in the GUV membranes. (b) Fluorescence micrograph showing the specific mEGFP fluorescence of the same section as in (a). Areas with high mEGFP signals are shown in blue. Images were acquired after 2 h incubation. White bars scale for 20 μm .

Next, the influence of different nucleotides on GUV binding of mEGFP-*SynDLP* was tested. Interestingly, the protein did not bind significantly to the GUV surface in the apo state even after 2 h of incubation (Fig. 4.37). The addition of GTP resulted in a clearly detectable membrane binding of the protein. The same result was observed in the presence of GDP, suggesting that the GTP hydrolysis energy is not the driving force triggering membrane binding of mEGFP-*SynDLP*. However, the addition of the non-hydrolysable GTP analog GMPPnP did not lead to detectable GUV binding events. In contrast to previously performed membrane binding assays, the GUV membrane binding assay showed a nucleotide-dependent membrane binding of *SynDLP*. Noteworthy, after 1 – 2 hours of incubation, most of the GTP should have been hydrolyzed by mEGFP-*SynDLP*.

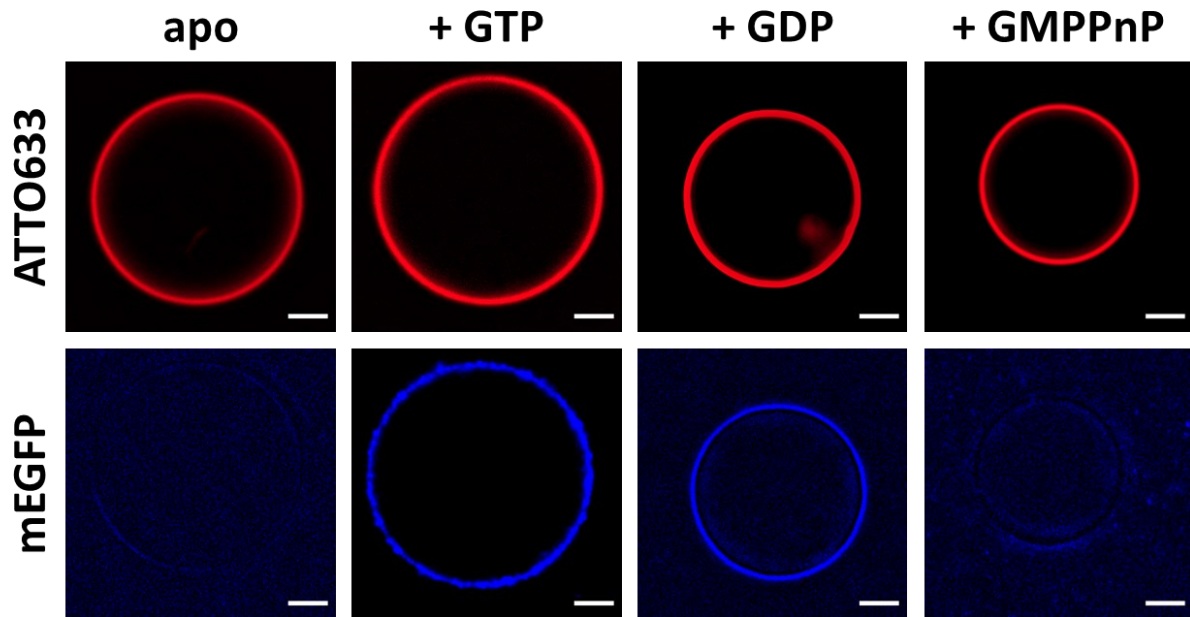


Figure 4.37: Nucleotide-dependent binding of mEGFP-*SynDLP* to GUV membranes.

Membrane binding of mEGFP-*SynDLP* was investigated using GUVs (70% DOPC/30% DOPG, *w/w*, ATTO633-PE as fluorescent dye). 0.8 μ M mEGFP-*SynDLP* was added to the GUVs and after 5 min, 1 mM of the nucleotides GTP, GDP or GMPPnP were added. The fluorescence of the GUVs (red) and of the mEGFP (blue) were recorded in the ATTO633 and the mEGFP channel, respectively. Images were acquired after 1 to 2 h incubation. The white bars scale for 5 μ m.

Since the GUV membrane binding assay indicated membrane interaction of *SynDLP* in the presence of GTP as well as GDP (Fig. 4.37), a putative GDP hydrolysis activity of *SynDLP* was next tested. The ability to hydrolyze GDP is not typically reported for DLPs. However, the DLP subgroup of GBPs make an exception as they show a pronounced GDPase activity, resulting in the formation of the product guanosine monophosphate (GMP) (Schwemmle and Staeheli, 1994; Ghosh *et al.*, 2006; Kutsch and Coers, 2021). Thus, a GDP hydrolysis activity of *SynDLP* is conceivable. The usually applied continuous, regenerative, coupled GTPase assay could not be used to determine any potential GDP hydrolysis activity of *SynDLP*, as the assay components constitutively phosphorylate GDP to GTP. Therefore, a malachite green phosphate assay was applied to study a potential GDPase activity. This is a colorimetric assay that measures the formation of the by-product inorganic phosphate (P_i) formed during the hydrolysis of GDP to GMP. The incubation of 0.5 mM GDP with increasing *SynDLP* concentrations indeed showed a protein-dependent formation of P_i (Fig. 4.38) and, thus, a GDP hydrolysis activity. However, the amount of resulting P_i was rather small, and the reaction was very slow as it required incubation times of several hours to detect the P_i formation. Thus, it was shown that *SynDLP* is indeed capable of hydrolyzing not only GTP but also GDP.

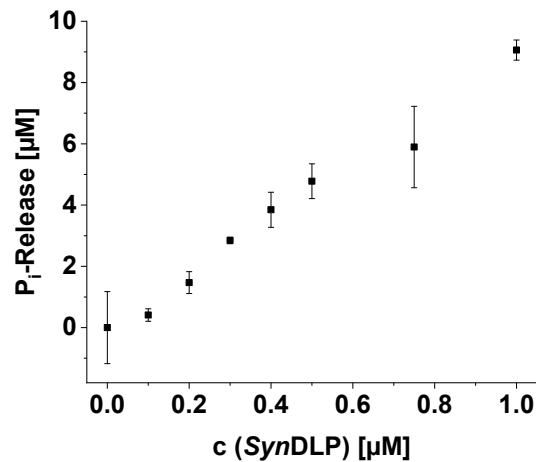


Figure 4.38: *SynDLP* can hydrolyze GDP.

GDP hydrolysis was quantified via measuring the formation of the product phosphate (P_i). After 6 h incubation at 30°C with 0.5 mM GDP and increasing *SynDLP* concentrations, the P_i -release was determined using a malachite green phosphate assay and calculated via a P_i standard series (Fig. A10). Mean ($n = 3$) and error bars (S.D.) are shown.

Analysis of potential MIDs based on the primary sequence of SynDLP

Next, I tried to identify the MID of *SynDLP*. Therefore, protein regions that carry the potential MID were replaced by a flexible GS-linker and membrane interaction of the mutant proteins was investigated using a Laurdan fluorescence assay and the established GUV membrane binding assay, as described above. The results from two of these mutants (*SynDLP*_{648-665GS} and *SynDLP*_{667-675GS}) were already described in Chapter 4.1 (Gewehr *et al.*, 2023). However, in the following paragraphs, additional results obtained with these two mutants as well as analyses of three other *SynDLP* variants with a substituted putative MID will be presented.

Analysis of *SynDLP*_{558-565GS}

The first mutants with a potential substitution of the MID were designed based on the primary sequence of *SynDLP*, as the protein structure was not available at the beginning of my analyses. A hydrophobicity plot of the amino acid sequence of *SynDLP* revealed eight hydrophobic amino acids in a row (A558 – V565) outside the presumed GD (Fig. 4.39a, Fig. A7). It was reasonable to assume an involvement of this very hydrophobic region in membrane interaction. The eight residues were substituted by a (GS)₄-linker to obtain the mutant *SynDLP*_{558-565GS}. The protein was expressed as the *SynDLP* wt and purified based on a purification protocol without a DTT incubation step, and the protein was stored in 20 mM HEPES buffer pH 7.4 (without DTT)

upon purification (see Chapter 4.2 for more information on the usage of DTT). Additionally, the purification step using preparative SEC was omitted as the mutant protein showed undesired interactions with the used Sephacryl[®] S-400 HR column material. Purified *SynDLP*_{558-565GS} revealed additional protein bands besides the dominant band caused by the target protein (Fig. 4.39b). Thus, the protein contained impurities and the following results must be handled with caution, as the purification protocol needs optimizations.

CD spectroscopic analysis of *SynDLP*_{558-565GS} showed a mainly α -helical secondary structure (Fig. 4.39c). The shape of the CD spectrum was similar to *SynDLP* wt. Thus, the mutant protein seemed to be correctly folded on secondary structure level. The thermal stability was also studied via CD spectroscopy. Here, the *SynDLP*_{558-565GS} variant revealed a decreased thermodynamic stability compared to *SynDLP* wt with a T_m reduced by 5.0°C (Fig. 4.39d, Table 4.8). Interestingly, the molecular mass of *SynDLP*_{558-565GS} assemblies was significantly decreased compared to *SynDLP* wt as shown by analytical SEC (Fig. 4.39e). Comparison of the elution volume of the mutant with typical standard proteins indicated the formation of mainly dimers or tetramers, considering the calculated molecular mass of *SynDLP*_{558-565GS} is 93 kDa. The mutation also affected the GTPase activity of *SynDLP*, since the *SynDLP*_{558-565GS} variant showed only approx. 40% of the wt maximum activity. The K_m value was slightly lowered in case of the mutant (Fig. 4.39f, Table 4.8).

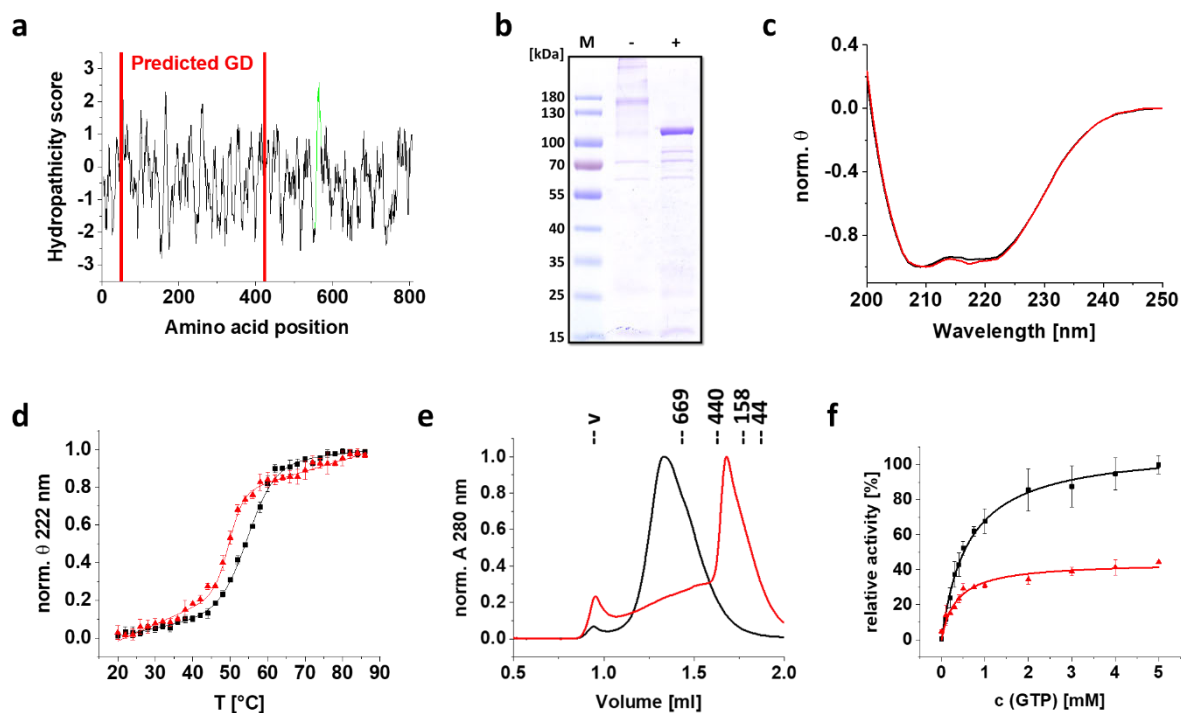


Figure 4.39: Biochemical analysis of the *SynDLP*_{558-565GS} variant.

(a) Hydropathicity plot of *SynDLP*'s primary sequence revealed one region outside the GD with a high hydrophaticity score (green peak) that exclusively consists of hydrophobic amino acids (A558 – V565). The plot was created with ExPASy ProtScale using the scale of Kyte & Doolittle (Kyte and Doolittle, 1982). (b) Analysis of 2 μ g purified *SynDLP*_{558-565GS} via SDS-PAGE in the presence of 0.1 mM DTT (lane -) or 100 mM DTT (lane +). The calculated molecular mass of the protein is 93 kDa. The SDS-PAGE analysis reveals a dominant band at \sim 100 kDa (lane +) and further additional protein bands, thus the protein contained small amounts of impurities. M = marker. (c) Normalized CD spectra of 1 μ M *SynDLP* wt (black) compared to *SynDLP*_{558-565GS} (red) measured in 1 mM NaP_i pH 7.4 ($n = 3$). (d) The thermal stability of *SynDLP* and *SynDLP*_{558-565GS} was monitored via CD spectroscopy in 1 mM NaP_i pH 7.4. The ellipticities at 222 nm were plotted against the temperature and were fitted with an adapted Boltzmann fit (Equation (6)). Fit curves are shown as lines. Mean ($n = 3$) and error bars (S.D.) are shown. © Analytical SEC of *SynDLP*_{558-565GS} (red) compared to *SynDLP* wt (black) loaded on a Superose™ 6 Increase 3.2/300 column revealed a hampered oligomerization of the mutant. Elution volumes of typical standard proteins as well as the void volume (v) are indicated. The column was equilibrated with reaction buffer (without DTT). (f) GTPase activity of *SynDLP* wt (black) and *SynDLP*_{558-565GS} (red) was measured in a continuous, regenerative, coupled assay. The mean ($n = 3$) and error bars (S.D.) are shown, and the data points were fitted using Equation (3). The maximum activity of *SynDLP* wt was set to 100% to obtain relative GTPase activities.

The membrane interaction properties of *SynDLP*_{558-565GS} were analyzed by a Laurdan-based fluorescence assay and a GUV membrane binding assay. For the latter one, a GFP-tagged variant of *SynDLP*_{558-565GS} was necessary. At the beginning, *SynDLP* was tagged with an eGFP-tag (Fig. A9) at the C-terminus. Yet, the C-terminal eGFP-tag had a strong influence on the GTPase activity of *SynDLP* wt, which was clearly decreased in the presence of the fluorescent tag (Fig. 4.40a). The C-terminally tagged *SynDLP*_{558-565GS} (*SynDLP*_{558-565GS}-eGFP) was purified as described above for untagged *SynDLP*_{558-565GS}. Purified *SynDLP*_{558-565GS}-eGFP revealed the

correct formation of the intramolecular disulfide bridge in an SDS-PAGE analysis (Fig. 4.40b, lane -), however, there were also some impurities observable (Fig. 4.40b, lane +). Interestingly, the GTPase activity of *SynDLP*_{558-565GS}-eGFP was essentially identical as the untagged *SynDLP*_{558-565GS} (Fig. 4.40c), which is in contrast to C-terminally eGFP-tagged *SynDLP* wt (Fig. 4.40a). Therefore, C-terminally tagged *SynDLP*_{558-565GS}-eGFP was assessed to be suitable for further experiments. As already shown, *SynDLP*_{558-565GS} forms smaller assemblies than *SynDLP* wt (Fig. 4.39e), indicating that the C-terminal eGFP-tag only affects the GTPase activity of *SynDLP* when the protein is organized in larger oligomeric assemblies.

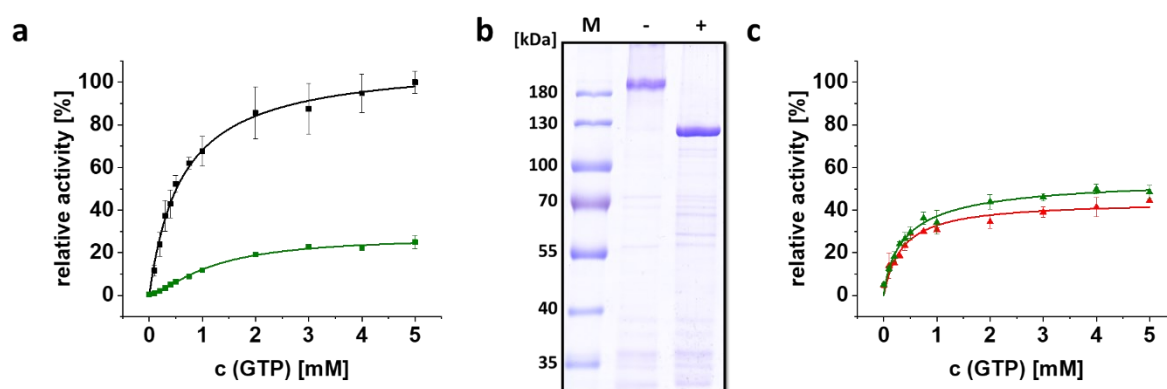


Figure 4.40: GTPase activities of *SynDLP* and *SynDLP*_{558-565GS} with a C-terminal eGFP-tag.

(a) GTPase activity of *SynDLP* wt without (black) and with a C-terminal eGFP-tag (green) was measured with a continuous, regenerative, coupled assay. The mean ($n = 3$) and error bars (S.D.) are shown. The data points were fitted with Equation (3). For relative GTPase activities, the maximum activity of *SynDLP* wt without eGFP-tag was set to 100%. (b) Analysis of purified *SynDLP*_{558-565GS}-eGFP via SDS-PAGE with 0.1 mM DTT (lane -) or 100 mM DTT (lane +). The calculated molecular mass of the protein is 122 kDa. The SDS-PAGE gel showed a dominant band below 130 kDa (lane +) and further additional protein bands, thus the protein contained small amounts of impurities. M = marker. (c) GTPase activity of *SynDLP*_{558-565GS} (red) and *SynDLP*_{558-565GS}-eGFP (green). Mean ($n = 3$) and S.D. are shown. Data points were fitted using Equation (3). The GTPase activities were normalized to the maximum activity of *SynDLP* wt in (a).

The Laurdan fluorescence assay was used to analyze liposome binding of *SynDLP* variants as already described in Chapter 4.1 (Fig. 4.16) (Gewehr *et al.*, 2023). Laurdan fluorescence measurements can be extended to membrane binding curves to obtain dissociation constants of protein-liposome complexes. In case of *SynDLP* wt, the binding curve of the protein to 30% DOPG/70% DOPC-containing liposomes revealed a biphasic binding behavior with a strong signal increase at low protein concentrations followed by a linear increase of the GP values at higher protein concentrations (Fig. 4.41a). Thus, a fit was applied using a biphasic model that combines a hyperbolic and a linear phase (Equation (9)) and a K_D of 28.3 ± 9.3 nM was extracted (Table 4.9). Monitoring membrane binding of *SynDLP*_{558-565GS} via Laurdan fluorescence measurements revealed that the protein bound to DOPG-containing membranes,

yet a slightly changed course of the curve was observed as well as a significantly higher GP value with increasing protein concentrations compared to *SynDLP* wt (Fig. 4.41b). The K_D value was determined to be 17.1 ± 8.3 nM, which indicates a negligible increase of the binding affinity compared to *SynDLP* wt (Table 4.9). In the GUV membrane binding assay, *SynDLP*_{558-565GS}-eGFP showed the same behavior as fluorescently tagged *SynDLP* wt (Fig. 4.37, Table 4.9). The mutant protein strongly bound to the GUV surface in a nucleotide-dependent manner only in the presence of GTP or GDP (Fig. 4.41c).

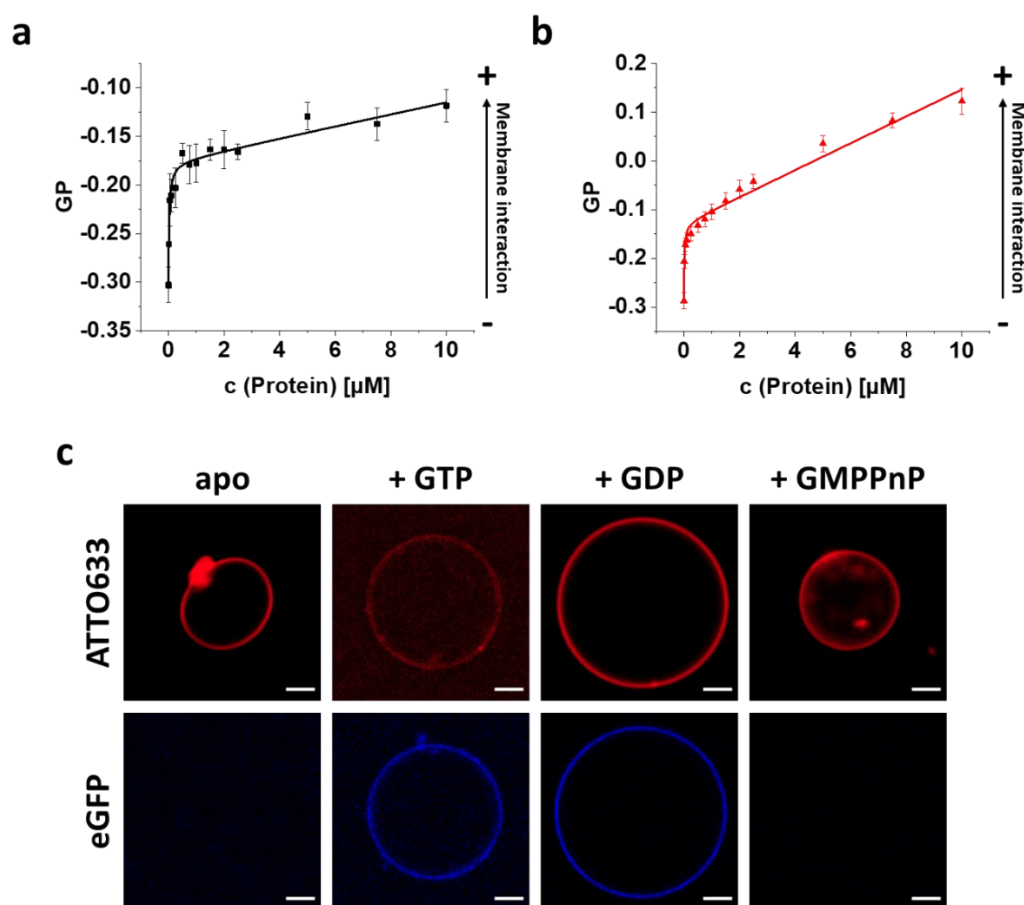


Figure 4.41: Membrane interaction properties of *SynDLP*_{558-565GS}.

(a) Membrane binding of *SynDLP* determined via fluorescence spectroscopy using Laurdan as a fluorescent probe. LUVs were prepared with 30% DOPG and 70% DOPC (*w/w*) mixed with Laurdan at a 1:500 molar ratio. Laurdan fluorescence spectra were recorded after 1 h incubation of the corresponding *SynDLP* concentrations with the LUVs and the ΔGP value was calculated from the spectra. Mean ($n = 3$) and error bars (S.D.) are shown. The data points were fitted using Equation (9). Arrow indicates increasing membrane interaction. (b) Membrane binding of *SynDLP*_{558-565GS} determined using Laurdan as a probe. LUVs (prepared as described in (a)) were incubated for 1 h with different *SynDLP*_{558-565GS} concentrations. Mean ($n \geq 3$) and S.D. are shown. The data points were fitted using Equation (9). The arrow shows increasing membrane interaction. (c) The binding of *SynDLP*_{558-565GS} to GUV membranes was investigated with GUVs (30% DOPG/70% DOPC, *w/w*, ATTO633-PE as fluorescent dye). 5 min after addition of $0.8 \mu\text{M}$ *SynDLP*_{558-565GS}-eGFP, 1 mM nucleotide was added to the GUVs. The GUV fluorescence (red) was recorded in the ATTO633 channel and the eGFP fluorescence (blue) in the eGFP channel. Images were acquired after 1 to 2 h incubation. White bars scale for 5 μm .

Analysis of *SynDLP*_{694-705GS}

As *SynDLP*_{558-565GS} was still able to interact with membranes, another putative MID was identified based on the primary sequence of *SynDLP* and inspired by the BDLP *MsIniA* structure. *MsIniA* interacts with negatively charged lipids via a membrane interacting loop, which mainly consists of hydrophobic and positively charged amino acids (Fig. 4.42) (Wang *et al.*, 2019). The sequence of *SynDLP* includes a similar motif at the amino acid positions 694 – 705 (Fig. 4.42) and, like *MsIniA*, *SynDLP* was shown to especially interact with negatively charged lipids. Therefore, a *SynDLP* mutant was generated in which the residues P694 – R705 are substituted by a (GS)₆-linker (*SynDLP*_{694-705GS}) to test whether these residues form a potential MID.

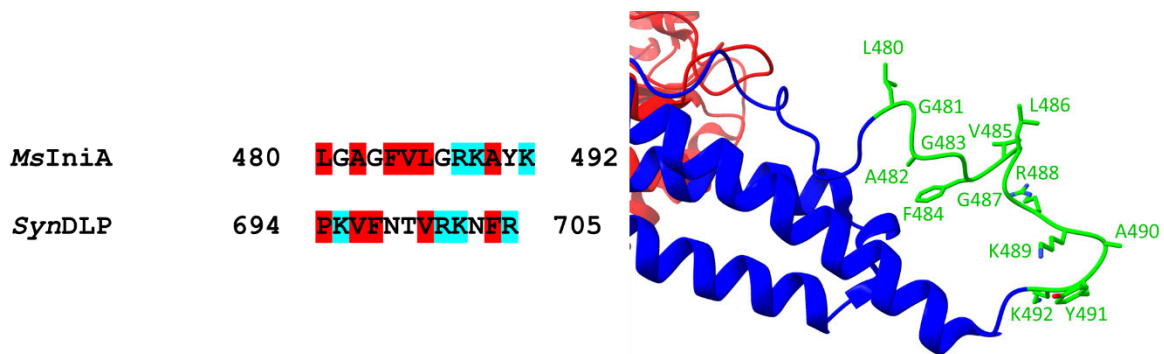


Figure 4.42: Putative membrane interacting loops in BDLPs.

Sequence of the MID in the BDLP *MsIniA* (amino acids 480 – 492) and the derived sequence of a putative MID in *SynDLP* (amino acids 694 – 705). Hydrophobic and positively charged amino acids are labeled in red and cyan, respectively. A section of the *MsIniA* structure (PDB: 6J72) highlighting the membrane interacting loop is shown on the right in ribbon representation. GD, stalk and MID are colored red, blue and green, respectively. The residues of the MID are shown as sticks and labeled.

*SynDLP*_{694-705GS} was heterologously expressed in *E. coli* Rosetta-gamiTM 2(DE3) cells as described for *SynDLP* wt. An SDS-PAGE analysis with subsequent Coomassie Brilliant Blue staining indicated a low expression level of the overexpressed target protein, as no dominant band was observable (Fig. 4.43a). A Western Blot analysis revealed the successful expression of *SynDLP*_{694-705GS} (Fig. 4.43b, lane +), since an α -*SynDLP* antibody recognized a band at a mass of approx. 100 kDa, where also *SynDLP* wt, which was analyzed in a control Western Blot analysis, was detected (Fig. 4.43c). However, non-reducing SDS-PAGE and subsequent Western Blot analysis (Fig. 4.43b, lane -) showed a dominant band at the same height at approx. 100 kDa with similar intensity compared to reducing conditions (Fig. 4.43b, lane +). In addition, the expected band at approx. 180 kDa caused by the intramolecular disulfide bridge (Chapter 4.1, Fig. 4.2) was absent under non-reducing conditions. This band can be used as an indication

for a correctly folded *SynDLP* variant, if the mutation did not affect the two involved cysteines C8 and C777. Conclusively, the *SynDLP*_{694-705GS} mutant appeared to not fold properly, and thus this variant was not further purified and analyzed. Potentially, another expression protocol or the choice of another overexpression strain could yield in a correctly folded protein.

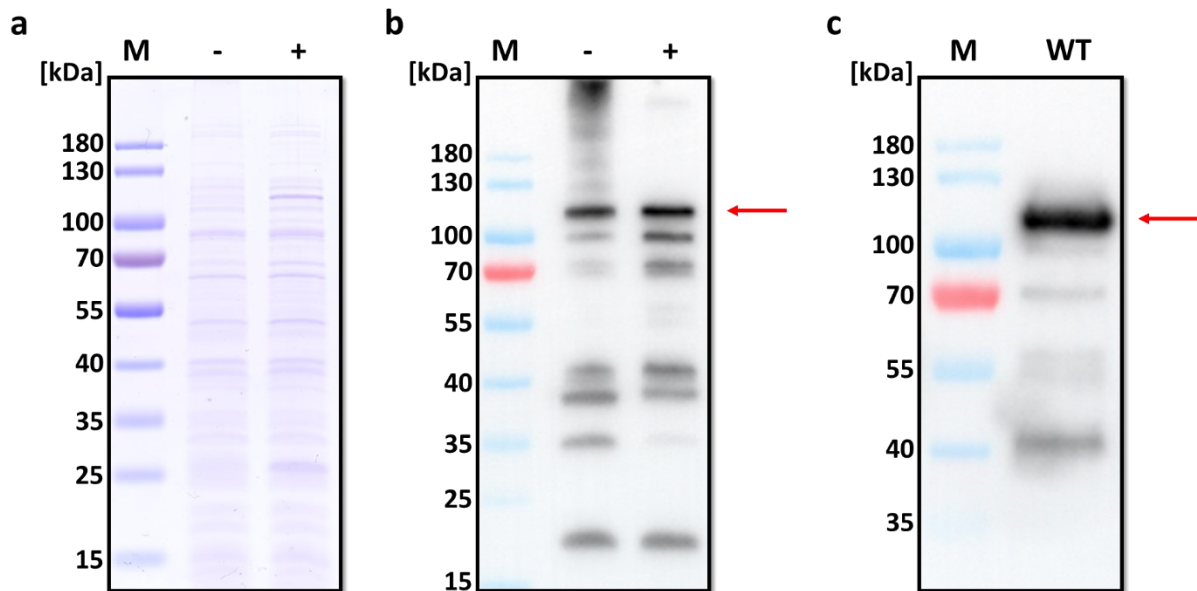


Figure 4.43: Heterologous expression of *SynDLP*_{694-705GS}.

(a) Recombinant *SynDLP*_{694-705GS} was overexpressed in *E. coli* Rosetta-gamiTM 2(DE3) cells and a boiled culture (after IPTG induction) was loaded on an SDS-PAGE gel in presence of 0 mM DTT (lane -) or 100 mM DTT (lane +). Proteins were stained by Coomassie Brilliant Blue. (b) Western Blot analysis after SDS-PAGE (performed analogously to (a)) using an α -*SynDLP* antibody as primary and an α -rabbit-HRP conjugate as secondary antibody. The red arrow indicates the band corresponding to *SynDLP*_{694-705GS}, which has a calculated molecular mass of 93 kDa. M = marker. (c) Western Blot analysis of recombinant and purified *SynDLP* wt. SDS-PAGE was performed under reducing conditions (100 mM DTT) and the protein was visualized using an α -*SynDLP* antibody as primary and an α -rabbit-HRP conjugate as secondary antibody. The red arrow shows the position of the *SynDLP* wt band. M = marker.

With the determination of the *SynDLP* structure (Chapter 4.1) (Gewehr *et al.*, 2023), the potential MIDs initially identified solely based on the primary sequence could be evaluated based on their localizations in the protein structure. The mutated residues in *SynDLP*_{694-705GS} (P694 – R705) are clearly not located at the tip of the stalk and, thus, are most likely not involved in membrane interaction (Fig. 4.44, gray). Therefore, the production of *SynDLP*_{694-705GS} was not further optimized. The residues A558 – V565 are located at one distal end of the stalk and could potentially be part of an MID (Fig. 4.44, cyan). However, biochemical analysis of *SynDLP*_{558-565GS} revealed intact lipid binding of the mutant (Fig. 4.41) and, conclusively, other protein regions must be responsible for membrane interaction.

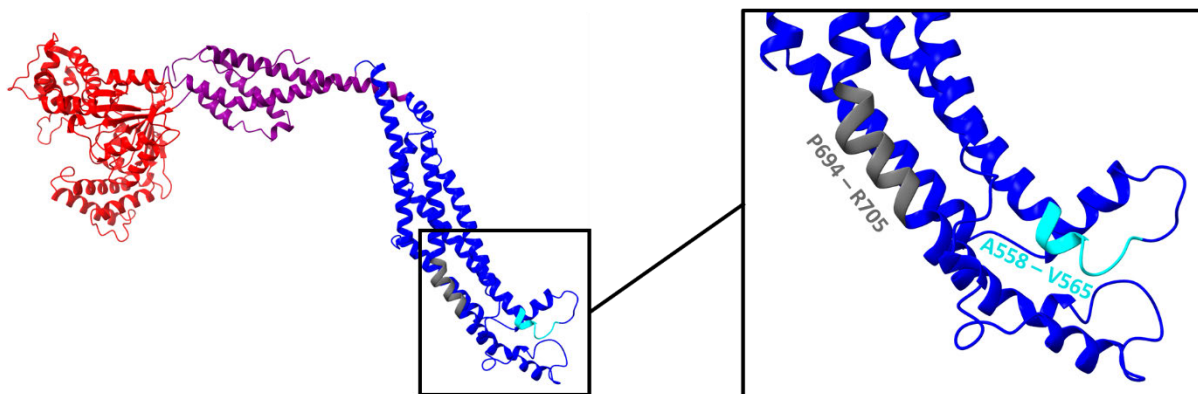


Figure 4.44: The structure of *SynDLP* wt clarifies the position of two putative MIDs that were identified solely based on the amino acid sequence.

Ribbon representation of the *SynDLP* monomer structure (PDB: 7ZW6). GD, BSE and stalk colored in red, purple and blue, respectively. The zoomed area highlights the positions of the amino acids A558 – V565 and P694 – R705 colored in cyan and gray, respectively.

*Analysis of potential MIDs based on the *SynDLP* structure*

The mutants analyzed in this chapter were generated based on the positions of the residues in the determined *SynDLP* structure. The mutants have already been introduced and their partial characterization described in Chapter 4.1 (Fig. 4.17) (Gewehr *et al.*, 2023). The results of further biochemical analysis of the *SynDLP* variants are presented below.

Analysis of *SynDLP*_{667-675GS}

Based on the *SynDLP* tertiary structure, a putative MID was identified as a loop at the tip of the stalk (Fig. 4.45a). The monomer model revealed that the loop includes amino acids Q667 – Q675 and, thus, a mutant with the substitution of Q667 – Q675 by a (GSGSGSGSG)-linker was created (*SynDLP*_{667-675GS}). The mutant was expressed and purified as described for *SynDLP* wt. An SDS-PAGE gel of the purified protein with an intact intramolecular disulfide bridge is shown in Chapter 4.1, Fig. 4.17c. The secondary structure of *SynDLP*_{667-675GS} was checked via CD spectroscopy. The wt-like shape of the CD spectrum indicated proper folding of the mutant protein on a secondary structure level (Fig. 4.45b). The thermodynamic stability of the mutant protein was investigated by means of CD spectroscopy and an ANS-FTSA. Both experiments showed a slight decrease in the melting temperature of *SynDLP*_{667-675GS} compared to *SynDLP* wt by either 1.0°C ($T_{m, CD}$) or 2.6°C ($T_{m, ANS-FTSA}$) (Fig. 4.45c, d, Table 4.8). Protein oligomerization was studied by analytical SEC, indicating a wt-like oligomerization of *SynDLP*_{667-675GS} with a tendency to form partially larger assemblies than *SynDLP* wt (Fig.

4.45e). The GTPase activity of *SynDLP*_{667-675GS} was slightly reduced and reached approx. 80% of the wt. The K_m value of the mutant was decreased compared to *SynDLP* wt (Fig. 4.45f, Table 4.8).

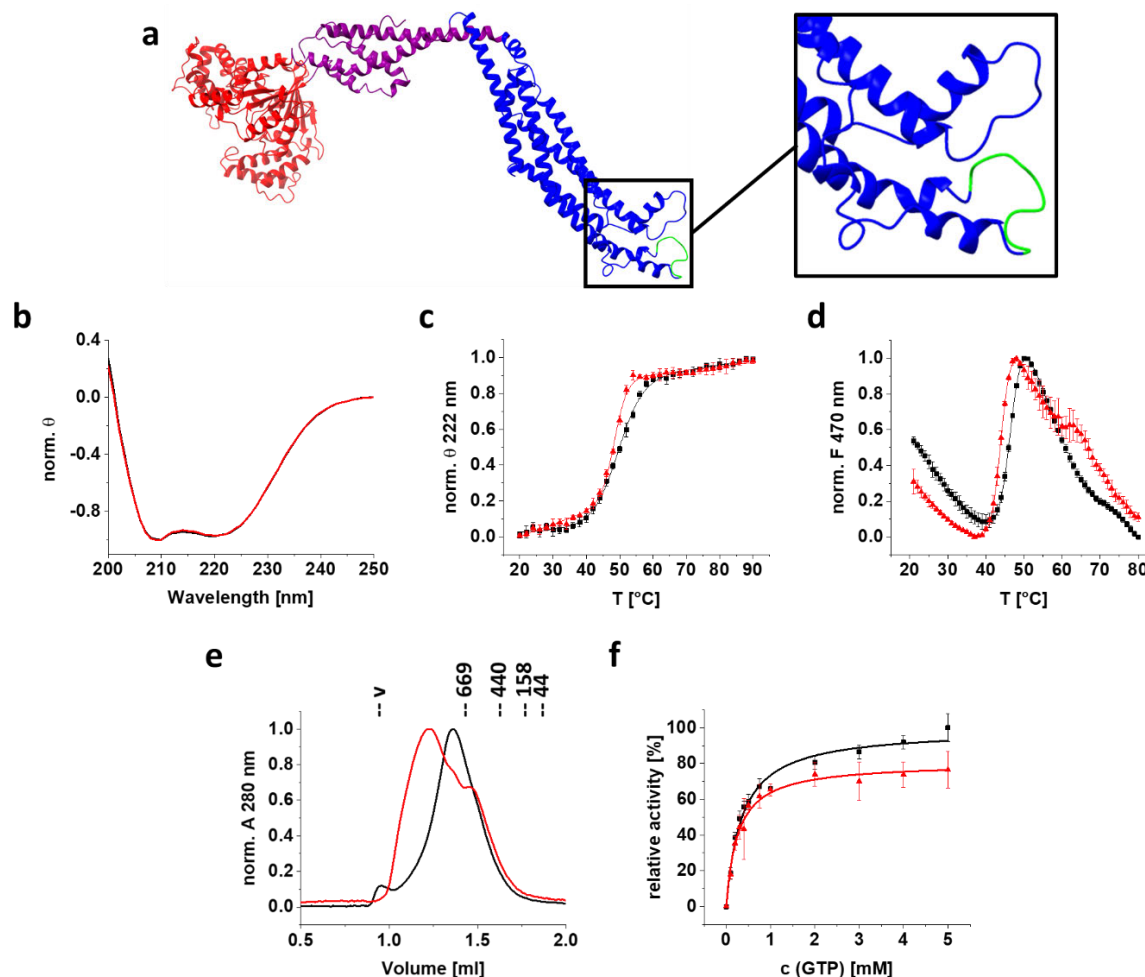


Figure 4.45: Biochemical analysis of the *SynDLP*_{667-675GS} mutant.

(a) Structure of a *SynDLP* monomer (PDB: 7ZW6) in ribbon representation. The GD, BSE and stalk are colored in red, purple and blue, respectively, and the zoomed area highlights the loop containing the mutated residues Q667 – Q675 colored in green. (b) Comparison of the CD spectra of *SynDLP* wt (black) and *SynDLP*_{667-675GS} (red) measured in 10 mM HEPES buffer pH 7.4. The mean ($n = 3$) is shown. (c) CD spectra of *SynDLP* wt (black) and *SynDLP*_{667-675GS} (red) were recorded at increasing temperatures. The ellipticities at 222 nm were plotted against the temperature, normalized and fitted with an adapted Boltzmann fit (Equation (6)). The fit curves are displayed as lines. Mean ($n = 3$) and error bars (S.D.) are shown. (d) ANS-FTSA measurements of *SynDLP* wt (black) and *SynDLP*_{667-675GS} (red). ANS fluorescence intensities at 470 nm were plotted against the temperature and normalized. The temperature range that captures the transition phase was fitted with an adapted Boltzmann fit (Equation (7)). Fit curves are shown as lines. Mean ($n = 3$) and error bars representing S.D. are displayed. © Protein molecular mass estimation was performed using analytical SEC of *SynDLP* wt (black) and *SynDLP*_{667-675GS} (red) with a Superose™ 6 Increase 3.2/300 column equilibrated with reaction buffer. The elution peak positions of common standard proteins and their corresponding molecular masses are indicated (v = void volume). (f) GTPase activity of *SynDLP* wt (black) compared to *SynDLP*_{667-675GS} (red). Mean ($n = 3$) and error bars (S.D.) are shown. Data points were fitted using the Michaelis-Menten equation (Equation (3)). The fit curves are displayed as lines. Relative activities were obtained by setting the maximum activity of *SynDLP* wt to 100%.

Next, membrane interaction of *SynDLP*_{667-675GS} was investigated. The results of the Laurdan fluorescence assay with the mutant were already presented and discussed in Chapter 4.1 (Fig. 4.17d) (Gewehr *et al.*, 2023). A gene encoding a *SynDLP*_{667-675GS} variant with an N-terminal mEGFP-tag (mEGFP-*SynDLP*_{667-675GS}) was constructed. The resulting gene was expressed and the protein was purified as *SynDLP*_{667-675GS}, yielding a pure protein (Fig. 4.46a, lane +) with an intact intramolecular disulfide bridge (Fig. 4.46a, lane -). The mEGFP-tag slightly inhibited the GTPase activity of *SynDLP*_{667-675GS} (Fig. 4.46b). However, the fluorescently tagged protein was still a highly active GTPase and therefore used for the GUV membrane binding assay. Here, mEGFP-*SynDLP*_{667-675GS} was able to bind to GUVs only in the presence of GTP and GDP (Fig. 4.46c), as observed before with the mEGFP-*SynDLP* wt (Fig. 4.37, Table 4.9). Conclusively, the GUV membrane binding assay confirmed a wt-like membrane interaction of *SynDLP*_{667-675GS}, as already shown by the Laurdan fluorescence assay (Fig. 4.17d), proving that the residues Q667 – Q675 are not (alone) responsible for membrane binding.

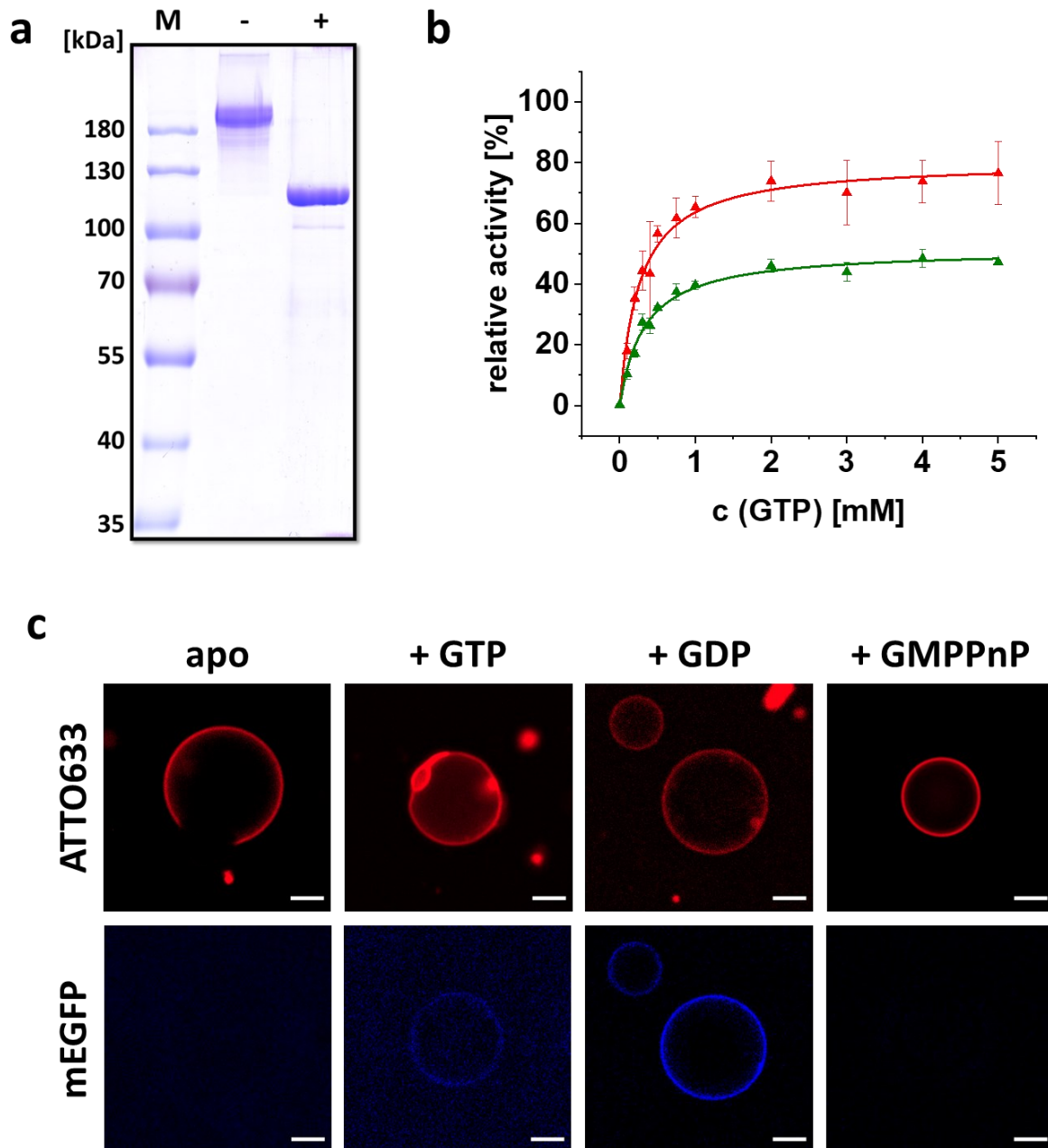


Figure 4.46: Membrane interaction of *SynDLP*_{667-675GS}.

(a) The purity of isolated mEGFP-*SynDLP*_{667-675GS} was checked via SDS-PAGE in the presence of 0.1 mM DTT (lane -) or 100 mM DTT (lane +). The calculated molecular mass of the chimeric protein is 122 kDa. As the SDS-PAGE analysis revealed a single band between 100 and 130 kDa (lane +) without further protein bands, the protein was $\geq 95\%$ pure. M = marker. (b) GTPase activities of *SynDLP*_{667-675GS} with (green) and without (red) an N-terminal mEGFP-tag measured with a continuous, regenerative, coupled assay. Mean ($n = 3$) and error bars (S.D.) are shown. The data points were fitted with Equation (3). GTPase activities are shown relative to the maximum activity of *SynDLP* wt as shown in Fig. 4.45f. (c) Binding of *SynDLP*_{667-675GS} to GUV membranes was tested using GUVs (70% DOPC/30% DOPG, w/w , ATTO633-PE as fluorescent dye). 0.8 μ M mEGFP-*SynDLP*_{667-675GS} was added to the GUVs. After 5 min 1 mM nucleotide was added. GUV fluorescence (red) and mEGFP fluorescence (blue) were recorded in the ATTO633 and the mEGFP channel, respectively. Image acquisition was conducted after 1 to 2 h incubation. White bars scale for 5 μ m.

Analysis of *SynDLP*_{648-665GS}

Another potential membrane binding site of *SynDLP* formed by the residues P648 – L665 at the tip of the stalk domain was identified based on the quaternary structure of filamentous *SynDLP* oligomers (Fig. 4.17a) (Fig. 4.47a). This protein region is partially α -helical and the thermal denaturation curve of *SynDLP* wt in the presence of DOPG liposomes indicated that a potentially α -helical part of the protein exhibited a higher thermodynamic stability after membrane binding (Figs. 4.33, 4.34). In the mutated protein (*SynDLP*_{648-665GS}) the residues P648 – L665 were replaced by a (GS)₉-linker. *SynDLP*_{648-665GS} was expressed and purified like *SynDLP* wt and the purity of the protein as well as the correct formation of the intramolecular disulfide bridge were already shown in Chapter 4.1 (Fig. 4.17c) (Gewehr *et al.*, 2023). The wt-like shape of the CD spectrum indicated proper folding of *SynDLP*_{648-665GS} on a secondary structure level (Fig. 4.47b). The thermodynamic stability of the mutant was measured via CD spectroscopy and an ANS-FTSA. Both methods showed a lowered melting temperature of *SynDLP*_{648-665GS} compared the *SynDLP* wt, as the $T_{m, CD}$ and the $T_{m, ANS-FTSA}$ were reduced by 3.6°C and 1.7°C, respectively (Fig. 4.47c, d, Table 4.8). Noteworthy, the initial $F_{470\text{ nm}}$ values determined in the ANS-FTSA at low temperatures were increased for the *SynDLP*_{648-665GS} mutant, probably due to more ANS accessible surface regions in the mutant protein before thermal denaturation. This is in line with a hampered oligomerization of *SynDLP*_{648-665GS} as shown by analytical SEC (Fig. 4.47e). The mutant formed smaller assemblies than the wt, approx. in the range of tetramers and, thus, provided a larger ANS accessible protein surface. The GTPase activity of *SynDLP*_{648-665GS} was lowered and reached approx. 60% of the GTPase activity of *SynDLP* wt. The K_m of the mutant was also slightly reduced (Fig. 4.47f, Table 4.8).

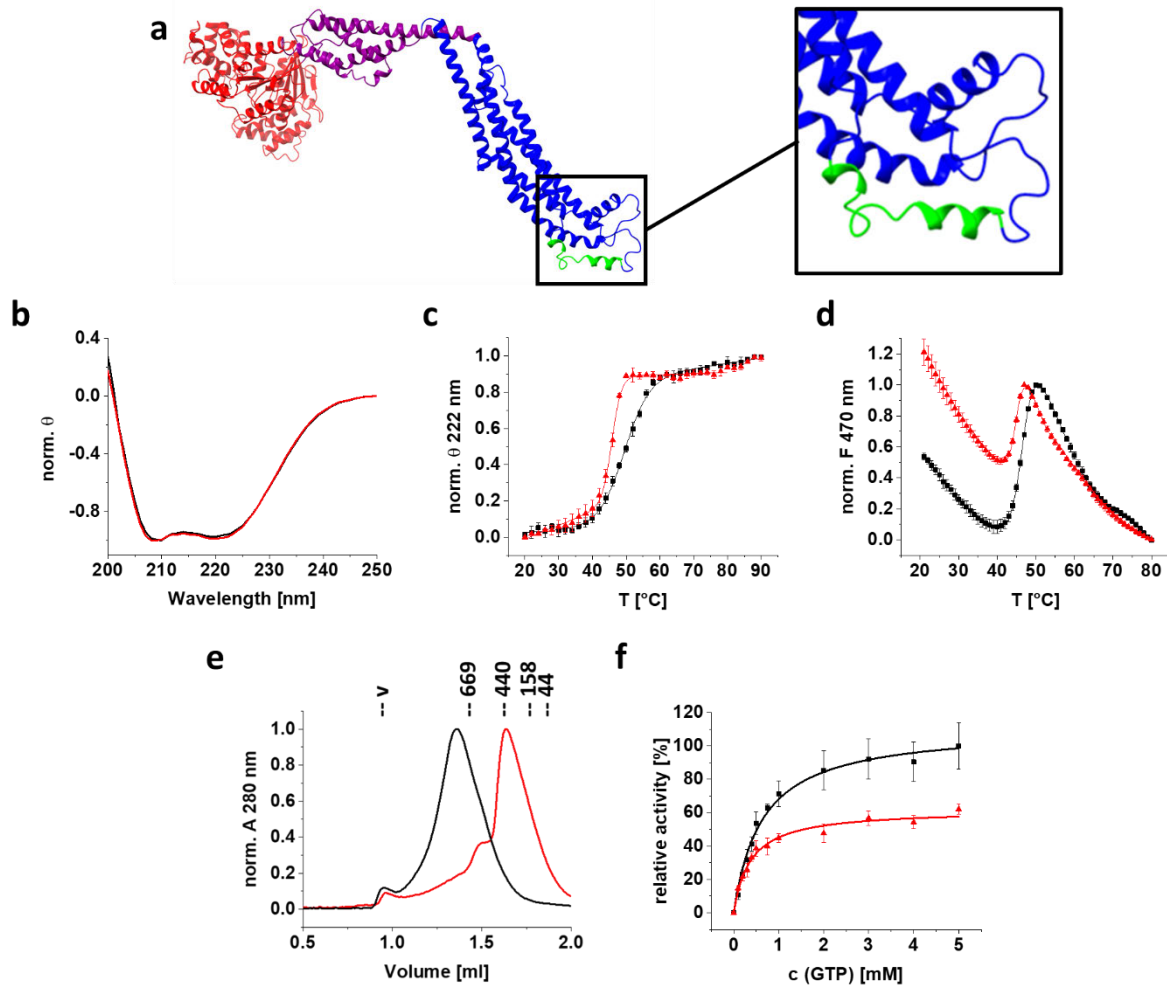


Figure 4.47: Biochemical analysis of the *SynDLP*_{648-665GS} mutant.

(a) *SynDLP* monomer structure (PDB: 7ZW6) in ribbon representation. The GD, BSE and stalk are colored red, purple and blue, respectively. The zoomed section shows the region containing the residues P648 – L665, which were mutated to a GS-linker in *SynDLP*_{648-665GS}, colored in green. (b) CD spectra of *SynDLP* wt (black) and *SynDLP*_{648-665GS} (red) measured in 10 mM HEPES buffer pH 7.4. Mean ($n = 3$) is shown. (c) Thermodynamic stability of *SynDLP* wt (black) and *SynDLP*_{648-665GS} (red) were analyzed by recording CD spectra at increasing temperatures. The ellipticities at 222 nm were plotted against the temperature and then normalized and fitted with an adapted Boltzmann fit (Equation (6)). The fit curves are shown as lines. Mean ($n = 3$) and error bars (S.D.) are shown. (d) ANS-FTSA measurements of *SynDLP* wt (black) and *SynDLP*_{648-665GS} (red) at increasing temperatures. ANS fluorescence intensities at 470 nm were plotted against the temperature, normalized to the main peak and the temperature range that captures the transition phase was fitted with an adapted Boltzmann fit (Equation (7)). Fit curves are displayed as lines. Mean ($n = 3$) and S.D. are shown. (e) Analytical SEC of *SynDLP* wt (black) and *SynDLP*_{648-665GS} (red) was performed using a SuperoseTM 6 Increase 3.2/300 column equilibrated with reaction buffer. The elution volumes of common standard proteins together with their corresponding molecular masses are indicated ($v =$ void volume). (f) GTPase activity of *SynDLP* wt (black) and *SynDLP*_{648-665GS} (red). Mean ($n = 3$) and error bars (S.D.) are shown. Data points were fitted using the Michaelis-Menten equation (Equation (3)). The fit curves are displayed as lines. The maximum activity of *SynDLP* wt was set to 100%.

The membrane interaction properties of *SynDLP*_{648-665GS} were studied via the Laurdan fluorescence assay and the GUV membrane binding assay. Binding of *SynDLP*_{648-665GS} to

DOPG-containing liposomes was previously shown in Chapter 4.1 with the Laurdan fluorescence assay (Fig. 4.17d) (Gewehr *et al.*, 2023). Now, a membrane binding curve with increasing *SynDLP*_{648-665GS} concentrations was measured to obtain information about the binding affinity of *SynDLP*_{648-665GS} to DOPG-containing liposomes. The binding curve showed the same biphasic behavior (Fig. 4.48a) as observed for other *SynDLP* variants (Fig. 4.41a, b) and therefore the data points were fitted using Equation (9). The resulting K_D value was determined to be 62.5 ± 9.1 nM, indicating a lowered liposome-binding affinity compared to *SynDLP* wt (Table 4.9). For the GUV membrane binding assay, an N-terminally mEGFP-tag was fused to *SynDLP*_{648-665GS} to generate the protein mEGFP-*SynDLP*_{648-665GS}, which was expressed and purified as described for untagged *SynDLP*_{648-665GS}. The purity as well as proper formation of the intramolecular disulfide bridge were verified via SDS-PAGE analysis (Fig. 4.48b). The GTPase activity measurement revealed a rather small influence of the mEGFP-tag on the activity of *SynDLP*_{648-665GS} (Fig. 4.48c). The GUV binding behavior of the mutant was exactly like all other so far analyzed *SynDLP* variants as the protein bound to GUVs solely in presence of GTP or GDP (Fig. 4.48d, Table 4.9). Taken together, these additional studies on the membrane interaction properties of *SynDLP*_{648-665GS} confirmed that the investigated region is not solely responsible for membrane binding of *SynDLP*.

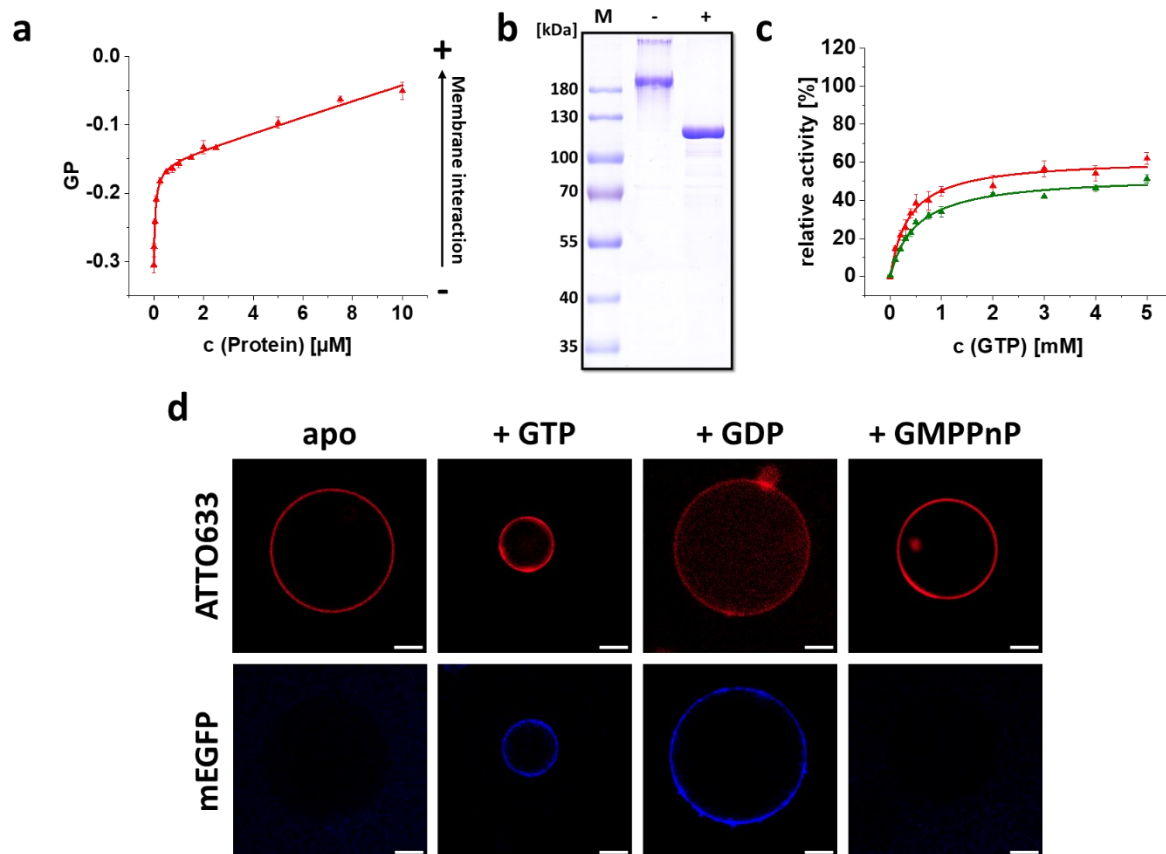


Figure 4.48: Membrane interaction of *SynDLP*_{648-665GS}.

(a) Fluorescence spectroscopy using Laurdan as a fluorescent probe. A binding curve showing binding of increasing *SynDLP*_{648-665GS} concentrations to LUVs (30% DOPG/70% DOPC, w/w, mixed with Laurdan at a 1:500 molar ratio) was generated. Laurdan fluorescence spectra were recorded after 1 h incubation of LUVs and protein. The ΔGP values were calculated from the spectra. Mean ($n = 3$) and error bars (S.D.) are shown. The data points were fitted using Equation (9). Arrow indicates increasing membrane interaction. (b) Purified mEGFP-*SynDLP*_{648-665GS} was analyzed via SDS-PAGE with 0.1 mM DTT (lane -) or 100 mM DTT (lane +). The protein has a calculated molecular mass of 122 kDa. The SDS-PAGE showed a single band between 100 and 130 kDa (lane +) without showing further protein bands, thus the protein was $\geq 95\%$ pure. M = marker. (c) GTPase activity of *SynDLP*_{648-665GS} (red) compared with an N-terminally mEGFP-tagged variant measured with a continuous, regenerative, coupled assay. Mean ($n = 3$) and error bars (S.D.) are shown. The data points were fitted using Equation (3). GTPase activities are shown relative to the maximum activity of the *SynDLP* wt (Fig. 4.47f). (d) Binding of *SynDLP*_{648-665GS} to GUVs was monitored using GUVs (70% DOPC/30% DOPG, w/w, ATTO633-PE as fluorescent dye). 5 min after the addition of 0.8 μM mEGFP-*SynDLP*_{648-665GS}, 1 mM nucleotide was added to the GUVs. The fluorescence of the GUVs (red) and mEGFP (blue) were recorded in the ATTO633 or the mEGFP channel, respectively. Images were acquired after incubation of 1 to 2 h. The white bars scale for 5 μm .

Analysis of *SynDLP*_{HPRN-AAAA}

The biochemical characterization of *SynDLP*_{HPRN-AAAA} has been described previously in Chapter 4.1 (Fig. 4.15) (Gewehr *et al.*, 2023). It was shown that the residues ⁵⁵²HPRN⁵⁵⁵ are critical for assembly of higher-order *SynDLP* oligomers. As the HPRN-motif is located at one distal end of the stalk domain (Figs. 4.3h, 4.14a), an involvement of these residues in membrane interaction cannot be excluded. Therefore, membrane binding of *SynDLP*_{HPRN-AAAA} was tested. A membrane binding curve was measured in presence of DOPG-containing liposomes using the Laurdan fluorescence assay. The protein clearly bound to the liposomes and the curve followed a biphasic course (Fig. 4.49a). The dissociation constant was determined to be 36.3 ± 3.1 nM, and, thus, the *SynDLP*_{HPRN-AAAA} membrane-binding affinity is comparable to *SynDLP* wt (Table 4.9). For GUV binding studies, *SynDLP*_{HPRN-AAAA} containing an N-terminal mEGFP-tag (mEGFP-*SynDLP*_{HPRN-AAAA}) was expressed and purified as described for untagged *SynDLP*_{HPRN-AAAA}, resulting in a pure mEGFP-fusion protein (Fig. 4.49b, lane +) with an established intramolecular disulfide bridge (Fig. 4.49b, lane -). The mEGFP-tag slightly reduced the GTPase activity of *SynDLP*_{HPRN-AAAA} (Fig. 4.49c). Nevertheless, mEGFP-*SynDLP*_{HPRN-AAAA} still was a functional GTPase and therefore used in the GUV membrane binding assay. Binding of *SynDLP*_{HPRN-AAAA} to the GUV surface was only observable after the addition of GTP or GDP (Fig. 4.49d), as observed before for other *SynDLP* variants (Table 4.9). Conclusively, these experiments showed that neither the residues of the HPRN-motif nor the ability to oligomerize are critical for membrane binding of *SynDLP*.

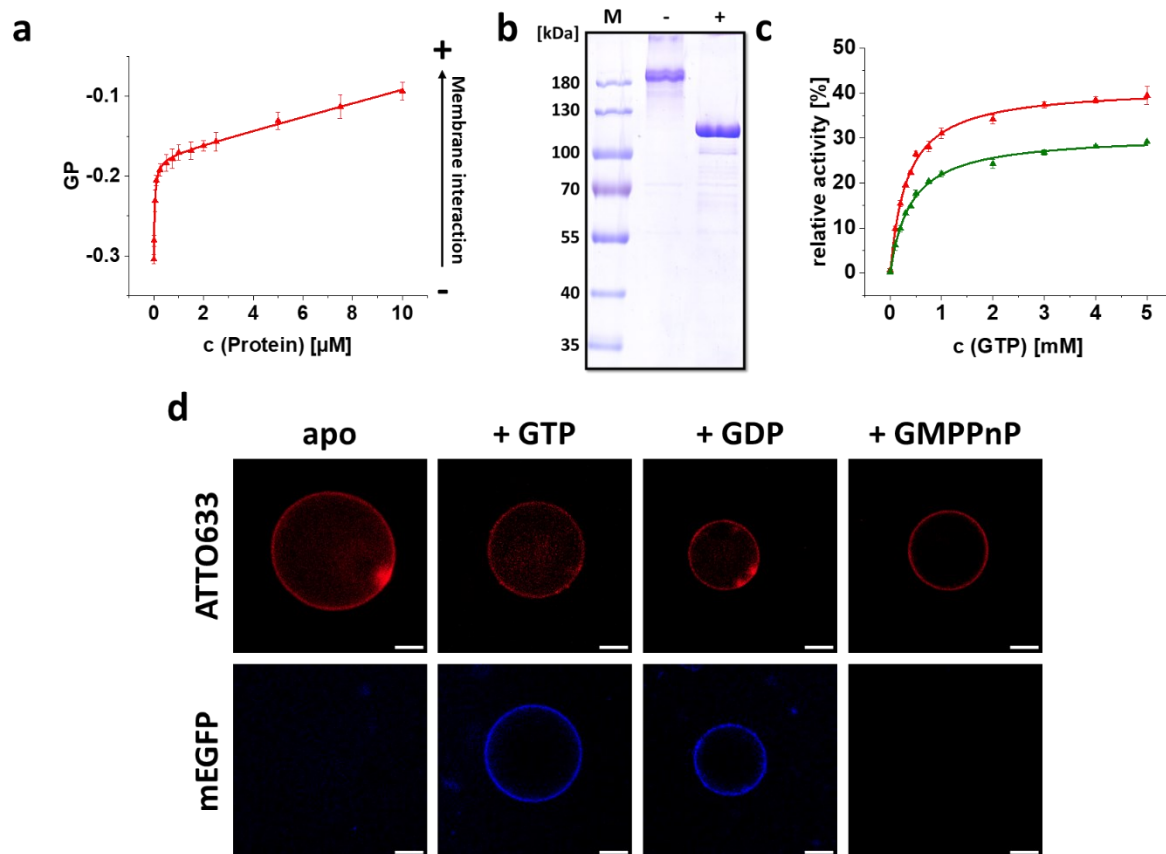


Figure 4.49: Membrane interaction of $\text{SynDLP}_{\text{HPRN-AAAA}}$.

(a) Fluorescence spectroscopy monitoring the fluorescent probe Laurdan. The curve shows binding of different $\text{SynDLP}_{\text{HPRN-AAAA}}$ concentrations to LUVs (30% DOPG/70% DOPC, w/w, mixed with Laurdan at a 1:500 molar ratio). Laurdan fluorescence spectra were recorded after 1 h incubation of protein and LUVs, and ΔGP values were calculated from the spectra. Mean ($n = 3$) and error bars (S.D.) are shown. The data points were fitted using Equation (9). The arrow indicates increasing membrane interaction. (b) Purity of mEGFP- $\text{SynDLP}_{\text{HPRN-AAAA}}$ was analyzed by SDS-PAGE in the presence of 0.1 mM DTT (lane -) or 100 mM DTT (lane +). The calculated molecular mass of the protein is 122 kDa. The SDS-PAGE revealed a single band between 100 and 130 kDa (lane +) without showing further protein bands, thus the protein was $\geq 95\%$ pure. M = marker. (c) GTPase activity of $\text{SynDLP}_{\text{HPRN-AAAA}}$ (red, data from Chapter 4.1, Fig. 4.15f (Gewehr *et al.*, 2023)) compared with the N-terminally mEGFP-tagged variant measured in a continuous, regenerative, coupled assay. Mean ($n = 3$) and error bars (S.D.) are shown. The data points were fitted using Equation (3). The GTPase activities are shown relative to the maximum activity of the SynDLP wt measurement in Chapter 4.1, Fig. 4.15f (Gewehr *et al.*, 2023). (d) A membrane binding assay was performed with GUVs (70% DOPC/30% DOPG, w/w, ATTO633-PE as fluorescent dye). 5 min after the addition of $0.8 \mu\text{M}$ mEGFP- $\text{SynDLP}_{\text{HPRN-AAAA}}$, 1 mM nucleotide was added to the GUVs. The GUV fluorescence (red) and the mEGFP fluorescence (blue) were recorded in the ATTO633 and the mEGFP channel, respectively. Images were acquired after incubation of 1 to 2 h. The white bars scale for $5 \mu\text{m}$.

The results from the characterization of several mutants lacking a potential MID of SynDLP are summarized in Tables 4.8, 4.9. Albeit the mutations partially influenced the biochemical properties of SynDLP , e.g. oligomerization and GTPase activity, none of the mutations completely abolished the membrane binding ability of SynDLP .

Table 4.8: Biochemical properties of proteins analyzed in this study. The values derived from experiments shown in Figs. 4.15, 4.39, 4.45, 4.47.

Mutation	$\Delta T_{m, CD}$ [°C]	$\Delta T_{m, ANS-FTSA}$ [°C]	Oligomerization relative to wt	GTPase activity [% wt]	K_m [mM]
wt	± 0	± 0	=	100	0.53 ± 0.16
558-565GS	-5.0	-*	↓	40.1 ± 1.8	0.35 ± 0.06
667-675GS	-1.0	-2.6	↑	81.0 ± 2.0	0.26 ± 0.03
648-665GS	-3.6	-1.7	↓	57.6 ± 2.4	0.40 ± 0.06
HPRN-AAAA	-3.1	-1.8	↓	38.2 ± 0.5	0.33 ± 0.02

* Not measured in this study.

Table 4.9: Membrane interaction properties of proteins analyzed in this study. K_D values and GUV observations derived from Figs. 4.37, 4.41, 4.46, 4.48, 4.49.

Mutation	$K_D, \text{Laurdan}$ [nM]	GUV binding			
		apo	+ GTP	+ GDP	+ GMPPnP
wt	28.3 ± 9.3	×	✓	✓	×
558-565GS	17.1 ± 8.3	×	✓	✓	×
667-675GS	-*	×	✓	✓	×
648-665GS	62.5 ± 9.1	×	✓	✓	×
HPRN-AAAA	36.3 ± 3.1	×	✓	✓	×

* Not measured in this study.

Quantification of SynDLP-membrane interaction via SPR spectroscopy

Membrane binding of *SynDLP* was so far quantified using the fluorescent probe Laurdan incorporated into model membrane systems. Laurdan changes its fluorescent properties dependent on the direct membrane environment of the fluorophore. Thus, protein binding to the membrane surface is only indirectly measured via the Laurdan fluorescence emission. Therefore, in the literature the fluorescent probe Laurdan is typically not used to determine dissociation constants. Common applications of Laurdan are the determination of phase transitions in membranes via fluorescent spectroscopic measurements or the observation of spatially resolved membrane dynamics under the fluorescence microscope (Bagatolli, 2013; Gunther *et al.*, 2021).

For a more reliable quantification of *SynDLP* binding to model membranes, the method of SPR spectroscopy was tested, which is an optical method allowing a highly sensitive determination of binding affinities between an immobilized ligand and a soluble analyte. In an initial approach, an L1 sensor chip (Cytiva, Munich, GER) was used. The L1 sensor chip is covered with lipophilic groups and can be used to capture intact LUVs while maintaining the lipid bilayer. However, experiments with the L1 sensor chip failed, since the analyte *SynDLP* unspecifically bound to the surface of the L1 sensor chip, probably due to interactions of hydrophobic patches of the protein with the lipophilic groups of the chip surface.

Next, the SA sensor chip was tested, which is covered with streptavidin and, thus, should not interact with *SynDLP*. LUVs were prepared containing 99.5% DOPG to allow *SynDLP* binding plus 0.5% biotinyl-Cap-DOPE to allow immobilization of the biotinylated LUVs on the SA sensor chip surface. The LUVs were successfully immobilized on the surface of an SA sensor chip, as indicated by increasing RU values after the flow of liposomes over the flow cell (Fig. 4.50a). Noteworthy, the following results, which represent sensorgrams after protein injection, show the net response after subtracting the blank sensorgrams. The blank sensorgrams were obtained by the injection of protein over a flow cell without immobilized LUVs, and therefore the blank sensorgrams correct for non-specific protein binding to the chip surface. In a test run, the injection of 500 nM of the analyte *SynDLP* over a flow cell immobilized with LUVs showed a clear RU increase and, thus, binding of the protein to the LUVs (Fig. 4.50b). To determine protein binding affinities, the usual SPR spectroscopy workflow would include the following steps: 1) immobilization of the ligand (LUVs); 2) binding of a small concentration of the analyte (*SynDLP*) to the ligand = association; 3) complete dissociation of the analyte from the ligand by rinsing with buffer; 4) repetition of the steps 2 and 3 with increasing analyte concentrations to finally obtain an analyte binding curve. However, *SynDLP* binds tightly to 99.5% DOPG-containing LUVs and the protein could not be rinsed off the liposomes with buffer. Even substances that are commonly used to wash off proteins, *e.g.*, 10% DMSO, were not applicable, as the response stayed constant after flowing 10% DMSO over the flow cell. A second addition of 500 nM *SynDLP* even led to a further increase of the RU value (Fig. 4.50b).

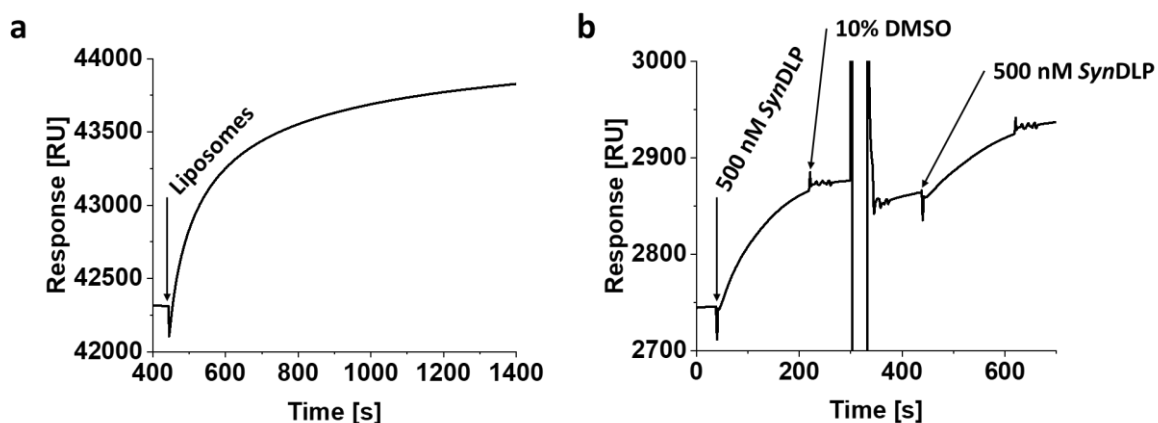


Figure 4.50: Immobilization of liposomes on an SA sensor chip.

(a) Liposomes (99.5% DOPG/0.5% biotinyl-Cap-DOPE, *w/w*) were loaded on an SA sensor chip at the time point indicated by an arrow and the change in response was measured over the time. Flow rate = 10 $\mu\text{l}/\text{min}$. (b) After immobilization of the ligand (liposomes, shown in (a)), 500 nM *SynDLP* was added as the analyte to the flow cell (time point marked by an arrow). Then 10% DMSO was added to remove the bound protein from the liposomes. As the measured response did not fall to the initial level, the protein remained bound to the liposomes. A second addition of 500 nM *SynDLP* led to a further response increase.

Therefore, the typical SPR spectroscopic workflow was adapted towards a single cycle measurement. Here, increasing protein concentrations were injected over identical immobilized liposomes. The protein injections were interrupted by short dissociation phases with reaction buffer and not by a complete dissociation of bound protein. A single cycle measurement with increasing *SynDLP* concentrations is shown in Fig. 4.51a. The measurement again showed binding of the protein to the liposomes. From the fit curve the maximum responses after injection of the increasing *SynDLP* concentrations were obtained and plotted against the protein concentration (Fig. 4.51b). The binding curve was plotted assuming a 1:1 binding model and a K_D value of $2.29 \pm 0.49 \mu\text{M}$ was determined.

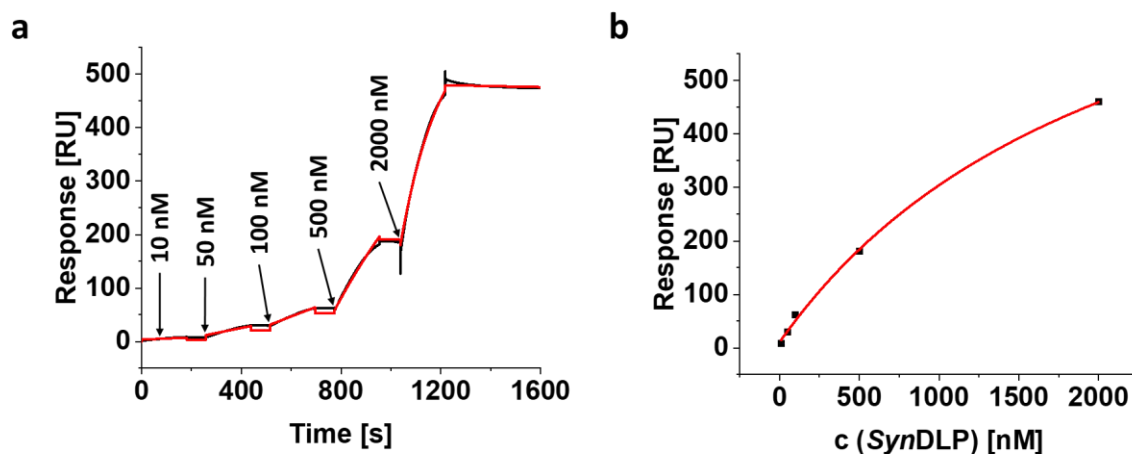


Figure 4.51: Single cycle measurement of *SynDLP* binding to DOPG liposomes.

(a) Liposomes (99.5% DOPG/0.5% biotinyl-Cap-DOPE, *w/w*) were immobilized on an SA sensor. The SPR sensorgram showed binding of increasing *SynDLP* concentrations in a single cycle measurement. The time points of the addition of the respective *SynDLP* concentrations are marked by arrows. The measured response over time is shown in black and the fit curve generated using the software supplied by the manufacture in red. Flow rate = 30 $\mu\text{l}/\text{min}$, contact time = 180 s per protein concentration. (b) The maximum responses from the fit curve in (a) of the respective *SynDLP* concentrations were plotted against the protein concentration. The data points were fitted by the manufacture's software using Equation (11) and the fit curve is shown in red.

A single cycle measurement was also performed in the presence of 2 mM GTP to test a potential influence of a nucleotide on the binding affinity of *SynDLP* to DOPG-containing membranes (Fig. 4.52a). After fitting the plotted maximum responses at the increasing *SynDLP* concentrations (Fig. 4.52b), the K_D value was determined to be $3.79 \pm 0.83 \mu\text{M}$ and, thus, in a similar range as determined for nucleotide-free *SynDLP*. Conclusively, SPR spectroscopy can be used to quantify membrane interaction of *SynDLP*. With this method, no significant influence of GTP on binding of *SynDLP* to DOPG liposomes was detected.

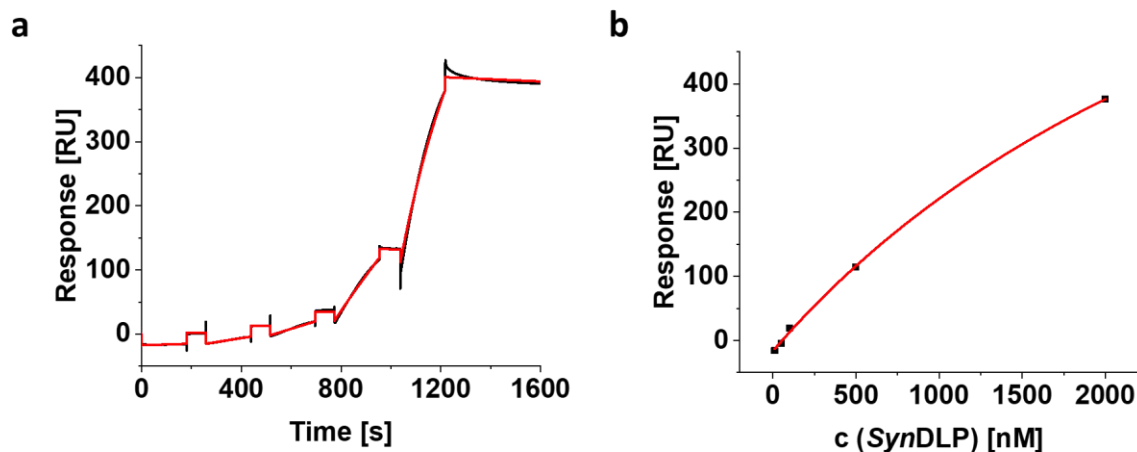


Figure 4.52: Single cycle measurement of *SynDLP* binding to DOPG liposomes in the presence of GTP.

(a) Liposome immobilization (99.5% DOPG/0.5% biotinyl-Cap-DOPE, *w/w*) was performed on an SA sensor. The single cycle measurement showed binding of *SynDLP* (concentrations and time points analogous to Fig. 4.51a) in the presence of 2 mM GTP. The kinetic of the measured response is shown in black and fitted by the manufacturer's software (red curve). Flow rate = 30 μ l/min, contact time = 180 s per protein concentration. (b) The maximum RU values from the fit curve in (a) were plotted against the protein concentration. The data points were fitted by the manufacturer's software using Equation (11). The fit curve is shown as a red line.

4.3.3 Discussion

A prerequisite of a membrane remodeling DLP is its interaction with membranes. The membrane interaction properties of *SynDLP* have already been analyzed to some extent using different methods. A Laurdan fluorescence assay revealed binding of *SynDLP* to liposomes that contain negatively charged lipids. The strongest interaction was observed with the phospholipid PG (Chapter 4.1, Fig. 4.16a, b). SFG spectroscopy showed binding and intercalation of *SynDLP* into a planar DMPG monolayer (Chapter 4.1, Fig. 4.16c, d) (Jilly, 2018; Gewehr *et al.*, 2023). The effect of nucleotide addition on *SynDLP*'s membrane interaction has been investigated using SFG spectroscopy, which indicated no dramatic conformational changes of membrane-bound *SynDLP* in the presence of GTP (Chapter 4.1, Fig. 4.20) (Gewehr *et al.*, 2023).

Here, membrane binding to GUVs was tested as an alternative method to analyze membrane interaction of *SynDLP*, particularly with respect to nucleotide-dependent membrane binding. Therefore, an mEGFP-tagged *SynDLP* variant was produced to directly observe binding of the protein to fluorescently labeled GUVs under the fluorescence microscope. GTPase activity and oligomerization of the mEGFP-*SynDLP* fusion protein were hardly influenced (Fig. 4.35b, c) and mEGFP-*SynDLP* bound to DOPG-containing GUVs after addition of a nucleotide (Fig. 4.36). Thus, the GUV membrane binding assay works in principle and can also be performed

in the presence of nucleotides. Binding of mEGFP-*SynDLP* to GUVs strictly depended on the addition of the nucleotides GTP or GDP, albeit the membrane interaction of *SynDLP* was nucleotide-independent in former experiments (Chapter 4.1, Figs. 4.16, 4.20, 4.21, 4.22, 4.24) (Gewehr *et al.*, 2023). SPR spectroscopy was tested in this study as a method to quantitatively describe the binding of *SynDLP* to liposomes. While binding of *SynDLP* to DOPG could be confirmed (Fig. 4.51), SPR spectroscopy also showed no effect of GTP on membrane interaction of *SynDLP* (Fig. 4.52). For the bent half-moon shaped *SynDLP* oligomers (Chapter 4.1, Fig. 4.3b), the GUV membrane surface probably appears rather planar due to the relatively large size of the GUVs in the range of 5 – 20 μm . Thus, the nucleotide-dependent GUV membrane interaction of mEGFP-*SynDLP* could be a result of the altered membrane surface geometry compared to extruded LUVs with a size of ~ 100 nm, which likely appear as a curved surface for the *SynDLP* oligomers. However, this is in contrast to measurements on a planar DMPG monolayer using SFG spectroscopy, which revealed no impact of GTP at least on the conformation of membrane-bound *SynDLP* oligomers (Chapter 4.1, Fig. 4.20) (Gewehr *et al.*, 2023). Thus, the nucleotide-dependent membrane binding of *SynDLP* to GUVs most likely cannot be explained by nucleotide-induced conformational changes of *SynDLP* oligomers.

Interestingly, *SynDLP* bound to GUV membranes not only in the presence of GTP, but also when GDP was present (Fig. 4.37). The binding processes with both nucleotides were observed after a few minutes (< 20 min) incubation. A GDPase activity of *SynDLP* was identified using a malachite green phosphate assay (Fig. 4.38). In the field of DLPs, a similar function has been described so far only for the DLP subfamily of GBPs (Schwemmle and Staeheli, 1994; Prakash, Praefcke, *et al.*, 2000; Ghosh *et al.*, 2006; Kutsch and Coers, 2021). The GDs of DLPs are characterized by the four conserved motifs G1 – G4, as described above (Fig. 1.4) (Praefcke and McMahon, 2004; Daumke and Praefcke, 2016). In GBPs, the G4 motif, which is responsible for binding the guanine moiety of the substrate, differs from the conserved (N/T)KxD motif in that it contains no lysine and instead a functionally important arginine, resulting in an RD motif (Praefcke *et al.*, 1999; Prakash, Renault, *et al.*, 2000; Kutsch and Coers, 2021). The G4 motif of *SynDLP* consists of the amino acids $^{296}\text{NRID}^{299}$ (Fig. 4.3h, Fig. A7) and, thus, also contains an arginine near the conserved aspartate that is possibly involved in GDP hydrolysis catalyzed by *SynDLP*. Note that although several structures of GBP GDs exist, a comparison of active sites on a structural level between *SynDLP* and GBPs was not possible due to the intermediate resolution of the *SynDLP* GD in the cryo-EM structure (Chapter 4.1, Fig. 4.3d) (Gewehr *et al.*, 2023). However, the GDPase activity of *SynDLP* was very low with a calculated turnover number of $\sim 0.03 \text{ min}^{-1}$. The described high basal GTPase activity

revealed a >1000-fold higher turnover number (Chapter 4.1) (Gewehr *et al.*, 2023). As GUV membrane binding of *SynDLP* in the presence of GDP was observable after a few minutes, the measured GDP hydrolysis cannot explain this process. Moreover, the rather inefficient GDPase activity of *SynDLP* calls into question a physiological role of GDP hydrolysis by *SynDLP*. Apparently, the nucleotide hydrolysis energy is not the driving force for nucleotide-induced binding of *SynDLP* to GUV membranes. The observations indicate that the binding of GDP is critical for binding of *SynDLP* to GUV membranes.

Membrane binding and remodeling of other DLPs was also studied using GUVs. Eukaryotic Drp1 binds to GUVs mimicking the mitochondrial outer membrane in a nucleotide-independent manner. GUV membrane remodeling events caused by Drp1 are visible as membrane tubes under the fluorescence microscope (Ugarte-Urbe *et al.*, 2014). GUV membrane remodeling events were not observed for *SynDLP* regardless of the addition of GTP or GDP. The BDLP *MsIniA* binds and deforms GUVs in the apo state or in the presence of the non-hydrolysable GTP analog GMPPnP. Membrane remodeling by continuous cutting and finally rupture of GUVs can be observed for *MsIniA* after the addition of GTP. Thus, GUV membrane remodeling of *MsIniA* depends on the energy gained via GTP hydrolysis (Wang *et al.*, 2019). In summary, the GUV membrane activities of Drp1 and *MsIniA* differ from that of *SynDLP* as they bind to GUV membranes in the apo state and remodel GUV membranes. *SynDLP* bound to GUV membranes only in the presence of GTP or GDP. The nucleotide hydrolysis energy could not explain such a behavior (see above). Taken together, the mechanism behind the GTP/GDP-dependent GUV binding of *SynDLP* remains largely elusive and requires further experiments in the future.

In previous studies, typical methods for demonstrating the binding of a DLP to liposomes, such as *e.g.* a co-sedimentation assay, failed to detect the binding of *SynDLP* to DOPG liposomes (Jilly, 2018). As already mentioned, SPR spectroscopy was established in this study as a potential method to quantify binding of *SynDLP* to liposomes. In addition, the binding affinity of *SynDLP* was quantified using a Laurdan fluorescence assay. However, the Laurdan fluorescence assay is not an optimal method to determine dissociation constants of protein-liposome complexes, as discussed already above. Thus, the K_D values determined for *SynDLP* wt and mutants binding to liposomes containing 30% DOPG in the range of 10 – 70 nM appear to be unreliable (Table 4.9). Consequently, SPR spectroscopy was used to analyze *SynDLP* binding to liposomes for the first time with a BDLP. Liposomes containing 99.5% DOPG were immobilized on an SA sensor chip, as *SynDLP* showed strong unspecific interaction with the

L1 sensor chip surface. K_D values in the one-digit micromolar range for the binding of *SynDLP* to such liposomes were determined (Figs. 4.51, 4.52). Liposome binding of eukaryotic DLPs has been investigated in the past using SPR spectroscopy. Typically, the L1 sensor chip with a lipophilic surface is used for liposome immobilization (Jong and Lemmon, 2001; Kenniston and Lemmon, 2010; Bustillo-Zabalbeitia *et al.*, 2014). The specific interaction of Drp1 with cardiolipin was shown by SPR spectroscopy using liposomes immobilized on an L1 sensor chip (Bustillo-Zabalbeitia *et al.*, 2014). However, the experimental setup in said study did not include a suitable reference as the protein solution was not injected over a ligand-free flow cell. Therefore, possible nonspecific binding of Drp1 to the L1 sensor chip surface cannot be excluded and the results of this study are highly questionable. In another study, binding of Dyn1 to liposomes containing 3% phosphatidylinositol-(4,5)-bisphosphate was studied via SPR spectroscopy using the L1 sensor chip, resulting in a K_D value of 130 nM (Kenniston and Lemmon, 2010). The PH domain of dynamins is known to bind with high affinity to phosphatidylinositol-(4,5)-bisphosphate (Tuma, Stachniak and Collins, 1993; Salim *et al.*, 1996; Zheng *et al.*, 1996; Stowell *et al.*, 1999). The experimental setup for the investigation of Dyn1 binding to liposomes via SPR spectroscopy took advantage of the high affinity for phosphatidylinositol-(4,5)-bisphosphate, as the reference flow cell was simply coated with liposomes containing no phosphatidylinositol-(4,5)-bisphosphate (Jong and Lemmon, 2001; Kenniston and Lemmon, 2010). In summary, SPR spectroscopy is a valid method to study the liposome binding kinetics of DLPs. The binding of *SynDLP* to liposomes consisting of varying lipid species as well as the comparison of different *SynDLP* variants can be quantitatively measured via SPR spectroscopy in future experiments.

As described above, SFG spectroscopy measurements showed that *SynDLP* intercalates into PG-containing membranes (Chapter 4.1, Fig. 4.16) (Jilly, 2018; Gewehr *et al.*, 2023). Thermal denaturation in the presence of liposomes monitored via CD spectroscopy revealed an altered unfolding process of *SynDLP* in the presence of DOPG liposomes (Fig. 4.33). While the melting temperature is significantly decreased by $\sim 5^\circ\text{C}$ in presence of DOPG liposomes, a second denaturation step of a putatively α -helical protein region is initiated at temperatures $>70^\circ\text{C}$ (Figs. 4.33b, 4.34). This protein region is probably the MID of *SynDLP*, which is intercalated into the DOPG bilayer. However, the exact location of *SynDLP*'s MID could not be identified, albeit the cryo-EM structure was available. Several putative MIDs, identified based either on the primary sequence or the *SynDLP* structure (Fig. 4.53), were investigated in mutational studies. All mutant proteins were still able to interact with DOPG-containing model membranes as verified by the Laurdan fluorescence assay and the GUV membrane binding assay (Figs.

4.41, 4.46, 4.48, 4.49, Table 4.9). Thus, the MID of *SynDLP* probably consists of other protein regions or larger areas, *e.g.*, a combination of P648 – L665 and Q667 – Q675 (Fig. 4.53a). Identifying the position of the MID in *SynDLP* will be addressed in future studies and may benefit from more quantitative analyses of potential MID mutant proteins, *e.g.*, by SPR spectroscopy.

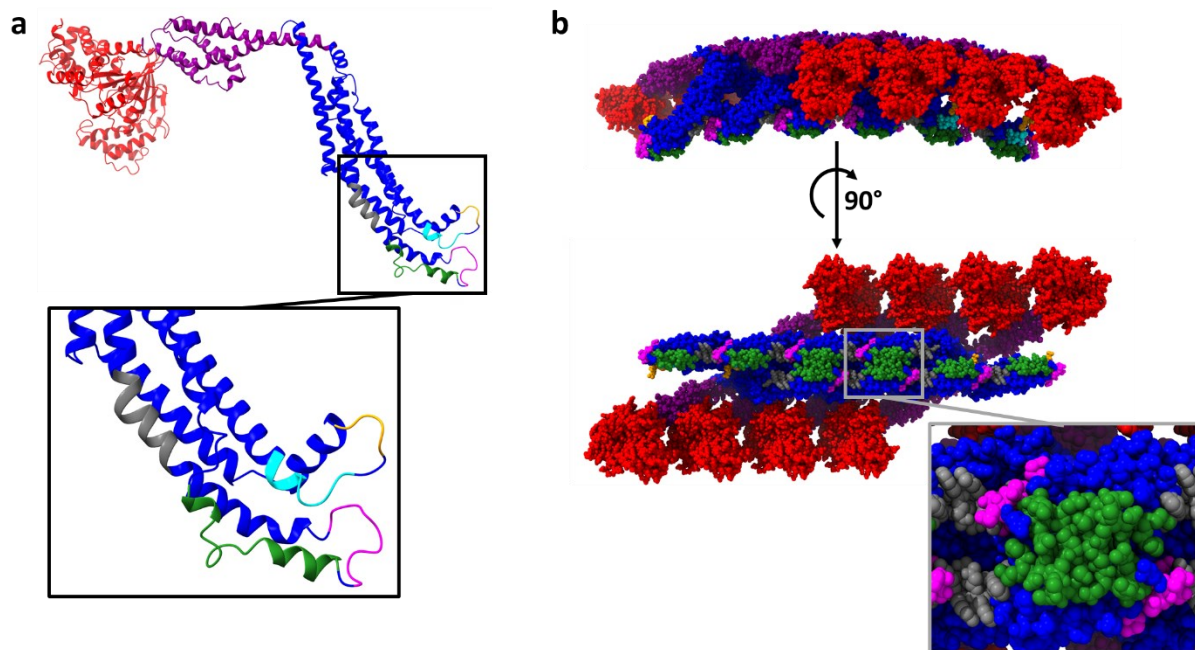


Figure 4.53: Localization of all *SynDLP* regions analyzed in this mutational study.

(a) *SynDLP* monomer structure (PDB: 7ZW6) in ribbon representation. Zoomed section highlights the spots of mutations that were biochemically analyzed. GD, BSE, and stalk are colored red, purple and blue, respectively. The mutated potential MIDs A558 – V565, Q667 – Q675 and P648 – L665 are colored in cyan, magenta and dark green, respectively, and the HPRN loop in orange. The residues P694 – R705, which were not biochemically characterized as the mutation resulted in an incorrectly folded protein, are colored in gray. (b) Oligomer model of *SynDLP* from two perspectives. Coloration as in (a).

The importance of oligomerization for the *SynDLP* GTPase activity has been discussed above (Chapter 4.1) (Gewehr *et al.*, 2023). In this study, each mutation of a potential MID affected the thermal stability, oligomerization and GTPase activity of *SynDLP* (Figs. 4.15, 4.39, 4.45, 4.47, Table 4.8), likely due to the complex and extensive interaction network in the stalk domain of oligomerized *SynDLP* (Figs. 4.7, 4.8a). While most mutations impaired the oligomerization ability of *SynDLP* (*SynDLP*_{558-565GS}, *SynDLP*_{648-665GS}, *SynDLP*_{HPRN-AAAA}), one mutation resulted in the formation of larger assemblies (*SynDLP*_{667-675GS}) (Table 4.8). However, intact filamentous shape and organization of such larger *SynDLP*_{667-675GS} assemblies could not be verified, since EM data of the mutants are not available. The stimulation of *SynDLP*'s GTPase activity by assembly was confirmed by significantly reduced GTPase activities of mutants in

which assembly was disrupted (Table 4.8). Apparently, the ability to form oligomers in solution is not a prerequisite for membrane binding of *SynDLP*.

Taken together, the membrane interaction properties of *SynDLP* were characterized. Therefore, two new methods were established: a GUV membrane binding assay for visualization of membrane binding events, which revealed membrane interaction of an mEGFP-labeled *SynDLP* variant in response to the addition of GTP or GDP, and SPR spectroscopy for quantitative analysis of liposome binding kinetics. Several mutants with substituted putative MIDs were biochemically characterized. While the mutations affected the thermodynamic stability, oligomerization and GTPase activity of *SynDLP*, none of the mutants showed impaired membrane interaction. Thus, the location of the MID in *SynDLP* remains elusive. Future studies will address the mechanism of nucleotide-dependent GUV membrane binding, quantification of membrane binding under different conditions by SPR spectroscopy as well as the location of the MID in *SynDLP*.

4.4 Nucleotide-dependent conformational changes in *SynDLP*

4.4.1 Introduction

DLPs are multidomain proteins that interact with membranes and hydrolyze GTP. They remodel membranes using the energy gained by GTP hydrolysis (Daumke and Praefcke, 2016). Typically, DLPs consist of a GD, BSE, stalk domain and MID (Chapter 1.3, Fig. 1.5) (Jimah and Hinshaw, 2018; Ford and Chappie, 2019). After binding to a membrane template, DLPs bind and hydrolyze GTP, which triggers conformational changes, such as relative movements of the domains to each other. The GTP hydrolysis cycle of DLPs has been elucidated in more detail: one GTP per monomer is bound in the GD in a conserved binding pocket and the GTP gets hydrolyzed. The cleavage of the λ -phosphate induces conformational changes and eventually domain movements. The DLP is in a GDP-bound state after release of the P_i . Upon GDP dissociation from the GD, a DLP structure switches back to the starting conformation. A new GTP molecule can bind to the enzyme in the apo state and the cycle is repeated (Chappie *et al.*, 2010; Wittinghofer and Vetter, 2011; Anand, Eschenburg and Reubold, 2016; Daumke and Praefcke, 2016).

Compared to other GTPases, such as Ras-like GTP-binding proteins, DLPs show a relatively high basal GTPase activity and therefore act independently of GAPs (Praefcke and McMahon, 2004; Gasper *et al.*, 2009; Chappie *et al.*, 2010; Karim and Aronsson, 2014; Karim *et al.*, 2014). However, fast GTP hydrolysis complicates the investigation of different DLP conformations during the GTP hydrolysis cycle. *E.g.*, the k_{cat} of the *SynDLP* GTPase activity is approx. 45 min^{-1} (Chapter 4.1) (Gewehr *et al.*, 2023), which complicates investigations of the GTP-bound state due to its short lifespan. It is possible to freeze the GTP-bound state by using a non-hydrolysable GTP analog, such as GMPPnP. Another tool for the investigation of the GTP hydrolysis cycle are nucleotide analogs, *e.g.*, GDP-AlF₄, that mimic the transition state after GTP hydrolysis and before P_i release (Fig. 4.54).

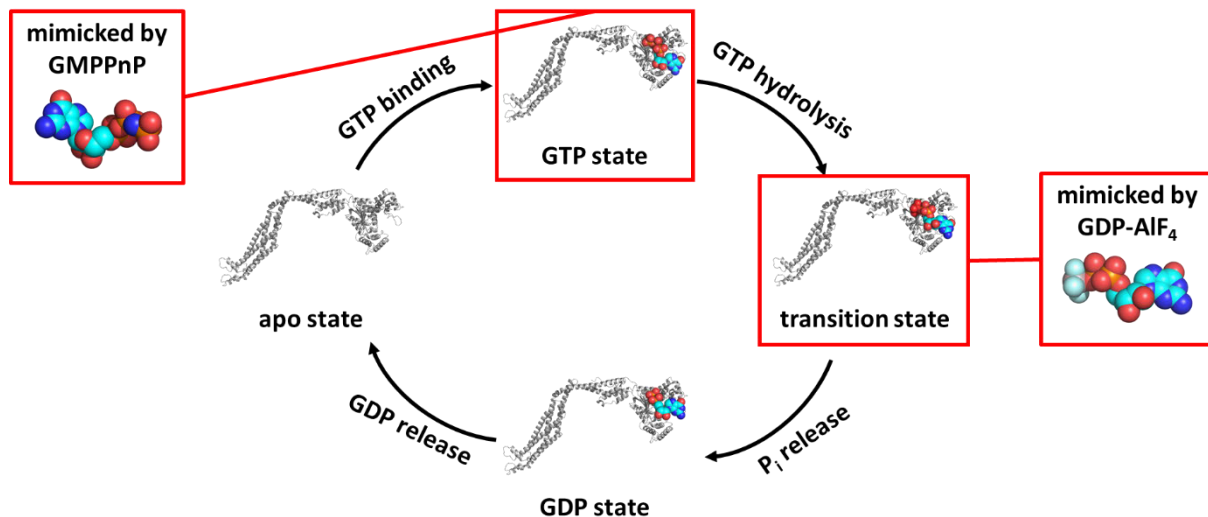


Figure 4.54: The GTP hydrolysis cycle of a DLP.

The individual steps during a GTPase cycle of a DLP are shown, starting from GTP binding to the enzyme in the apo state. The GTP-bound state can be frozen by GMPPnP binding. After GTP hydrolysis, the DLP-nucleotide complex is in a transition state, which can be mimicked by GDP-AIF₄ binding. P_i is released, resulting in a DLP in the GDP-bound state. Finally, GDP dissociates from the DLP and a new cycle starts by binding of GTP. The *SynDLP* structure (PDB: 7ZW6) was used as schematic DLP model. Models of the bound nucleotide analogs are shown as a calotte model.

I have shown above that the addition of the nucleotides GTP and GDP to *SynDLP*, the BDLP of *Synechocystis*, had a weak influence on the *SynDLP* oligomeric state when analyzed via a sedimentation assay (Fig. 4.4). In addition, the presence of GTP had no significant effect on membrane binding as detected by SFG and SPR spectroscopy (Figs. 4.20, 4.52) or on the membrane fusion activity of *SynDLP* (Fig. 4.24). Albeit the enhancement of the GTPase activity by membrane binding is reported for other DLPs (Jimah and Hinshaw, 2018), *SynDLP* did not exhibit a lipid-stimulated GTPase activity under all conditions tested so far (Fig. 4.21). The GTPase activity has been shown to follow a typical Michaelis-Menten kinetic (Jilly, 2018; Gewehr *et al.*, 2023). However, in the presence of low concentrations of GMPPnP, the enzymatic activity of *SynDLP* showed a sigmoid curve, suggesting cooperativity (Jilly, 2018). Moreover, *SynDLP* bound to GUV membranes in a GTP/GDP-dependent manner (Fig. 4.37).

Now, the effect of nucleotides, particularly GMPPnP and GDP-AIF₄, on oligomerization and conformational changes of *SynDLP* was investigated in more detail. Therefore, *SynDLP* was characterized and EM micrographs were taken in the presence of GMPPnP. Moreover, potential nucleotide-induced monomer interactions were studied by analyzing a truncated monomeric *SynDLP* variant.

4.4.2 Results

GMPPnP induces the formation of SynDLP aggregates with higher thermodynamic stability

The oligomerization of *SynDLP* in the presence of the nucleotides GTP and GDP was previously investigated using a sedimentation assay, which revealed only minor changes compared to the apo state of *SynDLP* (Chapter 4.1, Fig. 4.4). To obtain more information about oligomerization, and in particular the shape of the oligomers, negative stain EM micrographs of *SynDLP* were acquired in the presence of both nucleotides. Again, no significant differences were observed between *SynDLP* in its apo and GTP/GDP-bound states, since the oligomers appeared as bent half-moon shaped, highly ordered filaments in the presence of the nucleotides (Fig. 4.55).

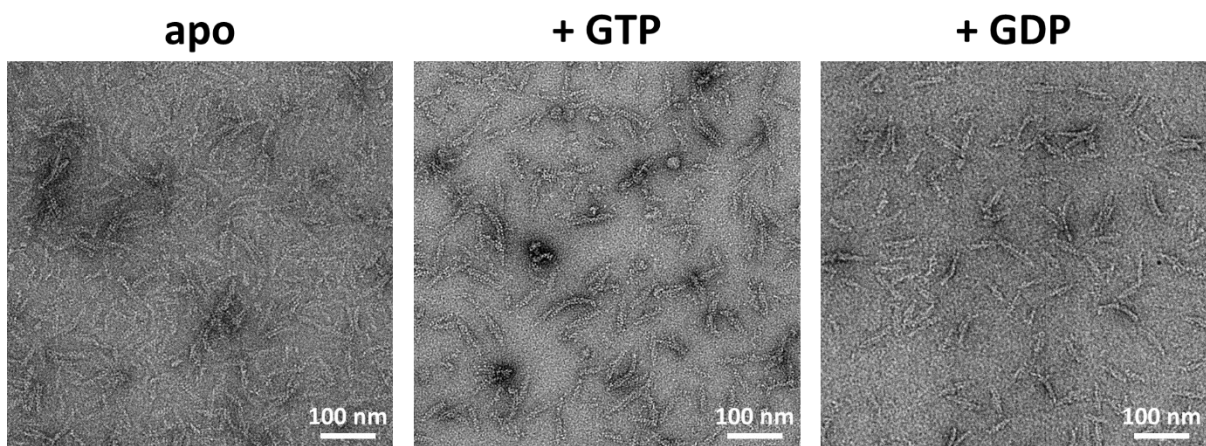


Figure 4.55: *SynDLP* oligomers in the presence of GTP and GDP.

Representative negative stain EM micrographs of 1 μ M *SynDLP* (apo) or 0.5 μ M *SynDLP* (+ GTP/GDP) in reaction buffer. 2 mM GTP or GDP were added, accordingly.

Next, oligomerization of *SynDLP* was studied in the presence of the non-hydrolysable GTP analog GMPPnP, which freezes the GTP-bound state of *SynDLP* (Fig. 4.54). Here, the sedimentation assay revealed a clear shift of *SynDLP* into the pellet fraction and, thus, indicating the formation of larger oligomers with GMPPnP (Fig. 4.56a, b). These GMPPnP-induced oligomers appeared as large, unstructured aggregates in EM micrographs that did not show the typical *SynDLP* filament structure observed for the apo state (Fig. 4.56c, d). Overall, the addition of GMPPnP resulted in dramatic conformational changes in the structure of *SynDLP* oligomers.

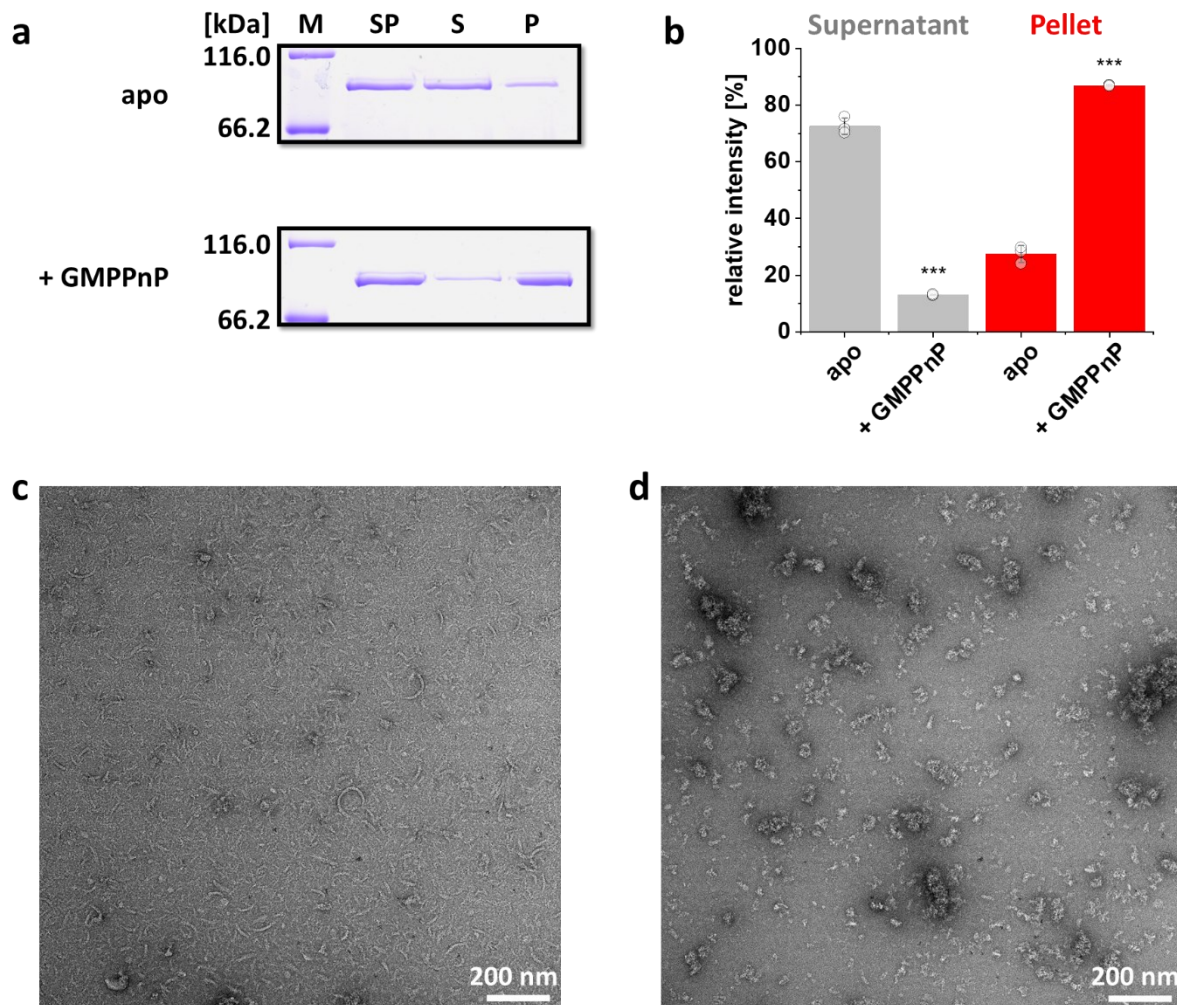


Figure 4.56: GMPPnP binding alters the structure of *SynDLP* oligomers.

(a) In a sedimentation assay, $0.5 \mu\text{M}$ *SynDLP* was incubated with or without 2 mM GMPPnP in reaction buffer at 4°C for 30 min. A representative gel showing *SynDLP* before ultracentrifugation (SP) and changes in the distribution of *SynDLP* into supernatant (S) and pellet (P) fractions depending on GMPPnP. (b) The band intensities of SDS-PAGE gels as shown in (a) were determined. Gray bars represent relative band intensities of the supernatant and red bars those of the pellet. Mean of independent experiments ($n = 3$) and error bars (S.D.) are shown. Single measurements are displayed as circles. ns = not significant ($P > 0.05$), * $P < 0.05$, ** $P < 0.01$, *** $P < 0.001$ based on a two-sided unpaired Student's t-test. The GMPPnP ($P = 0.000004$) bound state is compared to the respective apo state. (c) Representative negative stain EM image of $10 \mu\text{M}$ *SynDLP* in 20 mM HEPES pH 7.4, 50 mM NaCl, 7.5 mM KCl, 5 mM MgCl₂. (d) Representative EM micrograph of *SynDLP* at the same conditions as in (c) plus 0.1 mM GMPPnP.

Next, an ANS-FTSA was performed in the presence of nucleotides to elucidate nucleotide-dependent alterations of the thermal stability of the *SynDLP* tertiary and/or quaternary structure. The transition temperature of *SynDLP* oligomers was increased by $\sim 5^\circ\text{C}$ in the presence of GDP (Fig. 4.57), indicating an increased thermodynamic stability when GDP is bound. A measurement with GTP yielded essentially the same transition curve (Fig. A11). Due to the high basal GTPase activity of *SynDLP* and the time needed for the FTSA measurement of one

transition curve, the condition with GTP in fact likely resembles the GDP-bound state. When the non-hydrolysable GTP analog GMPPnP was present, the transition temperature showed an even more pronounced shift of $\sim 10^{\circ}\text{C}$ to 57°C (Fig. 4.57).

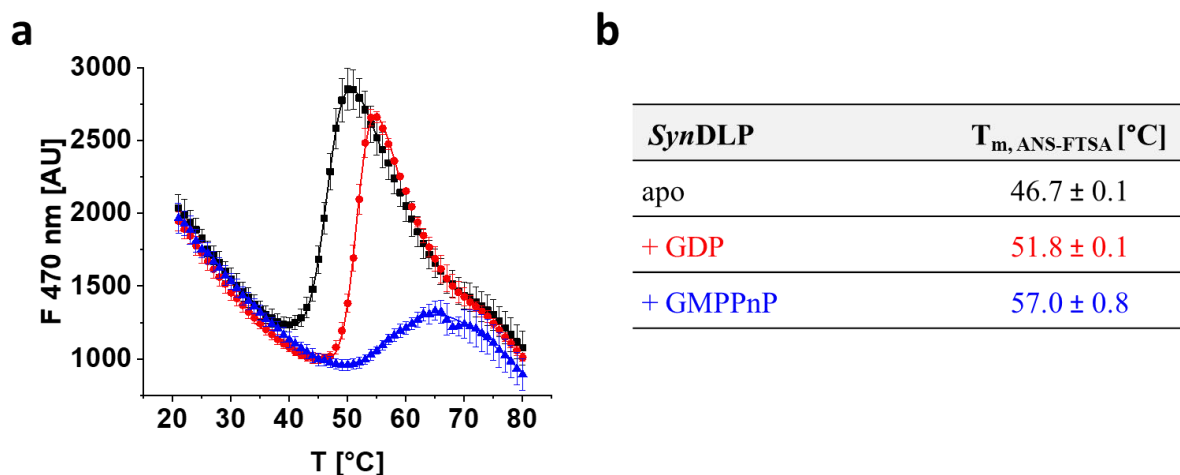


Figure 4.57: Nucleotide-binding increases the thermodynamic stability of *SynDLP* oligomers.

ANS-FTSA of $5\ \mu\text{M}$ *SynDLP* was measured in the apo state (black), the presence of $2\ \text{mM}$ GDP (red) or GMPPnP (blue). ANS fluorescence intensities at $470\ \text{nm}$ were plotted against the temperature. A temperature range capturing the transition phase was fitted with an adapted Boltzmann fit (Equation (7)). Fit curves are displayed as lines. The mean of independent experiments ($n = 3$) and error bars (S.D.) are shown. (b) A table summarizing the melting temperatures derived from the fit curves in (a).

Expression and purification of a SynDLP minimal GD construct

GMPPnP clearly induced conformational changes in *SynDLP* oligomers. Next, distinct interactions in GMPPnP-bound *SynDLP* were investigated. However, the *SynDLP* aggregates forming in the presence of GMPPnP (Fig. 4.56d) are structurally too disordered for a single particle analysis. Furthermore, *SynDLP* oligomerizes without externally added nucleotides via a complex interaction network in the stalk domain (Chapter 4.1, Fig. 4.7). In fact, such stalk-mediated oligomerization is conserved in some eukaryotic DLPs (Chapter 4.1, Fig. 4.8) (Gao *et al.*, 2010; Reubold *et al.*, 2015; Kalia *et al.*, 2018; Gewehr *et al.*, 2023). This interaction network complicates the study of nucleotide-dependent conformational changes in DLPs, especially when intermolecular GD interactions are involved. For this purpose, the concept of a truncated minimal construct consisting of only the GD and the stalk (minimal GD construct, MGD) has been established as a tool in dynamin biology for several DLPs (Chappie *et al.*, 2010; Wenger *et al.*, 2013; Rennie *et al.*, 2014; Qi *et al.*, 2016; Varlakhanova *et al.*, 2018; Yu *et al.*, 2020). With the *SynDLP* structure at hands (Chapter 4.1, Fig. 4.3), it was possible to design an MGD construct of *SynDLP*. Therefore, the amino acids forming the stalk domain

were substituted by a GS-linker, which connects the BSE2 and BSE3 part of the BSE domain (Fig. 4.58a). The hypothetical structure of *SynDLP*-MGD is shown in Fig. 4.58b. For the amino acid sequence of the recombinant protein, see appendix (Fig. A12).

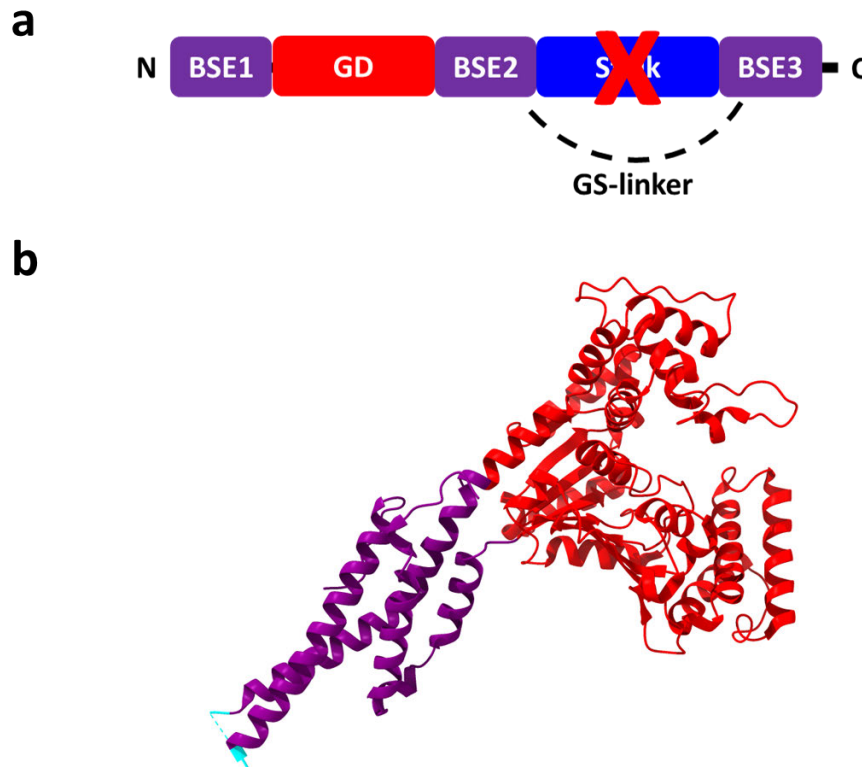


Figure 4.58: Design of a *SynDLP*-MGD construct.

(a) Domain arrangement of *SynDLP*-MGD that consists only of the GD and the BSE. The stalk is substituted by a GS-linker and the amino acids at the very C-terminus are deleted from the final construct. (b) Hypothetical structure of *SynDLP*-MGD based on the structure of full-length *SynDLP* (PDB: 7ZW6) in ribbon representation. GD and BSE are colored in red and purple, respectively. The stalk from the full-length *SynDLP* is omitted and the positions in BSE2 and BSE3 that are connected via a GS-linker are colored in cyan.

The recombinant protein is encoded on the plasmid pET303-*SynDLP*-MGD and was heterologously expressed in chemically competent *E. coli* Rosetta-gamiTM 2(DE3) cells as described for *SynDLP* wt (Chapter 4.1) (Gewehr *et al.*, 2023). Noteworthy, no DLP construct consisting of only the globular and soluble GD (without the BSE) has yet been described in the literature. Thus, in addition to *SynDLP*-MGD, a sequence comprising only the GD residues L41 – P441 (+ an N-terminal methionine and a C-terminal His₆-tag) was cloned into an expression vector (pET303-*SynDLP*-GD). To verify expression, Western Blot analysis of liquid cultures overexpressing *SynDLP*-MGD and -GD after IPTG induction was performed using an antibody against the His₆-tag. Upon separating proteins from the cultures expressing *SynDLP*-MGD,

bands at the expected height were clearly visible, whereas *SynDLP*-GD-containing bands were not observed in the respective samples (Fig. 4.59). Consequently, *SynDLP*-GD did not appear to be expressed, at least not under the tested expression conditions, and solely *SynDLP*-MGD was purified and further analyzed.

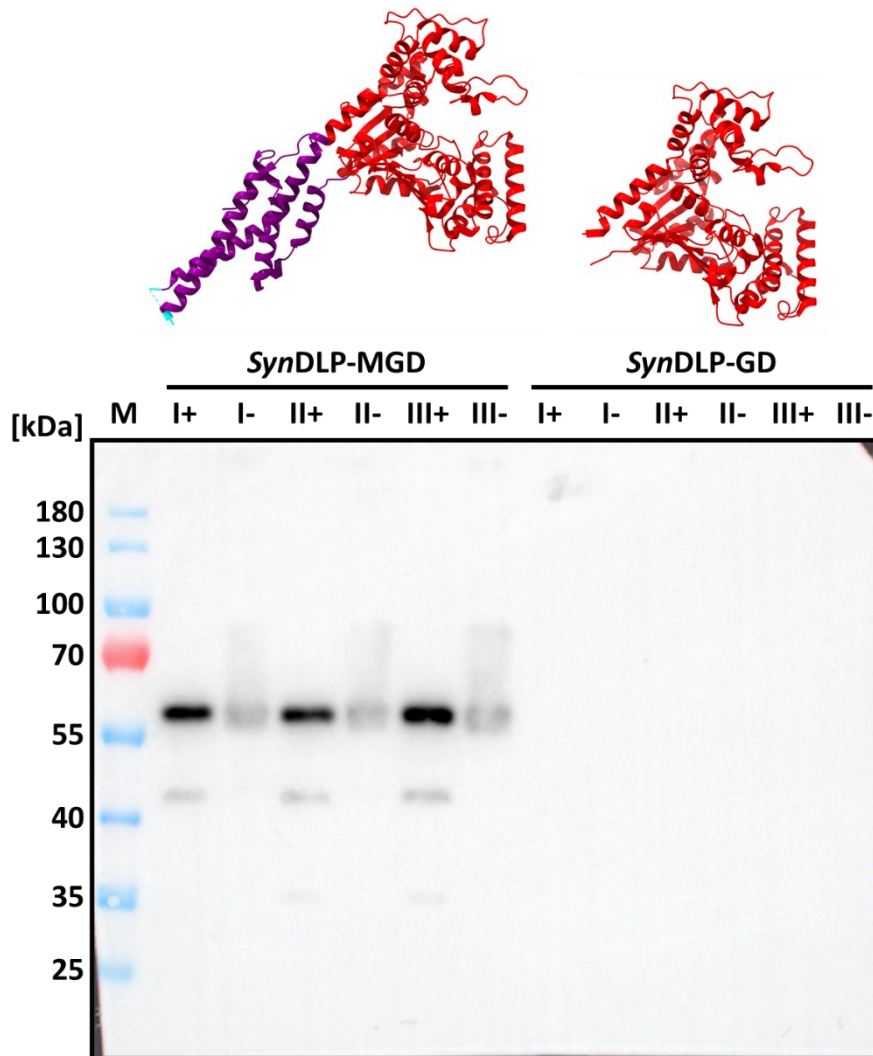


Figure 4.59: Expression of *SynDLP*-MGD and *SynDLP*-GD.

SynDLP-MGD and *SynDLP*-GD were expressed using the plasmids pET303-*SynDLP*-MGD and pET303-*SynDLP*-GD in chemically competent Rosetta-gamiTM 2(DE3) cells as described for *SynDLP* wt. Samples of three cultures each were boiled in the presence (+) or absence (-) of 100 mM DTT. After SDS-PAGE, bands containing protein with a His₆-tag were detected by Western Blot analysis using a His•Tag[®] antibody HRP conjugate. M = marker. Structural models at the top were generated using the *SynDLP* full-length structure (PDB: 7ZW6). Calculated molecular masses of the proteins are 59 kDa (*SynDLP*-MGD) and 45 kDa (*SynDLP*-GD), respectively.

For purification of *SynDLP*-MGD, the cells that overexpressed the protein were lysed using a LM20 Microfluidizer[®] and purified by affinity chromatography using a Ni-NTA matrix, as described for *SynDLP* wt (Chapter 4.1) (Gewehr *et al.*, 2023). After binding of the His₆-tagged *SynDLP*-MGD, the Ni-NTA matrix was washed with increasing imidazole concentrations (2 x 20 mM, 2 x 40 mM, 2 x 50 mM). The target protein was eluted in four steps using a buffer containing 500 mM imidazole. The eluate was combined, concentrated and loaded onto a preparative SEC column for further purification. The SEC chromatogram revealed three main peaks (Fig. 4.60a). The first peak, eluting at approx. 40 – 50 ml, was not further considered because it represented the void volume and the likely monomeric target protein was not expected to elute in the void volume. The fractions comprising the other two peaks were each combined and concentrated. SDS-PAGE analysis revealed that both pool 1 and 2 contained *SynDLP*-MGD (Fig. 4.60a, lane Pool 1c+ and Pool 2c+). However, only pool 2 consisted of pure protein with only minor contamination visible as additional bands (Fig. 4.60a, lane Pool 2c+). Moreover, the protein from pool 2 established the intramolecular disulfide bridge within the BSE domain (Fig. 4.60a, lane Pool 2c-), indicating the presence of pure and correctly folded *SynDLP*-MGD. Thus, protein from Pool 2 was used for further experiments. The individual steps of the *SynDLP*-MGD purification were documented by SDS-PAGE analysis (Fig. 4.60b).

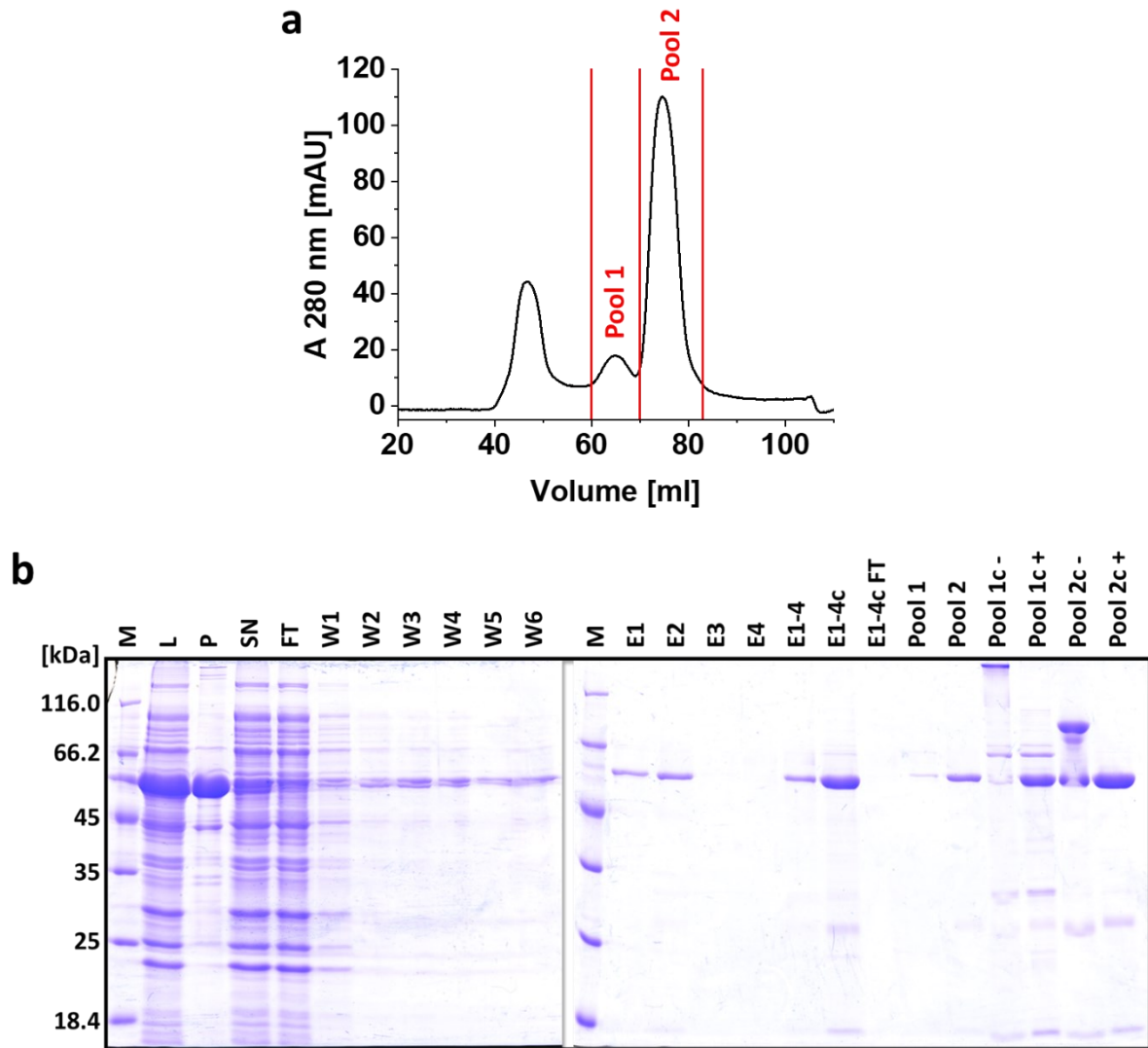


Figure 4.60: Purification of *SynDLP-MGD*.

(a) Chromatogram of the preparative SEC step. After affinity chromatography, the sample was incubated with 20 mM DTT for 30 min on ice and then loaded on a Superdex[®] 200 Hi-Load 16/600 column equilibrated with 20 mM HEPES buffer pH 7.4, 0.2 mM DTT at a flow rate of 0.25 ml/min. Two different peak fractions (Pool 1 and Pool 2) were collected as shown in the chromatogram. (b) Individual steps of purifying recombinantly expressed *SynDLP-MGD* documented via SDS-PAGE and subsequent Coomassie Brilliant Blue staining. The protein was purified by affinity chromatography using the C-terminally attached His₆-tag. The cell lysate (L) was centrifuged to remove a pellet (P) consisting of intact cells and/or cell debris. The supernatant (SN) was loaded onto a Ni-NTA matrix and the flow-through (FT) containing unbound proteins was discarded. The column was washed six times with increasing imidazole concentrations (W1-6). Next, the target protein was eluted in four steps (E1-4) with a buffer supplemented with 500 mM imidazole. The combined eluate (E1-4) was concentrated (E1-4c) and further purified via preparative SEC. The SEC fractions representing two peaks (Pool 1 and Pool 2) were concentrated (Pool 1c and Pool 2c) and analyzed under reducing (+) or non-reducing (-) conditions. The target protein has a calculated molecular mass of 59 kDa. M = marker.

SynDLP-MGD forms monomers with a GTP hydrolyzing activity

Oligomerization and the GTPase activity of *SynDLP-MGD* were tested by analytical SEC and the established GTPase assay. Since the stalk domain was deleted from the *SynDLP-MGD* construct, no stalk-mediated oligomerization of the protein was expected. In fact, analytical SEC revealed the presence of a monomeric protein, as indicated by comparing the elution volume of *SynDLP-MGD* with common standard proteins (Fig. 4.61a). Yet, the seemingly monomeric *SynDLP-MGD* was an active GTPase, as shown by the GTPase assay (Fig. 4.61b, red). The turnover number was determined to be $12.5 \pm 0.4 \text{ min}^{-1}$ (about 30% of *SynDLP* wt). The K_m value was calculated to be 0.38 mM.

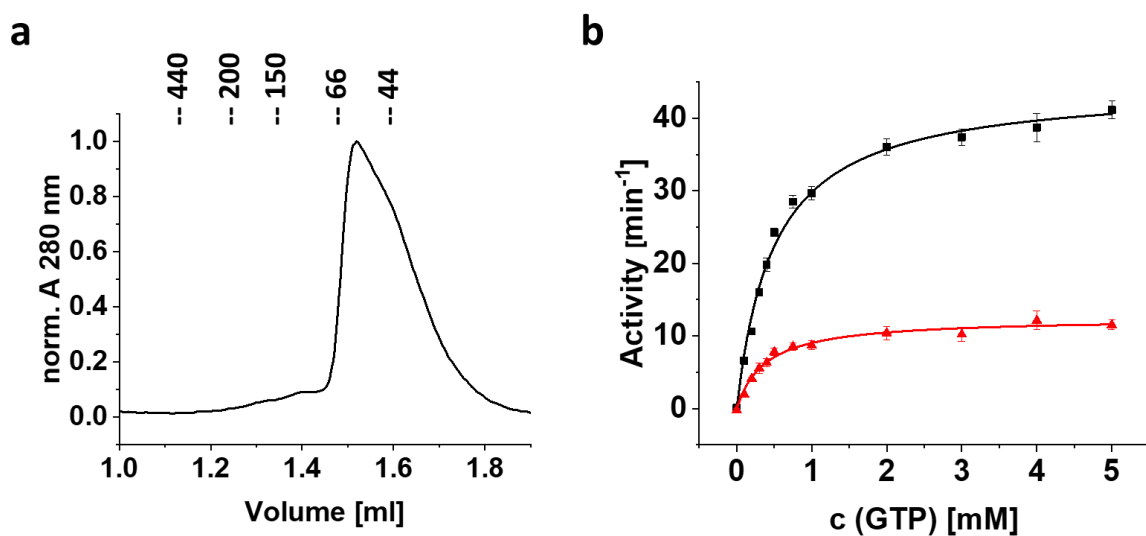


Figure 4.61: *SynDLP-MGD* is monomeric and shows a lowered GTPase activity.

(a) For analytical SEC, 10 μM *SynDLP-MGD* was incubated in reaction buffer for 30 min at 4°C and then 30 μl was loaded on a Superdex 200 Increase 3.2/300 column equilibrated with reaction buffer. The elution volumes of commonly used standard proteins and their respective molecular masses in kDa are indicated. Flow rate = 0.04 ml/min. (b) The GTPase activities of *SynDLP* wt (black) and *SynDLP-MGD* (red) were measured in a continuous, regenerative, coupled assay. The mean of independent measurements ($n = 3$) and error bars (S.D.) are shown. Data points were fitted using the Michaelis-Menten equation (Equation (3)). Fit curves are displayed as lines.

SynDLP-MGD dimerizes during a GTP hydrolysis cycle

Finally, the influence of different nucleotides on a potential interaction of *SynDLP-MGD*s was investigated using analytical SEC (Fig. 4.62). As already mentioned, *SynDLP-MGD* formed monomers in the apo state. After incubation of *SynDLP-MGD* with GTP or GDP, no difference was observed in the SEC chromatograms (Fig. 4.62, red and blue). Yet, addition of the transition state analog GDP-AlF₄ resulted in the formation of at least two fractions: a monomeric peak

and a peak eluting at a higher molecular mass (Fig. 4.62, green). The peak at a higher molecular mass probably corresponds to a dimeric fraction. When the non-hydrolysable GTP analog GMPPnP was added, the entire protein population eluted as dimers (Fig. 4.62, orange).

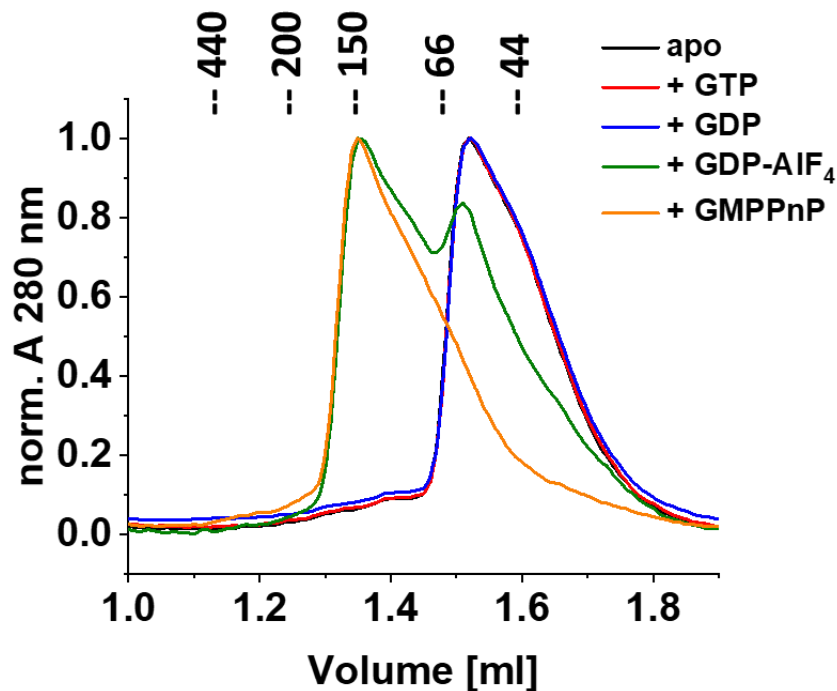


Figure 4.62: Nucleotide-dependent dimerization of *SynDLP*-MGD.

The assembly of *SynDLP*-MGD was analyzed using analytical SEC. Therefore, 10 μ M *SynDLP*-MGD was incubated in reaction buffer with 2 mM of the respective nucleotides (GTP, GDP, GDP-AlF₄ or GMPPnP) for 30 min at 4°C. 30 μ l of the mixtures was loaded on a Superdex 200 Increase 3.2/300 column equilibrated with reaction buffer. The elution volumes of common standard proteins and their respective molecular masses in kDa are indicated. Flow rate = 0.04 ml/min.

4.4.3 Discussion

DLPs remodel membranes by applying mechanical force. The energy for this process comes from hydrolysis of the substrate GTP and is translated into the mechanical energy via conformational changes of the relatively large multidomain proteins. Such conformational changes include relative movements of domains within single monomers and different arrangements of the monomers within the oligomer (Jimah and Hinshaw, 2018; Ford and Chappie, 2019). Oligomerization of DLPs is typically triggered by the addition of an appropriate membrane template or nucleotides. In bacterial members of the dynamin superfamily, larger oligomers have been observed thus far solely on membrane tubes. *E.g.*, *NpBDLP* forms dimeric assemblies in solution in the apo state or in the presence of GDP, which

oligomerize in a helical fashion on membranes in the presence of GMPPnP (Low and Löwe, 2006; Low *et al.*, 2009). Nucleotide-free *BsDynA* dimerizes in solution, but oligomerization on membranes has not been observed yet (Bürmann *et al.*, 2011). *MsIniA* and *EcLeoA* form monomers in solution that do not appear to be affected by nucleotide addition (Michie *et al.*, 2014; Wang *et al.*, 2019). *Cj-DLP1/2*, the BDLP pair of *Campylobacter jejuni*, builds heterotetramers through a unique DLP assembly mechanism using a specific assembly domain (Liu, Noel and Low, 2018).

In this thesis, *SynDLP* was shown to be the first BDLP described thus far to form oligomers in solution without externally added nucleotides or membranes (Chapter 4.1) (Gewehr *et al.*, 2023). Here, the structure of *SynDLP* oligomers was studied in the presence of nucleotides. EM micrographs revealed no significant changes in the size and shape of *SynDLP* oligomers in the presence of GTP or GDP, respectively (Fig. 4.55). However, the addition of GMPPnP, which freezes the GTP-bound state (Fig. 4.54), resulted in the formation of relatively unstructured *SynDLP* aggregates (Fig. 4.56), which showed increased thermodynamic stability (Fig. 4.57). Conclusively, *SynDLP* appears to undergo a dramatic structural rearrangement during the GTP hydrolysis cycle that can only be observed using a non-hydrolysable GTP analog, such as GMPPnP, likely due to the high basal GTPase activity of *SynDLP* (Chapter 4.1) (Gewehr *et al.*, 2023).

Next, a potential nucleotide-dependent structural rearrangement was investigated in more detail using a truncated *SynDLP* variant (*SynDLP*-MGD) consisting of only the GD and BSE domain (Fig. 4.58). As expected, isolated nucleotide-free *SynDLP*-MGD forms monomers in solution (Fig. 4.61a), as the stalk domain, including the oligomerization interfaces 1 – 3 (Chapter 4.1, Fig. 4.7), is missing in the construct. The GTPase activity of *SynDLP*-MGD was determined to be approx. 30% of *SynDLP* wt (Fig. 4.61b), *i.e.*, within the range of the GTPase activity determined for the dimeric *SynDLP*_{HPRN-AAAA} mutant (Chapter 4.1, Fig. 4.15f) (Gewehr *et al.*, 2023). Thus, the determined GTPase activity of *SynDLP*-MGD confirmed an assembly-stimulated GTPase activation mechanism in oligomerized *SynDLP* filaments. Nucleotide-dependent oligomerization of *SynDLP*-MGD was studied by analytical SEC and revealed no assembly of *SynDLP*-MGD monomers in the presence of GDP or GTP (Fig. 4.62), respectively, consistent with EM micrographs of full-length *SynDLP* wt in the presence of both nucleotides that also showed no significant structural changes (Fig. 4.55). Yet, the addition of nucleotide analogs resulted in the formation of partial (GDP-AlF₄) or complete dimerization (GMPPnP) of *SynDLP*-MGD monomers (Fig. 4.62). This strongly suggests that *SynDLP* dimerizes via

canonical transverse GD-GD contacts during the GTP hydrolysis cycle after GTP binding and before P_i release (Fig. 4.63). Albeit the analytical SEC experiment did not provide high-resolution structural information on *SynDLP*-MGD dimers in the GMPPnP-bound state, dimerization via transverse GD contacts is very likely, as dimerization, e.g., via longitudinal GD-BSE contacts, which can be observed in *SynDLP* wt oligomers (Chapter 4.1, Figs. 4.3, 4.8b), would also lead to the formation of assemblies larger than dimers and, thus, no clear dimer peak would be observed in an analytical SEC chromatogram.

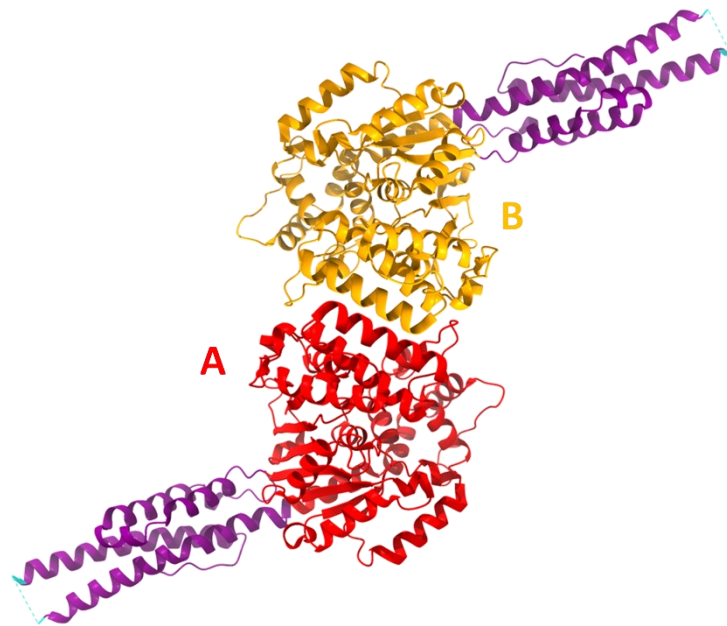


Figure 4.63: *SynDLP*-MGD likely dimerizes via GD-GD contacts.

Hypothetical structure and assembly of a *SynDLP*-MGD dimer. The BSE domains and GS-linker are colored in purple and cyan, respectively. The GDs of monomer A and monomer B are colored in red and orange, respectively. The structures were derived from the full-length *SynDLP* structure (PDB: 7ZW6).

The design and use of MGD constructs is well established for a variety of eukaryotic DLPs (Chappie *et al.*, 2010; Wenger *et al.*, 2013; Rennie *et al.*, 2014; Anand, Eschenburg and Reubold, 2016; Qi *et al.*, 2016; Varlakhonova *et al.*, 2018; Yan *et al.*, 2018; Yu *et al.*, 2020). However, *SynDLP*-MGD is the first stalkless GD-BSE fusion construct described thus far for a BDLP. Nucleotide-dependent dimerization observed for *SynDLP*-MGD was previously shown for MGD constructs of human Dyn1, MxA, Drp1, mitofusin 1, OPA1 as well as Vps1 of *Chaetomium thermophilum* (*CtVps1*). All of these eukaryotic MGD constructs are monomeric in the nucleotide-free state and dimerize in the presence of a transition state analog such as GDP-AlF₄. However, in contrast to *SynDLP*, none of the eukaryotic MGD constructs

dimerize in the presence of non-hydrolysable GTP analogs such as GMPPnP (Chappie *et al.*, 2010; Wenger *et al.*, 2013; Rennie *et al.*, 2014; Qi *et al.*, 2016; Varlakhanova *et al.*, 2018; Yan *et al.*, 2018; Yu *et al.*, 2020). This suggests slight differences in GD-GD dimerization of *SynDLP* during the GTP hydrolysis cycle as observed before with eukaryotic DLPs. These differences may relate to additional features of the *SynDLP* GD, as the cryo-EM structure of full-length *SynDLP* revealed an enlarged GD with additional α -helices (Chapter 4.1, Figs. 4.9b, 4.10a). However, a high-resolution structure of *SynDLP*-MGD dimers is required to elucidate the molecular details of transverse GD interactions in *SynDLP*.

In summary, a truncated monomeric *SynDLP* variant (*SynDLP*-MGD) consisting of solely the GD and BSE domain was successfully expressed and purified. *SynDLP*-MGD is an active GTPase resembling the basic GTPase activity of *SynDLP* without stimulation by intermolecular GD-BSE contacts. Furthermore, *SynDLP* showed a dramatic structural rearrangement during a GTP hydrolysis cycle. More specifically, *SynDLP* dimerizes likely via transverse GD-GD contacts in the GTP-bound state (mimicked by GMPPnP), which was demonstrated using the *SynDLP*-MGD construct. Comparison to other MGD constructs of DLPs suggests differences in the GD-GD dimerization of *SynDLP* during the GTPase cycle. Future studies will include high-resolution structural analysis of full-length *SynDLP* wt as well as *SynDLP*-MGD in the presence of nucleotides to elucidate molecular details of nucleotide-dependent conformational changes.

4.5 Regulation of a disulfide bridge in *SynDLP* by thioredoxin

4.5.1 Introduction

Photosynthesis can be divided into the photosynthetic electron transport in the light reaction and the process of CO₂ fixation. In all organisms that perform oxygenic photosynthesis, many enzymes involved in CO₂ fixation as well as several other metabolic processes contain disulfide bridges. The redox state of the disulfide bridges often regulates their enzymatic activity. The reduction of the disulfide bridges is usually catalyzed by the activity of Trxs. Trxs in turn obtain electrons from reducing equivalents from the light reaction (Wolosiuk and Buchanan, 1977; Buchanan, 1980; Mallén-Ponce, Huertas and Florencio, 2022). Trxs are characterized by a low molecular mass of 12 – 14 kDa. Structure determinations revealed a typical fold and a highly conserved motif in the active site with two cysteines (Fig. 4.64) (Holmgren *et al.*, 1975; Peterson *et al.*, 2005; Dai *et al.*, 2007; Juniar *et al.*, 2020). Sequence analyses of multiple genomes revealed a high diversity of Trxs in plants, algae and cyanobacteria (Meyer, Reichheld and Vignols, 2005; Florencio *et al.*, 2006; Geigenberger *et al.*, 2017; Mallén-Ponce, Huertas and Florencio, 2022).

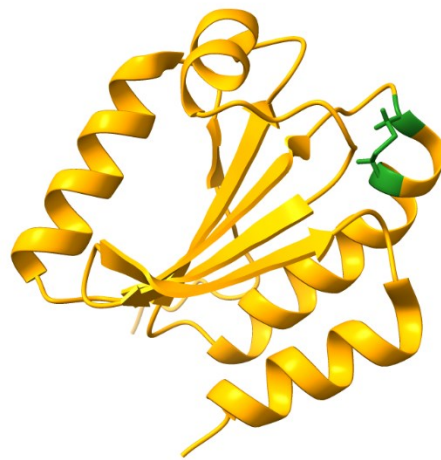


Figure 4.64: Typical structure of a Trx.

The structure of a Trx from *Arabidopsis thaliana* in the oxidized state (PDB: 1XFL) is shown in ribbon representation and colored in orange. The two cysteines in the active site are shown as sticks and colored in green.

The genome of *Synechocystis* encodes four different Trx isoforms (*SynTrxA*, *SynTrxB*, *SynTrxC* and *SynTrxQ*) (Florencio *et al.*, 2006; Mallén-Ponce, Huertas and Florencio, 2022). The *SynTrxA* isoform has been shown to be the only Trx essential for *Synechocystis* under photoautotrophic and heterotrophic growth conditions (Navarro and Florencio, 1996; Mallén-

Ponce *et al.*, 2021). Proteomic studies have revealed interaction of *SynTrxA* with several cytosolic as well as (peripheral) membrane proteins (Lindahl and Florencio, 2003; Mata-Cabana, Florencio and Lindahl, 2007). As *SynDLP* contains an intramolecular disulfide bridge that influences the GTPase activity (Chapter 4.1) (Gewehr *et al.*, 2023), a regulation of the disulfide bridge by a Trx was feasible to assume.

In this study, the interaction of *SynDLP* with a Trx encoded in *Synechocystis* was investigated. Since *SynTrxA* has been shown to interact with peripheral membrane proteins (Lindahl and Florencio, 2003; Mata-Cabana, Florencio and Lindahl, 2007), it was selected as a potential interaction partner of *SynDLP*. Therefore, the gene coding for *SynTrxA* (orf *slr0623* of *Synechocystis*) was cloned into an expression vector and the target protein was heterologously expressed in *E. coli*. After purification, the *in vitro* functionality of recombinant *SynTrxA* as well as a potential interaction with *SynDLP* were tested.

4.5.2 Results

Expression and purification of recombinant SynTrxA

For the production of recombinant *SynTrxA*, the gene encoding *SynTrxA* (orf *slr0623* of *Synechocystis*) was cloned into a pET303 vector to allow for the overexpression of *SynTrxA* in *E. coli*. The recombinant protein was C-terminally elongated with a His₆-tag to enable the purification via Ni-NTA affinity chromatography. The amino acid sequence of recombinant *SynTrxA* is shown in the appendix (Fig. A13).

Next, heterologous expression of *SynTrxA* was tested and optimized. Therefore, several genetically engineered *E. coli* strains were transformed with the plasmid encoding *SynTrxA* (pET303-*SynTrxA*). At first, small scale expressions were performed under different growth conditions (37°C for 3 h and 20°C overnight). The expression levels of *SynTrxA* were checked by Western Blot analysis using an antibody directed against the His₆-tag (His•Tag[®] antibody HRP). The Western Blot analysis of the three strains that exhibited the highest expression levels of *SynTrxA* is shown in Fig. 4.65. Protein expression in a larger scale for production of isolated *SynTrxA* was finally performed using BL21-gold(DE3) cells grown at 37°C, 120 rpm for 3 h after IPTG-induction.

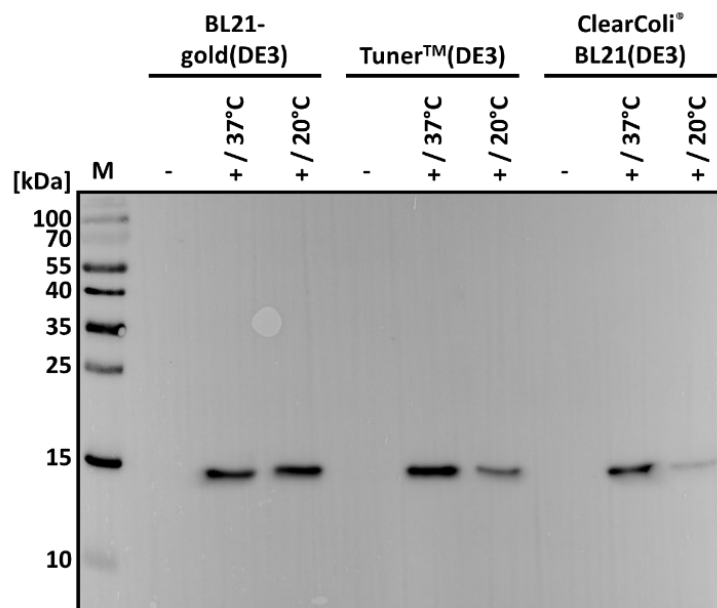


Figure 4.65: Expressions of *SynTrxA* in different *E. coli* strains.

SynTrxA encoded on the plasmid pET303-*SynTrxA* was overexpressed in *E. coli*. Western Blot analysis of boiled cultures from three selected strains before IPTG addition (-) and after addition of 0.5 mM IPTG (+) and then grown under two different conditions (37°C for 3 h and 20°C overnight) is shown. The protein was visualized using a His-Tag[®] antibody HRP conjugate. M = marker. *SynTrxA* has a calculated molecular mass of 14.3 kDa.

As the Trxs of *Synechocystis* were already isolated and characterized in previous studies in the literature, the applied purification protocol of *SynTrxA* was taken from published protocols with minor modifications (Lindahl and Florencio, 2003; Pérez-Pérez, Florencio and Lindahl, 2006). As described for the purification of *SynDLP* (Chapter 4.1) (Gewehr *et al.*, 2023), cells that overexpressed *SynTrxA* were lysed using a LM20 Microfluidizer[®] and purified via affinity chromatography using a Ni-NTA matrix. After the His₆-tagged protein bound to the Ni-NTA matrix, washing steps with increasing imidazole concentrations (4 x 20 mM, 2 x 40 mM) were performed prior to elution of the target protein in four steps with a buffer containing 500 mM imidazole. The imidazole and other salts from the purification buffers were removed using commercial PD10 columns to buffer the protein into 20 mM HEPES buffer pH 7.4. These steps were documented by an SDS-PAGE analysis (Fig. 4.66a) revealing additional protein bands and, thus, impurities in the protein solution (Fig. 4.66a, lane Ec). A preparative SEC step using an appropriate column was performed to further increase the purity of *SynTrxA*. Before that, the protein was incubated with 20 mM DTT for 1 h on ice to break any disulfide bridges between the Trx and protein substrates from *E. coli*. The chromatogram of the preparative SEC step revealed a dominant peak that was separated from several impurities (Fig. 4.66b). Fractions representing the dominant peak were collected, concentrated, and analyzed via SDS-PAGE,

indicating a pure protein migrating at the expected molecular mass (Fig. 4.66c, lane +). Under non-reducing conditions, purified *SynTrxA* migrated at a slightly increased molecular mass (Fig. 4.66c, lane -).

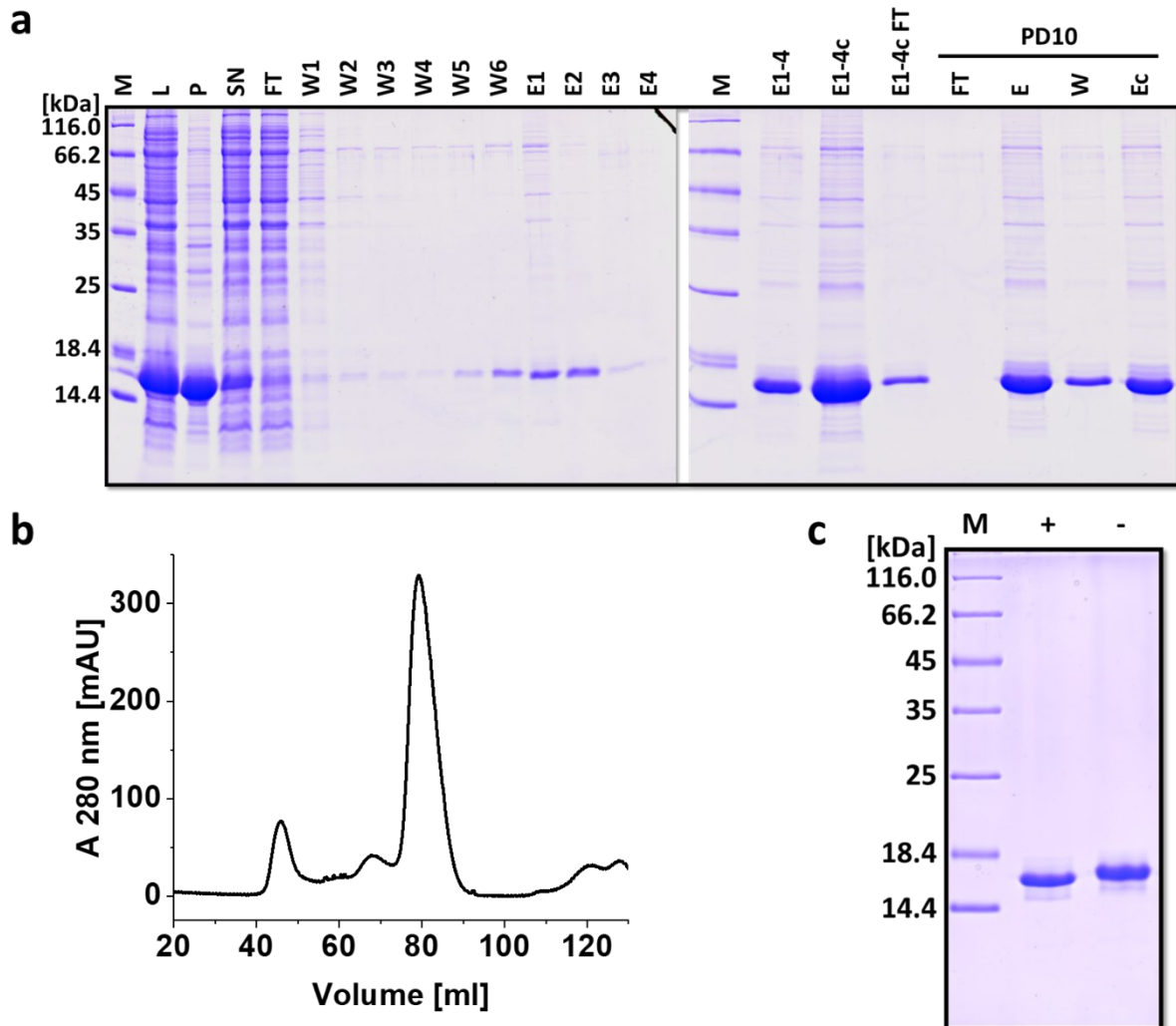


Figure 4.66: Purification of recombinantly expressed *SynTrxA*.

(a) Documentation of *SynTrxA* purification steps via SDS-PAGE and subsequent Coomassie Brilliant Blue staining. The protein was initially purified via affinity chromatography using the genetically attached His₆-tag. The cell lysate (L) was centrifuged to remove a pellet (P) consisting of cell debris and/or intact cells. The supernatant (SN) was loaded onto a Ni-NTA matrix and the flow-through (FT) was discarded. After six washing steps (W1-6) with increasing imidazole concentrations, the target protein was eluted in four steps (E1-4) with a buffer containing 500 mM imidazole. The combined eluate (E1-4) was concentrated (E1-4c), desalted via a PD10 column and again concentrated leading to the final protein sample (Ec). The target protein has a calculated molecular mass of 14.3 kDa. M = marker.

(b) After affinity chromatography (a), *SynTrxA* was incubated with 20 mM DTT for 1 h on ice and further purified via preparative SEC using a Superdex[®] 75 Hi-Load 16/600 pg column equilibrated with 20 mM HEPES buffer pH 7.4 at a flow rate of 1 ml/min. Peak fractions eluting from 75 – 86 ml were collected.

(c) SDS-PAGE analysis of 2.7 µg purified *SynTrxA* after preparative SEC under reducing (+) and non-reducing (-) conditions. The gel was stained with Coomassie Brilliant Blue. The calculated molecular mass of *SynTrxA* is 14.3 kDa. The SDS-PAGE revealed a single band between 14 and 18 kDa (lane +) without showing further protein bands, thus the protein was ≥ 95% pure. M = marker.

Determination of the molecular mass of purified *SynTrxA*

The molecular mass of purified *SynTrxA* was estimated using analytical SEC. Here, the protein eluted as one sharp peak (Fig. 4.67), indicating a monodisperse protein solution. The elution volume of *SynTrxA* was in the range of the smallest used standard protein (cytochrome c, 12.4 kDa). Thus, isolated *SynTrxA* probably forms solely monomers, considering the calculated molecular mass of 14.3 kDa per monomer and the conserved globular structure of Trxs (Fig. 4.64).

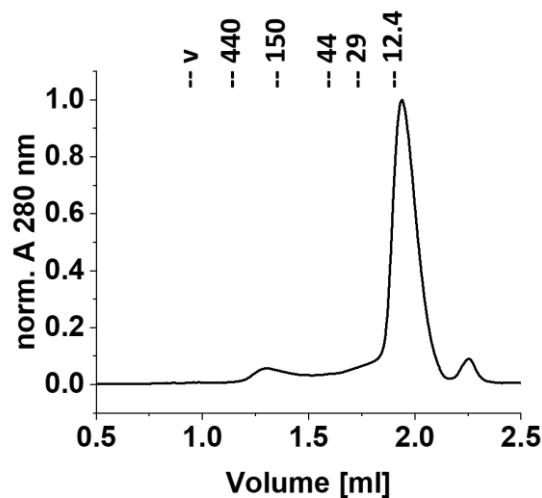


Figure 4.67: Molecular mass estimation of purified *SynTrxA*.

For analytical SEC, 30 μ l of a 65 μ M *SynTrxA* solution was applied to a Superdex 200 Increase 3.2/300 column equilibrated with reaction buffer. The elution volumes of common standard proteins and their respective molecular masses in kDa are indicated. Flow rate = 0.04 ml/min.

In vitro activity of *SynTrxA*

Next, the *in vitro* activity of *SynTrxA* was measured using an insulin reduction assay as described by Holmgren (1979) with modifications. The heterodimeric insulin consists of two subunits, chain A and B, which are linked via two disulfide bridges. A functional Trx can break the disulfide bridges, resulting in free insulin chains A and B. As the isolated B chain precipitates in aqueous buffer systems, liberation of the free B chain can be monitored via light scattering, as the solution gets turbid.

When the intact insulin heterodimer was incubated with small amounts of the reducing agent DTT, no significant increase of the turbidity was measured after 1 h (Fig. 4.68, black). The addition of 3 μ M *SynTrxA* led to a clear increase of the turbidity after a lag phase of approx. 10

min (Fig. 4.68, red). Conclusively, the recombinant, isolated *SynTrxA* is an active Trx *in vitro* and suitable for further experiments.

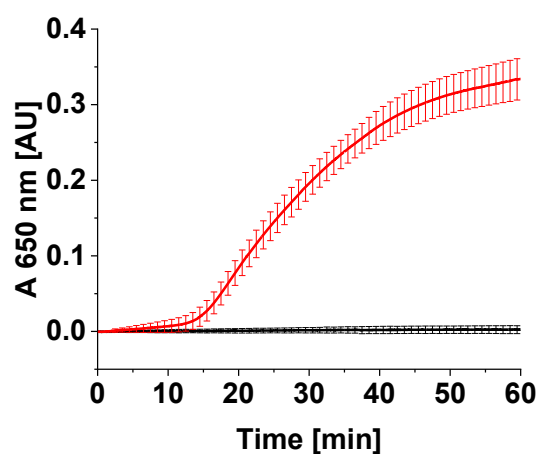


Figure 4.68: *In vitro* activity of purified *SynTrxA*.

SynTrxA *in vitro* activity was measured in an insulin reduction assay. The reduction of 130 μ M insulin in buffer containing 2 mM EDTA, 330 μ M DTT, 20 mM HEPES buffer pH 7.4 was monitored as scattering via measuring the absorption at 650 nm in the presence (red curve) or absence (black curve) of 3 μ M *SynTrxA* at 25°C. Mean ($n = 3$) and error bars (S.D.) are shown.

Interaction of SynTrxA with SynDLP

Finally, a potential interaction between *SynDLP* and *SynTrxA* was tested. Therefore, both proteins were incubated at increasing DTT concentrations and the redox state of the intramolecular disulfide bridge of *SynDLP* was analyzed via SDS-PAGE. A catalyzing function of *SynTrxA* would have been indicated in this experiment by the breakage of the disulfide bridge of *SynDLP* at lower DTT concentrations. However, the SDS-PAGE gels revealed the same pattern of oxidized and reduced *SynDLP* bands under both conditions, indicating a complete reduction of *SynDLP* at DTT concentrations >10 mM (Fig. 4.69). This approach provided no evidence for a regulation of *SynDLP* by *SynTrxA*.

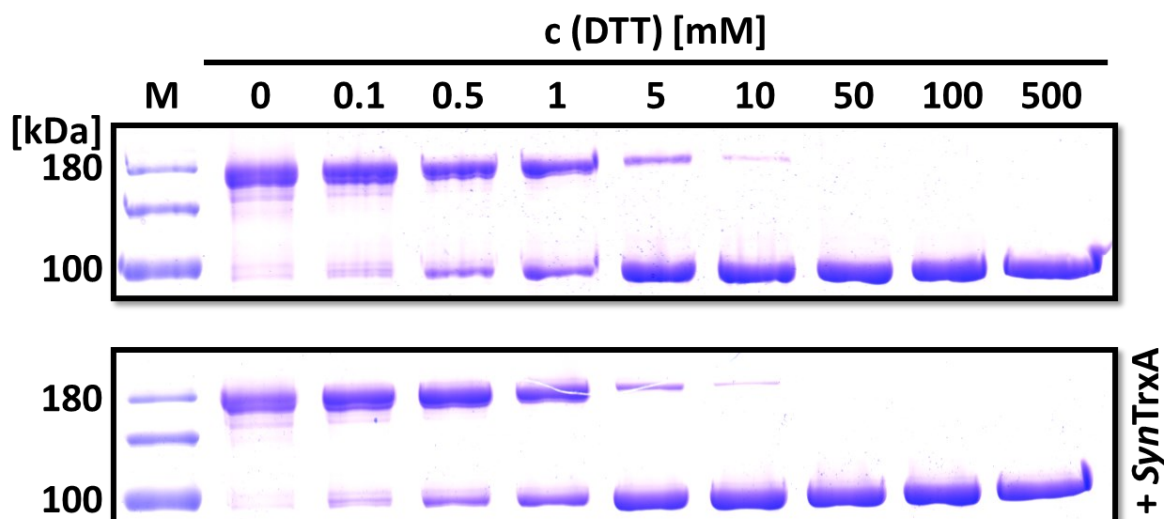


Figure 4.69: DTT titration to check for an interaction of *SynDLP* with *SynTrxA*.

2 μM *SynDLP* was incubated in buffer containing 2 mM EDTA, 20 mM HEPES buffer pH 7.4 with increasing DTT concentrations in the presence or absence of 6 μM *SynTrxA* for 30 min at RT. The reactions were analyzed by SDS-PAGE. The gel was stained with Coomassie Brilliant Blue. M = marker. The calculated molecular mass of *SynDLP* is 93 kDa.

4.5.3 Discussion

SynDLP, the BDLP of *Synechocystis*, has an intramolecular disulfide bridge that influences its thermodynamic stability as well as GTPase activity (Chapter 4.1, Fig. 4.11) (Gewehr *et al.*, 2023). A potential regulation of the *SynDLP* activity via reduction/oxidation of this disulfide bridge by a Trx was tested. Therefore, recombinant *SynTrxA*, a Trx isoform of *Synechocystis*, was successfully expressed and purified (Figs. 4.65, 4.66). The protein formed mainly monomers as revealed by analytical SEC (Fig. 4.67), which indicates an active Trx. Noteworthy, Trxs can get inactivated by homodimerization (Weichsel *et al.*, 1996; Du *et al.*, 2013; e Costa *et al.*, 2020). The *in vitro* activity of recombinant *SynTrxA* was verified in an insulin reduction assay revealing a typical lag phase before the reduction of the insulin heterodimer (Fig. 4.68) (Holmgren, 1979).

After showing the functionality of recombinant *SynTrxA*, potential interaction with *SynDLP* was tested via a DTT titration. SDS-PAGE analysis of the DTT titration indicated no interaction between the two proteins (Fig. 4.69). Eventually, interaction of *SynDLP* and *SynTrxA* requires additional accessory proteins and would thus only be observed in *in vivo* experiments. It might also be possible that the conditions chosen for the *in vitro* experiment with the isolated proteins are not suitable for the reduction of *SynDLP* catalyzed by *SynTrxA*. As already mentioned, the genome of *Synechocystis* contains three more Trx isoforms besides *SynTrxA* (Florencio *et al.*,

2006; Mallén-Ponce, Huertas and Florencio, 2022). Proteomic studies revealed a variety of potential protein substrates for *SynTrxB* and *SynTrxQ* (Pérez-Pérez, Florencio and Lindahl, 2006; Pérez-Pérez, Martín-Figueroa and Florencio, 2009). Thus, interaction of *SynTrxB* or *SynTrxQ* with *SynDLP* would also be conceivable. *SynTrxC*, the fourth Trx of *Synechocystis*, occurs exclusively in cyanobacteria and exhibits atypical features, however, interaction partners of *SynTrxC* have not yet been identified (López-Maury, Heredia-Martínez and Florencio, 2018).

Taken together, recombinant *SynTrxA* was successfully expressed and purified. The isolated protein was monomeric and active in an *in vitro* activity assay. In the experiment performed, no interaction between *SynTrxA* and *SynDLP* was observed. Thus, it is assumed that the intramolecular disulfide bridge in *SynDLP* is not reduced by *SynTrxA*. Future studies will target a potential interaction of *SynDLP* and another Trx isoform of *Synechocystis*.

4.6 *In vivo* role of *SynDLP* in the cyanobacterium *Synechocystis*

4.6.1 Introduction

DLPs were assumed to be eukaryotic inventions and the physiological functions of many eukaryotic DLPs have been elucidated. However, a sequence analysis revealed the presence of potential BDLPs in bacterial genomes (Blick, 1999). The first potential BDLP was characterized in 2006 and originated from the cyanobacterium *Nostoc punctiforme* (*NpBDLP*) (Low and Löwe, 2006), but the defined *in vivo* function of *NpBDLP* still remains unknown. Other BDLPs have been identified in *Bacillus subtilis* (*BsDynA*), *E. coli* (*EcLeoA*), *Mycobacterium smegmatis* (*MsIniA/C*), *Mycobacterium tuberculosis* (*MtIniA/C*), *Streptomyces venezuelae* (*SvDynA/B*) and *Campylobacter jejuni* (*Cj-DLP1/2*) (Brown and Hardwidge, 2007; Bürmann *et al.*, 2011; Michie *et al.*, 2014; Schlimpert *et al.*, 2017; Liu, Noel and Low, 2018; Wang *et al.*, 2019; Gupta *et al.*, 2023). Nevertheless, only for *BsDynA* a distinct physiological function has been identified thus far, as *BsDynA* is involved in a novel resistance mechanism of a bacterium against phage infection. After infection of *Bacillus subtilis* with a bacteriophage, the *fusion DLP* *BsDynA* stabilizes the CM, which is damaged in the final step of the lytic cycle, and therefore prevents the phages from escaping from an infected cell. This protects other host cells from infection (Guo *et al.*, 2022).

As described above in more detail (Chapter 1.2), cyanobacteria perform oxygenic photosynthesis. The light reaction of photosynthesis takes place in the cyanobacterial TM (Lea-Smith *et al.*, 2016; Liu, 2016). There are still many open questions concerning the biogenesis as well as remodeling of the TM (Rast, Heinz and Nickelsen, 2015; Siebenaller and Schneider, 2023), yet an involvement of BDLPs in cyanobacterial TM remodeling is assumed (Jilly, 2018; Jilly *et al.*, 2018). Pioneering work on potential BDLPs of the cyanobacterial model organism *Synechocystis* revealed the presence of five candidate genes in the genome of *Synechocystis* that presumably encode a BDLP (Jilly, 2018). The corresponding gene loci include the orfs *slr0179*, *slr0869*, *slr1462*, *sll0503* and *sll0804*. Knock-out strains have been generated for the genes *slr0869* and *sll0503*, while the other three genes could only be depleted and, thus, appear to be essential under the selected growth conditions (Jilly, 2018). The orf *slr0869* codes for *SynDLP* and, consequently, the *slr0869* knock-out strain of *Synechocystis* is termed Δ *syndlp*.

In parallel with the analysis of isolated recombinant *SynDLP*, the Δ *syndlp* strain has been investigated in *in vivo* experiments to obtain information on the physiological function of *SynDLP*. Therefore, *Synechocystis* wt and Δ *syndlp* were grown and characterized under

different conditions. Under both standard growth conditions as well as phosphate depletion conditions, no differences have been observed between the two strains. The $\Delta syndlp$ strain revealed a slightly altered phenotype under high light conditions. *E.g.*, the oxygen production of $\Delta syndlp$ appeared to be reduced under high light conditions. In addition, $\Delta syndlp$ showed decreased PS II activity and enhanced content of carotenoids under both normal and high light conditions (Jilly, 2018). However, the previous characterization of $\Delta syndlp$ did not provide clear evidence for a physiological *SynDLP* function.

In this study, *SynDLP* was already shown to be natively expressed in *Synechocystis* under standard growth conditions (Chapter 4.1, Fig. 4.1) (Gewehr *et al.*, 2023). Electron micrographs of whole *Synechocystis* wt and $\Delta syndlp$ were acquired to identify potential morphological changes in the *syndlp* knock-out strain. An important information for understanding the physiological role of a protein is its *in vivo* localization within the cell. Therefore, *Synechocystis* wt cells were fractionated and the presence of *SynDLP* in the corresponding fractions was analyzed by IP and Western Blot analysis. In addition, a gene coding for an mEGFP-tagged *SynDLP* variant was introduced into the *Synechocystis* genome to visualize the target protein in the cyanobacterial cell under the fluorescence microscope. Following the function of *BsDyna* (Guo *et al.*, 2022), I suggest a role of *SynDLP* in resistance to cell lysis after phage infection. Since no cyanophage of *Synechocystis* has yet been discovered, *Synechocystis* cells were transformed with an inducible cell lysis system (Asada, Shiraiwa and Suzuki, 2019), which allows investigation of a possible *SynDLP* function in protection against cell lysis.

4.6.2 Results

Electron micrographs of Synechocystis cells

EM micrographs of ultrathin sections of *Synechocystis* cells were recorded to investigate morphological differences between *Synechocystis* wt and the *syndlp* knock-out strain. Both strains were photomixotrophically grown under standard conditions. A typical EM micrograph of a *Synechocystis* wt cell is shown in Fig. 4.70a. Some of the cellular substructures can be observed, *e.g.*, carboxysomes or the fine structure of the TM, which can be assigned by comparison with EM images of *Synechocystis* cells from the literature (Yamauchi *et al.*, 2011; Kaniya *et al.*, 2013; Damrow, Maldener and Zilliges, 2016). The outer membrane of the cell was coated by a clearly visible S-layer. EM micrographs of *Synechocystis* $\Delta syndlp$ cells showed no dramatic morphological changes compared with wt cells (Fig. 4.70b). However, two features

appeared to be slightly altered in the *syndlp* knock-out strain: 1) Many white spots were observable between the individual membrane sheets of the TM. These were also observed in *Synechocystis* wt cells, yet to a much lesser extent. Such white spots probably consisted of glycogen granules. 2) The S-layer appeared to be thicker in most observed Δ *syndlp* cells compared with wt cells.

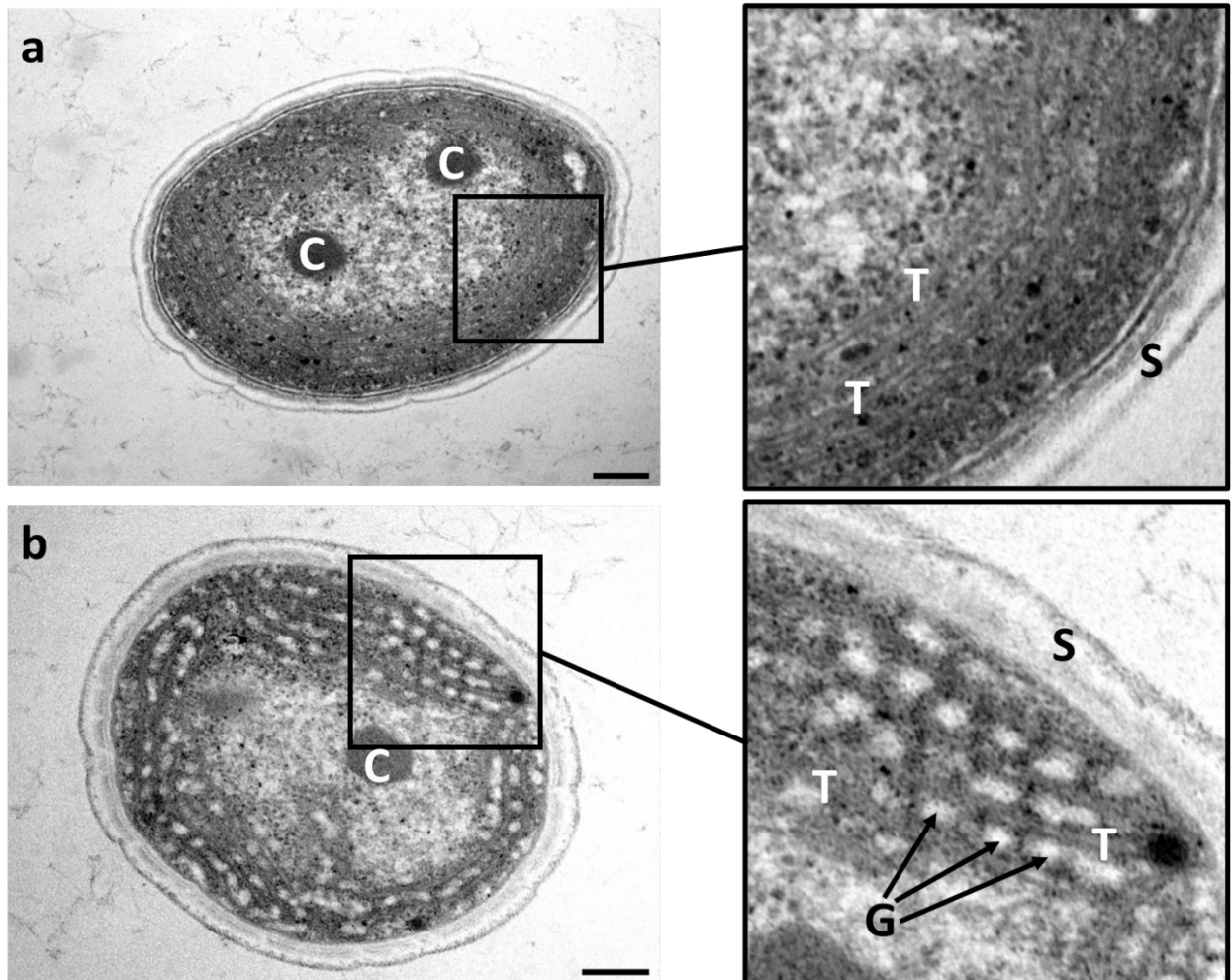


Figure 4.70: Transmission electron micrographs of an ultrathin section of *Synechocystis* cells.

Liquid cultures of *Synechocystis* strains were photomixotrophically grown. (a) A typical *Synechocystis* wt cell. The enlargement of the boxed area highlights the TM fine structure. (b) Typical Δ *syndlp* cell. The boxed area is enlarged on the right and shows increased contents of glycogen granules in between the TM layers as well as a thicker S-layer. C = carboxysomes, T = TM, G = glycogen granule, S = S-layer. Black bars scale for 200 nm.

In vivo localization of SynDLP

The identification of the localization of proteins within the cell is an important information to understand their *in vivo* function. The localization of SynDLP in the cyanobacterium was investigated via two different methods. It was already shown in an IP experiment that SynDLP

is expressed in *Synechocystis* under standard photomixotrophic growth conditions (Chapter 4.1, Fig. 4.1) (Gewehr *et al.*, 2023). The experimental setup of the IP was modified by an additional fractionation step before the actual IP to separate potentially membrane-bound *SynDLP* from unbound protein. The subsequent Western Blot analysis of membrane and soluble fractions of *Synechocystis* cells with the *SynDLP*-specific α -*SynDLP* antibody revealed the presence of a *SynDLP*-containing band in both fractions (Fig. 4.71, bands at approx. 100 kDa). The *SynDLP* band in the soluble fraction seemed to be more intense and sharpened. Noteworthy, the lower bands at approx. 55 and 30 kDa resulted from cross-reactions of the antibodies, heavy and light chains, respectively, used for IP and Western Blot analysis.

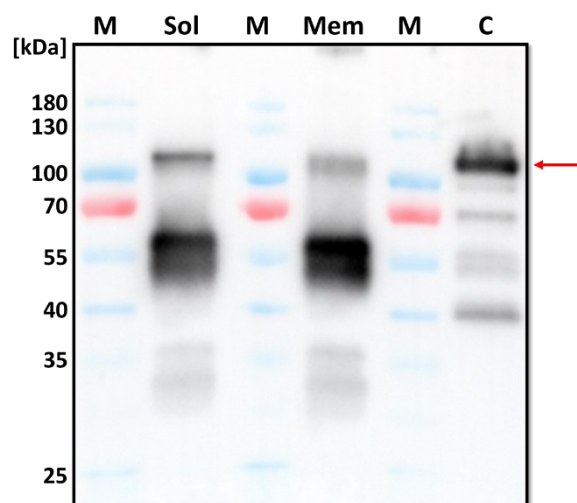


Figure 4.71: IP of fractionated *Synechocystis* cells.

A *Synechocystis* wt cell culture was photomixotrophically grown under standard conditions and was separated into a soluble (lane Sol) and a membrane (lane Mem) fraction by ultracentrifugation after cell disruption. Native *SynDLP* was immunoprecipitated in both fractions using the α -*SynDLP* antibody and Protein A-Sepharose beads. After separation of the immunoprecipitated proteins via SDS-PAGE, *SynDLP*-containing bands were visualized by Western Blot analysis using α -*SynDLP* as primary and an α -Rabbit-HRP conjugate as secondary antibody. Recombinant and purified *SynDLP* was loaded as a control (lane C) and the height of the prominent band representing *SynDLP* is marked by a red arrow. M = marker. The calculated molecular mass of *SynDLP* is 93 kDa.

Fluorescence microscopy of *Synechocystis* cells transformed with a GFP-tagged *SynDLP* was used as the second method to study the *in vivo* localization of the protein. Therefore, a gene coding for an mEGFP-tagged *SynDLP* variant (mEGFP-*SynDLP*) was introduced into the *Synechocystis* genome using the vector pCK306, which substitutes the gene locus *sll0410* of the *Synechocystis* genome (Fig. 4.72a). In *Synechocystis* cells transformed with the pCK306 vector, the (over-)expression of the target protein is regulated by the *rhaBAD* promoter, which allows induction of protein expression by the addition of rhamnose (Kelly *et al.*, 2018). The

successful transformation of *Synechocystis* wt with the plasmid pCK306-mEGFP-*SynDLP* was checked via PCR and subsequent agarose gel electrophoresis (Fig. 4.72b). In addition to the transformation with pCK306-mEGFP-*SynDLP*, *Synechocystis* wt was also transformed with pCK306-*SynDLP* to obtain a *Synechocystis* strain capable of inducible overexpression of native and untagged *SynDLP*. The resulting *Synechocystis* strain pCK306-*syndlp* can be used in future studies (see below). Both transformed *Synechocystis* strains pCK306-*syndlp* and pCK306-*megfp-syndlp* were completely segregated as only one PCR product band at the correct height was observed in agarose gel electrophoresis (Fig. 4.72b). Note that *SynDLP* and mEGFP-*SynDLP* encoded by the pCK306 vector have no additional N- or C-terminal residues like, e.g., a linker plus His₆-tag. This differs from *SynDLP* and mEGFP-*SynDLP* encoded by the pET303 plasmids, which were used for heterologous expression in *E. coli* and subsequent isolation of the proteins as described above.

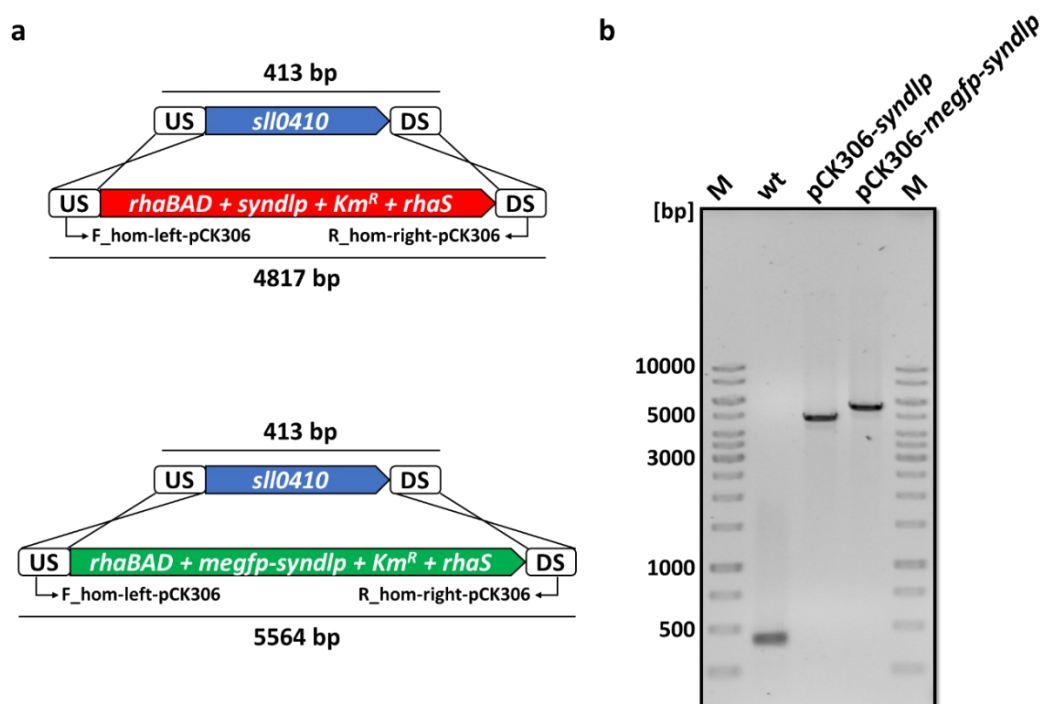


Figure 4.72: Complete segregation of *Synechocystis* strains transformed with pCK306-based plasmids coding for *SynDLP* and mEGFP-*SynDLP*.

(a) Schemes illustrating the generation of the *Synechocystis* strains pCK306-*syndlp* and pCK306-*megfp-syndlp* via homologous recombination using a plasmid containing flanking regions up- and downstream (US and DS) of the gene locus *sll0410* and an insert containing the *rhaBAD* promoter, the *syndlp* or *megfp-syndlp* gene, respectively, a kanamycin resistance cassette (*Km^R*) and the *rhaS* gene between the flanking regions. (b) *Synechocystis* wt was transformed with the plasmids pCK306-*SynDLP* and pCK306-mEGFP-*SynDLP* in BG11 medium containing up to 100 μ g/ml kanamycin. Genomic DNA of the strains was prepared by phenolic DNA extraction and PCRs with the primer pair F_hom-left-pCK306 and R_hom-right-pCK306 were performed to check for complete segregation of the transformed *Synechocystis* strains pCK306-*syndlp* (expected size of the PCR product: 4817 bp) and pCK306-*megfp-syndlp* (expected size: 5564 bp) in comparison with the wt (expected size: 413 bp). M = marker.

Next, the rhamnose-inducible expression of the mEGFP-tagged *SynDLP* variant in the *Synechocystis* strain pCK306-*megfp-syndlp* was tested. The cyanobacterial cells were grown under standard photomixotrophic conditions and one day after the addition of rhamnose a fluorescence spectrum of the cell suspension was measured. Therefore, the fluorescent mEGFP-tag was specifically excited. Fluorescence spectra of cell suspensions of *Synechocystis* pCK306-*megfp-syndlp* without the addition of rhamnose as well as of *Synechocystis* wt were measured as controls. In the *Synechocystis* wt culture, an mEGFP signal in the fluorescence emission spectrum was not observable (Fig. 4.73, black). The clear peak in the fluorescence emission spectrum of pCK306-*megfp-syndlp* plus rhamnose (Fig. 4.73, blue) indicated the successful induction of the expression of mEGFP-*SynDLP* in the cyanobacterium. However, a distinct mEGFP signal in the fluorescence emission was also observed in the pCK306-*megfp-syndlp* suspension in the absence of rhamnose (Fig. 4.73, red), and, thus, a basal expression of the protein controlled by the *rhaBAD* promoter is indicated.

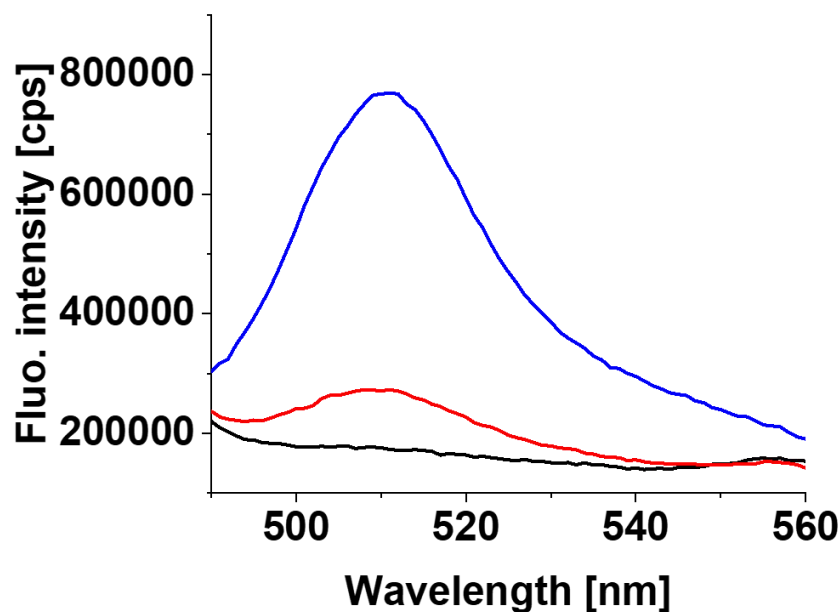


Figure 4.73: Induction of the expression of an mEGFP-tagged *SynDLP* variant *in vivo*.

Liquid cultures of *Synechocystis* strains were photomixotrophically grown to an OD₇₅₀ of approx. 1. Eventually, 1 mg/ml rhamnose was then added to the cultures. Fluorescence emission spectra of the cell suspensions were measured after 24 h. The typical spectrum of a *Synechocystis* wt culture is shown in black and compared to typical spectra of a strain transformed with the plasmid pCK306-mEGFP-*SynDLP* without rhamnose (red) and with the addition of 1 mg/ml rhamnose (blue). For the measurements, the optical density of the cell suspensions was adjusted to 0.5 and the mEGFP-tag was specifically excited ($\lambda_{\text{ex}} = 470 \text{ nm}$).

Fluorescence microscopy was next performed to obtain information about the spatial position of mEGFP-*SynDLP* within the cyanobacterial cell. The TMs of cyanobacteria can be visualized

under the fluorescence microscope due to the pigments of the photosynthetic apparatus. A typical fluorescence micrograph of *Synechocystis* wt is shown in Fig. 4.74a. The TM (Fig. 4.74a, red fluorescence) was surrounded by the cell wall, which was visible in the bright field channel. In a third channel, the mEGFP-tag was specifically excited. Here, *Synechocystis* wt showed no distinct mEGFP signal except a weak background signal caused by the fluorescence of the TM pigments. The same was observed for *Synechocystis* wt after rhamnase addition (Fig. 4.74b). The *Synechocystis* strain pCK306-*megfp-syndlp* revealed green fluorescent spots even without the addition of rhamnase, potentially located on the TM (Fig. 4.74c), which is in line with the basal expression of mEGFP-*SynDLP* in this strain, as shown above (Fig. 4.73). One spot per cell was frequently observed. With the induction of mEGFP-*SynDLP* expression using rhamnase, the number of green fluorescent spots per cell increased (Fig. 4.74d). The positions of the spots again indicated a localization of the fluorescent protein on the TM. However, the exact *in vivo* localization of (mEGFP-)*SynDLP* remains unclear due to the low resolution of the used fluorescence microscope instrument.

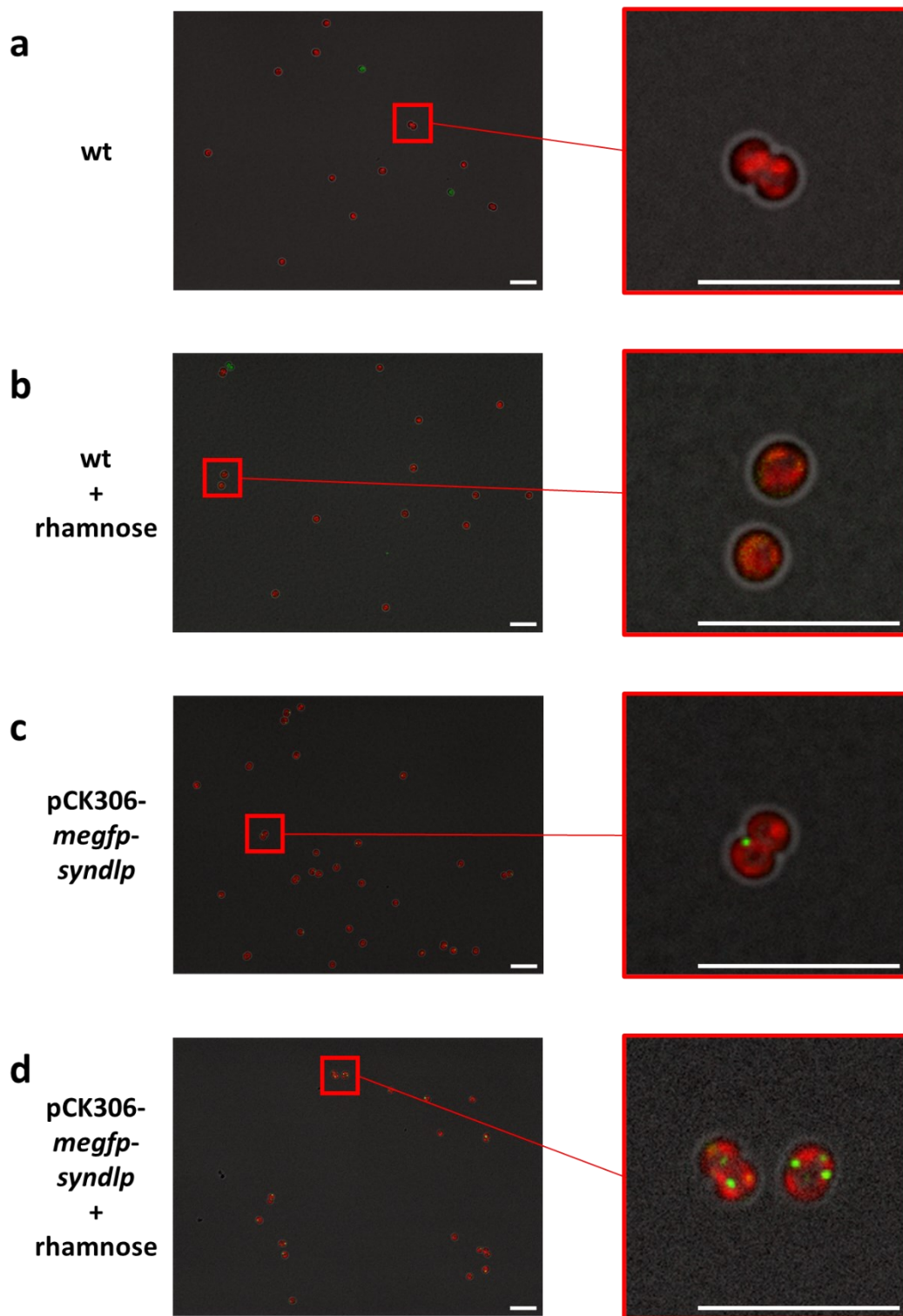


Figure 4.74: *In vivo* localization of mEGFP-tagged *SynDLP* in *Synechocystis* cells.

Cyanobacterial liquid cultures were photomixotrophically grown to an OD_{750} of approx. 1 before the addition of rhamnose. Images of whole cells (bright field channel), TMs (Chl a channel, red) and the N-terminal mEGFP-tag (GFP channel, green) were acquired in a row and the images of one section were overlaid. (a) Micrograph of a *Synechocystis* wt culture 1 d after reaching an OD_{750} of approx. 1 without the addition of rhamnose and (b) with addition of 1 mg/ml rhamnose. (c) Micrograph of *Synechocystis* pCK306-*megfp-syndlp* cells 1 d after reaching an OD_{750} of approx. 1 without the addition of rhamnose and (d) after growth in the presence of 1 mg/ml rhamnose. The zoomed sections highlight single cells in a magnified view. White bars scale for 10 μ m.

Lysis-inducible Synechocystis cells

A distinct *in vivo* function of *SynDLP* could not be identified so far. The knock-out strain Δ *syndlp* showed only minor phenotypic differences compared to *Synechocystis* wt in previous studies (Jilly, 2018). In general, a precise physiological role of a BDLP in the cell has been described so far exclusively for *BsDynA*, which is involved in protecting the plasma membrane against cell lysis caused by bacteriophage infection (Guo *et al.*, 2022). Inspired by this, an involvement of *SynDLP* in membrane protection against cell lysis was assumed. This is supported by the fact that *SynDLP* is capable of membrane fusion *in vitro* (Chapter 4.1, Fig. 4.22) (Gewehr *et al.*, 2023). However, no cyanophage of *Synechocystis* has yet been discovered. Therefore, a genetic lysis system was introduced into the genome of different *Synechocystis* strains (for details see Chapter 3.2.6.2) to investigate the susceptibility of the respective *Synechocystis* cells to induced cell lysis.

The plasmids used for the transformation of *Synechocystis* cells to obtain LICs were kindly provided by [REDACTED] (Asada, Shiraiwa and Suzuki, 2019). *Synechocystis* wt was transformed with the plasmid pGEM-T-Easy-PhoA-LIC to obtain the lysis-inducible *Synechocystis* strain *lic*. Here, a native gene locus of *Synechocystis* (orf *sll0654* encoding an alkaline phosphatase (PhoA)) is substituted by the coding sequences of the genes holin, endolysin and a lysis-associated protein from the bacteriophage *S. enterica* phage P22. *Synechocystis* wt was additionally transformed with the plasmid pGEM-T-Easy-PhoA, which does not carry the three lysis genes from *S. enterica* phage P22 and, thus, served as the EVC (Fig. 4.75a). The resulting strain was termed Δ *phoA*. Complete segregation of the transformed *Synechocystis* strains Δ *phoA* and *lic* was verified by PCR and agarose gel electrophoresis as shown in Fig. 4.75b.

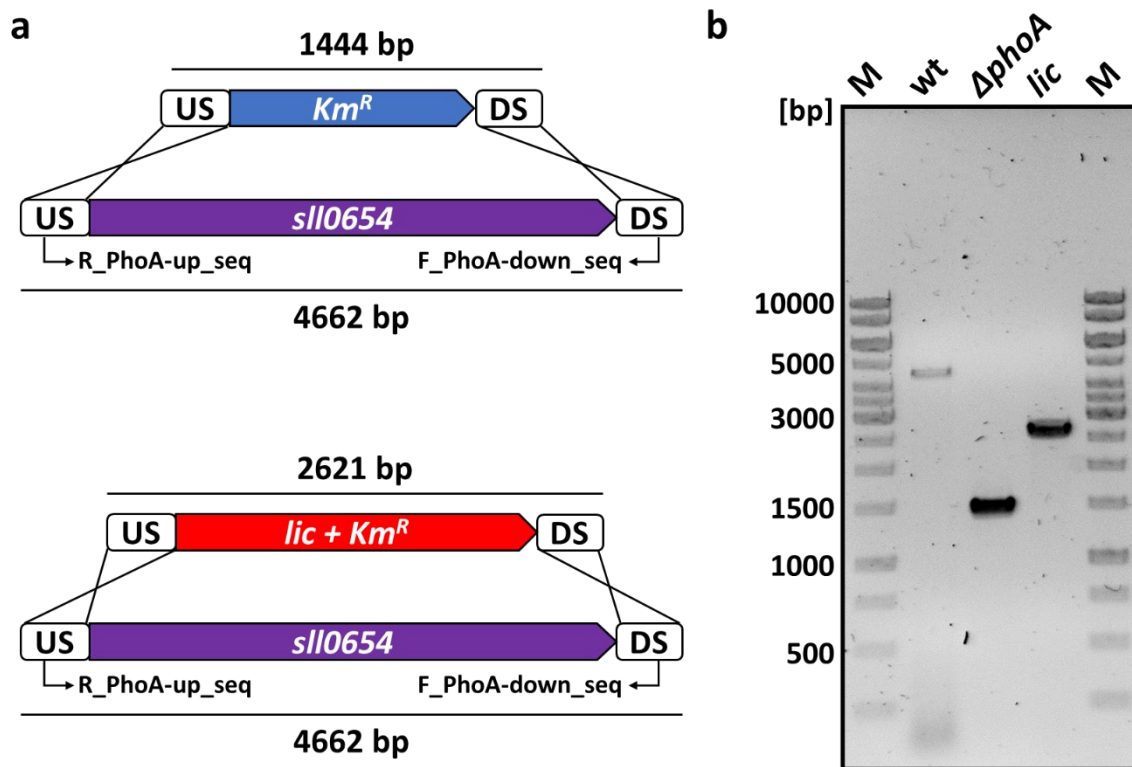


Figure 4.75: Complete segregation of *Synechocystis* wt transformed with *lic* genes plus the EVC.

(a) Schemes illustrating the generation of the *Synechocystis* strains $\Delta phoA$ and *lic* via homologous recombination using a plasmid containing flanking regions up- and downstream (US and DS) of the gene locus *sll0654* and an insert containing a kanamycin resistance cassette (Km^R) and optionally the *lic* genes between the flanking regions. (b) *Synechocystis* wt was transformed with the plasmids pGEM-T-Easy-PhoA and pGEM-T-Easy-PhoA-LIC in BG11 medium containing up to 100 $\mu\text{g/ml}$ kanamycin generating the strains $\Delta phoA$ (EVC) and *lic*. After phenolic DNA extraction, PCRs with the primer pair F_PhoA-down_seq and R_PhoA-up_seq were carried out to check if the transformed *Synechocystis* strains are completely segregated. For the wt, $\Delta phoA$ and *lic* strain the expected PCR product sizes were 4662, 1444 and 2621 bp, respectively. M = marker.

Next, the functionality of the inducible cell lysis system was tested. The PhoA encoded by the *phoA* gene in *Synechocystis* wt is regulated by the phosphate availability in the cell. The expression is initiated under phosphate-deficient conditions. As the three lysis genes introduced in *Synechocystis lic* are still regulated by the native promoter of *sll0654*, cell lysis can be induced by growing the cells in phosphate-free BG11 medium. Growth curves of *Synechocystis* wt, $\Delta phoA$ and *lic* in BG11 medium with or without phosphate showed similar growth of all strains independent from the presence of phosphate in the first two days (Fig. 4.76a). After two days, the three strains showed an impaired growth in phosphate-free BG11 medium. However, no clear difference was observable between the three strains. The Chl a content of the cells was determined after three days to obtain further information about the growth of the strains. Here, the Chl a content was significantly reduced in all strains under phosphate-deficient conditions.

Again, no significant differences were found between the individual strains (Fig. 4.76b). These initial results suggested either that the expression of lysis genes in *Synechocystis lic* did not affect the growth of the entire cyanobacterial population or that the lysis induction system was not functioning properly.

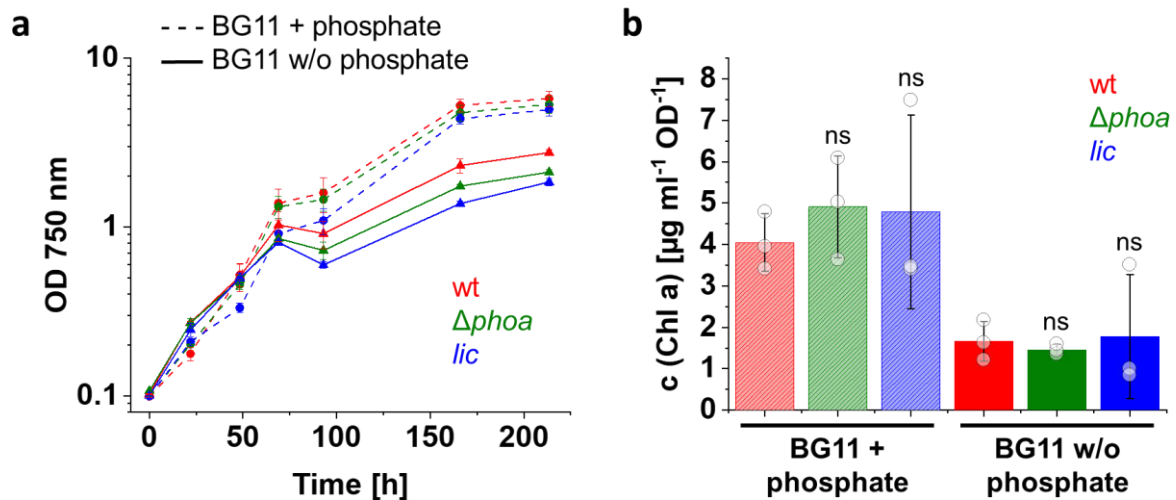


Figure 4.76: Growth in phosphate-limited medium and Chl a content of different *Synechocystis* strains.

Liquid cultures of *Synechocystis* strains were photomixotrophically grown. (a) Optical densities of cultures of wt cells (red), $\Delta phoA$ cells (green) and *lic* cells (blue) under phosphate-sufficient (dashed lines) or phosphate-deficient (solid lines) conditions. Values show the mean of three biological replicates and error bars (S.D.). (b) Chl a content of wt, $\Delta phoA$ and *lic* cells was determined after 3 days growth. *Synechocystis* wt, $\Delta phoA$ and *lic* strains are colored in red, green and blue, respectively. Values represent the mean of three biological replicates and error bars (S.D.). ns = not significant ($P > 0.05$), * $P < 0.05$, ** $P < 0.01$, *** $P < 0.001$ based on a two-sided unpaired Student's t-test. The values of $\Delta phoA$ or *lic* cultures are compared to the wt under the respective phosphate conditions.

The induction of cell lysis in the *Synechocystis lic* strain was next investigated on an individual cell level, as the first characterization of whole populations indicated no differences of the *Synechocystis lic* strain to *Synechocystis* wt and $\Delta phoA$ (Fig. 4.76). Therefore, the strains were cultivated under phosphate-deficient conditions for 1 d and individual cells were observed using fluorescence microscopy. The liquid cultures were incubated with propidium iodide before image acquisition to identify lysed *Synechocystis* cells. Propidium iodide intercalates into DNA and then shows an increased fluorescence emission intensity. As propidium iodide is not membrane-permeable, it can only enter the cytoplasm and, thus, the DNA of lysed cells. A representative fluorescence micrograph of *Synechocystis* wt grown under phosphate-deficient conditions confirmed the typical shape of *Synechocystis* cells with an intact TM (Fig. 4.77, wt bright field + Chl a channel). An increased propidium iodide fluorescence signal was observed

in a few cells. However, most cells were not stained by propidium iodide (Fig. 4.77, wt propidium iodide channel). Similar observations were made in case of a *Synechocystis* $\Delta phoA$ culture, which was used as the EVC. Cells were spherically shaped, and determination of the chlorophyll fluorescence indicated a functional TM (Fig. 4.77, $\Delta phoA$ bright field + Chl a channel). Almost no individual *Synechocystis* $\Delta phoA$ cells showed an increased propidium iodide fluorescence (Fig. 4.77, $\Delta phoA$ propidium iodide channel).

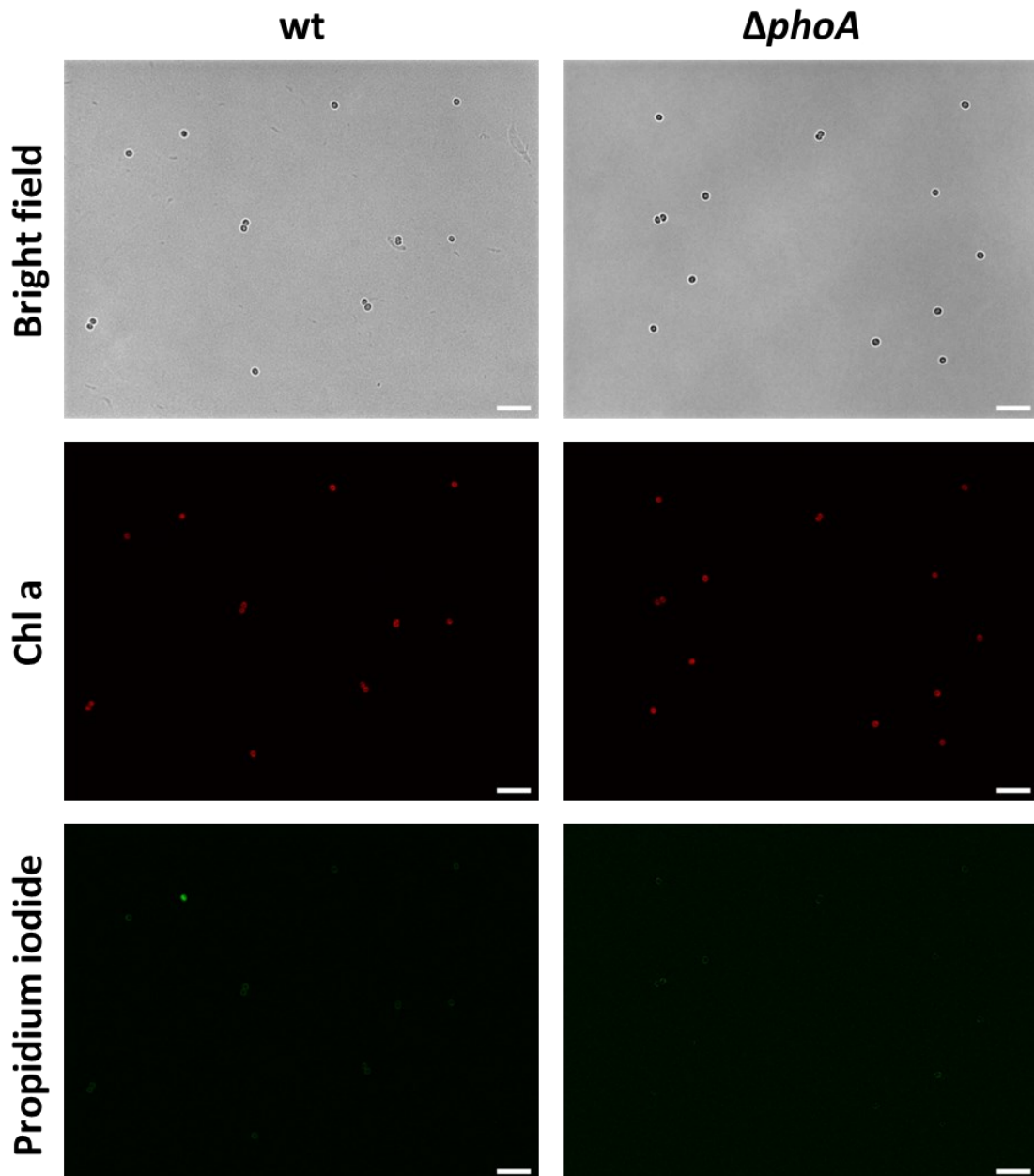


Figure 4.77: Images of wt and $\Delta phoA$ cultured under phosphate-deficient conditions.

Liquid cultures of *Synechocystis* wt and $\Delta phoA$ were photomixotrophically grown for 1 d in phosphate-free BG11 medium. Whole cells were observed via bright field microscopy. TMs were observed using the Chl a autofluorescence, the DNA of lysed cells was stained with propidium iodide, and both visualized via fluorescence microscopy. The white bars scale for 10 μm .

When *Synechocystis lic* cells were cultivated under phosphate-deficient conditions, stained with propidium iodide, and visualized under the fluorescence microscope, the cells showed a spherical shape with an intact TM (Fig. 4.78, bright field + Chl a channel). Yet, propidium iodide staining revealed a high number of lysed cells (Fig. 4.78, propidium iodide channel), indicating proper functioning of the lysis induction system in *Synechocystis* cells.

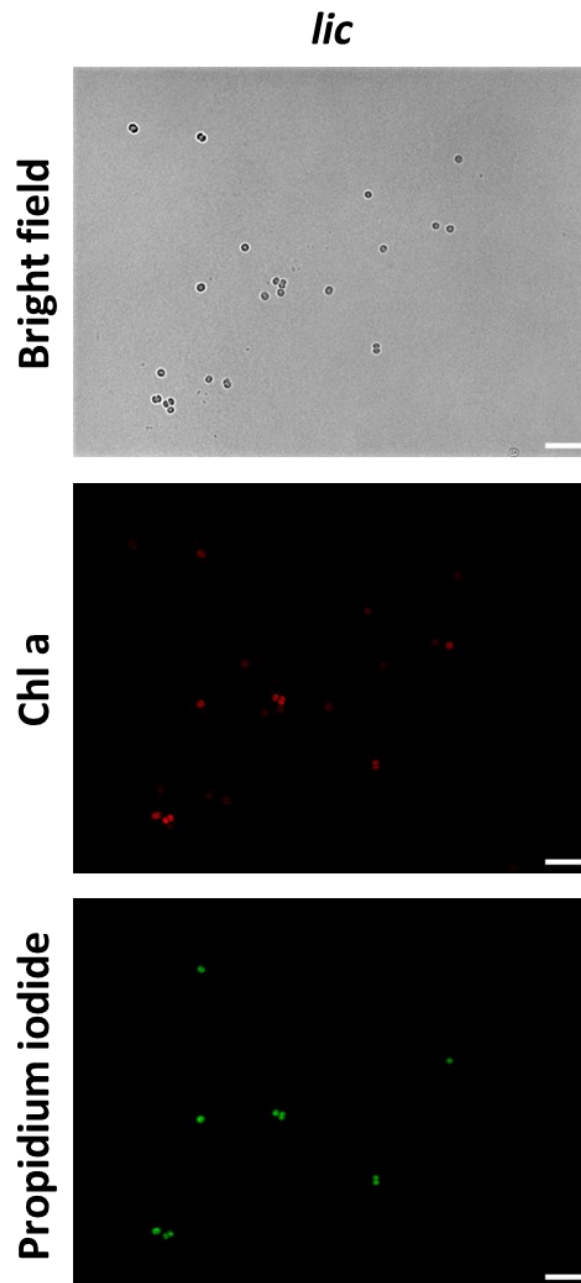


Figure 4.78: Micrographs of lysis-inducible *Synechocystis* cells.

A *Synechocystis lic* liquid culture was photomixotrophically grown for 1 d under phosphate-deficient conditions. Bright field images were acquired to observe whole cells. TMs were visualized using the Chl a autofluorescence and the DNA of lysed cells was stained with propidium iodide and imaged via fluorescence microscopy. The white bars scale for 10 μ m.

After demonstrating the functioning of the lysis induction system in cyanobacterial cells, the *Synechocystis* Δ *syndlp* knock-out strain was transformed with the *lic* genes and the EVC, resulting in the new strains Δ *syndlp-lic* and Δ *syndlp- Δ phoA*. The successful transformation was verified by PCR and agarose gel electrophoresis. Initially, the *syndlp* knock-out in the different *Synechocystis* strains based on Δ *syndlp* was checked at the *slr0869* gene locus encoding SynDLP, indicating an intact *syndlp* knock-out in Δ *syndlp*, Δ *syndlp- Δ phoA* and Δ *syndlp-lic* (Fig. 4.79a). Next, complete transformation of the *phoA* gene locus was verified in the *Synechocystis* Δ *syndlp- Δ phoA* and Δ *syndlp-lic* strains (Fig. 4.79b).

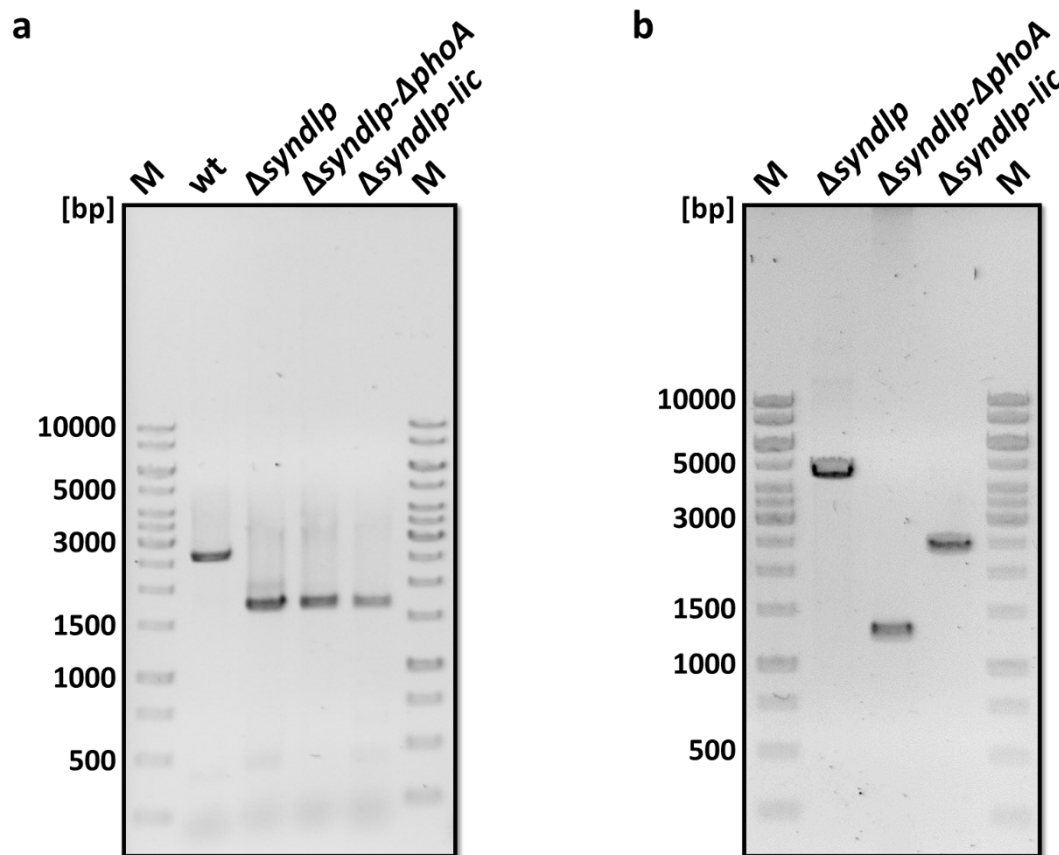


Figure 4.79: Complete segregation of *Synechocystis* Δ *syndlp* cells transformed with *lic* genes.

Synechocystis Δ *syndlp* was transformed with the plasmids pGEM-T-Easy-PhoA-Cm^R and pGEM-T-Easy-PhoA-LIC-Cm^R in BG11 medium supplemented with up to 100 μ g/ml chloramphenicol resulting in the strains Δ *syndlp- Δ phoA* (EVC) and Δ *syndlp-lic*. Genomic DNAs were obtained by phenolic DNA extraction and PCRs were performed to verify the mutation. (a) Initially, it was checked whether the knock-out of the *syndlp* gene was still intact in the corresponding strains. Therefore, a PCR with the primers F_slr0869_upstream and R_slr0869_downstream was performed. For the wt, the expected PCR product size was 2660 bp and for the other three strains with a knocked-out *syndlp* gene 1684 bp (for details on the generation of Δ *syndlp*, see Jilly, 2018). (b) Successful introduction of the *lic* genes was verified by PCR using the primer pair F_PhoA-down_seq and R_PhoA-up_seq. Here, the expected PCR product sizes for Δ *syndlp*, Δ *syndlp- Δ phoA* and Δ *syndlp-lic* were 4662, 1268 and 2445 bp, respectively (for more details see Fig. 4.75). M = marker.

The strains $\Delta syndlp$, $\Delta syndlp-\Delta phoA$ and $\Delta syndlp-lic$ were cultivated in phosphate-free BG11 medium, stained with propidium iodide and visualized under the fluorescence microscope to test for induced cell lysis. The control strains $\Delta syndlp$ and $\Delta syndlp-\Delta phoA$ showed the typical cell shape and fluorescence signal from the TM (Fig. 4.80, bright field + Chl a channel). In both strains the propidium iodide staining indicated no cell lysis under phosphate-deficient conditions (Fig. 4.80, propidium iodide channel).

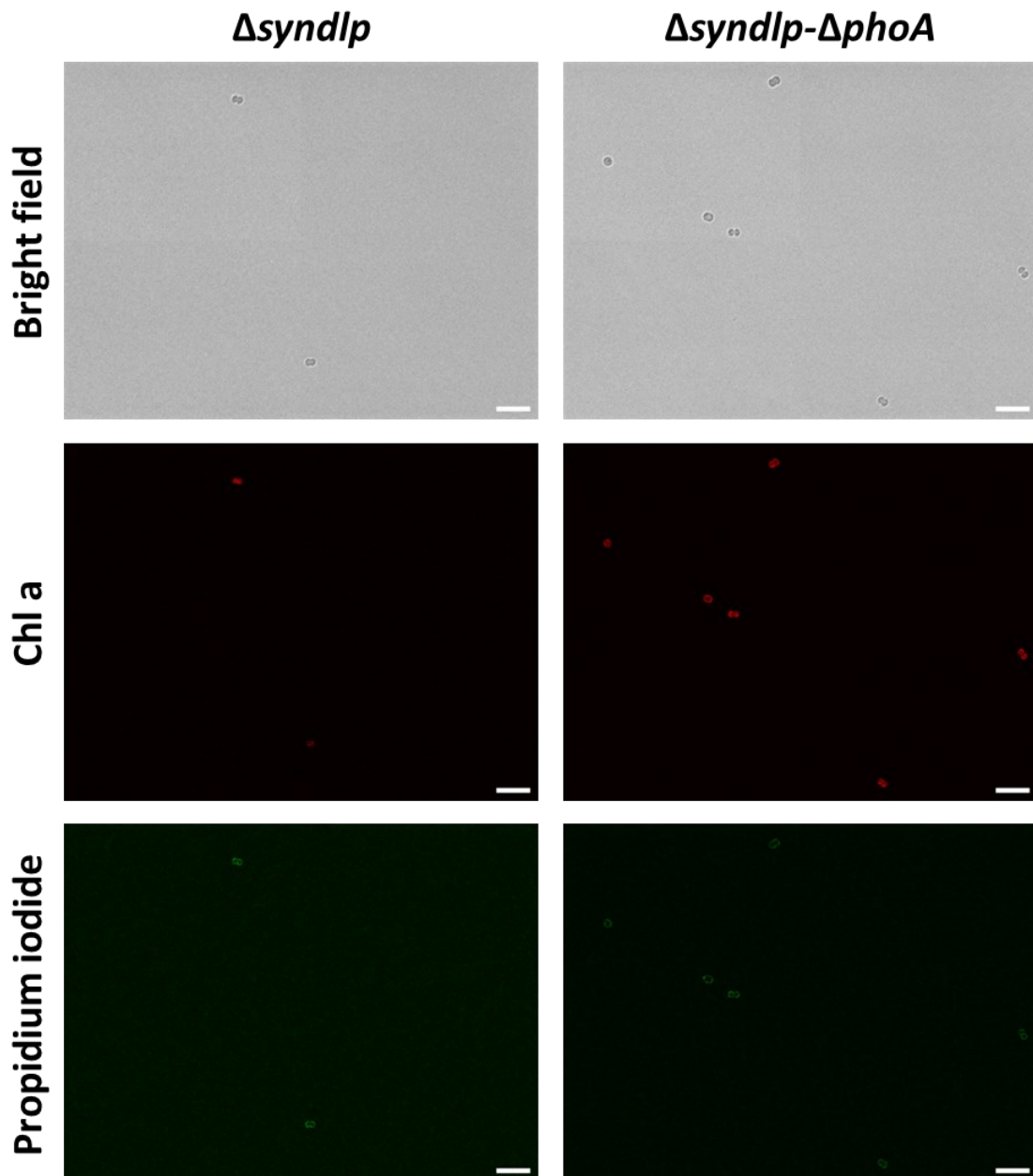


Figure 4.80: *Synechocystis* strains $\Delta syndlp$ and $\Delta syndlp-\Delta phoA$ grown under phosphate-deficient conditions visualized via fluorescence microscopy.

Liquid cultures of *Synechocystis* $\Delta syndlp$ and $\Delta syndlp-\Delta phoA$ were photomixotrophically grown for 1 d in phosphate-free BG11 medium. Whole cells were observed via bright field microscopy. TMs were visualized using the Chl a autofluorescence. In lysed cells the DNA was stained with propidium iodide and visualized via fluorescence microscopy. The white bars scale for 10 μm .

The observation of individual *Synechocystis* Δ *syndlp-lic* cells revealed an intact internal TM system (Fig. 4.81, bright field + Chl a channel). However, partial lysis of the outer membrane and the CM in some of the cells was indicated by an increased propidium iodide fluorescence (Fig. 4.81, propidium iodide channel). This demonstrated the functioning of the *lic* genes in the Δ *syndlp-lic* strain, which now allows to investigate cell lysis in *Synechocystis lic* vs. Δ *syndlp-lic* in future experiments.

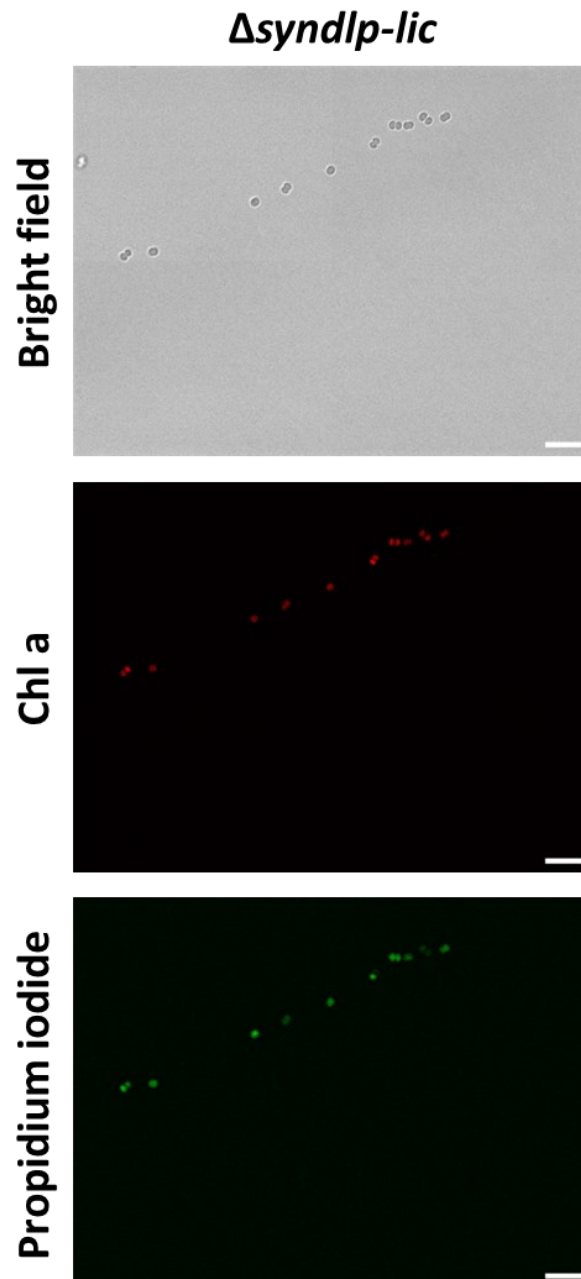


Figure 4.81: Fluorescence micrographs of lysis-inducible *Synechocystis* Δ *syndlp* cells.

A *Synechocystis* Δ *syndlp-lic* liquid culture was photomixotrophically grown for 1 d under phosphate-deficient conditions. Bright field images were acquired to observe whole cells. The TM was observed using the Chl a autofluorescence and the DNA of lysed cells was stained with propidium iodide and imaged via fluorescence microscopy. The white bars scale for 10 μ m.

4.6.3 Discussion

While eukaryotic DLPs with various physiological functions have been characterized, the *in vivo* role of most BDLPs is still largely enigmatic. A distinct function of a cyanobacterial DLP has not yet been described. The genome of *Synechocystis* contains five putative BDLP genes (Jilly, 2018; Jilly *et al.*, 2018). One of the genes encodes *SynDLP*, which has been unequivocally identified as a BDLP (Jilly, 2018; Gewehr *et al.*, 2023). Previous analysis of a *Synechocystis syndlp* knock-out strain ($\Delta syndlp$) revealed no clear phenotype under phototrophic conditions at both normal and high light growth conditions. In addition, no differences between $\Delta syndlp$ and wt were observed under phosphate depletion conditions (Jilly, 2018).

In this study, EM micrographs of ultrathin sections of *Synechocystis* wt and $\Delta syndlp$ cells revealed slight morphological changes in $\Delta syndlp$ cells, such as an enlarged S-layer and multiple glycogen granules between the TM layers (Fig. 4.70). The S-layer is an additional layer on the outer membrane present in a wide variety of prokaryotes and functions as a protective coat, molecule and ion trap as well as molecular sieve in cyanobacteria. S-layers are also involved in surface recognition and cell adhesion (Šmarda *et al.*, 2002; Trautner and Vermaas, 2013). Proteinaceous S-layers typically consist of only one S-layer protein and therefore have a relatively simple architecture. The S-layer protein of *Synechocystis* was identified to be encoded by orf *sll1951* (Trautner and Vermaas, 2013). There are many open questions concerning the S-layer biogenesis in *Synechocystis*, however, two proteins that are encoded by the orfs *sll1180* and *sll1181* are involved in the type 1 secretion of Sll1951. Sll1180 and Sll1181 are homologs of an ABC transporter and a membrane fusion protein, respectively, involved in the type 1 secretion pathway in *E. coli* (Thomas, Holland and Schmitt, 2014; Agarwal *et al.*, 2018). Potentially, *SynDLP* is involved in regulation of the type 1 secretion of Sll1951 as an additional membrane fusion protein, since *SynDLP* has been shown to fuse membranes *in vitro* (Chapter 4.1, Fig. 4.22). In addition to the enlarged S-layer, $\Delta syndlp$ cells had clearly visible white patches between the individual TM layers, which probably resemble glycogen granules (Yamauchi *et al.*, 2011; Kaniya *et al.*, 2013; Damrow, Maldener and Zilliges, 2016). Glycogen is a storage polymer that can rapidly provide sugar compounds as an energy source in *Synechocystis* cells (Prats, Graham and Shearer, 2018). An increase of glycogen granules in $\Delta syndlp$ cells can occur for many reasons, *e.g.*, under nutrient deprivation and subsequent shutdown of the metabolism (Damrow, Maldener and Zilliges, 2016; Dutt and Srivastava, 2018). Direct involvement of *SynDLP* in glycogen degradation is also conceivable.

The literature reports that expression of the *slr0869* gene encoding *SynDLP* is enhanced by the sigma factor SigE (Osanai *et al.*, 2011; Turunen *et al.*, 2022). Sigma factors are required for proper gene transcription in bacteria. Remarkably, SigE enhances the expression of sugar catabolic genes (Osanai *et al.*, 2005, 2011; Kaniya *et al.*, 2013). Thus, the phenotype of *Synechocystis* Δ *syndlp* cells along with the expression of *slr0869* controlled by SigE suggest an involvement of *SynDLP* in sugar catabolism. However, further studies are needed to verify whether *SynDLP* is involved in sugar catabolism or whether the observations from electron micrographs show only secondary effects of *SynDLP*'s *in vivo* role.

In addition to the possible physiological functions of *SynDLP* inferred from EM micrographs of Δ *syndlp* cells, literature research suggests an *in vivo* role of *SynDLP* in stressed *Synechocystis* cells. The protein encoded by *sll1130* was identified as a transcription factor that represses the expression of heat-responsive genes in *Synechocystis*. Transcription of *slr0869* (encoding *SynDLP*) is regulated by Sll1130, as shown by enhanced *slr0869* transcription in a *Synechocystis* Δ *sll1130* strain and a conserved inverted repeat upstream of *slr0869* (Krishna *et al.*, 2013). Thus, down-regulation of *sll1130* in response to heat stress leads to up-regulation of *slr0869* transcription, suggesting a *SynDLP* involvement in protecting the cell from heat stress. A proteomic study revealed increased *SynDLP* expression in a *Synechocystis* Δ *sll0794* strain upon ethanol treatment. Sll0794 was identified as a transcriptional factor involved in ethanol tolerance. Increased ethanol tolerance of *Synechocystis* cells is of great biotechnological importance for the production of ethanol as biofuel using cyanobacteria. Knocking out the *sll0794* gene leads to decreased ethanol tolerance of the cells. However, up-regulation of *SynDLP* expression under these conditions suggests an involvement of *SynDLP* in ethanol tolerance (Song *et al.*, 2014). Remarkably, both ethanol and heat stress damage the membrane integrity and, thus, a role of *SynDLP* as a fusogenic protein protecting membranes against both stresses is quite conceivable. Future studies on *Synechocystis* Δ *syndlp* could include analyses of the mutant strain under heat stress or in the presence of ethanol.

The *in vivo* localization of a protein can provide hints about its putative *in vivo* function. Western Blot analysis of immunoprecipitated *Synechocystis* fractions confirmed that *SynDLP* is a peripherally membrane-attached protein, as it was found in both soluble and membrane fractions (Fig. 4.71). Fluorescence micrographs of mEGFP-labeled *SynDLP* in *Synechocystis* cells indicated the localization of the protein on the TM (Fig. 4.74), which strengthens the hypothesis of a TM remodeling activity of *SynDLP*. However, the limited resolution of the used fluorescence microscopy instrument makes it difficult to determine the exact subcellular protein

localization. In future experiments, using a confocal fluorescence microscope could help to better determine the position of mEGFP-*SynDLP* in *Synechocystis* under different growth conditions. Before that, the Δ *syndlp* strain should be transformed with a plasmid encoding mEGFP-*SynDLP* to observe the signal of the mEGFP-tagged protein in a background without unlabeled *SynDLP*. Additionally, the localization of unlabeled *SynDLP* could be investigated using immunogold staining and EM.

In vivo localization of other BDLPs has also been investigated using fluorescent tags attached to the BDLPs. *MsIniA* is uniformly distributed at the plasma membrane of *Mycobacterium smegmatis* under standard growth conditions (Wang *et al.*, 2019). *EcLeoA* appears as punctate foci that preferentially accumulate at cell poles of *E. coli* (Michie *et al.*, 2014). *SvDynA* and *SvDynB* likely colocalize as heterodimers at nascent sites of sporulation-specific cell division in *Streptomyces venezuelae* (Schlimpert *et al.*, 2017). The cyanobacterial DLP *NpBDLP* localizes in a punctate pattern predominantly at the cell septum of filamentous *Nostoc punctiforme* cells (Low and Löwe, 2006). Also, the localization of *BsDynA* in *Bacillus subtilis* is well studied. Under non-stress conditions, *BsDynA* accumulates at the sites of septation, likely to protect stressed membranes during septation (Bürmann *et al.*, 2011; Sawant *et al.*, 2016). However, under stress conditions, *e.g.*, caused by phage infection, *BsDynA* is located at stressed plasma membrane regions, likely to protect the plasma membrane (Sawant *et al.*, 2016; Guo *et al.*, 2022). This highlights the importance of studying the localization of a BDLP not only under standard conditions but also in stressed cells. Future experiments will therefore include the investigation of *SynDLP*'s *in vivo* localization in stressed *Synechocystis* cells, *e.g.*, upon treatment with heat or ethanol (see above).

Inspired by the physiological function of *BsDynA* (Guo *et al.*, 2022), lysis-inducible *Synechocystis* cells were generated to investigate a potential influence of *SynDLP* on cell lysis (Asada, Shiraiwa and Suzuki, 2019). For this purpose, *Synechocystis* wt and Δ *syndlp* were successfully transformed with *lic* genes (Figs. 4.75, 4.79). Analysis of the *Synechocystis lic* strain revealed no effect of *lic* gene expression on the whole population (Fig. 4.76). However, successful implementation of the lysis induction system in both *Synechocystis* wt and Δ *syndlp* was demonstrated on the single cell level using fluorescence microscopy (Figs. 4.77, 4.78, 4.80, 4.81) (compare with (Asada, Shiraiwa and Suzuki, 2019)). The next step will be the quantification of *Synechocystis* cell lysis, either by statistical analysis of fluorescence micrographs or by fluorescence spectroscopic measurements of the propidium iodide fluorescence intensity. After transformation of the *Synechocystis* strain pCK306-*syndlp* (Fig.

4.72), which can overexpress *SynDLP*, with *lic* genes, the degree of cell lysis can be compared between *Synechocystis* wt, Δ *syndlp* (absence of *SynDLP*) and pCK306-*syndlp* (overexpression of *SynDLP*).

In conclusion, the *in vivo* characterization of *SynDLP* was extended. EM micrographs of the *syndlp* knock-out strain Δ *syndlp*, which showed no clear phenotype in previous studies (Jilly, 2018), revealed an enlarged S-layer and an increased amount of glycogen granules between TM layers, potentially indicating a role of *SynDLP* in sugar catabolism. Analyses of the *in vivo* localization confirmed that *SynDLP* is a peripheral membrane protein. However, the exact localization in the cyanobacterial cell and under changing growth or stress conditions remains elusive. Finally, lysis-inducible *Synechocystis* cells were generated, which now allow the investigation of a presumed effect of *SynDLP* in protection against cell lysis.

5 Conclusion

DLPs are mechanochemical GTPases that remodel membranes. While the functions of several eukaryotic DLPs have been elucidated, the physiological role of most BDLPs remains unclear. In a photosynthetic cyanobacterium, such as *Synechocystis*, a role in remodeling the TM, which harbors the protein complexes for the photosynthetic light reaction, is suggested. *SynDLP*, the BDLP of *Synechocystis*, has previously been shown to hydrolyze GTP, form large oligomers and interact with negatively charged TM lipids. In *in vivo* experiments, a *syndlp* knock-out strain of *Synechocystis* (Δ *syndlp*) has not shown an essential function of *SynDLP* under standard growth conditions.

The results presented in this thesis unequivocally identified *SynDLP* as a BDLP based on the cryo-EM structure of *SynDLP* oligomers. The structure showed a monomer arrangement and oligomerization interfaces previously known exclusively for eukaryotic DLPs. Thus, *SynDLP* represents the closest known prokaryotic ancestor of eukaryotic DLPs. Moreover, the oligomer structure revealed special features of a DLP such as an intramolecular disulfide bridge in the BSE domain and an expanded intermolecular GD-BSE interface. Both regulate the GTPase activity of *SynDLP* (**Chapter 4.1**). An intermolecular salt bridge between the GD and the stalk domain was observed in the *SynDLP* oligomer structure. This GD-stalk connection is also present in human dynamin and likely influences the structure and GTPase activity of oligomeric (B)DLPs (**Chapter 4.2**).

The described intramolecular disulfide bridge in the BSE domain suggests regulation of *SynDLP* by a Trx. Thus, in this work, a gene encoding a Trx isoform of *Synechocystis* (*SynTrxA*) was cloned from the *Synechocystis* genome in an overexpression vector. Recombinant *SynTrxA* was expressed and purified. The activity of isolated *SynTrxA* was confirmed in an established insulin reduction assay. However, regulation of *SynDLP* by *SynTrxA* could not be demonstrated (**Chapter 4.5**).

DLPs typically show conformational changes during the GTP hydrolysis cycle. The addition of GTP/GDP did not result in significant changes in the structure of *SynDLP* oligomers. However, freezing the GTP-bound state using GMPPnP showed aggregation of *SynDLP* oligomers. The interaction was further investigated by design and establishment of a stalkless *SynDLP* variant that revealed transverse GD-GD dimerization of *SynDLP* during GTP hydrolysis (**Chapter 4.4**).

Since DLPs are membrane-active enzymes, the *SynDLP*'s membrane interaction was further studied in this work, extending previous studies. New methods were established to describe the membrane binding of *SynDLP*. A GUV membrane binding assay visualized membrane binding of a fluorescently labeled *SynDLP* variant and SPR spectroscopy was assessed as a suitable method to quantify the membrane interaction propensity of *SynDLP*. Several mutants were biochemically characterized in detail to identify the MID of *SynDLP*. However, each mutant still interacted with membranes and, thus, the identification of *SynDLP*'s MID turned out not to be straightforward (**Chapter 4.3**). Finally, a FRET-based membrane fusion assay revealed a fusogenic activity of *SynDLP*, at least *in vitro* (**Chapter 4.1**).

In this work, expression of native *SynDLP* in *Synechocystis* was detected for the first time (**Chapter 4.1**). Comparison of EM micrographs of *Synechocystis* wt and Δ *syndlp* cells suggested the possible involvement of *SynDLP* in sugar catabolism. Analysis of the *in vivo* localization confirmed that *SynDLP* is a peripheral membrane protein likely attached to the TM, which was studied by transformation of *Synechocystis* cells with a gene encoding a fluorescently labeled *SynDLP* variant. In addition, *Synechocystis* wt and Δ *syndlp* were transformed with genes encoding a controlled lysis induction system. Such strains will allow the investigation of a potential *SynDLP* function under cell lysis conditions in future experiments (**Chapter 4.6**).

Taken together, the results presented in this thesis expand our understanding of BDLPs in general and indicate potential functions of BDLPs in cyanobacteria. The eukaryotic-like architecture of *SynDLP* oligomers indicates a close relationship between eukaryotic and prokaryotic DLPs.

6 Literature

Abed, R.M.M., Dobretsov, S. and Sudesh, K. (2009) 'Applications of cyanobacteria in biotechnology', *Journal of applied microbiology*, 106(1), pp. 1–12.

Accola, M.A. *et al.* (2002) 'The antiviral dynamin family member, MxA, tubulates lipids and localizes to the smooth endoplasmic reticulum', *Journal of Biological Chemistry*, 277(24), pp. 21829–21835. Available at: <https://doi.org/10.1074/jbc.M201641200>.

Adam, Z. *et al.* (2011) 'Biogenesis of thylakoid networks in angiosperms: Knowns and unknowns', *Plant Molecular Biology*, 76(3–5), pp. 221–234. Available at: <https://doi.org/10.1007/s11103-010-9693-5>.

Afonine, P. V *et al.* (2018) 'New tools for the analysis and validation of cryo-EM maps and atomic models', *Acta Crystallographica Section D: Structural Biology*, 74(9), pp. 814–840.

Agarwal, R. *et al.* (2010) 'Heterogeneity in thylakoid membrane proteome of *Synechocystis* 6803', *Journal of Proteomics*, 73(5), pp. 976–991.

Agarwal, R. *et al.* (2018) 'The S-layer biogenesis system of *Synechocystis* 6803: role of Sll1180 and Sll1181 (*E. coli* HlyB and HlyD analogs) as type-I secretion components for Sll1951 export', *Biochimica et Biophysica Acta (BBA)-Biomembranes*, 1860(7), pp. 1436–1446.

Al-Haj, L. *et al.* (2016) 'Cyanobacteria as Chassis for Industrial Biotechnology: Progress and Prospects', *Life*, 6(4), p. 42. Available at: <https://doi.org/10.3390/life6040042>.

Allen, L. *et al.* (2014) 'Publishing: Credit where credit is due', *Nature*, 508(7496), pp. 312–313.

Anand, R., Eschenburg, S. and Reubold, T.F. (2016) 'Crystal structure of the GTPase domain and the bundle signalling element of dynamin in the GDP state', *Biochemical and biophysical research communications*, 469(1), pp. 76–80.

Anderson, S.L. and McIntosh, L. (1991) 'Light-activated heterotrophic growth of the cyanobacterium *Synechocystis* sp. strain PCC 6803: A blue-light-requiring process', *Journal of Bacteriology*, 173(9), pp. 2761–2767. Available at: <https://doi.org/10.1128/jb.173.9.2761-2767.1991>.

Andrews, N.W., Almeida, P.E. and Corrotte, M. (2014) 'Damage control: cellular mechanisms of plasma membrane repair', *Trends in cell biology*, 24(12), pp. 734–742.

- Antonny, B. *et al.* (2016) ‘Membrane fission by dynamin: what we know and what we need to know’, *The EMBO Journal*, 35(21), pp. 2270–2284. Available at: <https://doi.org/10.15252/emboj>.
- Anwar, K. *et al.* (2012) ‘The dynamin-like GTPase Sey1p mediates homotypic ER fusion in *S. cerevisiae*’, *Journal of Cell Biology*, 197(2), pp. 209–217.
- Aoki, M. *et al.* (2004) ‘Differing involvement of sulfoquinovosyl diacylglycerol in photosystem II in two species of unicellular cyanobacteria’, *European Journal of Biochemistry*, 271(4), pp. 685–693. Available at: <https://doi.org/10.1111/j.1432-1033.2003.03970.x>.
- Arimura, S. and Tsutsumi, N. (2002) ‘A dynamin-like protein (ADL2b), rather than FtsZ, is involved in Arabidopsis mitochondrial division.’, *Proceedings of the National Academy of Sciences of the United States of America*, 99, pp. 5727–5731. Available at: <https://doi.org/10.1073/pnas.082663299>.
- Asada, R., Shiraiwa, Y. and Suzuki, I. (2019) ‘A novel cell lysis system induced by phosphate deficiency in the cyanobacterium *Synechocystis* sp. PCC 6803’, *Journal of applied phycology*, 31, pp. 1069–1076.
- Ashkenazy, H. *et al.* (2010) ‘ConSurf 2010: calculating evolutionary conservation in sequence and structure of proteins and nucleic acids’, *Nucleic acids research*, 38(suppl_2), pp. W529–W533.
- Ashkenazy, H. *et al.* (2016) ‘ConSurf 2016: an improved methodology to estimate and visualize evolutionary conservation in macromolecules’, *Nucleic acids research*, 44(W1), pp. W344–W350.
- Aung, K. and Hu, J. (2009) ‘The Arabidopsis peroxisome division mutant pdd2 is defective in the dynamin-related protein3A (DRP3A) gene’, *Plant Signaling and Behavior*, 4(6), pp. 542–544. Available at: <https://doi.org/10.4161/psb.4.6.8699>.
- Aung, K. and Hu, J. (2012) ‘Differential Roles of Arabidopsis Dynamin-Related Proteins DRP3A, DRP3B, and DRP5B in Organelle Division’, *Journal of Integrative Plant Biology*, 54(11), pp. 921–931. Available at: <https://doi.org/10.1111/j.1744-7909.2012.01174.x>.
- Bagatolli, L.A. (2013) ‘LAURDAN fluorescence properties in membranes: a journey from the fluorometer to the microscope’, *Fluorescent methods to study biological membranes*, pp. 3–35.

- Ban, T. *et al.* (2017) ‘Molecular basis of selective mitochondrial fusion by heterotypic action between OPA1 and cardiolipin’, *Nature cell biology*, 19(7), pp. 856–863.
- Barten, R. and Lill, H. (1995) ‘DNA-uptake in the naturally competent cynaobacterium, *Synechocystis* sp. PCC 6803’, *FEMS Microbiology Letters*, 129, pp. 83–88.
- Barthel, S. *et al.* (2013) ‘Thylakoid membrane maturation and PSII activation are linked in greening *Synechocystis* sp. PCC 6803 cells.’, *Plant physiology*, 163(2), pp. 1037–1046. Available at: <https://doi.org/10.1104/pp.113.224428>.
- Bernát, G., Waschewski, N. and Rögner, M. (2009) ‘Towards efficient hydrogen production: The impact of antenna size and external factors on electron transport dynamics in *Synechocystis* PCC 6803’, *Photosynthesis Research*, 99(3), pp. 205–216. Available at: <https://doi.org/10.1007/s11120-008-9398-7>.
- Bian, X. *et al.* (2011) ‘Structures of the atlastin GTPase provide insight into homotypic fusion of endoplasmic reticulum membranes.’, *Proceedings of the National Academy of Sciences of the United States of America*, 108(10), pp. 3976–3981. Available at: <https://doi.org/10.1073/pnas.1101643108>.
- Bleazard, W. *et al.* (1999) ‘The dynamin-related GTPase Dnm1 regulates mitochondrial fission in yeast’, *Nature cell biology*, 1(5), pp. 298–304.
- Blik, A.M. Van Der (1999) ‘Functional diversity in the dynamin family’, *Trends in Cell Biology*, 9(3), pp. 96–102. Available at: [https://doi.org/10.1016/S0962-8924\(98\)01490-1](https://doi.org/10.1016/S0962-8924(98)01490-1).
- Block, M.A. *et al.* (2007) ‘Chloroplast envelope membranes: a dynamic interface between plastids and the cytosol’, *Photosynthesis Research*, 92(2), pp. 225–244. Available at: <https://doi.org/10.1007/s11120-007-9195-8>.
- Bohuszewicz, O., Liu, J. and Low, H.H. (2016) ‘Membrane remodelling in bacteria’, *Journal of Structural Biology*, 196(1), pp. 3–14. Available at: <https://doi.org/10.1016/j.jsb.2016.05.010>.
- Bohuszewicz, O. and Low, H.H. (2018) ‘Structure of a mitochondrial fission dynamin in the closed conformation’, *Nature structural & molecular biology*, 25(8), pp. 722–731.
- Bork, P., Sander, C. and Valencia, A. (1992) ‘An ATPase domain common to prokaryotic cell cycle proteins, sugar kinases, actin, and hsp70 heat shock proteins.’, *Proceedings of the National Academy of Sciences*, 89(16), pp. 7290–7294.

- Boudière, L. *et al.* (2014) ‘Glycerolipids in photosynthesis: Composition, synthesis and trafficking’, *Biochimica et Biophysica Acta (BBA) - Bioenergetics*, 1837(4), pp. 470–480. Available at: <https://doi.org/10.1016/j.bbabi.2013.09.007>.
- Bramkamp, M. (2018) ‘Bacterial dynamin-like proteins reveal mechanism for membrane fusion’, *Nature communications*, 9(1), pp. 1–3.
- Brown, E.A. and Hardwidge, P.R. (2007) ‘Biochemical characterization of the enterotoxigenic *Escherichia coli* LeoA protein’, *Microbiology*, 153(11), pp. 3776–3784. Available at: <https://doi.org/10.1099/mic.0.2007/009084-0>.
- Buchanan, B.B. (1980) ‘Role of light in the regulation of chloroplast enzymes’, *Annual Review of Plant Physiology*, 31(1), pp. 341–374.
- Bürmann, F. *et al.* (2011) ‘A bacterial dynamin-like protein mediating nucleotide-independent membrane fusion.’, *Molecular microbiology*, 79(5), pp. 1294–1304. Available at: <https://doi.org/10.1111/j.1365-2958.2011.07523.x>.
- Bustillo-Zabalbeitia, I. *et al.* (2014) ‘Specific interaction with cardiolipin triggers functional activation of Dynamin-Related Protein 1.’, *PLoS one*. Edited by S. Strack, 9(7), p. e102738. Available at: <https://doi.org/10.1371/journal.pone.0102738>.
- Byrne, B. and Iwata, S. (2002) ‘Membrane protein complexes’, *Current opinion in structural biology*, 12(2), pp. 239–243.
- Cao, Y.L. *et al.* (2017) ‘MFN1 structures reveal nucleotide-triggered dimerization critical for mitochondrial fusion’, *Nature*, 542(7641), pp. 372–376. Available at: <https://doi.org/10.1038/nature21077>.
- Celniker, G. *et al.* (2013) ‘ConSurf: using evolutionary data to raise testable hypotheses about protein function’, *Israel Journal of Chemistry*, 53(3-4), pp. 199–206.
- Chandhok, G., Lazarou, M. and Neumann, B. (2018) ‘Structure, function, and regulation of mitofusin-2 in health and disease’, *Biological Reviews*, 93(2), pp. 933–949.
- Chapman, D.J., De-Felice, J. and Barber, J. (1983) ‘Growth temperature effects on thylakoid membrane lipid and protein content of pea chloroplasts.’, *Plant physiology*, 72(1), pp. 225–228. Available at: <http://www.ncbi.nlm.nih.gov/pubmed/16662966>.

Chappie, J.S. *et al.* (2010) ‘G domain dimerization controls dynamin’s assembly-stimulated GTPase activity’, *Nature*, 465(7297), pp. 435–440. Available at: <https://doi.org/10.1038/nature09032>.

Chappie, J.S. *et al.* (2011) ‘A pseudoatomic model of the dynamin polymer identifies a hydrolysis-dependent powerstroke’, *Cell*, 147(1), pp. 209–222. Available at: <https://doi.org/10.1016/j.cell.2011.09.003>.

Choi, H. *et al.* (2012) ‘Honauicins A-C, potent inhibitors of inflammation and bacterial quorum sensing: Synthetic derivatives and structure-activity relationships’, *Chemistry and Biology*, 19(5), pp. 589–598. Available at: <https://doi.org/10.1016/j.chembiol.2012.03.014>.

Cook, T., Mesa, K. and Urrutia, R. (1996) ‘Three dynamin-encoding genes are differentially expressed in developing rat brain.’, *Journal of neurochemistry*, 67(3), pp. 927–931. Available at: <http://www.ncbi.nlm.nih.gov/pubmed/8752097>.

Cook, T.A., Urrutia, R. and McNiven, M.A. (1994) ‘Identification of dynamin 2, an isoform ubiquitously expressed in rat tissues.’, *Proceedings of the National Academy of Sciences of the United States of America*, 91(2), pp. 644–648. Available at: <http://www.ncbi.nlm.nih.gov/pubmed/8290576>.

Cooley, J.W., Howitt, C.A. and Vermaas, W.F.J. (2000) ‘Succinate: quinol oxidoreductases in the cyanobacterium *Synechocystis* sp. strain PCC 6803: presence and function in metabolism and electron transport’, *Journal of Bacteriology*, 182(3), pp. 714–722.

Croll, T.I. (2018) ‘ISOLDE: a physically realistic environment for model building into low-resolution electron-density maps’, *Acta Crystallographica Section D: Structural Biology*, 74(6), pp. 519–530.

Dai, S. *et al.* (2007) ‘Structural snapshots along the reaction pathway of ferredoxin–thioredoxin reductase’, *Nature*, 448(7149), pp. 92–96.

Damrow, R., Maldener, I. and Zilliges, Y. (2016) ‘The multiple functions of common microbial carbon polymers, glycogen and PHB, during stress responses in the non-diazotrophic cyanobacterium *Synechocystis* sp. PCC 6803’, *Frontiers in Microbiology*, 7, p. 966.

Daumke, O. *et al.* (2007) ‘Architectural and mechanistic insights into an EHD ATPase involved in membrane remodelling.’, *Nature*, 449(7164), pp. 923–927. Available at: <https://doi.org/10.1038/nature06173>.

Daumke, O. and Praefcke, G.J.K. (2016) 'Invited review: Mechanisms of GTP hydrolysis and conformational transitions in the dynamin superfamily', *Biopolymers*, 105(8), pp. 580–593. Available at: <https://doi.org/10.1002/bip.22855>.

Dorne, A.-J., Joyard, J. and Douce, R. (1990) 'Do thylakoids really contain phosphatidylcholine?', *Proceedings of the National Academy of Sciences of the United States of America*, 87(January), pp. 71–74. Available at: <https://doi.org/10.1073/pnas.87.1.71>.

Du, Y. *et al.* (2013) 'Thioredoxin 1 is inactivated due to oxidation induced by peroxiredoxin under oxidative stress and reactivated by the glutaredoxin system', *Journal of Biological Chemistry*, 288(45), pp. 32241–32247.

Dutt, V. and Srivastava, S. (2018) 'Novel quantitative insights into carbon sources for synthesis of poly hydroxybutyrate in *Synechocystis* PCC 6803', *Photosynthesis research*, 136, pp. 303–314.

e Costa, R.A.P. *et al.* (2020) 'ADAM17 cytoplasmic domain modulates Thioredoxin-1 conformation and activity', *Redox Biology*, 37, p. 101735.

Emsley, P. *et al.* (2010) 'Features and development of Coot', *Acta Crystallographica Section D: Biological Crystallography*, 66(4), pp. 486–501.

Essigmann, B. *et al.* (1998) 'Phosphate availability affects the thylakoid lipid composition and the expression of SQD1, a gene required for sulfolipid biosynthesis in *Arabidopsis thaliana*', *Proceedings of the National Academy of Sciences*, 95(4), pp. 1950–1955. Available at: <https://doi.org/10.1073/pnas.95.4.1950>.

Faelber, K. *et al.* (2011) 'Crystal structure of nucleotide-free dynamin.', *Nature*, 477(7366), pp. 556–560. Available at: <https://doi.org/10.1038/nature10369>.

Faelber, K. *et al.* (2019) 'Structure and assembly of the mitochondrial membrane remodelling GTPase Mgm1', *Nature*, 571(7765), pp. 429–433.

Findinier, J., Delevoye, C. and Cohen, M.M. (2019) 'The dynamin-like protein Fzl promotes thylakoid fusion and resistance to light stress in *Chlamydomonas reinhardtii*', *PLoS genetics*, 15(3), p. e1008047.

Florencio, F.J. *et al.* (2006) 'The diversity and complexity of the cyanobacterial thioredoxin systems', *Photosynthesis Research*, 89(2–3), pp. 157–171.

- Ford, M.G.J. and Chappie, J.S. (2019) 'The structural biology of the dynamin-related proteins: New insights into a diverse, multitasking family', *Traffic*, 20(10), pp. 717–740.
- Ford, M.G.J., Jenni, S. and Nunnari, J. (2011) 'The crystal structure of dynamin.', *Nature*, 477(7366), pp. 561–566. Available at: <https://doi.org/10.1038/nature10441>.
- Franz, J., Zadel, M.J. Van and Weidner, T. (2017) 'A trough for improved SFG spectroscopy of lipid monolayers', *Review of Scientific Instruments*, 88(5). Available at: <https://doi.org/10.1063/1.4982050>.
- Fres, J.M., Müller, S. and Praefcke, G.J.K. (2010) 'Purification of the CaaX-modified, dynamin-related large GTPase hGBP1 by coexpression with farnesyltransferase [S]', *Journal of lipid research*, 51(8), pp. 2454–2459.
- Frezza, C. *et al.* (2006) 'OPA1 Controls Apoptotic Cristae Remodeling Independently from Mitochondrial Fusion', *Cell*, 126(1), pp. 177–189. Available at: <https://doi.org/10.1016/j.cell.2006.06.025>.
- Fribourgh, J.L. *et al.* (2014) 'Structural insight into HIV-1 restriction by MxB', *Cell host & microbe*, 16(5), pp. 627–638.
- Fröhlich, C. *et al.* (2013) 'Structural insights into oligomerization and mitochondrial remodelling of dynamin 1-like protein', *EMBO Journal*, 32(9), pp. 1280–1292. Available at: <https://doi.org/10.1038/emboj.2013.74>.
- Fuhrmann, E. *et al.* (2009) 'The Vesicle-inducing Protein 1 from *Synechocystis* sp. PCC 6803 Organizes into Diverse Higher-Ordered Ring Structures', *Molecular Biology of the Cell*, 20(21), pp. 4620–4628. Available at: <https://doi.org/10.1091/mbc.E09-04-0319>.
- Fujimoto, M. *et al.* (2009) 'Arabidopsis dynamin-related proteins DRP3A and DRP3B are functionally redundant in mitochondrial fission, but have distinct roles in peroxisomal fission', *Plant Journal*, 58(3), pp. 388–400. Available at: <https://doi.org/10.1111/j.1365-3113.2009.03786.x>.
- Gao, H. *et al.* (2003) 'ARC5, a cytosolic dynamin-like protein from plants, is part of the chloroplast division machinery', *Proceedings of the National Academy of Sciences*, 100(7), pp. 4328–4333. Available at: <https://doi.org/10.1073/pnas.0530206100>.

- Gao, H., Sage, T.L. and Osteryoung, K.W. (2006) 'FZL, an FZO-like protein in plants, is a determinant of thylakoid and chloroplast morphology', *Proc Natl Acad Sci USA*, 103(17), pp. 6759–6764. Available at: <https://doi.org/10.1073/pnas.0507287103>.
- Gao, H. and Xu, X. (2009) 'Depletion of Vipp1 in *Synechocystis* sp. PCC 6803 affects photosynthetic activity before the loss of thylakoid membranes', *FEMS microbiology letters*, 292(1), pp. 63–70.
- Gao, S. *et al.* (2010) 'Structural basis of oligomerization in the stalk region of dynamin-like MxA', *Nature*, 465(7297), pp. 502–506. Available at: <https://doi.org/10.1038/nature08972>.
- Gasper, R. *et al.* (2009) 'It takes two to tango: regulation of G proteins by dimerization', *Nature reviews Molecular cell biology*, 10(6), pp. 423–429.
- Gaysina, L.A., Saraf, A. and Singh, P. (2019) 'Cyanobacteria in diverse habitats', *Cyanobacteria*. Elsevier, pp. 1–28.
- Geigenberger, P. *et al.* (2017) 'The unprecedented versatility of the plant thioredoxin system', *Trends in plant science*, 22(3), pp. 249–262.
- Gewehr, L. *et al.* (2023) 'SynDLP is a dynamin-like protein of *Synechocystis* sp. PCC 6803 with eukaryotic features', *Nature Communications*, 14(1), p. 2156.
- Ghosh, A. *et al.* (2006) 'How guanylate-binding proteins achieve assembly-stimulated processive cleavage of GTP to GMP', *Nature*, 440(7080), pp. 101–104.
- Gibson, D.G. *et al.* (2009) 'Enzymatic assembly of DNA molecules up to several hundred kilobases', *Nature methods*, 6(5), pp. 343–345.
- Glaser, F. *et al.* (2003) 'ConSurf: identification of functional regions in proteins by surface-mapping of phylogenetic information', *Bioinformatics*, 19(1), pp. 163–164.
- Goddard, T.D. *et al.* (2018) 'UCSF ChimeraX: Meeting modern challenges in visualization and analysis', *Protein Science*, 27(1), pp. 14–25.
- Gounaris, K. *et al.* (1983) 'Lateral heterogeneity of polar lipids in the thylakoid membranes of spinach chloroplasts', *FEBS Letters*, 156(1), pp. 170–174. Available at: [https://doi.org/10.1016/0014-5793\(83\)80271-3](https://doi.org/10.1016/0014-5793(83)80271-3).
- Griese, M., Lange, C. and Soppa, J. (2011) 'Ploidy in cyanobacteria', *FEMS microbiology letters*, 323(2), pp. 124–131.

- Güler, S. *et al.* (1996) 'A null mutant of *Synechococcus* sp. PCC7942 deficient in the sulfolipid sulfoquinovosyl diacylglycerol', *Journal of Biological Chemistry*, 271(13), pp. 7501–7507. Available at: <https://doi.org/10.1074/jbc.271.13.7501>.
- Gunther, G. *et al.* (2021) 'LAURDAN since Weber: The quest for visualizing membrane heterogeneity', *Accounts of chemical research*, 54(4), pp. 976–987.
- Guo, L. *et al.* (2022) 'A Bacterial Dynamin-Like Protein Confers a Novel Phage Resistance Strategy on the Population Level in *Bacillus subtilis*', *mBio*, 13(1), pp. e03753-21. Available at: <https://doi.org/10.1128/mbio.03753-21>.
- Guo, L. and Bramkamp, M. (2019) 'Bacterial dynamin-like protein DynA mediates lipid and content mixing', (14). Available at: <https://doi.org/10.1096/fj.201900844RR>.
- Gupta, S. *et al.* (2020) 'Dynamin-like proteins are essential for vesicle biogenesis in *Mycobacterium tuberculosis*.', *bioRxiv* [Preprint].
- Gupta, S. *et al.* (2023) 'Dynamin-like proteins mediate extracellular vesicle secretion in *Mycobacterium tuberculosis*', *EMBO reports*, p. e55593.
- Gupta, T.K. *et al.* (2021) 'Structural basis for VIPP1 oligomerization and maintenance of thylakoid membrane integrity', *Cell* [Preprint].
- Hale, C.A. and Boer, P.A.J. De (1997) 'Direct binding of FtsZ to ZipA, an essential component of the septal ring structure that mediates cell division in *E. coli*', *Cell*, 88(2), pp. 175–185. Available at: [https://doi.org/10.1016/S0092-8674\(00\)81838-3](https://doi.org/10.1016/S0092-8674(00)81838-3).
- Hauke, V. and Kozlov, M.M. (2018) 'Membrane remodeling in clathrin-mediated endocytosis', *Journal of cell science*, 131(17), p. jcs216812.
- Heidrich, J., Thurotte, A. and Schneider, D. (2017) 'Specific interaction of IM30/Vipp1 with cyanobacterial and chloroplast membranes results in membrane remodeling and eventually in membrane fusion', *Biochimica et Biophysica Acta - Biomembranes*. Elsevier B.V., pp. 537–549. Available at: <https://doi.org/10.1016/j.bbamem.2016.09.025>.
- Heinz, S. *et al.* (2016) 'Thylakoid membrane architecture in *Synechocystis* depends on CurT, a homolog of the granal CURVATURE THYLAKOID1 proteins', *The Plant Cell*, 28(9), pp. 2238–2260.
- Hennig, R. *et al.* (2015) 'IM30 triggers membrane fusion in cyanobacteria and chloroplasts', *Nature Communications*, 6(May). Available at: <https://doi.org/10.1038/ncomms8018>.

Herrero, Antonia. and Flores, E. (2008) *The cyanobacteria: molecular biology, genomics, and evolution*, Caister Academic Press. Caister Academic Press. Available at: <http://www.caister.com/cyan>.

Hinshaw, J.E. and Schmid, S.L. (1995) 'Dynamain self-assembles into rings suggesting a mechanism for coated vesicle budding.', *Nature*, pp. 190–192. Available at: <https://doi.org/10.1038/374190a0>.

Holland, H.D. (2006) 'The oxygenation of the atmosphere and oceans', *Philosophical transactions of the Royal Society of London. Series B, Biological sciences*, 361(May), pp. 903–915. Available at: https://doi.org/10.1007/3-540-33088-7_2.

Holmgren, A. *et al.* (1975) 'Three-dimensional structure of Escherichia coli thioredoxin-S2 to 2.8 Å resolution.', *Proceedings of the National Academy of Sciences*, 72(6), pp. 2305–2309.

Holmgren, A. (1979) 'Thioredoxin catalyzes the reduction of insulin disulfides by dithiothreitol and dihydrolipoamide.', *Journal of Biological Chemistry*, 254(19), pp. 9627–9632.

Hosseinpour, S. *et al.* (2020) 'Structure and dynamics of interfacial peptides and proteins from vibrational sum-frequency generation spectroscopy', *Chemical reviews*, 120(7), pp. 3420–3465.

Huokko, T. *et al.* (2021) 'Probing the biogenesis pathway and dynamics of thylakoid membranes', *Nature communications*, 12(1), pp. 1–14.

Ikeuchi, M. and Tabata, S. (2001) 'Synechocystis sp. PCC 6803 - a useful tool in the study of the genetics of cyanobacteria.', *Photosynthesis research*, 70(1), pp. 73–83. Available at: <https://doi.org/10.1023/A:1013887908680>.

Ingerman, E. and Nunnari, J. (2005) 'A continuous, regenerative coupled GTPase assay for dynamain-related proteins', *Methods in enzymology*, 404, pp. 611–619.

Insinna, C. *et al.* (2019) 'Investigation of F-BAR domain PACSIN proteins uncovers membrane tubulation function in cilia assembly and transport', *Nature communications*, 10(1), p. 428.

Itsui, Y. *et al.* (2009) 'Antiviral effects of the interferon-induced protein guanylate binding protein 1 and its interaction with the hepatitis C virus NS5B protein', *Hepatology*, 50(6), pp. 1727–1737. Available at: <https://doi.org/10.1002/hep.23195>.

Jahn, R. and Scheller, R.H. (2006) 'SNAREs—engines for membrane fusion', *Nature reviews Molecular cell biology*, 7(9), pp. 631–643.

- Jakobi, A.J., Wilmanns, M. and Sachse, C. (2017) ‘Model-based local density sharpening of cryo-EM maps’, *Elife*, 6, p. e27131.
- Jiang, Y.-Y. *et al.* (2012) ‘The impact of oxygen on metabolic evolution: a chemoinformatic investigation’, *PLoS computational biology*, 8(3), p. e1002426.
- Jilly, R. *et al.* (2018) ‘Dynamain-Like Proteins Are Potentially Involved in Membrane Dynamics within Chloroplasts and Cyanobacteria’, *Frontiers in Plant Science*, 9(February), pp. 1–13. Available at: <https://doi.org/10.3389/fpls.2018.00206>.
- Jilly, R. (2018) ‘SynDLP: a new bacterial dynamain-like protein and its potential involvement in thylakoid membrane biogenesis’. Johannes Gutenberg-Universität Mainz.
- Jimah, J.R. and Hinshaw, J.E. (2018) ‘Structural Insights into the Mechanism of Dynamain Superfamily Proteins’, *Trends in Cell Biology*, 29(3), pp. 257–273. Available at: <https://doi.org/10.1016/j.tcb.2018.11.003>.
- Jong, W.Y. and Lemmon, M.A. (2001) ‘All phox homology (PX) domains from *Saccharomyces cerevisiae* specifically recognize phosphatidylinositol 3-phosphate’, *Journal of Biological Chemistry*, 276(47), pp. 44179–44184.
- Joshua, S. and Mullineaux, C.W. (2004) ‘Phycobilisome diffusion is required for light-state transitions in cyanobacteria’, *Plant physiology*, 135(4), pp. 2112–2119.
- Jouhet, J., Maréchal, E. and Block, M.A. (2007) ‘Glycerolipid transfer for the building of membranes in plant cells’, *Progress in Lipid Research*, pp. 37–55. Available at: <https://doi.org/10.1016/j.plipres.2006.06.002>.
- Jumper, J. *et al.* (2021) ‘Highly accurate protein structure prediction with AlphaFold’, *Nature*, 596(7873), pp. 583–589.
- Junge, W. and Nelson, N. (2015) ‘ATP synthase’, *Annu Rev Biochem*, 84(1), pp. 631–657.
- Junglas, B. *et al.* (2021) ‘PspA adopts an ESCRT-III-like fold and remodels bacterial membranes’, *Cell* [Preprint].
- Juniar, L. *et al.* (2020) ‘Structural basis for thioredoxin isoform-based fine-tuning of ferredoxin-thioredoxin reductase activity’, *Protein Science*, 29(12), pp. 2538–2545.
- Kalia, R. *et al.* (2018) ‘Structural basis of mitochondrial receptor binding and constriction by DRP1’, *Nature*, 558(7710), pp. 401–405.

Kaneko, T. *et al.* (1996) 'Sequence analysis of the genome of the unicellular cyanobacterium *Synechocystis* sp. strain PCC6803. II. Sequence determination of the entire genome and assignment of potential protein-coding regions', *DNA Research*, 3(3), pp. 109–136. Available at: <https://doi.org/10.1093/dnares/3.3.109>.

Kaniya, Y. *et al.* (2013) 'Deletion of the transcriptional regulator *cyAbrB2* deregulates primary carbon metabolism in *Synechocystis* sp. PCC 6803', *Plant physiology*, 162(2), pp. 1153–1163.

Karim, S. *et al.* (2014) 'A novel chloroplast localized Rab GTPase protein CPRabA5e is involved in stress, development, thylakoid biogenesis and vesicle transport in *Arabidopsis*', *Plant molecular biology*, 84, pp. 675–692.

Karim, S. and Aronsson, H. (2014) 'The puzzle of chloroplast vesicle transport-involvement of GTPases', *Frontiers in Plant Science*, 5. Available at: <https://doi.org/10.3389/fpls.2014.00472>.

Keller, R. and Schneider, D. (2013) 'Homologs of the yeast Tvp38 vesicle-associated protein are conserved in chloroplasts and cyanobacteria', *Frontiers in Plant Science*, 4, p. 467. Available at: <https://doi.org/10.3389/fpls.2013.00467>.

Kelly, C.L. *et al.* (2018) 'A rhamnose-inducible system for precise and temporal control of gene expression in cyanobacteria', *ACS synthetic biology*, 7(4), pp. 1056–1066.

Kenniston, J.A. and Lemmon, M.A. (2010) 'Dynamin GTPase regulation is altered by PH domain mutations found in centronuclear myopathy patients', *The EMBO journal*, 29(18), pp. 3054–3067.

Khan, Z., Bhadouria, P. and Bisen, P.S. (2005) 'Nutritional and therapeutic potential of *Spirulina*', *Current pharmaceutical biotechnology*, 6(5), pp. 373–379.

Kiran, R.R.S., Madhu, G. and Satyanarayana, S. V (2015) 'Spirulina in combating Protein Energy Malnutrition (PEM) and Protein Energy Wasting (PEW) - A review', *Journal of Nutrition Research*, 3(1), pp. 62–79. Available at: <http://www.jnutres.com/index.php/jnr/article/view/JNR315>.

Knoll, A.H. (2008) 'Cyanobacteria and earth history', *The cyanobacteria: molecular biology, genomics, and evolution*, 484.

Knoppová, J. *et al.* (2022) 'Assembly of D1/D2 complexes of photosystem II: Binding of pigments and a network of auxiliary proteins', *Plant Physiology*, 189(2), pp. 790–804.

- Kochs, G. *et al.* (2002) 'Self-assembly of Human MxA GTPase into Highly Ordered Dynamin-like Oligomers *', 277(16), pp. 14172–14176. Available at: <https://doi.org/10.1074/jbc.M200244200>.
- Kong, L. *et al.* (2018) 'Cryo-EM of the dynamin polymer assembled on lipid membrane', *Nature*, 560(7717), pp. 258–262.
- Kraus, F. and Ryan, M.T. (2017) 'The constriction and scission machineries involved in mitochondrial fission', *Journal of cell science*, 130(18), pp. 2953–2960.
- Kravets, E. *et al.* (2012) 'The GTPase activity of murine guanylate-binding protein 2 (mGBP2) controls the intracellular localization and recruitment to the parasitophorous vacuole of *Toxoplasma gondii*', *Journal of Biological Chemistry*, 287(33), pp. 27452–27466.
- Krishna, P.S. *et al.* (2013) 'A novel transcriptional regulator, Sll1130, negatively regulates heat-responsive genes in *Synechocystis* sp. PCC6803', *Biochemical Journal*, 449(3), pp. 751–760.
- Kutsch, M. and Coers, J. (2021) 'Human guanylate binding proteins: nanomachines orchestrating host defense', *The FEBS Journal*, 288(20), pp. 5826–5849.
- Kyte, J. and Doolittle, R.F. (1982) 'A simple method for displaying the hydrophobic character of a protein', *Journal of Molecular Biology*, 157(1), pp. 105–132. Available at: [https://doi.org/10.1016/0022-2836\(82\)90515-0](https://doi.org/10.1016/0022-2836(82)90515-0).
- Laemmli, U.K. (1970) 'Cleavage of structural proteins during the assembly of the head of bacteriophage T4', *nature*, 227(5259), pp. 680–685.
- Landau, M. *et al.* (2005) 'ConSurf 2005: the projection of evolutionary conservation scores of residues on protein structures', *Nucleic acids research*, 33(suppl_2), pp. W299–W302.
- Lea-Smith, D.J. *et al.* (2016) 'Photosynthetic, respiratory and extracellular electron transport pathways in cyanobacteria', *Biochimica et Biophysica Acta - Bioenergetics*, 1857(3), pp. 247–255. Available at: <https://doi.org/10.1016/j.bbabi.2015.10.007>.
- Lee, A.G. (2000) 'Membrane lipids : It ' s only a phase', pp. 377–380.
- Leonard, M. *et al.* (2005) 'Robust colorimetric assays for dynamin's basal and stimulated GTPase activities', *Methods in enzymology*, 404, pp. 490–503.

- Lindahl, M. and Florencio, F.J. (2003) ‘Thioredoxin-linked processes in cyanobacteria are as numerous as in chloroplasts, but targets are different’, *Proceedings of the National Academy of Sciences*, 100(26), pp. 16107–16112.
- Lindahl, M. and Kieselbach, T. (2009) ‘Disulphide proteomes and interactions with thioredoxin on the track towards understanding redox regulation in chloroplasts and cyanobacteria.’, *Journal of proteomics*, 72(3), pp. 416–438.
- Liu, J. *et al.* (2021) ‘Bacterial Vipp1 and PspA are members of the ancient ESCRT-III membrane-remodeling superfamily’, *Cell* [Preprint].
- Liu, J., Noel, J.K. and Low, H.H. (2018) ‘Structural basis for membrane tethering by a bacterial dynamin-like pair’, *Nature Communications*, 9(1), p. 3345. Available at: <https://doi.org/10.1038/s41467-018-05523-8>.
- Liu, L.-N. (2016) ‘Distribution and dynamics of electron transport complexes in cyanobacterial thylakoid membranes.’, *Biochimica et biophysica acta*, 1857(3), pp. 256–265. Available at: <https://doi.org/10.1016/j.bbabi.2015.11.010>.
- Liu, L.-N. *et al.* (2021) ‘Protein stoichiometry, structural plasticity and regulation of bacterial microcompartments’, *Current Opinion in Microbiology*, 63, pp. 133–141.
- Liu, T.Y. *et al.* (2012) ‘Lipid interaction of the C terminus and association of the transmembrane segments facilitate atlastin-mediated homotypic endoplasmic reticulum fusion’, *Proceedings of the National Academy of Sciences*, 109(32), pp. E2146–E2154.
- López-Maury, L., Heredia-Martínez, L. and Florencio, F. (2018) ‘Characterization of TrxC, an Atypical Thioredoxin Exclusively Present in Cyanobacteria’, *Antioxidants*, 7(11), p. 164.
- Low, H.H. *et al.* (2009) ‘Structure of a Bacterial Dynamin-like Protein Lipid Tube Provides a Mechanism For Assembly and Membrane Curving’, *Cell*, 139(7), pp. 1342–1352. Available at: <https://doi.org/10.1016/j.cell.2009.11.003>.
- Low, H.H. and Löwe, J. (2006) ‘A bacterial dynamin-like protein.’, *Nature*, 444(7120), pp. 766–769. Available at: <https://doi.org/10.1038/nature05312>.
- Löwe, J. and Amos, L.A. (1998) ‘Crystal structure of the bacterial cell-division protein FtsZ’, *Nature*, 391(6663), pp. 203–206.
- Lu, Q. *et al.* (2015) ‘Early steps in primary cilium assembly require EHD1/EHD3-dependent ciliary vesicle formation’, *Nature cell biology*, 17(3), pp. 228–240.

- Lu, S. *et al.* (2016) ‘Drugging Ras GTPase: a comprehensive mechanistic and signaling structural view’, *Chem. Soc. Rev.*, 45(18), pp. 4929–4952. Available at: <https://doi.org/10.1039/C5CS00911A>.
- Luan, G., Zhang, S. and Lu, X. (2020) ‘Engineering cyanobacteria chassis cells toward more efficient photosynthesis’, *Current opinion in biotechnology*, 62, pp. 1–6.
- Mallén-Ponce, M.J. *et al.* (2021) ‘Depletion of m-type thioredoxin impairs photosynthesis, carbon fixation, and oxidative stress in cyanobacteria’, *Plant Physiology*, 187(3), pp. 1325–1340.
- Mallén-Ponce, M.J., Huertas, M.J. and Florencio, F.J. (2022) ‘Exploring the Diversity of the Thioredoxin Systems in Cyanobacteria’, *Antioxidants*, 11(4), p. 654.
- Martin, W. *et al.* (2002) ‘Evolutionary analysis of Arabidopsis, cyanobacterial, and chloroplast genomes reveals plastid phylogeny and thousands of cyanobacterial genes in the nucleus’, *Proceedings of the National Academy of Sciences*, 99(19), pp. 12246–12251. Available at: <https://doi.org/10.1073/pnas.182432999>.
- Mata-Cabana, A., Florencio, F.J. and Lindahl, M. (2007) ‘Membrane proteins from the cyanobacterium *Synechocystis* sp. PCC 6803 interacting with thioredoxin’, *PROTEOMICS*, 7(21), pp. 3953–3963. Available at: <https://doi.org/10.1002/pmic.200700410>.
- McKenney, P.T., Driks, A. and Eichenberger, P. (2013) ‘The *Bacillus subtilis* endospore: assembly and functions of the multilayered coat’, *Nature Reviews Microbiology*, 11(1), pp. 33–44.
- McMahon, H.T. and Gallop, J.L. (2005) ‘Membrane curvature and mechanisms of dynamic cell membrane remodelling’, *Nature*, 438(7068), pp. 590–596.
- Mechela, A., Schwenkert, S. and Soll, J. (2019) ‘A brief history of thylakoid biogenesis’, *Royal Society Open Biology*, 9(1), p. 180237.
- Meene, A.M.L. Van De *et al.* (2006) ‘The three-dimensional structure of the cyanobacterium *Synechocystis* sp. PCC 6803’, *Archives of Microbiology*, 184(5), pp. 259–270. Available at: <https://doi.org/10.1007/s00203-005-0027-y>.
- Meeusen, S. *et al.* (2006) ‘Mitochondrial Inner-Membrane Fusion and Crista Maintenance Requires the??Dynamin-Related GTPase Mgm1’, *Cell*, 127(2), pp. 383–395. Available at: <https://doi.org/10.1016/j.cell.2006.09.021>.

- Meglei, G. and McQuibban, G.A. (2009) 'The dynamin-related protein Mgm1p assembles into oligomers and hydrolyzes GTP to function in mitochondrial membrane fusion', *Biochemistry*, 48(8), pp. 1774–1784.
- Mettlen, M. *et al.* (2009) 'Dissecting dynamin's role in clathrin-mediated endocytosis', *Biochemical Society Transactions*, 37(5), pp. 1022–1026. Available at: <https://doi.org/10.1042/BST0371022>.
- Meyer, Y., Reichheld, J.P. and Vignols, F. (2005) 'Thioredoxins in Arabidopsis and other plants', *Photosynthesis Research*, 86(3), pp. 419–433.
- Michie, K.A. *et al.* (2014) 'LeoA, B and C from Enterotoxigenic Escherichia coli (ETEC) are bacterial dynamins', *PLoS ONE*, 9(9), p. e107211. Available at: <https://doi.org/10.1371/journal.pone.0107211>.
- Mim, C. and Unger, V.M. (2012) 'Membrane curvature and its generation by BAR proteins', *Trends in biochemical sciences*, 37(12), pp. 526–533.
- Mirdita, M. *et al.* (2021) 'ColabFold-Making protein folding accessible to all'.
- Moren, B. *et al.* (2012) 'EHD2 regulates caveolar dynamics via ATP-driven targeting and oligomerization', *Molecular Biology of the Cell*, 23(7), pp. 1316–1329. Available at: <https://doi.org/10.1091/mbc.E11-09-0787>.
- Morishima, K. *et al.* (2007) 'Erratum: Improving the performance of a direct photosynthetic/metabolic bio-fuel cell (DPBFC) using gene manipulated bacteria (Journal of Micromechanics and Microengineering (2007) 17 (S274-S279))', *Journal of Micromechanics and Microengineering*, p. 2391. Available at: <https://doi.org/10.1088/0960-1317/17/11/C01>.
- Mullineaux, C.W. (2014) 'Electron transport and light-harvesting switches in cyanobacteria', *Frontiers in Plant Science*, 5(January), pp. 1–6. Available at: <https://doi.org/10.3389/fpls.2014.00007>.
- Mullineaux, C.W. and Emlyn-Jones, D. (2005) 'State transitions: an example of acclimation to low-light stress', *Journal of experimental botany*, 56(411), pp. 389–393.
- Mullineaux, C.W. and Liu, L.-N. (2020) 'Membrane dynamics in phototrophic bacteria', *Annu. Rev. Microbiol.*, 74(633–546), p. 654.

- Murata, N. *et al.* (1981) 'Separation and characterization of thylakoid and cell envelope of the blue-green alga (cyanobacterium) *Anacystis nidulans*', *Plant and Cell Physiology*, 22(5), pp. 855–866.
- Muriel, M. *et al.* (2009) 'Atlastin-1, the dynamin-like GTPase responsible for spastic paraplegia SPG3A, remodels lipid membranes and may form tubules and vesicles in the endoplasmic reticulum', *Journal of neurochemistry*, 110(5), pp. 1607–1616.
- Nakamura, Y. *et al.* (1998) 'CyanoBase, a www database containing the complete nucleotide sequence of the genome of *Synechocystis* sp. strain PCC6803', *Nucleic Acids Research*, 26(1), pp. 63–67. Available at: <https://doi.org/10.1093/nar/26.1.63>.
- Navarro, F. and Florencio, F.J. (1996) 'The cyanobacterial thioredoxin gene is required for both photoautotrophic and heterotrophic growth', *Plant physiology*, 111(4), pp. 1067–1075.
- Nickelsen, J. *et al.* (2011) 'Biogenesis of the cyanobacterial thylakoid membrane system - an update', *FEMS Microbiology Letters*, 315(1), pp. 1–5. Available at: <https://doi.org/10.1111/j.1574-6968.2010.02096.x>.
- Ogawa, T. (1991) 'A gene homologous to the subunit-2 gene of NADH dehydrogenase is essential to inorganic carbon transport of *Synechocystis* PCC6803.', *Proceedings of the National Academy of Sciences*, 88(10), pp. 4275–4279.
- Ohkawa, H. *et al.* (2000) 'Mutation of *ndh* genes leads to inhibition of CO₂ uptake rather than HCO₃⁻ uptake in *Synechocystis* sp. strain PCC 6803', *Journal of Bacteriology*, 182(9), pp. 2591–2596.
- Olive, J. *et al.* (1997) 'Ultrastructure and light adaptation of phycobilisome mutants of *synechocystis* PCC 6803', *Biochimica et Biophysica Acta - Bioenergetics*, 1319(2–3), pp. 275–282. Available at: [https://doi.org/10.1016/S0005-2728\(96\)00168-5](https://doi.org/10.1016/S0005-2728(96)00168-5).
- Orso, G. *et al.* (2010) 'Homotypic fusion of ER membranes requires the dynamin-like GTPase Atlastin', *Nature*, 464(7290), p. 942. Available at: <https://doi.org/10.1038/nature08886>.
- Osanai, T. *et al.* (2005) 'Positive regulation of sugar catabolic pathways in the cyanobacterium *Synechocystis* sp. PCC 6803 by the group 2 σ factor SigE', *Journal of Biological Chemistry*, 280(35), pp. 30653–30659.

- Osanai, T. *et al.* (2011) ‘Genetic engineering of group 2 σ factor SigE widely activates expressions of sugar catabolic genes in *Synechocystis* species PCC 6803’, *Journal of Biological Chemistry*, 286(35), pp. 30962–30971.
- Ostermeier, M. *et al.* (2022) ‘Thylakoid attachment to the plasma membrane in *Synechocystis* sp. PCC 6803 requires the AncM protein’, *The Plant Cell*, 34(1), pp. 655–678.
- Parasassi, T. and Gratton, E. (1995) ‘Membrane lipid domains and dynamics as detected by Laurdan fluorescence’, *Journal of fluorescence*, 5(1), pp. 59–69.
- Pérez-Pérez, M.E., Florencio, F.J. and Lindahl, M. (2006) ‘Selecting thioredoxins for disulphide proteomics: target proteomes of three thioredoxins from the cyanobacterium *Synechocystis* sp. PCC 6803’, *Proteomics*, 6(S1), pp. S186–S195.
- Pérez-Pérez, M.E., Martín-Figueroa, E. and Florencio, F.J. (2009) ‘Photosynthetic Regulation of the Cyanobacterium *Synechocystis* sp. PCC 6803 Thioredoxin System and Functional Analysis of TrxB (Trx x) and TrxQ (Trx y) Thioredoxins’, *Molecular Plant*, 2(2), pp. 270–283. Available at: <https://doi.org/10.1093/MP/SSN070>.
- Peterson, F.C. *et al.* (2005) ‘Solution structure of thioredoxin h1 from *Arabidopsis thaliana*’, *Protein science*, 14(8), pp. 2195–2200.
- Pettersen, E.F. *et al.* (2021) ‘UCSF ChimeraX: Structure visualization for researchers, educators, and developers’, *Protein Science*, 30(1), pp. 70–82.
- Pickering, J.D. *et al.* (2022) ‘Tutorials in vibrational sum frequency generation spectroscopy. I. The foundations’, *Biointerphases*, 17(1), p. 11201.
- Porra, R.J., Thompson, W.A. and Kriedemann, P.E. (1989) ‘Determination of accurate extinction coefficients and simultaneous equations for assaying chlorophylls a and b extracted with four different solvents: verification of the concentration of chlorophyll standards by atomic absorption spectroscopy’, *BBA - Bioenergetics*, 975(3), pp. 384–394. Available at: [https://doi.org/10.1016/S0005-2728\(89\)80347-0](https://doi.org/10.1016/S0005-2728(89)80347-0).
- Praefcke, G.J.K. *et al.* (1999) ‘Nucleotide-binding characteristics of human guanylate-binding protein 1 (hGBP1) and identification of the third GTP-binding motif’, *Journal of molecular biology*, 292(2), pp. 321–332.

- Praefcke, G.J.K. and McMahon, H.T. (2004) ‘The dynamin superfamily: universal membrane tubulation and fission molecules?’, *Nature reviews. Molecular cell biology*, 5(2), pp. 133–147. Available at: <https://doi.org/10.1038/nrm1313>.
- Prakash, B., Praefcke, G.J.K., *et al.* (2000) ‘Structure of human guanylate-binding protein 1 representing a unique class of GTP-binding proteins’, *Nature*, 403(6769), pp. 567–571.
- Prakash, B., Renault, L., *et al.* (2000) ‘Triphosphate structure of guanylate-binding protein 1 and implications for nucleotide binding and GTPase mechanism’, *The EMBO journal*, 19(17), pp. 4555–4564.
- Prats, C., Graham, T.E. and Shearer, J. (2018) ‘The dynamic life of the glycogen granule’, *Journal of Biological Chemistry*, 293(19), pp. 7089–7098.
- Pribil, M., Labs, M. and Leister, D. (2014) ‘Structure and dynamics of thylakoids in land plants’, *Journal of experimental botany*, 65(8), pp. 1955–1972.
- Punjani, A. *et al.* (2017) ‘cryoSPARC: algorithms for rapid unsupervised cryo-EM structure determination’, *Nature methods*, 14(3), pp. 290–296.
- Punjani, A. (2020) ‘Algorithmic advances in single particle cryo-EM data processing using CryoSPARC’, *Microscopy and Microanalysis*, 26(S2), pp. 2322–2323.
- Qi, Y. *et al.* (2016) ‘Structures of human mitofusin 1 provide insight into mitochondrial tethering’, *Journal of Cell Biology*, 215(5), pp. 621–629.
- Ramachandran, R. (2011) ‘Vesicle scission: dynamin’, in *Seminars in cell & developmental biology*. Elsevier, pp. 10–17.
- Ramachandran, R. and Schmid, S.L. (2018) ‘The dynamin superfamily’, *Current Biology*, 28(8), pp. R411–R416.
- Rast, A. *et al.* (2019) ‘Biogenic regions of cyanobacterial thylakoids form contact sites with the plasma membrane’, *Nature plants*, 5(4), pp. 436–446.
- Rast, A., Heinz, S. and Nickelsen, J. (2015) ‘Biogenesis of thylakoid membranes’, *Biochimica et biophysica acta*, 1847(9), pp. 821–830. Available at: <https://doi.org/10.1016/j.bbabi.2015.01.007>.

- RayChaudhuri, D. (1999) 'ZipA is a MAP–Tau homolog and is essential for structural integrity of the cytokinetic FtsZ ring during bacterial cell division', *The EMBO journal*, 18(9), pp. 2372–2383.
- Rennie, M.L. *et al.* (2014) 'Transient dimerization of human MxA promotes GTP hydrolysis, resulting in a mechanical power stroke', *Structure*, 22(10), pp. 1433–1445.
- Reubold, T.F. *et al.* (2015) 'Crystal structure of the dynamin tetramer', *Nature*, 525(7569), pp. 404–408. Available at: <https://doi.org/10.1038/nature14880>.
- Richter, M.F. *et al.* (1995) 'Interferon-induced MxA Protein.: GTP BINDING AND GTP HYDROLYSIS PROPERTIES', *Journal of Biological Chemistry*, 270(22), pp. 13512–13517.
- Rippka, R. *et al.* (1979) 'Generic assignments, strain histories and properties of pure cultures of cyanobacteria', *Journal of General Microbiology*, 111, pp. 1–61. Available at: <https://doi.org/10.1099/00221287-111-1-1>.
- Rippka, R., Waterbury, J. and Cohen-Bazire, G. (1974) 'A cyanobacterium which lacks thylakoids', *Archives of Microbiology*, 100(1), pp. 419–436. Available at: <https://doi.org/10.1007/BF00446333>.
- Rosinski, J. and Rosen, W.G. (1972) 'Chloroplast development: fine structure and chlorophyll synthesis', *The Quarterly Review of Biology*, 47(2), pp. 160–191.
- Rottet, S., Besagni, C. and Kessler, F. (2015) 'The role of plastoglobules in thylakoid lipid remodeling during plant development', *Biochimica et Biophysica Acta (BBA)-Bioenergetics*, 1847(9), pp. 889–899.
- Salim, K. *et al.* (1996) 'Distinct specificity in the recognition of phosphoinositides by the pleckstrin homology domains of dynamin and Bruton's tyrosine kinase.', *The EMBO journal*, 15(22), pp. 6241–6250.
- Sanderson, P.W. and Williams, W.P. (1992) 'Low-temperature phase behaviour of the major plant leaf lipid monogalactosyldiacylglycerol', *Biochimica et Biophysica Acta (BBA)-Biomembranes*, 1107(1), pp. 77–85.
- Sato, N. *et al.* (2000) 'Requirement of phosphatidylglycerol for photosynthetic function in thylakoid membranes.', *Proceedings of the National Academy of Sciences of the United States of America*, 97(17), pp. 10655–10660. Available at: <https://doi.org/10.1073/pnas.97.19.10655>.

- Sato, N. (2015) ‘Is monoglucosyldiacylglycerol a precursor to monogalactosyldiacylglycerol in all cyanobacteria?’, *Plant and Cell Physiology*, 56(10), pp. 1890–1899.
- Saw, J.H.W. *et al.* (2013) ‘Cultivation and complete genome sequencing of *Gloeobacter kilaeensis* sp. nov., from a lava cave in Kīlauea Caldera, Hawai’i’, *PLoS one*, 8(10), p. e76376.
- Sawant, P. *et al.* (2016) ‘A dynamin-like protein involved in bacterial cell membrane surveillance under environmental stress’, *Environmental Microbiology*, 18(8), pp. 2705–2720. Available at: <https://doi.org/10.1111/1462-2920.13110>.
- Schindelin, J. *et al.* (2012) ‘Fiji: an open-source platform for biological-image analysis’, *Nature Methods*, 9(7), pp. 676–682. Available at: <https://doi.org/10.1038/nmeth.2019>.
- Schlimpert, S. *et al.* (2017) ‘Two dynamin-like proteins stabilize FtsZ rings during *Streptomyces* sporulation’, *Proceedings of the National Academy of Sciences*, p. 201704612. Available at: <https://doi.org/10.1073/pnas.1704612114>.
- Schneider, D. *et al.* (2007) ‘Fluorescence staining of live cyanobacterial cells suggest non-stringent chromosome segregation and absence of a connection between cytoplasmic and thylakoid membranes’, *BMC Cell Biology*, 8, p. 39. Available at: <https://doi.org/10.1186/1471-2121-8-39>.
- Schwemmler, M. and Staeheli, P. (1994) ‘The interferon-induced 67-kDa guanylate-binding protein (hGBP1) is a GTPase that converts GTP to GMP’, *Journal of Biological Chemistry*, 269(15), pp. 11299–11305.
- Shevela, D., Pishchalnikov, R. and Eichacker, L. (2013) ‘Oxygenic Photosynthesis in Cyanobacteria’, *Stress Biology of Cyanobacteria*, (March), pp. 3–40. Available at: <https://doi.org/10.1201/b13853-3>.
- Shpetner, H.S. and Vallee, R.B. (1992) ‘Dynamin is a GTPase stimulated to high levels of activity by microtubules.’, *Nature*, 355(6362), pp. 733–735. Available at: <https://doi.org/10.1038/355733a0>.
- Shpetner, H.S.H.S.S. *et al.* (1989) ‘Identification of dynamin, a novel mechanochemical enzyme that mediates interactions between microtubules’, *Cell*, 59(3), pp. 421–432. Available at: [https://doi.org/10.1016/0092-8674\(89\)90027-5](https://doi.org/10.1016/0092-8674(89)90027-5).

- Shydlovskiy, S. *et al.* (2017) 'Nucleotide-dependent farnesyl switch orchestrates polymerization and membrane binding of human guanylate-binding protein 1', *Proceedings of the National Academy of Sciences*, 114(28), pp. E5559–E5568.
- Siebenaller, C. and Schneider, D. (2023) 'Cyanobacterial membrane dynamics in the light of eukaryotic principles', *Bioscience Reports*, 43(2), p. BSR20221269.
- Simidjiev, I. *et al.* (2000) 'Self-assembly of large, ordered lamellae from non-bilayer lipids and integral membrane proteins in vitro.', *Proceedings of the National Academy of Sciences of the United States of America*, 97(4), pp. 1473–1476. Available at: <http://www.ncbi.nlm.nih.gov/pubmed/10677486>.
- Šmarda, J. *et al.* (2002) 'S-layers on cell walls of cyanobacteria', *Micron*, 33(3), pp. 257–277.
- Smirnova, E. *et al.* (2001) 'Dynamin-related Protein Drp1 Is Required for Mitochondrial Division in Mammalian Cells', *Molecular Biology of the Cell*, 12(8), pp. 2245–2256. Available at: <https://doi.org/10.1091/mbc.12.8.2245>.
- Solinger, J.A. *et al.* (2020) 'FERARI is required for Rab11-dependent endocytic recycling', *Nature cell biology*, 22(2), pp. 213–224.
- Song, T. *et al.* (2005) 'Biodiversity and seasonal variation of the cyanobacterial assemblage in a rice paddy field in Fujian, China', *FEMS Microbiology Ecology*, 54(1), pp. 131–140.
- Song, Z. *et al.* (2014) 'A transcriptional regulator Sll0794 regulates tolerance to biofuel ethanol in photosynthetic *Synechocystis* sp. PCC 6803', *Molecular & Cellular Proteomics*, 13(12), pp. 3519–3532.
- Stachowiak, J.C. *et al.* (2012) 'Membrane bending by protein–protein crowding', *Nature cell biology*, 14(9), pp. 944–949.
- Staeheli, P. *et al.* (1986) 'Mx protein: Constitutive expression in 3T3 cells transformed with cloned Mx cDNA confers selective resistance to influenza virus', *Cell*, 44(1), pp. 147–158. Available at: [https://doi.org/10.1016/0092-8674\(86\)90493-9](https://doi.org/10.1016/0092-8674(86)90493-9).
- Stanier, R.Y. (1977) 'Phototrophic prokaryotes: the cyanobacteria.'
- Stowell, M.H.B. *et al.* (1999) 'Nucleotide-dependent conformational changes in dynamin: evidence for a mechanochemical molecular spring', *Nature cell biology*, 1(1), pp. 27–32.

- Szwedziak, P. *et al.* (2014) ‘Architecture of the ring formed by the tubulin homologue FtsZ in bacterial cell division’, *eLife*, 3, p. e04601. Available at: <https://doi.org/10.7554/eLife.04601>.
- Terwilliger, T.C. *et al.* (2018) ‘Automated map sharpening by maximization of detail and connectivity’, *Acta Crystallographica Section D: Structural Biology*, 74(6), pp. 545–559.
- Thomas, S., Holland, I.B. and Schmitt, L. (2014) ‘The type 1 secretion pathway—the hemolysin system and beyond’, *Biochimica et Biophysica Acta (BBA)-Molecular Cell Research*, 1843(8), pp. 1629–1641.
- Trautner, C. and Vermaas, W.F.J. (2013) ‘The *sll1951* gene encodes the surface layer protein of *Synechocystis* sp. strain PCC 6803’, *Journal of bacteriology*, 195(23), pp. 5370–5380.
- Tuma, P.L., Stachniak, M.C. and Collins, C.A. (1993) ‘Activation of dynamin GTPase by acidic phospholipids and endogenous rat brain vesicles’, *Journal of Biological Chemistry*, 268(23), pp. 17240–17246.
- Turunen, O. *et al.* (2022) ‘Roles of Close Homologues SigB and SigD in Heat and High Light Acclimation of the Cyanobacterium *Synechocystis* sp. PCC 6803’, *Life*, 12(2), p. 162.
- Ugarte-Urbe, B. *et al.* (2014) ‘Dynamin-related protein 1 (Drp1) promotes structural intermediates of membrane division’, *Journal of Biological Chemistry*, 289(44), pp. 30645–30656. Available at: <https://doi.org/10.1074/jbc.M114.575779>.
- Varlakhanova, N. V *et al.* (2018) ‘Structures of the fungal dynamin-related protein Vps1 reveal a unique, open helical architecture’, *Journal of Cell Biology*, 217(10), pp. 3608–3624.
- Vega-Cabrera, L.A. and Pardo-López, L. (2017) ‘Membrane remodeling and organization: Elements common to prokaryotes and eukaryotes’, *IUBMB life*, 69(2), pp. 55–62.
- Vermaas, W.F.J. (2001) ‘Photosynthesis and respiration in cyanobacteria’, *eLS* [Preprint].
- Vermass, W.F., Rutherford, A.W. and Hansson, O. (1988) ‘Site-directed mutagenesis in photosystem II of the cyanobacterium *Synechocystis* sp. PCC 6803: Donor D is a tyrosine residue in the D2 protein.’, *Proceedings of the National Academy of Sciences of the United States of America*, 85(22), pp. 8477–8481. Available at: <http://www.ncbi.nlm.nih.gov/pubmed/16593992>.
- Vestal, D.J. and Jeyaratnam, J.A. (2011) ‘The Guanylate-Binding Proteins: Emerging Insights into the Biochemical Properties and Functions of This Family of Large Interferon-Induced

Guanosine Triphosphatase’, *Journal of Interferon & Cytokine Research*, 31(1), pp. 89–97. Available at: <https://doi.org/10.1089/jir.2010.0102>.

Wada, H. and Murata, N. (1989) ‘Synechocystis PCC6803 mutants defective in desaturation of fatty acids’, *Plant and cell physiology*, 30(7), pp. 971–978.

Wang, M. *et al.* (2019) ‘Mycobacterial dynamin-like protein IniA mediates membrane fission’, *Nature communications*, 10(1), pp. 1–13.

Warnock, D.E., Hinshaw, J.E. and Schmid, S.L. (1996) ‘Dynamin self-assembly stimulates its GTPase activity’, *Journal of Biological Chemistry*, 271(37), pp. 22310–22314.

Waters, M.T. and Langdale, J.A. (2009) ‘The making of a chloroplast’, *The EMBO journal*, 28(19), pp. 2861–2873.

Weichsel, A. *et al.* (1996) ‘Crystal structures of reduced, oxidized, and mutated human thioredoxins: evidence for a regulatory homodimer’, *Structure*, 4(6), pp. 735–751.

Weinberger, A. *et al.* (2013) ‘Gel-assisted formation of giant unilamellar vesicles’, *Biophysical journal*, 105(1), pp. 154–164.

Wenger, J. *et al.* (2013) ‘Functional mapping of human dynamin-1-like GTPase domain based on x-ray structure analyses.’, *PloS one*, 8(8), p. e71835. Available at: <https://doi.org/10.1371/journal.pone.0071835>.

Westphal, S. *et al.* (2001) ‘Vipp1 deletion mutant of Synechocystis: a connection between bacterial phage shock and thylakoid biogenesis?’, *Proceedings of the National Academy of Sciences of the United States of America*, 98(7), pp. 4243–4248. Available at: <https://doi.org/10.1073/pnas.061501198>.

Williams, C.J. *et al.* (2018) ‘MolProbity: More and better reference data for improved all-atom structure validation’, *Protein Science*, 27(1), pp. 293–315.

Williams, M. and Kim, K. (2014) ‘From membranes to organelles: emerging roles for dynamin-like proteins in diverse cellular processes.’, *European journal of cell biology*, 93(7), pp. 267–277. Available at: <https://doi.org/10.1016/j.ejcb.2014.05.002>.

Wittinghofer, A. and Vetter, I.R. (2011) ‘Structure-function relationships of the G domain, a canonical switch motif’, *Annual review of biochemistry*, 80, pp. 943–971.

- Wolosiuk, R.A. and Buchanan, B.B. (1977) 'Thioredoxin and glutathione regulate photosynthesis in chloroplasts', *Nature*, 266(5602), pp. 565–567.
- Yamauchi, Y. *et al.* (2011) 'Physiological roles of the cyAbrB transcriptional regulator pair Sll0822 and Sll0359 in *Synechocystis* sp. strain PCC 6803', *Journal of bacteriology*, 193(15), pp. 3702–3709.
- Yamori, W. and Shikanai, T. (2016) 'Physiological functions of cyclic electron transport around photosystem I in sustaining photosynthesis and plant growth', *Annual review of plant biology*, 67, pp. 81–106.
- Yan, L. *et al.* (2015) 'Structures of the yeast dynamin-like GTPase Sey1p provide insight into homotypic ER fusion', *Journal of Cell Biology*, 210(6), pp. 961–972.
- Yan, L. *et al.* (2018) 'Structural basis for GTP hydrolysis and conformational change of MFN1 in mediating membrane fusion', *Nature Structural & Molecular Biology*, 25(3), pp. 233–243. Available at: <https://doi.org/10.1038/s41594-018-0034-8>.
- Yan, L. *et al.* (2020) 'Structural analysis of a trimeric assembly of the mitochondrial dynamin-like GTPase Mgm1', *Proceedings of the National Academy of Sciences*, 117(8), pp. 4061–4070.
- Yokoo, R., Hood, R.D. and Savage, D.F. (2015) 'Live-cell imaging of cyanobacteria', *Photosynthesis research*, 126, pp. 33–46.
- Yoshihara, A. and Kobayashi, K. (2022) 'Lipids in photosynthetic protein complexes in the thylakoid membrane of plants, algae, and cyanobacteria', *Journal of experimental botany*, 73(9), pp. 2735–2750.
- Yu, C. *et al.* (2020) 'Structural insights into G domain dimerization and pathogenic mutation of OPA1', *Journal of Cell Biology*, 219(7).
- Zacharias, D.A. *et al.* (2002) 'Partitioning of lipid-modified monomeric GFPs into membrane microdomains of live cells', *Science*, 296(5569), pp. 913–916.
- Zhang, X. and Hu, J. (2009) 'Two small protein families, DYNAMIN-RELATED PROTEIN3 and FISSION1, are required for peroxisome fission in *Arabidopsis*', *Plant Journal*, 57(1), pp. 146–159. Available at: <https://doi.org/10.1111/j.1365-313X.2008.03677.x>.
- Zheng, J. *et al.* (1996) 'Identification of the binding site for acidic phospholipids on the PH domain of dynamin: Implications for stimulation of GTPase activity', *Journal of Molecular Biology*, 255(1), pp. 14–21. Available at: <https://doi.org/10.1006/jmbi.1996.0002>.

Zhou, L. *et al.* (1998) 'On the origin of membrane vesicles in gram-negative bacteria', *FEMS microbiology letters*, 163(2), pp. 223–228.

7 Appendix

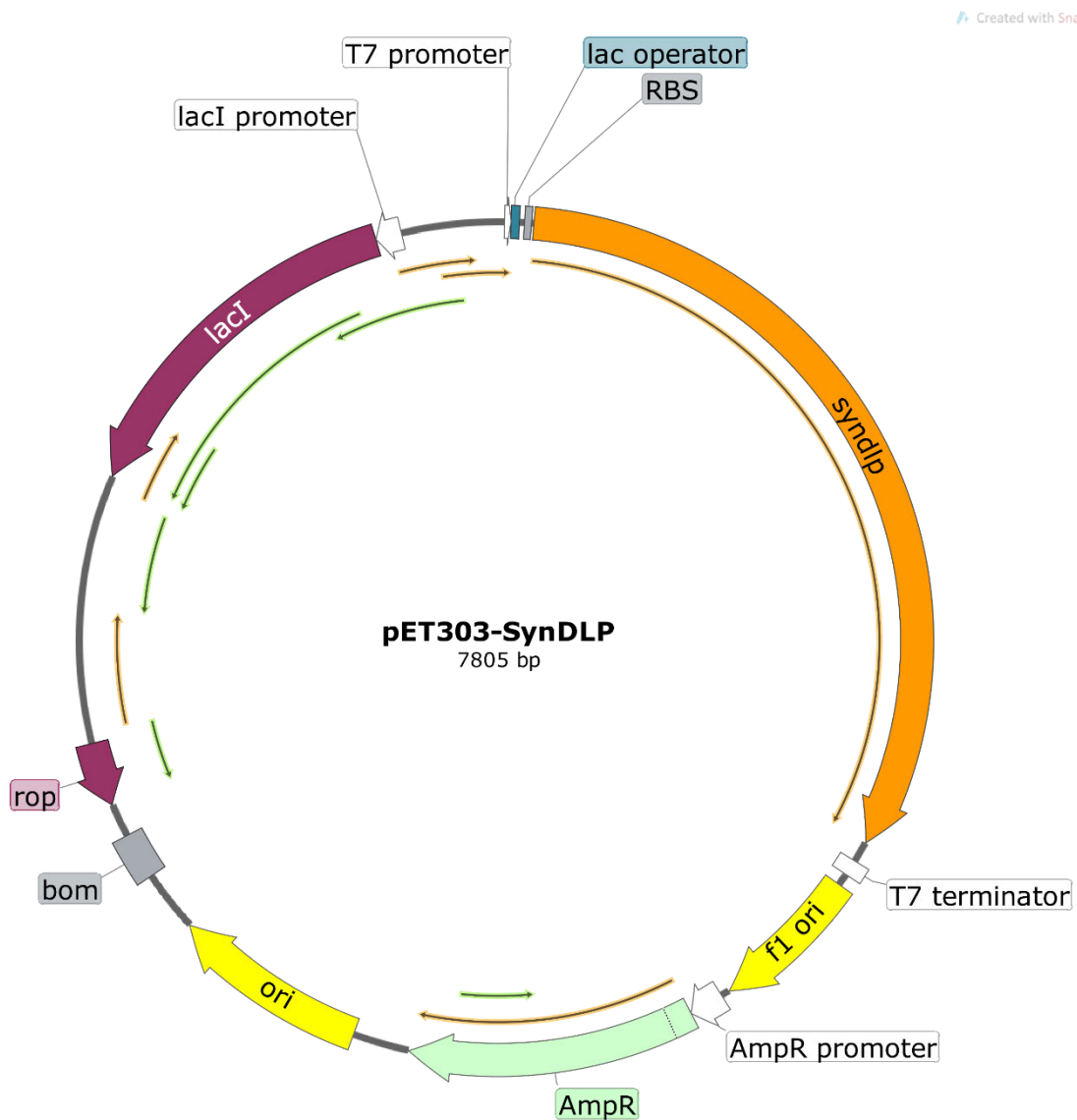


Figure A1: Map of pET303-SynDLP as an example of a pET303-based plasmid.

Plasmid map of pET303-SynDLP highlighting common features of pET303-based plasmids used in this study. RBS = ribosome binding site, bom = basis of mobility region, ori = origin of replication, AmpR = ampicillin resistance cassette. Plasmid map created with SnapGene® Viewer.

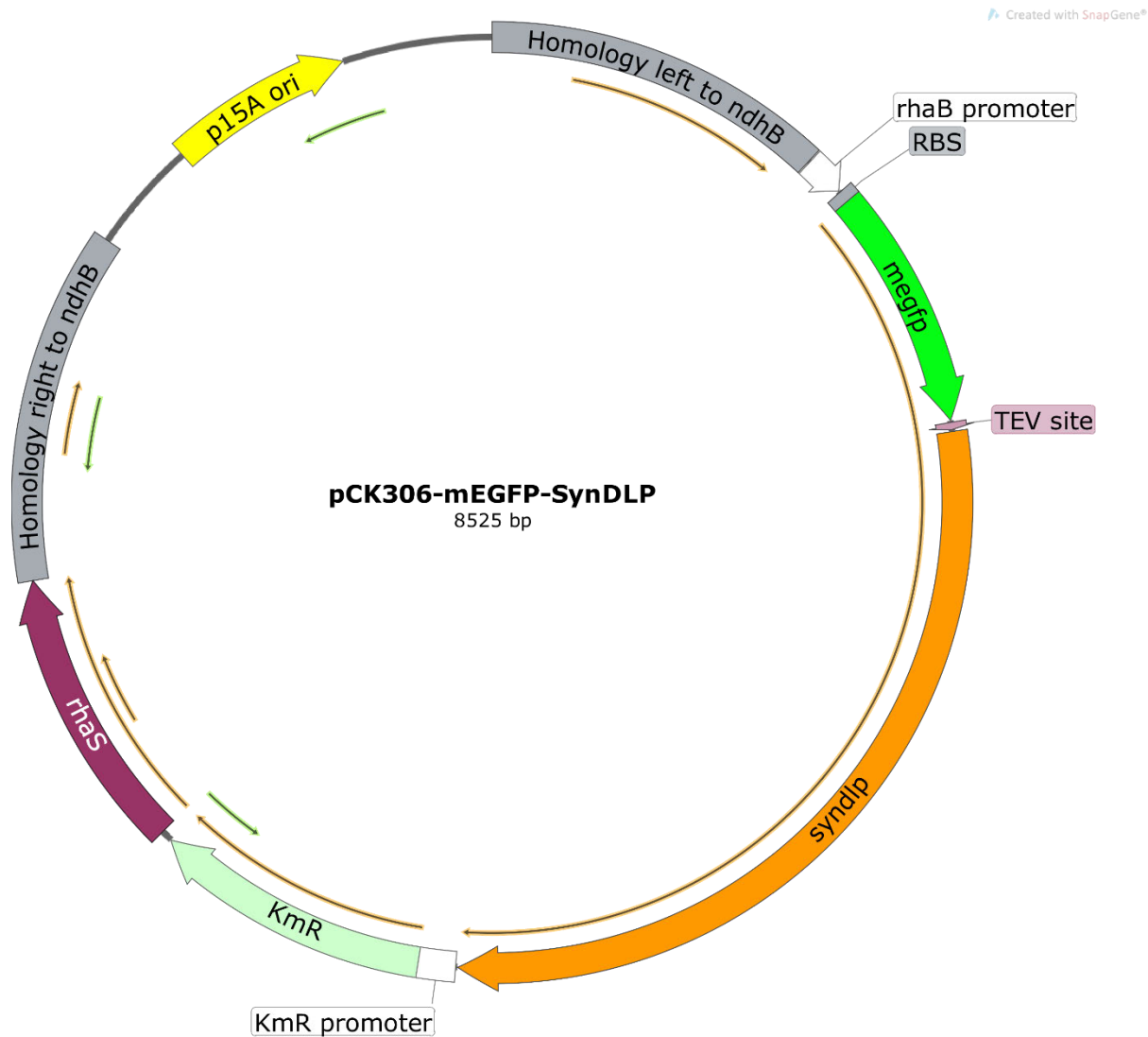


Figure A2: Map of pCK306-mEGFP-SynDLP as an example of a pCK306-based plasmid.

Plasmid map of pCK306-mEGFP-SynDLP showing common features of pCK306-based plasmids used in this study. RBS = ribosome binding site, ori = origin of replication, KmR = kanamycin resistance cassette. Plasmid map created with SnapGene® Viewer.

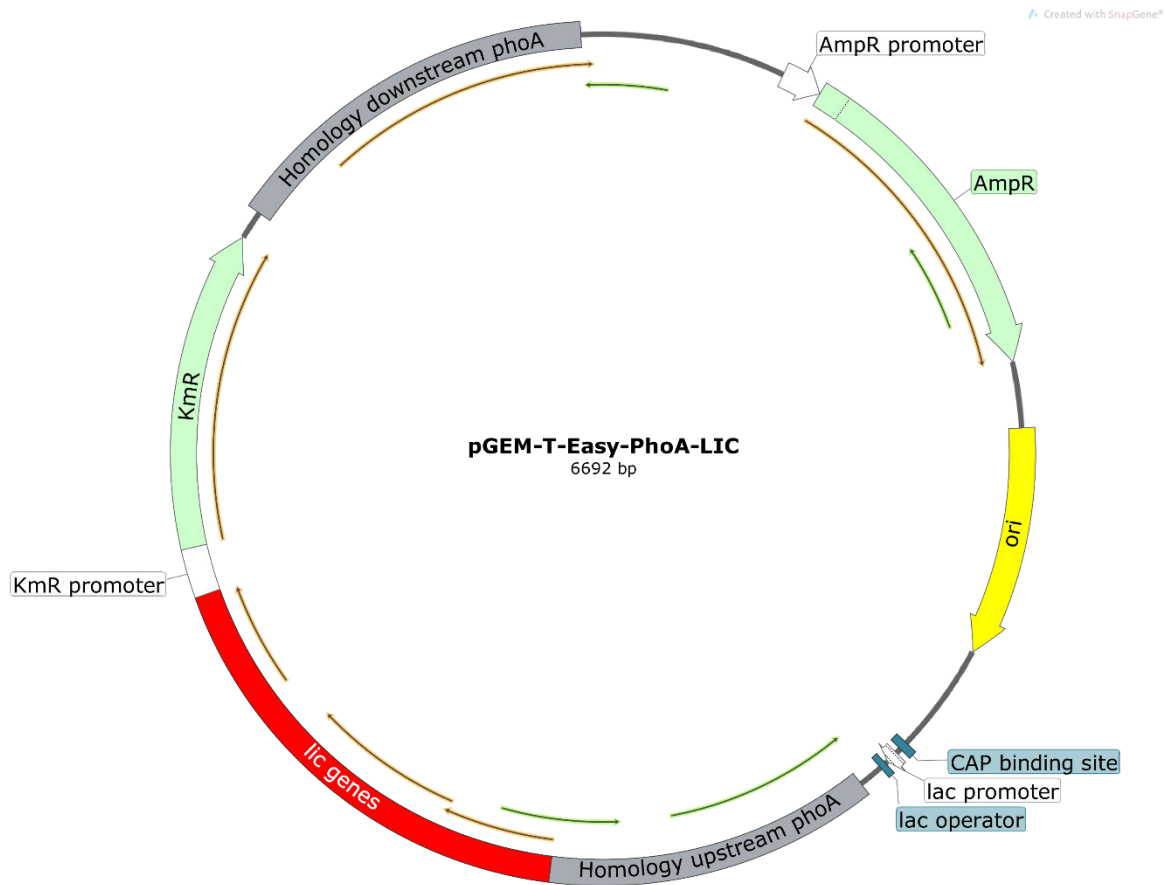


Figure A3: Map of pGEM-T-Easy-PhoA-LIC as an example of a pGEM-T-Easy-based plasmid.

Plasmid map of pGEM-T-Easy-PhoA-LIC highlighting common features of pGEM-T-Easy-based plasmids used in this study. ori = origin of replication, AmpR = ampicillin resistance cassette, KmR = kanamycin resistance cassette. Plasmid map created with SnapGene® Viewer.

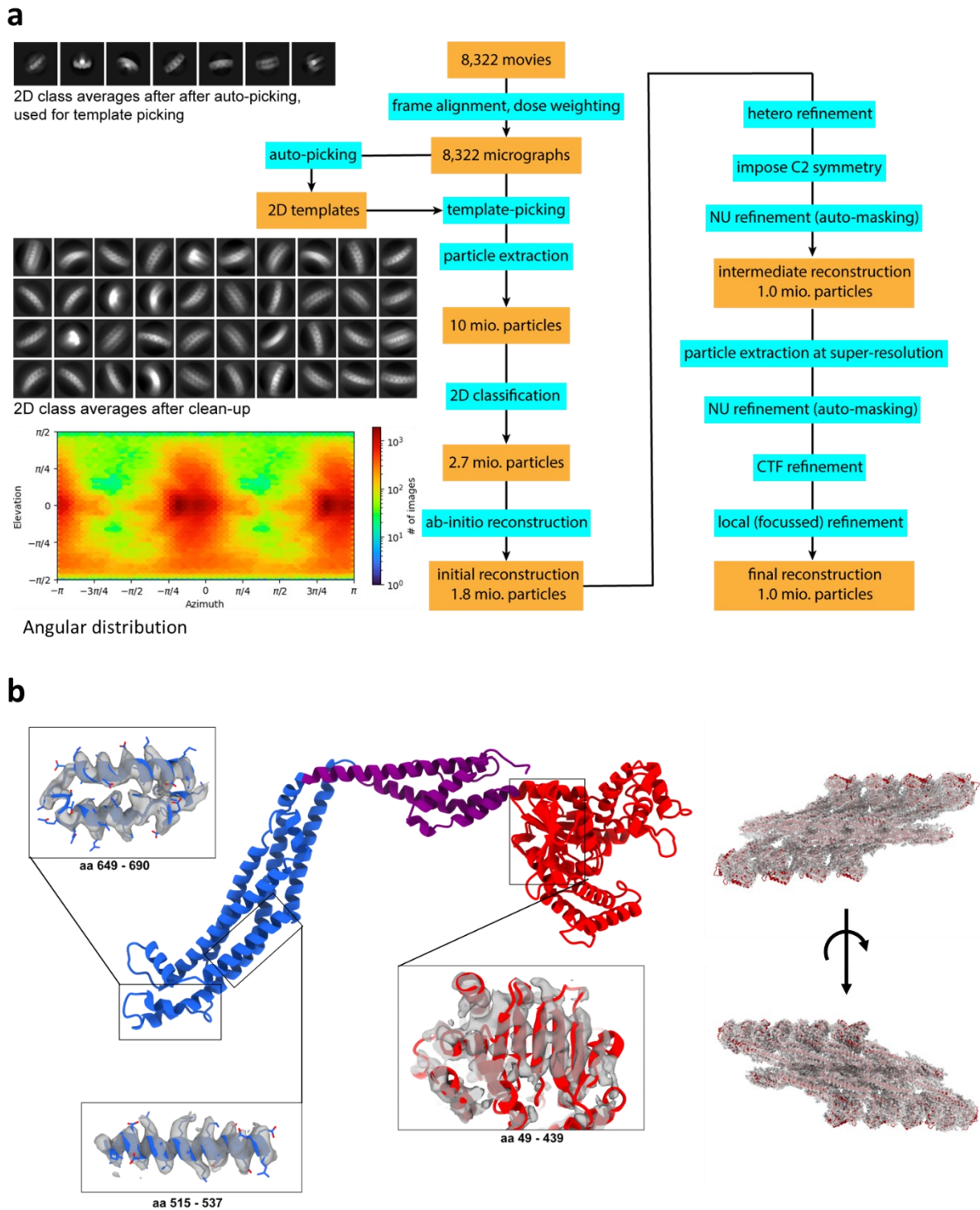


Figure A4: Experimental details of the structure determination of *SynDLP* oligomers.

(a) Flowchart of the applied data processing routines during *SynDLP* structure determination using cryo-EM. (b) Model of the *SynDLP* monomer, including insets showing the density fit of aa's 649 – 690, 515 – 537, and 49 – 439 (left) and model fit to map from two viewing angles (right). Figure taken from Gewehr et al., 2023.



Figure A5: Conservation of single residues in *SynDLP*.

The primary sequence of *SynDLP* is shown. The conservation of single *SynDLP* residues was evaluated based on a sequence alignment with 150 related DLP sequences selected by the online tool ConSurf (Glaser *et al.*, 2003; Landau *et al.*, 2005; Ashkenazy *et al.*, 2010, 2016; Celniker *et al.*, 2013). Amino acids are colored from dark cyan (variable) to red-violet (conserved). Figure taken from Gewehr *et al.*, 2023.

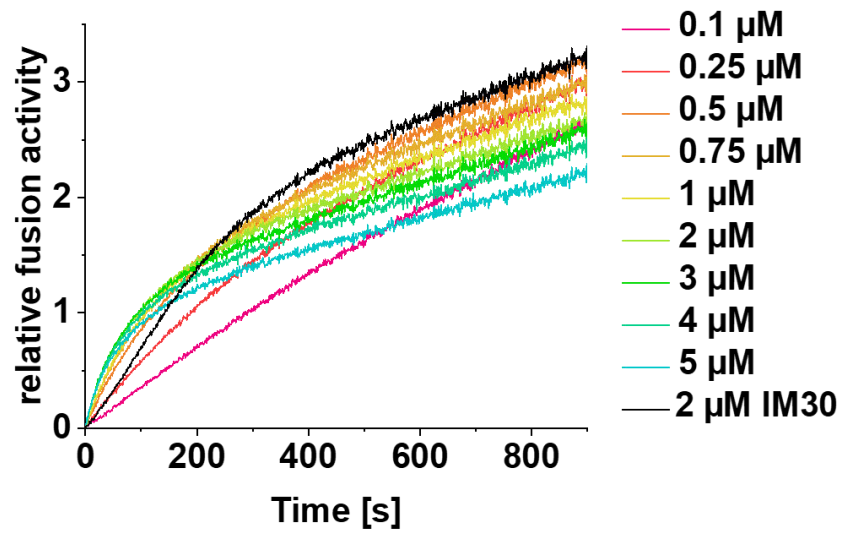


Figure A6: Membrane fusion curves of *SynDLP* and IM30.

Curves show the entire measurement over 900 s with increasing *SynDLP* concentrations as well as the positive control (2 μM IM30, black) as described in Fig. 4.22b. The curves represent the average of three measurements. Figure taken from Gewehr et al., 2023.

10 20 30 40 50 60
 MSKIAPQCQN LREQVNQLIE LLRQEPTLRS QQDTSIVETA LGKALSPRFE IVFAGAFSAG
 70 80 90 100 110 120
 KSMNLINALLE RELLYSAEGH ATGTECHIEY ANANEERVVL TFLSEAEIRQ QALILAKYLN
 130 140 150 160 170 180
 VNVGDLNINQ PEAVKVVSQY CQKIIEAEEGG ENKSERAKQA NALHLLLLIGF EQNRERINTV
 190 200 210 220 230 240
 QNSTYSMDQL NFSSLAEAAG YARRGANSAY LKRLDYFCNH SLLKDGNVLV DLPGIDAPVK
 250 260 270 280 290 300
 EDAERAYRKI ESPDTSAVIC VLKPAAGDM SAEETQLLER ISKNHGIRDR VFYVFNRRID
 310 320 330 340 350 360
 TWYNTQLRQR LEGLIQSQFR DNSRVYKTSG LLGFYGSQVK QTNSSTRFGL DSIFATTIKG
 370 380 390 400 410 420
 FDGEEETPQF VSEFNNYCAN SGKLLSTAFR VSVNGYETSN ENYVRILSEW GIPLVDQLIH
 430 440 450 460 470 480
 DSGIESFRSG IGLYLAEEKY PELFATLAND LQPLCIALRQ FYLENYRQLD SQPREIAAMK
 490 500 510 520 530 540
 AQELTLLNQE MQLNGIEFKK YMSAQINDVV IGNDREFDQD FTKLKARMVA RLDELKTFSS
 550 560 570 580 590 600
 VMNAYKRATE SHPRNSTAPF IAVLVEALYY LANELEDAFI EAIHELVKNF FQRLGDRLRK
 610 620 630 640 650 660
 VDCYHQVYRL VGNDGGIEQL LRRAEEDITK ALVNEARTEC DRYVRESRPF YDEGTFESIYQ
 670 680 690 700 710 720
 FRQTLQQTSQ GYDAQAIVEA EPAIKELLKL DFEPKVFNTV RKNFRQTVNN TLKTHLLPMA
 730 740 750 760 770 780
 EEQAQIILEQ YDVARKYREQ TLEQDAEEKI ARNSRLQSEI KQKIDLYQTS IVSINECLKA
 790 800 810
 MQIFEQLPVI TESDITKQAE IVADADFVEI VE

Figure A7: Amino acid sequence of *SynDLP* with annotations.

The *SynDLP* domains are derived from the structure and labeled as follows: BSE1-3 in violet, GD in red, stalk in blue. The HPRN-motif critical for oligomerization is typed orange. The two cysteines C8 and C777 involved in an intramolecular disulfide bridge are marked in yellow. The important active site residue K61 is highlighted in black. The two residues forming a salt bridge between GD and stalk (R320 and E585) are labeled in green. The investigated potential MIDs are marked in cyan (A558 – V565), dark green (P648 – L665), magenta (Q667 – Q675) or gray (P694 – R705), respectively.

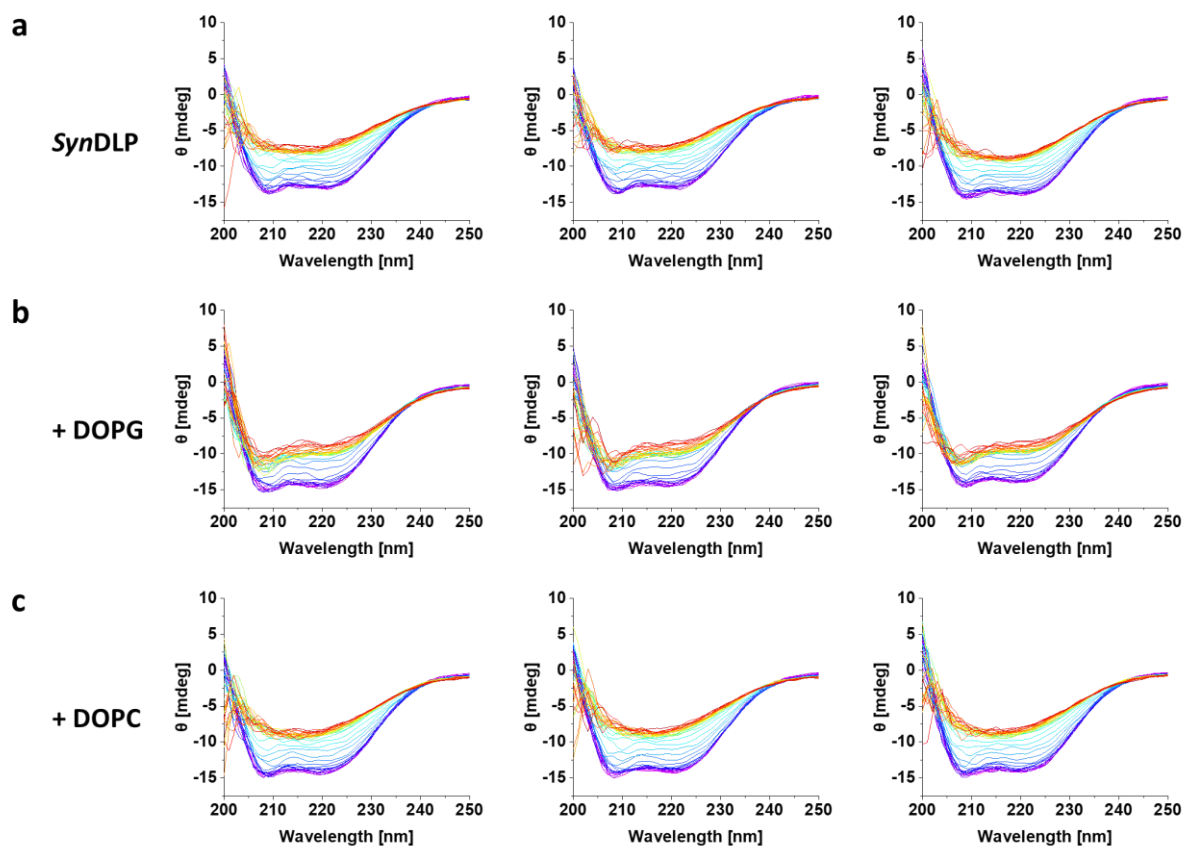


Figure A8: CD spectra of *SynDLP* in the presence of liposomes dependent on the temperature.

All three individual CD spectroscopic measurements of the thermal denaturation of the samples shown in Fig. 4.33b (example spectra are shown in Fig. 4.34). The CD spectra are colored by rainbow colors, starting from 20°C (violet) to 92°C (red).

10 20 30 40 50 60
 MSKGEELFTG VVPILVELDG DVNGHKFSVS GEGEGDATYG KLTLLKFICTT GKLPVPWPPTI
 70 80 90 100 110 120
 VTTLTYGVQC FSRYPDHMKR HDFFKSAMPE GYVQERTISF KDDGNYKTRA EVKFEGDTLV
 130 140 150 160 170 180
 NRIELKGIDF KEDGNILGHK LEYNYNSHNV YITADKQKNG IKANFKIRHN IEDGSVQLAD
 190 200 210 220 230 240
 HYQONTPIGD GPVLLPDNHY LSTQSKLSKD PNEKRDHMVL LEFVTAAGIT HGMDELYKGS
 250 260 270 280 290 300
 ENLYFQGQFM SKIAPQCQNL REQVNQLIEL LRQEPTLRSQ QDTSIVETAL GKALSPRFEI
 310 320 330 340 350 360
 VFAGAFSAGK SMLINALLER ELLYSAEGHA TGTECHIEYA NANEERVVLT FLSEAEIRQQ
 370 380 390 400 410 420
 ALILAKYLVN NVGDLNINQP EAVKVVSOYC QKIIAEEGGE NKSERAKQAN ALHLLLIGFE
 430 440 450 460 470 480
 QNRERINTVQ NSTYSMDQLN FSSLAEAAAGY ARRANSAYVL KRLDYFCNHS LLKDGNVLVD
 490 500 510 520 530 540
 LPGIDAPVKE DAERAYRKIE SPDTSAVICV LKPAAAGDMS AEETQLLERI SKNHGIRDRV
 550 560 570 580 590 600
 FVFNRRIDT WYNTQLRQRL EGLIQSQFRD NSRVYKTSGL LGFYGSQVKQ TNSSTRFGLD
 610 620 630 640 650 660
 SIFATTIKGF DGEETPOFV SEFNNYCANS GKLLSTAFRV SVNGYETSNE NYVRILSEWG
 670 680 690 700 710 720
 IPLVDQLIHD SGIESFRSGI GLYLAEKYP ELFATLANDL QPLCIALRQF YLENYRQLDS
 730 740 750 760 770 780
 QPREIAAMKA QELTLNQEM QNLGIEFKKY MSAQINDVVI GNDREFDQDF TKLKARMVAR
 790 800 810 820 830 840
 LDELLKTFV MNAKRATES HPRNSTAPFI AVLVEALYYL ANELEDAFIE AIHELKKNFF
 850 860 870 880 890 900
 QRLGDRLRKV DCYHQVYRLV GNDGGIEQLL RRAEEDITKA LVNEARTECD RYVRESPRFY
 910 920 930 940 950 960
 DEGTFSIYQF RQTLQOTSQG YDAQAIVEAE PAIKELLKLD FEPKVFNTVR KNFRQTVNNT
 970 980 990 1000 1010 1020
 LKTHLLPMAE EQAQIILEQY DVARKYREQT LEQDAEEKIA RNSRLQSEIK QKIDLYQTSI
 1030 1040 1050 1060
 VSINECLKAM QIFEQLPVIT ESDITKQAEI VADADFEIV ELEHHHHHH

Figure A9: Amino acid sequence of recombinant mEGFP-SynDLP with annotations.

The mEGFP-tag and *SynDLP* are colored in green and red, respectively. The TEV site between the mEGFP and *SynDLP* is highlighted in magenta and the C-terminal His₆-tag in yellow. The mEGFP-tag was generated from the eGFP-tag by point mutation of one residue (A206K) marked in light gray. The A206K mutation should reduce the tendency of the fluorescent tag to oligomerize (Zacharias *et al.*, 2002). The recombinant protein has a calculated molecular mass of 121.7 kDa.

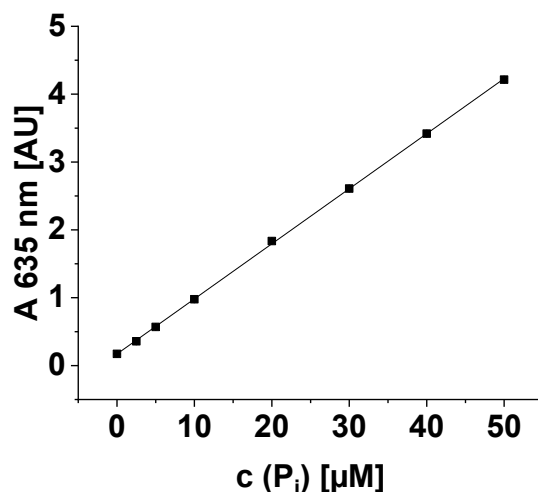


Figure A10: Standard curve of P_i-concentrations determined using the malachite green phosphate assay.

Different P_i-concentrations were obtained by dilution of a P_i-stock with MP-H₂O. The samples were prepared as described in the methods section and then the absorption at 635 nm was measured. Mean ($n = 3$) and error bars (S.D.) are shown. A linear fit (shown as line) was used to calculate the formation of P_i from measured A_{635 nm} values. The fit resulted in the following dependency: $A_{635 \text{ nm}} [\text{AU}] = 0.0812 * c (\text{P}_i) [\mu\text{M}] + 0.1713$ ($r^2 = 0.9999$).

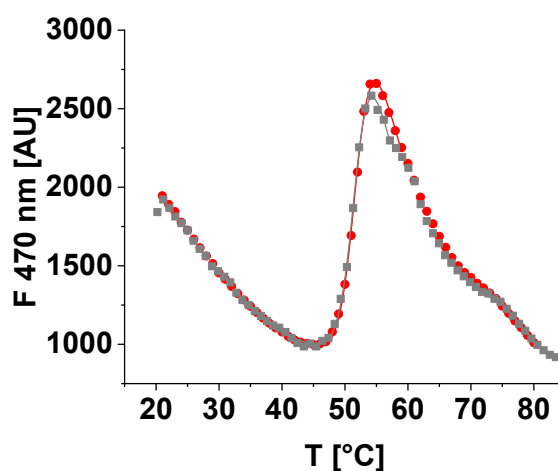


Figure A11: Thermal stability of *SynDLP* in the presence of GTP and GDP.

ANS-FTSA of 5 μM *SynDLP* was measured in the presence of 2 mM GTP (gray) or GDP (red). ANS fluorescence intensities at 470 nm were plotted against the temperature and a temperature range capturing the transition phase was fitted with an adapted Boltzmann fit (Equation (7)). The fit curves are shown as lines. For the condition with GDP, the mean ($n = 3$) is shown. For *SynDLP* in the presence of GTP, a single measurement is displayed.

```

      10           20           30           40           50           60
MSKIAPQCON LREQVNQLIE LLRQEPILRS QQDTSIVETA LGKALSPRE IVFAGAFSAG

      70           80           90           100          110          120
KSMLINALLE RELLYSAEGH ATGTECHIEY ANANEERVVL TFLSEAEIRQ QALILAKYLN

     130          140          150          160          170          180
VNVGDLNINQ PEAVKVVSQY CQKIIAEEGG ENKSERAKQA NALHLLLIGF EQNRERINTV

     190          200          210          220          230          240
QNSTYSMDQL NFSSLAEAAG YARRGANSAY LKRLDYFCNH SLLKDGNVLV DLPGIDAPVK

     250          260          270          280          290          300
EDAERAYRKI ESPDTSAVIC VLKPAAAGDM SAEETQLLER ISKNHGIRDR VFYVFENRIDD

     310          320          330          340          350          360
TWYNTQLRQR LEGLIQSQFR DNSRVYKTSG LLGFYGSQVK QTNSSTRFGL DSIFATTIKG

     370          380          390          400          410          420
FDGEEETPQF VSEFNNYCAN SGKLLSTAFR VSVNGYETSN ENYVRILSEW GIPLVDQLIH

     430          440          450          460          470          480
DSGIESFRSG IGLYLAEKY PELFATLAND LQPLCIALRQ FYLENYRQLD SQPGSGSGSG

     490          500          510          520
GSKIARNSRL QSEIKQKIDL YQTSIVSINE CLKAMQIFEQ LPHHHHHH

```

Figure A12: Amino acid sequence of the *SynDLP-MGD* construct with annotations.

Amino acid sequence of *SynDLP-MGD*. GD, BSE, GS-linker and the C-terminal His₆-tag are highlighted in red, purple, cyan and yellow, respectively.

```

      10           20           30           40           50           60
MHMSATPQVS DASFKEDVLD SELPVLVDFW APWCGPCRMV APVVDEISQQ YEGKVKVVKL

      70           80           90           100          110          120
NTDENPNTAS QYGIRSIPTL MIFKGGQRVD MVVGAVPKTT LASTLEKYLS ENLYFQGQFL

EHHHHHHH

```

Figure A13: Amino acid sequence of recombinant *SynTrxA* with annotations.

Amino acids encoded by *slr0623* of *Synechocystis* are marked in cyan. TEV cleavage site and C-terminal His₆-tag are highlighted in magenta and yellow, respectively. The full-length recombinant protein has a calculated molecular mass of 14.3 kDa.

Abbreviations

Å	Ångström, 10^{-10} m
ADP	adenosine diphosphate
ANS	8-anilinonaphthalene-1-sulfonic acid
APS	ammonium peroxodisulfate
Atl1	atlastin1
ATP	adenosine triphosphate
<i>AtDRP3A</i>	<i>Arabidopsis thaliana</i> DRP3A
<i>AtDRP3B</i>	<i>Arabidopsis thaliana</i> DRP3B
<i>AtDRP5B</i>	<i>Arabidopsis thaliana</i> DRP5B
<i>AtFzl</i>	<i>Arabidopsis thaliana</i> Fzl
ATTO633-PE	ATTO633-1,2-dioleoyl- <i>sn</i> -glycero-3-phosphoethanolamine
BDLP	bacterial dynamin-like protein
biotinyl-Cap-DOPE	1,2-dioleoyl- <i>sn</i> -glycero-3-phosphoethanolamine-N-(cap biotinyl)
bp	base pairs
BSE	bundle signaling element
CD	circular dichroism
Chl a	chlorophyll <i>a</i>
<i>Cj-DLP1/2</i>	<i>Campylobacter jejuni</i> DLP pair 1/2
CM	cytoplasmic membrane
<i>CrFzl</i>	<i>Chlamydomonas reinhardtii</i> Fzl
cryo-EM	cryo-electron microscopy
CTAB	cetyltrimethylammoniumbromide
<i>CtMgm1</i>	<i>Chaetomium thermophilum</i> Mgm1
<i>CtVps1</i>	<i>Chaetomium thermophilum</i> Vps1
CV	column volume
cyt b_6f	cytochrome b_6f complex
DGDG	digalactosyldiacylglycerol
DLP	dynamin-like protein
DMPG	1,2-dimyristoyl- <i>sn</i> -glycero-3-phosphoglycerol
DMSO	dimethyl sulfoxide
DNA	deoxyribonucleic acid

dNTP	deoxynucleotide triphosphate
DOPC	1,2-dioleoyl- <i>sn</i> -glycero-3-phosphocholine
DOPG	1,2-dioleoyl- <i>sn</i> -glycero-3-phosphoglycerol
Drp	dynamain-related protein
DTT	dithiothreitol
Dyn1-3	dynamain isoform 1-3
<i>Ec</i> LeoA	<i>Escherichia coli</i> LeoA
EDTA	ethylenediaminetetraacetic acid
eGFP	enhanced GFP
EHD	Eps15-homology domain-containing protein
EM	electron microscopy
EVC	empty vector control
FD	ferredoxin
FNR	FD-NADP ⁺ reductase
FRET	Förster resonance energy transfer
FSC	Fourier shell correlation
FTSA	fluorescence thermal shift assay
GAP	GTPase-activating protein
GBP	guanylate-binding protein
GD	GTPase domain
GDP	guanosine diphosphate
GFP	green fluorescence protein
GMP	guanosine monophosphate
GMPPnP	guanosine-5'-[(β,γ)-imido]triphosphate
GP	generalized polarization
GTP	guanosine triphosphate
GTPase	GTP hydrolyzing enzyme
GUV	giant unilamellar vesicle
IR	infrared
IP	immunoprecipitation
IPTG	isopropyl- β -D-thiogalactopyranoside
LIC	lysis-inducible cells
LissRhod-PE	1,2-dioleoyl- <i>sn</i> -glycero-3-phosphoethanolamine-N-(Lissamine Rhodamine B sulfonyl)

LUV	large unilamellar vesicle
MDFP	molecular dynamics flexible fitting
mEGFP	monomeric enhanced GFP
MGD	minimal GTPase domain
MGDG	monogalactosyldiacylglycerol
MID	membrane interaction domain
MP-H ₂ O	Millipore water
<i>Ms</i> IniA/C	<i>Mycobacterium smegmatis</i> IniA/C
<i>Mt</i> IniA/C	<i>Mycobacterium tuberculosis</i> IniA/C
Mx	myxovirus resistance protein
NAD ⁺	oxidized nicotinamide adenine dinucleotide
NADH	reduced nicotinamide adenine dinucleotide
NADP ⁺	oxidized nicotinamide adenine dinucleotide phosphate
NADPH	reduced nicotinamide adenine dinucleotide phosphate
NaP _i	sodium phosphate
NBD-PE	1,2-distearoyl- <i>sn</i> -glycero-3-phosphoethanolamine-N-(7-nitro-2-1,3-benzoxadiazol-4-yl)
NCS	non-crystallographic symmetry
<i>Np</i> BDLP	<i>Nostoc punctiforme</i> BDLP
OD	optical density
orf	open reading frame
PBS	phycobilisomes
PC	plastocyanin
PCR	polymerase chain reaction
PG	phosphatidylglycerol
PH	pleckstrin homology
phoA	alkaline phosphatase
P _i	inorganic phosphate
PK/LDH	pyruvate kinase/lactic dehydrogenase mix
PQ	plastoquinone
PRD	proline-rich domain
PS I	photosystem I
PS II	photosystem II
psi	pound-force per square inch

PVA	polyvinyl alcohol
PVDF	polyvinylidene difluoride
RMSD	root-mean-square deviation
RNase	ribonuclease
RT	room temperature
RU	response unit
<i>ScMgm1</i>	<i>Saccharomyces cerevisiae</i> Mgm1
S.D.	standard deviation
SDS-PAGE	sodium dodecyl sulfate polyacrylamide gel electrophoresis
SEC	surface layer
S-layer	surface layer
SPR	surface plasmon resonance
SQDG	sulfoquinovosyldiacylglycerol
SUV	small unilamellar vesicle
<i>SvDynA/B</i>	<i>Streptomyces venezuelae</i> DynA/B
<i>SynDLP</i>	<i>Synechocystis</i> sp. PCC 6803 DLP
<i>SynTrxA</i>	<i>Synechocystis</i> sp. PCC 6803 thioredoxin A
<i>SynTrxB</i>	<i>Synechocystis</i> sp. PCC 6803 thioredoxin B
<i>SynTrxC</i>	<i>Synechocystis</i> sp. PCC 6803 thioredoxin C
<i>SynTrxQ</i>	<i>Synechocystis</i> sp. PCC 6803 thioredoxin Q
TEMED	tetramethylethylenediamine
TM	thylakoid membrane
TMD	transmembrane domain
Trx	thioredoxin
UV	ultraviolet

List of Figures

Figure 1.1: Schematic representation of a <i>Synechocystis</i> cell.....	9
Figure 1.2: Schematic overview of the photosynthetic light reaction in the TMs.	11
Figure 1.3: Lipid composition of <i>Synechocystis</i> total membranes.....	12
Figure 1.4: Conserved GTP-binding motifs in DLPs.....	17
Figure 1.5: Monomer structure of DLPs.....	17
Figure 1.6: Structure-based domain architecture of DLPs.	18
Figure 1.7: Dynamin-mediated membrane constriction.	22
Figure 4.1: <i>SynDLP</i> expression <i>in vivo</i>	83
Figure 4.2: The C777A mutation abolishes the formation of the intramolecular disulfide bridge.	84
Figure 4.3: Cryo-EM structure of oligomeric <i>SynDLP</i>	86
Figure 4.4: Oligomerization of <i>SynDLP</i> in the presence of nucleotides.	87
Figure 4.5: Effect of increasing NaCl concentration on shape and size of <i>SynDLP</i> oligomers.	87
Figure 4.6: Annotated amino acid sequence of <i>SynDLP</i>	89
Figure 4.7: Oligomerization interfaces in <i>SynDLP</i>	90
Figure 4.8: Comparison of oligomeric interfaces in different DLPs.....	92
Figure 4.9: Structural comparison of <i>SynDLP</i> with other bacterial and eukaryotic DLP structures.	93
Figure 4.10: Structural comparison of DLP domains.....	94
Figure 4.11: Structural stabilization and enhanced GTPase activity by an intramolecular disulfide bridge in the BSE domain.....	96
Figure 4.12: The <i>SynDLP</i> s GTPase activity.	98
Figure 4.13: GTP binding affinities of <i>SynDLP</i> variants.	99
Figure 4.14: Mutation of oligomerization interface 3 residues.....	100
Figure 4.15: Biochemical analysis of <i>SynDLP</i> _{HPRN-AAAA}	102
Figure 4.16: Membrane interaction of <i>SynDLP</i>	104
Figure 4.17: Putative membrane interaction domains in <i>SynDLP</i>	105
Figure 4.18: SFG spectra of a deuterated DMPG monolayer.....	107
Figure 4.19: Time-dependent SFG spectra of <i>SynDLP</i> membrane binding.	108
Figure 4.20: SFG spectrum of membrane-bound <i>SynDLP</i> with GTP.....	109
Figure 4.21: Lipid-stimulation of the <i>SynDLP</i> GTPase activity.....	110

Figure 4.22: Membrane fusion activity of <i>SynDLP</i>	111
Figure 4.23: Membrane fusion activity of <i>SynDLP</i> variants.	112
Figure 4.24: Influence of GTP on the membrane fusion activity.....	112
Figure 4.25: Disulfide forming cysteine residues are conserved within cyanobacterial KGK clade DLPs.	115
Figure 4.26: Intermolecular domain contacts in the <i>SynDLP</i> oligomer.	117
Figure 4.27: Effect of DTT on assembly and GTPase activity of <i>SynDLP</i>	122
Figure 4.28: Influence of different salt concentrations on the thermal stability, oligomerization and GTPase activity of <i>SynDLP</i>	124
Figure 4.29: Localization of an intermolecular salt bridge between GD and the stalk in the <i>SynDLP</i> structure.	125
Figure 4.30: Biochemical characterization of <i>SynDLP</i> _{R320A-E585A}	127
Figure 4.31: An intermolecular GD-stalk connection in <i>SynDLP</i> and Dyn3.	130
Figure 4.32: Structural comparison of MIDs from peripherally membrane-attached DLPs. .	132
Figure 4.33: CD spectra of <i>SynDLP</i> in the presence of liposomes.	134
Figure 4.34: Temperature-dependent CD spectra of <i>SynDLP</i> in the presence of liposomes..	134
Figure 4.35: Purification, GTPase activity and oligomerization of an mEGFP-tagged <i>SynDLP</i> variant.	135
Figure 4.36: Binding of mEGFP- <i>SynDLP</i> to GUV membranes.	136
Figure 4.37: Nucleotide-dependent binding of mEGFP- <i>SynDLP</i> to GUV membranes.	137
Figure 4.38: <i>SynDLP</i> can hydrolyze GDP.	138
Figure 4.39: Biochemical analysis of the <i>SynDLP</i> _{558-565GS} variant.	140
Figure 4.40: GTPase activities of <i>SynDLP</i> and <i>SynDLP</i> _{558-565GS} with a C-terminal eGFP-tag.	141
Figure 4.41: Membrane interaction properties of <i>SynDLP</i> _{558-565GS}	142
Figure 4.42: Putative membrane interacting loops in BDLPs.	143
Figure 4.43: Heterologous expression of <i>SynDLP</i> _{694-705GS}	144
Figure 4.44: The structure of <i>SynDLP</i> wt clarifies the position of two putative MIDs that were identified solely based on the amino acid sequence.	145
Figure 4.45: Biochemical analysis of the <i>SynDLP</i> _{667-675GS} mutant.	146
Figure 4.46: Membrane interaction of <i>SynDLP</i> _{667-675GS}	148
Figure 4.47: Biochemical analysis of the <i>SynDLP</i> _{648-665GS} mutant.	150
Figure 4.48: Membrane interaction of <i>SynDLP</i> _{648-665GS}	152
Figure 4.49: Membrane interaction of <i>SynDLP</i> _{HPRN-AAAA}	154

Figure 4.50: Immobilization of liposomes on an SA sensor chip.	157
Figure 4.51: Single cycle measurement of <i>SynDLP</i> binding to DOPG liposomes.	158
Figure 4.52: Single cycle measurement of <i>SynDLP</i> binding to DOPG liposomes in the presence of GTP.	159
Figure 4.53: Localization of all <i>SynDLP</i> regions analyzed in this mutational study.	163
Figure 4.54: The GTP hydrolysis cycle of a DLP.	166
Figure 4.55: <i>SynDLP</i> oligomers in the presence of GTP and GDP.	167
Figure 4.56: GMPPnP binding alters the structure of <i>SynDLP</i> oligomers.	168
Figure 4.57: Nucleotide-binding increases the thermodynamic stability of <i>SynDLP</i> oligomers.	169
Figure 4.58: Design of a <i>SynDLP</i> -MGD construct.	170
Figure 4.59: Expression of <i>SynDLP</i> -MGD and <i>SynDLP</i> -GD.	171
Figure 4.60: Purification of <i>SynDLP</i> -MGD.	173
Figure 4.61: <i>SynDLP</i> -MGD is monomeric and shows a lowered GTPase activity.	174
Figure 4.62: Nucleotide-dependent dimerization of <i>SynDLP</i> -MGD.	175
Figure 4.63: <i>SynDLP</i> -MGD likely dimerizes via GD-GD contacts.	177
Figure 4.64: Typical structure of a Trx.	179
Figure 4.65: Expressions of <i>SynTrxA</i> in different <i>E. coli</i> strains.	181
Figure 4.66: Purification of recombinantly expressed <i>SynTrxA</i>	182
Figure 4.67: Molecular mass estimation of purified <i>SynTrxA</i>	183
Figure 4.68: <i>In vitro</i> activity of purified <i>SynTrxA</i>	184
Figure 4.69: DTT titration to check for an interaction of <i>SynDLP</i> with <i>SynTrxA</i>	185
Figure 4.70: Transmission electron micrographs of an ultrathin section of <i>Synechocystis</i> cells.	189
Figure 4.71: IP of fractionated <i>Synechocystis</i> cells.	190
Figure 4.72: Complete segregation of <i>Synechocystis</i> strains transformed with pCK306-based plasmids coding for <i>SynDLP</i> and mEGFP- <i>SynDLP</i>	191
Figure 4.73: Induction of the expression of an mEGFP-tagged <i>SynDLP</i> variant <i>in vivo</i>	192
Figure 4.74: <i>In vivo</i> localization of mEGFP-tagged <i>SynDLP</i> in <i>Synechocystis</i> cells.	194
Figure 4.75: Complete segregation of <i>Synechocystis</i> wt transformed with <i>lic</i> genes plus the EVC.	196
Figure 4.76: Growth in phosphate-limited medium and Chl a content of different <i>Synechocystis</i> strains.	197
Figure 4.77: Images of wt and $\Delta phoA$ cultured under phosphate-deficient conditions.	198

Figure 4.78: Micrographs of lysis-inducible <i>Synechocystis</i> cells.	199
Figure 4.79: Complete segregation of <i>Synechocystis</i> Δ <i>syndlp</i> cells transformed with <i>lic</i> genes.	200
Figure 4.80: <i>Synechocystis</i> strains Δ <i>syndlp</i> and Δ <i>syndlp</i> - Δ <i>phoA</i> grown under phosphate-deficient conditions visualized via fluorescence microscopy.	201
Figure 4.81: Fluorescence micrographs of lysis-inducible <i>Synechocystis</i> Δ <i>syndlp</i> cells.	202
Figure A1: Map of pET303- <i>SynDLP</i> as an example of a pET303-based plasmid.	235
Figure A2: Map of pCK306-mEGFP- <i>SynDLP</i> as an example of a pCK306-based plasmid.	236
Figure A3: Map of pGEM-T-Easy-Phoa-LIC as an example of a pGEM-T-Easy-based plasmid.	237
Figure A4: Experimental details of the structure determination of <i>SynDLP</i> oligomers.....	238
Figure A5: Conservation of single residues in <i>SynDLP</i>	239
Figure A6: Membrane fusion curves of <i>SynDLP</i> and IM30.	240
Figure A7: Amino acid sequence of <i>SynDLP</i> with annotations.....	241
Figure A8: CD spectra of <i>SynDLP</i> in the presence of liposomes dependent on the temperature.	242
Figure A9: Amino acid sequence of recombinant mEGFP- <i>SynDLP</i> with annotations.....	243
Figure A10: Standard curve of P_i -concentrations determined using the malachite green phosphate assay.	244
Figure A11: Thermal stability of <i>SynDLP</i> in the presence of GTP and GDP.	244
Figure A12: Amino acid sequence of the <i>SynDLP</i> -MGD construct with annotations.....	245
Figure A13: Amino acid sequence of recombinant <i>SynTrxA</i> with annotations.	245

List of Tables

Table 3.1: Composition of used buffers and solutions.	29
Table 3.2: Bacterial strains used in this study.....	32
Table 3.3: Media used for growth of microorganisms.	34
Table 3.4: Oligonucleotides used in this study. F = forward, R = reverse.	35
Table 3.5: Plasmids used in this study.....	40
Table 3.6: Antibodies used in this study.....	41
Table 3.7: Enzymes used in this study and their manufacturers.	41
Table 3.8: Kits used in this study and their manufacturers.....	41
Table 3.9: Markers used in this study.....	42
Table 3.10: Instruments used in this study and their manufacturers.	43
Table 3.11: Software applied in this study.	45
Table 3.12: Typical pipetting scheme of a PCR reaction with a total volume of 50 µl used for molecular cloning.	47
Table 3.13: PCR program used for DNA amplification.	47
Table 3.14: Composition of SDS-PAGE separation and stacking gels.....	57
Table 3.15: Details of cryo-EM sample preparation and data collection.	73
Table 4.1: Author contributions of “ <i>SynDLP</i> is a dynamin-like protein of <i>Synechocystis</i> sp. PCC 6803 with eukaryotic features”.	78
Table 4.2: Cryo-EM data collection and refinement statistics.....	88
Table 4.3: Transition temperatures of <i>SynDLP</i> variants determined via CD spectroscopy and ANS-FTSA	97
Table 4.4: Kinetic parameters describing the GTPase activity of <i>SynDLP</i> variants.....	99
Table 4.5: Parameters describing DTT-dependent properties of <i>SynDLP</i>	122
Table 4.6: Parameters describing salt-dependent properties of <i>SynDLP</i>	125
Table 4.7: Biochemical properties of <i>SynDLP</i> _{R320A-E585A}	127
Table 4.8: Biochemical properties of proteins analyzed in this study.....	155
Table 4.9: Membrane interaction properties of proteins analyzed in this study.....	155

[Redacted text block]

[Redacted text block]

[Redacted text block]

[Redacted text block] 😊

Curriculum vitae

[Redacted]

[Redacted]	[Redacted]
[Redacted]	[Redacted]
[Redacted]	[Redacted]

[Redacted]

[Redacted]	[Redacted]
	[Redacted]
	[Redacted]
	[Redacted]
[Redacted]	[Redacted]
	[Redacted]
	[Redacted]
[Redacted]	[Redacted]
	[Redacted]
	[Redacted]
[Redacted]	[Redacted]
	[Redacted]
	[Redacted]
[Redacted]	[Redacted]
	[Redacted]
	[Redacted]

[REDACTED]

[REDACTED]

[REDACTED]
[REDACTED]
[REDACTED]
[REDACTED]
[REDACTED]

[REDACTED]

[REDACTED]
[REDACTED]
[REDACTED]
[REDACTED]
[REDACTED]

[REDACTED]

[REDACTED]
[REDACTED]
[REDACTED]

[REDACTED]

[REDACTED]

[REDACTED]

[REDACTED]
[REDACTED]
[REDACTED]

[REDACTED]

[REDACTED]
[REDACTED]
[REDACTED]

[REDACTED]

[REDACTED]

[REDACTED]
[REDACTED]
[REDACTED]

[REDACTED]

[REDACTED]

[REDACTED]

[REDACTED]

[REDACTED]

[REDACTED]

[REDACTED]

[REDACTED]

[REDACTED]

[REDACTED]

[REDACTED]

[REDACTED]

[REDACTED]

[REDACTED]

[REDACTED]

[REDACTED]

[REDACTED]

[REDACTED]

[REDACTED]

[REDACTED]

[REDACTED]

[REDACTED]

[REDACTED]

[REDACTED]

[REDACTED]

[REDACTED]

[REDACTED]

[REDACTED]

[REDACTED]

[REDACTED]

[REDACTED]

[REDACTED]

[REDACTED]

[REDACTED]

[REDACTED]

[REDACTED]

[REDACTED]

[REDACTED]

[REDACTED]

[REDACTED]

[REDACTED]
[REDACTED]
[REDACTED]
[REDACTED]
[REDACTED]
[REDACTED]
[REDACTED]
[REDACTED]
[REDACTED]
[REDACTED]
[REDACTED]
[REDACTED]
[REDACTED]